Gran Sasso Science Institute
Scuola Internazionale Superiore di Studi Avanzati

Advanced search for neutrinoless double beta decay in selenium-82 with CUPID-0

PhD thesis

submitted January 25, 2018

PhD Candidate
Lorenzo Pagnanini

Advisors

Prof. F. Bellini
Sapienza Università di Roma
INFN, Roma

Dott. S. Pirro
INFN, Laboratori Nazionali del Gran Sasso

Tutor

Dott. L. Pattavina
Gran Sasso Science Institute

Gran Sasso Science Institute
XXX Cycle – A.Y. 2014-2017

The greatest enemy of knowledge is not ignorance,
it is the illusion of knowledge.

Stephen Hawking

Abstract

The CUPID-0 detector hosted at the Laboratori Nazionali del Gran Sasso (LNGS), is the first large array of enriched scintillating cryogenic detectors for the investigation of ^{82}Se neutrinoless double-beta decay ($0\nu\beta\beta$). The assembly of the experiment ended in October 2016 and after four months of commissioning, debugging and performance optimization the data taking has started in March 2017.

No evidence of signal was found in a 1.83 kg $\cdot$ y ^{82}Se exposure, setting the best lower limit on the $0\nu\beta\beta$ ^{82}Se half-life $T^{0\nu}_{1/2}$ >$2.4 \cdot 10^{24}$ y (90% C.I.), which corresponds to an effective Majorana neutrino mass $m_{\beta\beta} <$ 376-770 meV depending on the nuclear matrix element calculations. The heat-light readout provided a powerful tool for α-particles rejection and allowed to suppress the background in the region of interest to $(3.6^{+1.9}_{-1.4}) \cdot 10^{-3}$ counts/(keV $\cdot$ kg $\cdot$ y), an unprecedented level for this technique. This result was achieved by a forefront technology for background suppression and thorough protocols and procedures for detector preparation.

This Ph.D. work describes all the different phases of the detector design, construction and optimization carried out at LNGS since February 2015. Moreover the analysis tasks such us pulse shape analysis, evaluation of internal contamination and eventually the fit in the region of interest are discussed.

Contents

Introduction

Almost all the known elementary particles are distinct from their own anti-particle by the opposite values of electric charge. Such a distinction is not obvious in the case of the neutrino, which is the only neutral elementary fermion. Ettore Majorana in 1937 was the first to tackle the problem of the symmetric description of particles and anti-particles: Dirac's theory exploits four different states to describe them while Majorana's theory simplified this representation, leading only to two neutrino states. The American theoretical physicist and mathematician Frank Wilczek, Nobel laureate in 2004, said *"Theoretical physics is a quest for simplicity"* [1]. In other words: why should Nature introduce two useless physical states?

The most sensitive probe to investigate the Dirac or Majorana character of the neutrino is the so called *Neutrinoless Double Beta Decay*. In spite of the ungenerous name towards the neutrino, it is the leading actor of the decay. Indeed it can happen if neutrino is a *Majorana particle*. A measurement of the decay rate may constrain the *absolute neutrino mass* scale. Additionally, the discovery of this nuclear transition would unambiguously demonstrate that *lepton number* is not a conserved. These fundamental implications call for a considerable worldwide effort in searching for this decay.

Several experiments in different underground laboratories are searching for neutrinoless double beta decay of different isotopes: GERDA (^{76}Ge), CUORE (^{130}Te) and CUPID-0 (^{82}Se) at LNGS (Italy), SuperNEMO (^{82}Se mainly) at LSM (France), MAJORANA (^{76}Ge) at SURF in USA, KamLandZEN (^{136}Xe) at Kamioka Observatory (Japan).

This thesis work is developed in the framework of the CUPID-0 experiment. CUPID-0 (CUORE Upgrade with Particle IDentification) is a pilot project for a future tonne-scale $0\nu\beta\beta$ experiment based on scintillating calorimeters. It is the first array of scintillating calorimeters made with 24 ZnSe enriched crystals and 2 natural ones. The main goal of CUPID-0 is to demonstrate the low background achievable exploiting this technique as well it will set a new lower limit on the half-life of the ^{82}Se $0\nu\beta\beta$ decay. Moreover it will provide a more precise measurement of the half-life of the ^{82}Se $2\nu\beta\beta$ decay. The data taking started in March 2017 and the first results after almost one year are detailed in this thesis and they will be released soon.

[1] From "This Explains Everything", Ed, John Brockman, Harper Perennial, New York, 2013

The main contribution of this Ph.D. work has been implementing and operating the first array of scintillating enriched calorimeters to search for $0\nu\beta\beta$ decay. During the crystal production (Sept. 2015 – Feb. 2016) I characterized several batches of ZnSe crystals to validate the powder purification protocol and crystal growth itself, as a first step towards CUPID-0. Afterwards I have been involved in all the phases of the detector preparation (Feb. 2016 – Sept 2016), mounting (Sept. 2016 – Nov. 2016) and commissioning (Nov. 2016 – Feb. 2017) at LNGS. When the data-taking has started I served as the first analysis shifter in charge of defining the standard procedure for signal processing, data quality check and data analysis. I have been responsible for data transfer and storage as well as for database interface to DAQ and analysis software. As a member of the analysis team I was involved in the pulse shape analysis, taking care of the normalization of the shape parameters as a function of the energy with periodical neutron calibrations. Moreover the background analysis carried out within this thesis demonstrate the feasibility of this technique for a future tonne-scale experiment, producing also a preliminary scientific result.

All the theoretical background needed to understand the crucial role of the Neutrinoless Double Beta Decay in the modern Astroparticle Physics is introduced in the Chapter 1. Starting from the neutrino picture given by the Standard Model, theoretical and phenomenological aspects concerning the Majorana's theory and its implications are detailed. The last section is instead dedicated to the experimental challenges, describing also the future perspectives of the most promising technologies.

The Chapter 2 illustrates the working principle of scintillating cryogenic calorimeters (usually called scintillating bolometers) as one of the leading technologies to face this challenge. The fundamental elements of a calorimeter are discussed exploiting a simplified thermal model, useful also to explain signal generation, performances and operating principle of these detectors. The chapter focuses on passive and active background reduction, in particular measuring the light to tag the α-particles. Finally the CUPID project and its R&D activities are detailed.

The Chapter 3 describes the whole route of the CUPID-0 detector construction, starting from the elemental zinc and selenium up to the data-taking. The first part details all the steps to produce radiopure good-quality enriched ZnSe crystals. After a brief discussion of the bolometric test with the first three enriched ZnSe crystals, the other detector components are described (i.e. light detectors, heaters, reflector foils, Ge-NTDs, copper). The detector assembly section starts with the thermal sensors gluing and follows all the stages up to the detector housing in the cryostat. The improvements of the cryogenic apparatus, the electronics system and DAQ are briefly introduced in separated sections, while the detector commissioning operation is deeply discussed in the last part.

The Chapter 4 details signal processing procedure, pulse shape analysis and data selection criteria quality cuts. Most of the analysis technique used in CUPID-0 are introduced in the first section. Crucial performances such as energy threshold and resolution are addressed in the following sections, together with the pulse shape analysis, the opti-

mization of the related shape cuts and the efficiency estimation.

In the Chapter 5 the first results of CUPID-0 are reported. The radiopurity of the crystals is studied analyzing the α-region of the energy spectrum. The background in the region of interest is reported and discussed applying the different selection criteria developed for the scintillating calorimeters. Finally the first limit on the half-life of the ^{82}Se $0\nu\beta\beta$ decay is reported.

Chapter 1

Neutrino physics and $0\nu\beta\beta$ decay

Since its debut in the scientific community, the neutrino plays a crucial role in the particle physics game, due to its peculiar cocktail of properties: at the same time the neutrino is the lightest massive particle in the Standard Model, the most elusive one and the only neutral fundamental fermion. This last feature in particular makes the neutrino the perfect probe for the Majorana hypothesis, exploiting the Neutrinoless Double Beta Decay. Being a neutral particle one can distinguish a neutrino from its anti-particle only indirectly, through its interactions with other particles. For this reason neutrino and anti-neutrino could be the same particle, interacting in two different ways according to the chirality. The discovery of the neutrino oscillations, uncovering its massive nature, pushed the research in this direction, because only a massive particle can flips its chirality. The challenges that must be addressed to clarify the neutrino nature imposed to cross the traditional disciplinary boundaries, establishing strong links among nuclear physics, astrophysics and cosmology.

In this chapter the theoretical framework to describe massive neutrinos, the role of the **neutrinoless double beta decay** and the recent experimental achievements in this field are introduced.

1.1 The Standard Model Neutrino

The neutrino hypothesis was introduced in 1930 by Wolfgang Pauli to explaining the continuum spectrum of the electrons in the β decay, preserving the energy conservation [1]. Considering also the conservation of electric charge and angular momentum, the neutrino had to be neutral with spin $1/2$. Following Pauli's idea, Enrico Fermi proposed his theory of β decay [2] in 1934, based on which Bethe and Peierls predicted the cross section for the neutrino-matter interaction to be very small, concluding that "there is no practically possible way of observing the neutrino" [3]. From this article Bruno Pontecorvo understood that only shooting a huge amount of neutrinos on a specific target it is possible to identify them through the interactions of the daughter-particles, so that the

vicinity of a nuclear reactor would be a good place to search for neutrinos. Thanks to the fundamental advises of Jules Guéron, who suggested that the production of radioactive argon could be the key point, Pontecorvo proposed the Chlorine experiment in 1946 [4], based on the reaction:

$$\nu_e + {}^{37}Cl \longrightarrow {}^{37}Ar + e^-. \tag{1.1}$$

The electronic anti-neutrino ($\bar{\nu}_e$) was the first discovered, by F. Reines and C. Cowan in 1956 [5] at the Savannah River Reactor in South Carolina: the electronic anti-neutrinos produced by the nuclear reactor interact in the detector according to the following process,

$$\bar{\nu}_e + p \longrightarrow n + e^+, \tag{1.2}$$

producing in the final state neutrons and positrons; the coincidence among the γs from the electron-positron annihilation and the nuclear capture of the neutron was the proof of the anti-neutrino reaction occurrence.

The muon neutrinos (ν_μ) and anti-neutrinos ($\bar{\nu}_\mu$) can be produced by pion and muon decay:

$$\pi^+ \longrightarrow \mu^+ + \nu_\mu, \tag{1.3}$$
$$\mu^+ \longrightarrow e^+ + \nu_e + \bar{\nu}_\mu. \tag{1.4}$$

When the pion decay in Eq. 1.3 was discovered, it was natural to ask if the missing particle produced in the decay was the same produced in the β-decay. The answer arrived in 1962 when L. Lederman, M. Schwartz and J. Steinberger, at the Brookhaven National Laboratory, performed the first experiment with neutrinos from accelerator [6]. A Beryllium target was bombarded with a 15 GeV proton beam, producing a beam of pions; 20 meters ahead the interaction point a 5000-tonne steel wall made of old battleship plates was placed. On the way, the pions decayed into muons and neutrinos, but only the latter particles could pass through the wall to be detected in a neon-filled detector, called a spark chamber. There, two interactions could happen among the incoming neutrinos (ν) and nucleons (N):

$$\nu + N \longrightarrow \mu^- + X, \tag{1.5}$$
$$\nu + N \longrightarrow e^- + X. \tag{1.6}$$

Only the first kind of interactions was detected, proving the existence of a new neutrino (i.e. ν_μ) different from the ν_e identified in the β-decay. The electronic channel of the pion decay, that can mimics the signal,

$$\pi^+ \longrightarrow e^+ + \nu_e, \tag{1.7}$$

is strongly suppressed, in spite of the large phase space, due to the V-A nature of the weak interaction.

A further step forward in understanding the neutrino properties was in 1957, when Goldhaber showed that neutrinos are left-handed particles [7]. No evidence for right-handed neutrinos, left-handed antineutrinos were founded.

The existence of a third neutrino (ν_τ) was postulated in 1975, contextually with the τ lepton discovery by M. L. Perl at SLAC [8], but its detection was made by the DONUT experiment only in 2001 [9]. The measurements performed at the electron-positron collider LEP at CERN showed that there are only 3 active light neutrinos [10].

Considering the experimental evidences so far discussed, neutrinos can be introduced as a massless neutral particles with spin $1/2$ represented by the spinor $\nu(x)$ in the Dirac Lagrangian:

$$\mathcal{L} = \bar{\nu}(x) i\gamma^\mu \partial_\mu \nu(x), \tag{1.8}$$

whence, imposing $\delta\mathcal{L} = 0$, one can get the Dirac equation:

$$i\gamma^\mu \partial_\mu \nu(x) = 0. \tag{1.9}$$

In the massless case, the Dirac equation can be solved in a 2-dimension space and the Lagrangian acquires an extended symmetry, i.e. the *chiral symmetry*; using the *chiral projectors*,

$$P_\pm = \frac{1 \pm \gamma^5}{2}, \tag{1.10}$$

one can separate the spinor ν in

$$\nu = \frac{1+\gamma^5}{2}\nu + \frac{1-\gamma^5}{2}\nu = \nu_R + \nu_L, \tag{1.11}$$

and write the Eq. 1.8 as[1]

$$\mathcal{L} = \bar{\nu}_R i\gamma^\mu \partial_\mu \nu_R + \bar{\nu}_L i\gamma^\mu \partial_\mu \nu_L, \tag{1.12}$$

which is symmetric under the transformations $U_R(1)$, $U_L(1)$, that act separately on ν_R and ν_L, establishing the chiral group $SU_L(2) \times SU_R(2) \times U_L(1) \times U_R(1)$. The V-A nature of the electroweak theory means that only the left-handed component of the neutrino (ν_L) and the right-handed one of the anti-neutrino ($\bar{\nu}_R$) are active. Therefore in the Standard Model neutrinos are produced with a defined chirality, which can not change if they are massless[2]. Whereby the **charge current** and **neutral current** interactions in the leptonic sector are described by the Lagrangians:

$$\mathcal{L}_W = -\frac{g}{\sqrt{2}} \sum_{\alpha=e,\mu,\tau} (\bar{l}_{L\alpha}\gamma^\lambda \nu_{L\alpha} W^-_\lambda + \bar{\nu}_{L\alpha}\gamma^\lambda l_{L\alpha} W^+_\lambda), \tag{1.13}$$

$$\mathcal{L}_Z = -\frac{g}{2\cos\theta_W} \sum_{\alpha=e,\mu,\tau} \bar{\nu}_{L\alpha}\gamma^\lambda \nu_{L\alpha} Z_\lambda. \tag{1.14}$$

The discovery of the neutrino oscillations changes this standard representation, showing the neutrinos are massive particles [11].

[1] The mixed terms vanish, because the products of the projectors $P_\pm P_\mp$ are zero.

[2] The Standard Model as it is can include massive neutrinos but if no right-handed neutrinos are added, the model becomes non-renormalisable. Adding right-handed neutrinos fixes this.

1.2 Flavor oscillations and neutrino mixing

The flavor oscillation of neutrinos is a quantum mechanical phenomenon due to the existence of two different sets of eigenstates, the flavor one for the weak interactions (ν_e, ν_μ, ν_τ) and the mass one (ν_1, ν_2, ν_3). The neutrinos are produced as flavor eigenstates but of course propagate as mass-defined states, resulting in a path-length dependence of the probability to find a certain neutrino flavor: different mass states acquire different phases on the path, it means to change the ratios among the three mass states, namely the flavor itself.

The two sets of eigenstates are connected by the Pontecorvo-Maki-Nakagawa-Sakata (PMNS) matrix [12, 13], the leptonic analogous of the Cabibbo, Kobayashi, Maskawa (CKM) matrix that describes the flavor changing in the quark sector. The U_{PMNS} matrix can be parametrized as:

$$U_{PMNS} = \begin{pmatrix} 1 & 0 & 0 \\ 0 & c_{23} & s_{23} \\ 0 & -s_{23} & c_{23} \end{pmatrix} \begin{pmatrix} c_{13} & 0 & s_{13}e^{-i\delta} \\ 0 & 1 & 0 \\ -s_{13}e^{i\delta} & 0 & c_{13} \end{pmatrix} \begin{pmatrix} c_{12} & s_{12} & 0 \\ -s_{12} & c_{12} & 0 \\ 0 & 0 & 1 \end{pmatrix}, \quad (1.15)$$

where s_{ij} and c_{ij} are the sine and the cosine of the mixing angles θ_{12}, θ_{23} and θ_{13} and δ_{CP} is the CP-violation phase.

Therefore a defined-flavor neutrino can be written as a function of the defined-mass neutrinos through the U_{PMNS} matrix:

$$|\nu_\alpha\rangle = \sum_{i=1}^{3} U^*_{\alpha i} |\nu_i\rangle \qquad \alpha = e, \mu, \tau, \quad (1.16)$$

and its time-evolution will be:

$$|\nu_\alpha\rangle = \sum_{i=1}^{3} U^*_{\alpha i} e^{-iE_i t} |\nu_i\rangle \qquad \alpha = e, \mu, \tau, \quad (1.17)$$

whence the oscillation probability of a certain flavor to a different one can be obtained as:

$$P(\nu_\alpha \to \nu_\beta) = |\langle \nu_\beta | \nu_\alpha(t) \rangle|^2 = \sum_{j=1}^{3} \left| U^*_{\alpha j} U_{\beta j} e^{-i\frac{m_j^2 L}{2E}} \right|, \quad (1.18)$$

where E is the ν_α neutrino energy and L is the distance among the production point and the interaction one. In the Eq. 1.15 the U_{PMNS} has been decomposed in three sub-matrices. The first one connects only $|\nu_2\rangle$ and $|\nu_3\rangle$, the second one involves $|\nu_1\rangle$ and $|\nu_3\rangle$, while the last one mixes $|\nu_1\rangle$ and $|\nu_2\rangle$. The presence of a small parameter in the central matrix (i.e. s^2_{13} ~0.02) makes the 3ν mixing approximately reducible to an effective 2ν mixing in several cases of experimental interest.

Indeed, considering oscillations only among two different flavors, the previous Eq. 1.18 becomes,

$$P(\nu_\alpha \to \nu_\beta) = sin^2(2\theta) sin^2 \left(1.27 \cdot \frac{\Delta m^2}{[eV^2]} \frac{L}{[m]} \frac{[MeV]}{E} \right), \quad (1.19)$$

where one can get an intuitive understanding of the dependence from the mixing angle θ and the parameter L/E. Moreover Eq. 1.19 shows clearly that, since the oscillation probability depends on $\Delta m^2 = m_i^2 - m_j^2$, flavor oscillations can happen only if neutrinos have different masses. Finally, under the *two-neutrino approximation*, the oscillation experiments can probe only the absolute value of Δm^2_{ij}, being the oscillation probability dependent on the sine-squared function. The so-called matter effect introduced in the next section allows us to overcame this hindrance and get the value of Δm^2_{21} from the solar neutrinos.

1.2.1 The MSW matter effect

In the ordinary matter the abundance of electrons provides an additional phase to the electronic component of the neutrinos. It corresponds to the forward coherent ν_e-e scattering:

$$\nu_e + e \longrightarrow \nu_e + e, \tag{1.20}$$

described by the Hamiltonian:

$$H = \frac{G_F}{\sqrt{2}} \int d^3x \; \overline{\nu_e}\gamma^\mu(1-\gamma_5)\nu_e \; \langle \bar{e}\gamma_\mu(1-\gamma_5)e\rangle. \tag{1.21}$$

Here the average is on the electron states, but the ordinary matter is at rest and unpolarized, so the only contribution is given by $\langle \bar{e}\gamma_0 e\rangle = \langle e^\dagger e\rangle \equiv n_e$, namely, the density of electrons. The scattering phase of ν_e in a sample of matter of size dx is given by $\sqrt{2}G_F n_e dx$, this term produces an effect on neutrino oscillations, the so called *MSW effect* (Mikheev, Smirnov [15] and Wolfenstein [14]). The ratio of this new phase and the ones acquired by the neutrinos in the solar and the atmospheric oscillations [16],

$$\frac{\sqrt{2}G_F n_e}{\Delta m^2/(2E_\nu)} \approx \begin{cases} \left(\frac{7.5 \cdot 10^{-5}\text{eV}^2}{\Delta m^2}\right)\left(\frac{E_\nu}{5 \text{ MeV}}\right)\left(\frac{\rho_e}{100 \text{ mol/cm}^3}\right) \\ \left(\frac{2.4 \cdot 10^{-3}\text{eV}^2}{\Delta m^2}\right)\left(\frac{E_\nu}{5 \text{ GeV}}\right)\left(\frac{\rho_e}{3 \text{ mol/cm}^3}\right) \end{cases} \tag{1.22}$$

allow to understand in which cases the presence of matter produces a measurable effect. The solar neutrinos from pp reaction (produced where $\rho_e \sim 100$ mol/cm^3 and with $\Delta m^2 = 7.5 \cdot 10^{-5}$ eV^2) have energy of about $E_\nu \ll 1$ MeV so that the matter effect can be neglected, instead for ^{8}B solar neutrinos, with energies above 5 MeV, this is important. The matter effect can play a role also for high energy neutrinos that cross the Earth (where $\rho_e \sim 3$ mol/cm^3 and $\Delta m^2 = 2.4 \cdot 10^{-3}$ eV^2) but this is not observed yet.

1.2.2 Experimental evidences

The first evidence of the *solar neutrinos deficit* was established in 1968 by the Homestake experiment in South Dakota [18], that observed only one third of the expected solar neutrino flux with respect to the prediction of Bahcall model in 1964 [17], exploiting the

reaction in Eq. 1.1 suggested by Pontecorvo, Guéron and Pryce. The result was confirmed by the experiments SAGE [19] and GALLEX/GNO [20], that achieve an unprecedented sensitivity using the ^{71}Ga reaction. These detectors were the first ones able to detect the neutrinos produced in the Sun from the proton-proton fusion reactions[3]. GALLEX and its successor GNO measured solar neutrinos at Laboratori Nazionali del Gran Sasso from 1992 to 2003. The solar neutrino anomaly was finally solved later by the Sudbury Neutrino Observatory (SNO) experiment [22] using a heavy water (D_2O) Cherenkov detector, sensible to neutrino interactions through three different interactions:

- Elastic scattering (ES): $\nu_\alpha + e^- \longrightarrow \nu_\alpha + e^-$ with $\alpha = e,\mu,\tau$, involving all neutrino flavors but with a different cross-section;
- Charged current (CC): $\nu_e + D \longrightarrow 2p + e^-$, involving only electron neutrinos;
- Neutral current (NC): $\nu_\alpha + D \longrightarrow p + n + \nu_\alpha$, involving all neutrino flavor with the same cross-section.

Naming ϕ_α the neutrino flux for the flavor α, ES allows to determine the flux $\phi_{ES} = \phi_e + 0.155\ (\phi_\mu + \phi_\tau\ )$, CC determines $\phi_{CC} = \phi_e$ and NC determines the total flux $\phi_{TOT} = \phi_e + (\phi_\mu + \phi_\tau\ )$. Thus, the ratio of CC/NC can be interpreted as a ratio of ν_e flux to the total flux of the three flavors. These three different reactions measured three independent linear combination of electron, muon and tau neutrino fluxes. Being the total initial ν_e flux determined independently from theoretical model, such measurements allowed to obtain clear evidence of solar neutrino transmutation that produces a mixed flux of ν_e, ν_μ, ν_τ, in which ν_e is only one third of the total.

The study of the anti-neutrinos produced by the nuclear reactors, performed by the KamLAND collaboration [23], allowed to obtain the survival probability of the electronic anti-neutrinos as a function of L/E, reconstructing for the first time the oscillation pattern showed in Fig. 1.1.

The neutrinos oscillation was observed also for the atmospheric neutrinos [24], produced by the cosmic rays interaction in the atmosphere through the following chain:

$$\pi^\pm \longrightarrow \mu^\pm + \nu_\mu(\bar{\nu}_\mu), \tag{1.23}$$

$$\mu^\pm \longrightarrow e^\pm + \nu_e(\bar{\nu}_e) + \bar{\nu}_\mu(\nu_\mu). \tag{1.24}$$

Their energy spans from a few MeV up to several GeV, while the flight path length depends by the zenith angle detection and varies from 10 to 30 km, for downward neutrinos, and up to thousands km, for upward neutrinos, running through the Earth. Since neutrinos can be generated at any point of the atmosphere, neutrinos of the same energy can travel very different distances before reaching the detector, giving different oscillation probabilities. Thus a detector able to distinguish muon neutrinos from electron neutrinos

[3] Of course GALLEX and GNO were not able to distinguish neutrinos from different sources (i.e. pep, ^{7}Be, ^{8}B) but integrating over the different fluxes there was a statistical evidence of p-p neutrinos. Only in 2014, the Borexino collaboration published an analysis of the p-p fusion activity in the solar core [21].

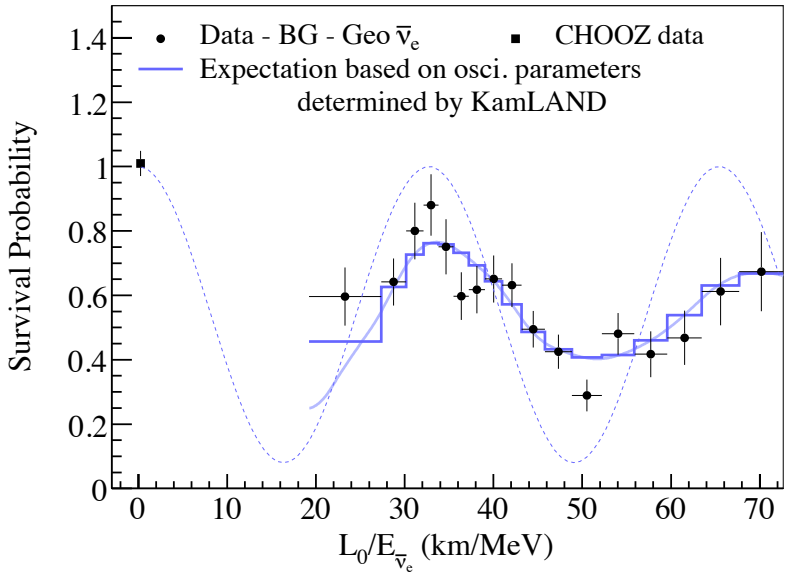

Figure 1.1: Ratio of the background subtracted $\bar{\nu}_e$ spectrum to the expectation for no-oscillation as a function of L_0/E, where L_0 is the effective baseline taken as a flux-weighted average (L_0 = 180 km). The point derived from the Chooz data (short baseline) is included. Figure and caption taken from [23].

and also able to determine their incoming direction is necessary. The SuperKamiokande experiment found an evident asymmetry among the neutrinos produced in overlying atmosphere and the ones that reach the detector after being produced at the antipodes and passing through the Earth [24].

From the solar neutrinos it was possible to measure the mixing angle θ_{12} and the mass difference Δm^2_{12}, while the atmospheric neutrinos are sensitive to θ_{23} and Δm^2_{23}. The matter effect in the solar oscillation allows to determine the sign of Δm^2_{12}, thanks to the additional phase acquired by electronic neutrinos.

The last mixing angle θ_{13} is the smallest one of the PMNS matrix. For this reason the related oscillations have been the most difficult to observe. Thanks to the current-generation reactor and accelerator experiments, which have provided a better sensitivity to small mixing angle, the value of θ_{13} has become accessible (T2K [25], Daya-Bay [26], Reno [27] and Double-CHOOZ [28]). The new measurement of θ_{13} has provided further constrains on the measurements of Δm^2_{12} and θ_{12}, based on a three flavor oscillation analysis [29], as shown in Fig. 1.2.

The three-flavor oscillation parameters from the global fit are detailed in Fig. 1.3. Here the mass splittings are labeled by Δm_{ij} following the same notation used in Sec. 1.2

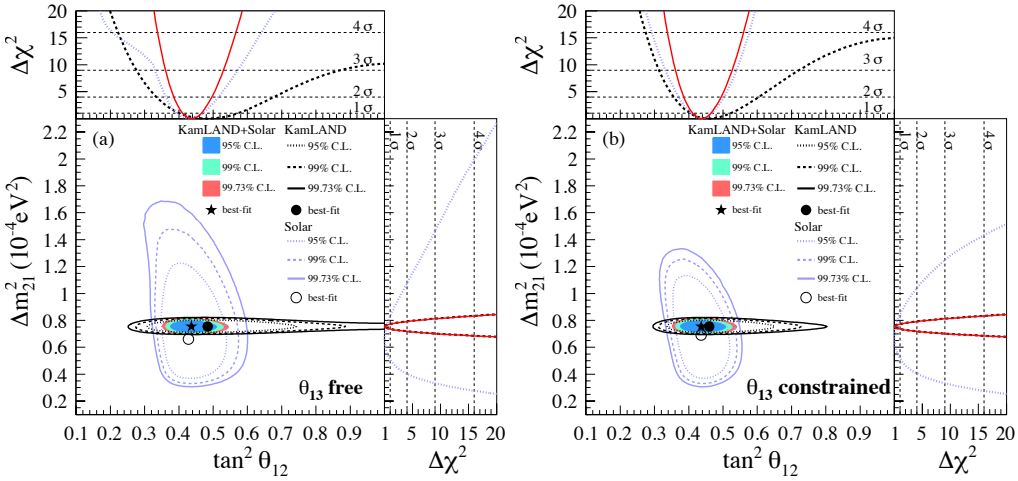

Figure 1.2: Comparison among the allowed region for neutrino oscillation parameters from KamLAND and solar neutrino experiments, with (right) and without (left) the experimental constrain on θ_{13}: the central value and the 1 σ uncertainty region are not changed but the significance of the result improves significantly making narrower the C.L. regions. The side panels show the χ^2 distribution for KamLAND (dashed light blue line) and solar experiments (dotted black line), as well as the combination of both (solid red line) [29].

but also the following notation will be useful for the next discussions:

$$\delta m^2 = m_2^2 - m_1^2 \quad \text{and} \quad \Delta m^2 = m_3^2 - \frac{m_1^2 + m_2^2}{2} \tag{1.25}$$

where δm^2 is the difference between ν_1 and ν_2, while Δm^2 is the difference between the ν_3 mass and the mid-point of ν_1 and ν_2 masses.

1.3 Which mass for which neutrino?

According to the Eq. 1.18 the neutrino oscillations imply they have different masses, but it is not so simple to measure them. In the PMNS matrix 1.15 there is a small parameter ($\sin^2\theta_{13} \simeq 0.02$), then the central matrix can be approximated with the identity. As a consequence the oscillations described by the other two matrices are decoupled: in the solar oscillation only ν_1 and ν_2 are involved while in the atmospheric case only ν_2 and ν_3. In both the situations the decoupling would prevent to know the sign of Δm^2_{ij}, but in the solar neutrinos experiments the matter effect provides an additional relative phase among the mass eigenstate ν_1 and ν_2 due to their different ν_e composition (see Fig. 1.4); conversely the path of the atmospheric neutrinos is too short so that the matter effect cannot be measured. The absolute mass scale for neutrinos is still unknown, so that the mass eigenstates can be classified according to two different *hierarchies*:

- *Direct hierarchy*, $\Delta m^2_{23} > 0$, i.e. $m_3 > m_2 > m_1$;

NuFIT 3.2 (2018)

	Normal Ordering (best fit)		Inverted Ordering ($\Delta\chi^2 = 4.14$)		Any Ordering
	bfp $\pm 1\sigma$	3σ range	bfp $\pm 1\sigma$	3σ range	3σ range
$\sin^2\theta_{12}$	$0.307^{+0.013}_{-0.012}$	$0.272 \to 0.346$	$0.307^{+0.013}_{-0.012}$	$0.272 \to 0.346$	$0.272 \to 0.346$
$\theta_{12}/^\circ$	$33.62^{+0.78}_{-0.76}$	$31.42 \to 36.05$	$33.62^{+0.78}_{-0.76}$	$31.43 \to 36.06$	$31.42 \to 36.05$
$\sin^2\theta_{23}$	$0.538^{+0.033}_{-0.069}$	$0.418 \to 0.613$	$0.554^{+0.023}_{-0.033}$	$0.435 \to 0.616$	$0.418 \to 0.613$
$\theta_{23}/^\circ$	$47.2^{+1.9}_{-3.9}$	$40.3 \to 51.5$	$48.1^{+1.4}_{-1.9}$	$41.3 \to 51.7$	$40.3 \to 51.5$
$\sin^2\theta_{13}$	$0.02206^{+0.00075}_{-0.00075}$	$0.01981 \to 0.02436$	$0.02227^{+0.00074}_{-0.00074}$	$0.02006 \to 0.02452$	$0.01981 \to 0.02436$
$\theta_{13}/^\circ$	$8.54^{+0.15}_{-0.15}$	$8.09 \to 8.98$	$8.58^{+0.14}_{-0.14}$	$8.14 \to 9.01$	$8.09 \to 8.98$
$\delta_{\rm CP}/^\circ$	234^{+43}_{-31}	$144 \to 374$	278^{+26}_{-29}	$192 \to 354$	$144 \to 374$
$\frac{\Delta m^2_{21}}{10^{-5}\ \text{eV}^2}$	$7.40^{+0.21}_{-0.20}$	$6.80 \to 8.02$	$7.40^{+0.21}_{-0.20}$	$6.80 \to 8.02$	$6.80 \to 8.02$
$\frac{\Delta m^2_{3\ell}}{10^{-3}\ \text{eV}^2}$	$+2.494^{+0.033}_{-0.031}$	$+2.399 \to +2.593$	$-2.465^{+0.032}_{-0.031}$	$-2.562 \to -2.369$	$\begin{bmatrix}+2.399 \to +2.593\\ -2.536 \to -2.395\end{bmatrix}$

Figure 1.3: Three-flavor oscillation parameters from our fit to global data as of November 2017. The numbers in the 1st (2nd) column are obtained assuming NH (IH), *i.e.*, relative to the respective local minimum, whereas in the 3rd column the minimization is performed also with respect to the ordering. Note that $\Delta m^2_{3\ell} = \Delta m^2_{31} > 0$ for NH and $\Delta m^2_{3\ell} = \Delta m^2_{32} < 0$ for IH. Figure and caption taken from [30].

- *Inverted hierarchy*, $\Delta m^2_{23} < 0$, i.e. $m_2 > m_1 > m_3$.

The hierarchy puzzle will be probably solved in the near future by the accelerator based long-baseline (i.e. NOνA [31] and T2K [32]) and reactor (i.e. JUNO [33]) experiments since they will be sensitive enough to recognize the three oscillation pattern. Finally, to reveal the absolute scale different informations have to be collected exploiting different experimental approaches (see Sec. 1.4.3).

1.3.1 Dirac and Majorana theories

From the theoretical point of view the neutrino mass term can be introduced in the Lagrangian following the same way used in the Standard Model for the massive fermions:

$$\mathcal{L}_D = -m_D\bar{\nu}\nu = -m_D(\bar{\nu}_R\nu_L + \bar{\nu}_L\nu_R), \tag{1.26}$$

where the neutrino field ν is written as a function of the chiral projections ν_L(left-handed) and ν_R (right-handed). The Eq. 1.26 describes a neutrino and its anti-neutrino as 4-components independent spinors, symmetrical with respect to the CP operator. In the framework of the Dirac theory for the neutrino either $m_D = 0$ or ν_R exists.

The Majorana theory [34] allows to eliminate two of the four components, if the mass eigenstate are its own charge conjugate (namely is a Majorana particle),

$$\nu^c = C\bar{\nu}^T = C(\gamma^0)^T\nu^* = \nu. \tag{1.27}$$

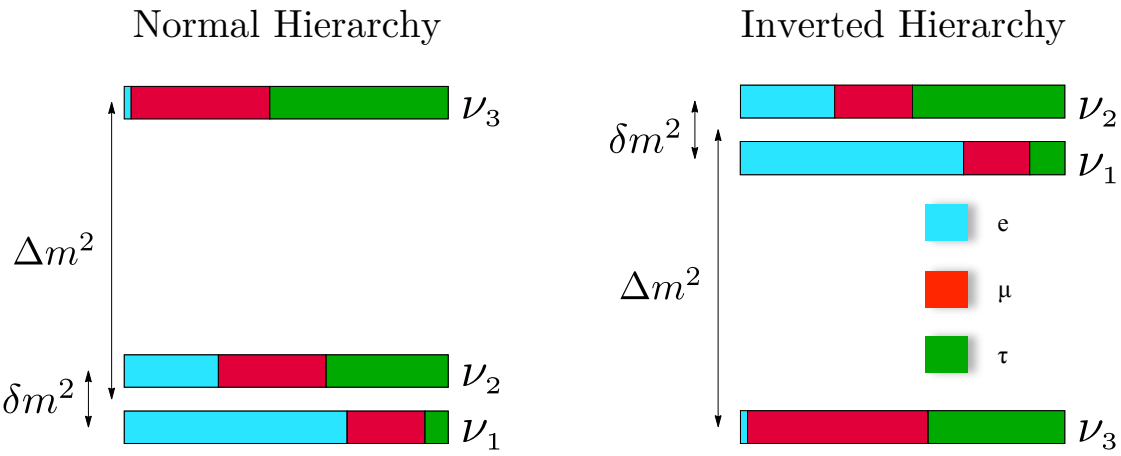

Figure 1.4: Neutrino mass hierarchies. The different colors show the flavor composition of the mass eigenstates. [11]

Applying the chiral projectors on the Majorana condition implies:

$$\nu_R = C\bar{\nu}_L^T = \nu_L^C, \tag{1.28}$$

and the neutrino field becomes,

$$\nu = \nu_L + \nu_R = \nu_L + \nu_L^C, \tag{1.29}$$

in other words the neutrino is its own anti-particle, being $\nu = \nu^C$.
Let us consider the extension of the SM that includes also right-handed neutrinos, whose Lagrangian for the Majorana mass is

$$\mathcal{L}_M = \mathcal{L}_L + \mathcal{L}_R = -\frac{1}{2}\left[m_L(\bar{\nu}_L\nu_L^c + \bar{\nu}_L^c\nu_L) + m_R(\bar{\nu}_R\nu_R^c + \bar{\nu}_R^c\nu_R)\right]. \tag{1.30}$$

The full Lagrangian for the neutrino mass, including the Eq. 1.26 and the Eq. 1.30, can be written in a compact notation as:

$$\mathcal{L}_{D+M} = \mathcal{L}_D + \mathcal{L}_M = -\frac{1}{2}\bar{N}_L^c M N_L + h.c. \tag{1.31}$$

where

$$N_L = \begin{bmatrix} \nu_L \\ \nu_R^c \end{bmatrix} \tag{1.32}$$

and the neutrino mass matrix looks like

$$M = \begin{bmatrix} m_L & m_D \\ m_D & m_R \end{bmatrix}. \tag{1.33}$$

Assuming the $SU(3)_C \times SU(2)_L \times U(1)_Y$ gauge invariance valid and the fundamental Lagrangian strictly renormalizable, the ν_L term should be zero. Relaxing the previous

constrains one can consider the ν_L term suppressed. Conversely the ν_R term is allowed, being ν_R a $SU(3)_C \times SU(2)_L \times U(1)_Y$ singlet. Therefore it follows that m_L has to assume a small value, so that the ν_L term is suppressed by several orders of magnitude over the m_R term, which on the contrary can assume an arbitrary big value, not being related to the vacuum expectation value of the Higgs field. The eigenvalues of the mass matrix 1.33, under the prescription $m_L = 0$ are,

$$m_{\pm} = \frac{m_R}{2} \pm \frac{m_R}{2}\sqrt{1 + 4\frac{m_D^2}{m_R^2}}, \tag{1.34}$$

and with the further hypothesis $m_R \gg m_D$, they become

$$m_- \simeq \frac{m_D^2}{m_R} \tag{1.35}$$

$$m_+ \simeq m_R \tag{1.36}$$

The eigenstate associates with m_- is mostly the familiar left-handed light Majorana neutrino, instead to one associates with m_+ is mostly its heavy sterile right-handed partner. This is the famous *see-saw mechanism* of type I [35–37] (if one state goes up the other goes down). It provides an elegant explanation to the question of why the neutrino has a mass so much smaller than the other charged leptons. The assumption $m_L = 0$ is natural, since a Majorana mass term for the left-handed chiral field ν_L breaks the symmetries and the renormalizability of the SM. Taking $m_- \sim 0.05$ eV and $m_D \sim m_{top} \sim 180$ GeV the result is $m_R \sim 0.3 \cdot 10^{15}$ GeV.

The ν_R field is usually called *sterile neutrino*, since it is not coupled with the neutral current. A heavy sterile neutrino corresponds to a light active neutrino and vice versa, explaining in this way why the masses in the neutrino sector are so small. The see-saw mechanism has further a advantage: the existence of a heavy Majorana neutrino that decays asymmetrically in leptons and anti-leptons may play a crucial role in explaining baryonic asymmetry through leptogenesis [38]. To determine the nature of the neutrino the most promising probe is the Neutrinoless Double Beta Decay ($0\nu\beta\beta$).

1.4 Neutrinoless double beta decay

The double beta decay is a second order weak nuclear process, in which the atomic number of the nucleus changes by two units following four possible decay modes, according to the relative numbers of protons and neutrons in the nucleus:

$$(A, Z) \rightarrow (A, Z+2) + 2e^- + 2\bar{\nu}_e \qquad (\beta^-\beta^-) \tag{1.37}$$

$$(A, Z) \rightarrow (A, Z-2) + 2e^+ + 2\nu_e \qquad (\beta^+\beta^+) \tag{1.38}$$

$$(A, Z) + 2e^- \rightarrow (A, Z-2) + 2\nu_e \qquad (EC - EC) \tag{1.39}$$

$$(A, Z) + e^- \rightarrow (A, Z-2) + e^+ + 2\nu_e \qquad (EC - \beta^+) \tag{1.40}$$

where β^- (β^+) represents the emission of an electron (positron) and EC indicates the electron capture (usually a K-shell electron is captured). This decay mode, namely

two-neutrino mode ($2\nu\beta\beta$), is allowed in the SM and was first introduced by Maria Goeppert-Mayer in 1935 [39]. Its first indirect evidence was in 1949 from geochemical experiment[4] based on ^{130}Te, which was transformed into ^{130}Xe after 2β decay [40]. It was directly observed only later in 1987 exploiting a more sensitive experimental based on a time-projection chamber [41]. Being a second order process this nuclear transition is strongly suppressed with respect to the single β-decay and the typical half-lives are of the order of 10^{20} y. To understand the reason for such a long half-life it is useful refer to the binding energy of a nucleon, given by the Weizsäcker formula,

$$E_{bind} = a_V A - a_S A^{2/3} - a_C \frac{Z(Z-1)}{A^{1/3}} - a_A \frac{(A-2Z)^2}{A} + \delta(A,Z), \tag{1.41}$$

where the first two terms are determined by the strong interaction among nucleons, the third takes into account the Coulomb's repulsion among protons, the fourth is given by the asymmetry in the protons/neutrons levels filling, and finally the fifth term, given by:

$$\delta(A,Z) = \begin{cases} -\frac{a_p}{A^{3/4}} & \text{A even - Z even nuclei} \\ 0 & \text{A odd nuclei} \\ \frac{a_p}{A^{3/4}} & \text{A even - Z odd nuclei} \end{cases} \tag{1.42}$$

where $a_p \simeq 12$ MeV, is due to the Pauli Exclusion Principle: the nucleus has a lower energy if the number of protons with spin up is equal to the number of those with spin down and the same holds for the neutrons; only if Z and N are both even protons and neutrons have the same number of spins up and down. The effect of the pairing term is well depicted in Fig. 1.5: for the odd nuclei there is only one parabola that describes the nuclear mass as a function of Z, so the $\beta\beta$-decay is strongly suppressed in favor of the single β-decay, while for the even nuclei the single β-decay is energetically forbidden due to the nucleons pairing and $\beta\beta$-decay allowed.

The $2\nu\beta\beta$ decay was measured for several isotopes listed in Tab. 1.6 with half-lives ranging from 10^{18} to 10^{24} y.

In 1937 Furry [42] introduced also an other version of the $2\nu\beta\beta$ in which a Majorana neutrino is exchanged among the two decaying nuclei, without neutrinos emissions in the final state, namely the **Neutrinoless Double Beta Decay** ($0\nu\beta\beta$). At that time the C.S. Wu had not yet discovered the parity violation and M. Goldhaber had not yet measured the neutrino helicity, in other word the V-A nature of the week interactions was unknown. For this region Furry did not assume any preferential handedness. In this way he estimated that the $0\nu\beta\beta$ decay half-life was shorter than the $2\nu\beta\beta$ one, due to the bigger phase space factor, being respectively a 2-body decay and a 4-body decay. In the current understanding, based on the Standard Model, the $0\nu\beta\beta$ decay picture is different: an anti-neutrino with positive chirality (right-handed) is emitted from the decay of the first W^- and a neutrino with negative chirality (left-handed) is absorbed by the second one (as depicted in Fig. 1.7). It can happen only if neutrino and anti-neutrino are the same particle, according to the Majorana theory; moreover it requires

[4]This method consists in the separation of xenon from ancient minerals (whose age is up to several billion years) and their subsequent isotope analysis to find an excess amount of ^{130}Xe

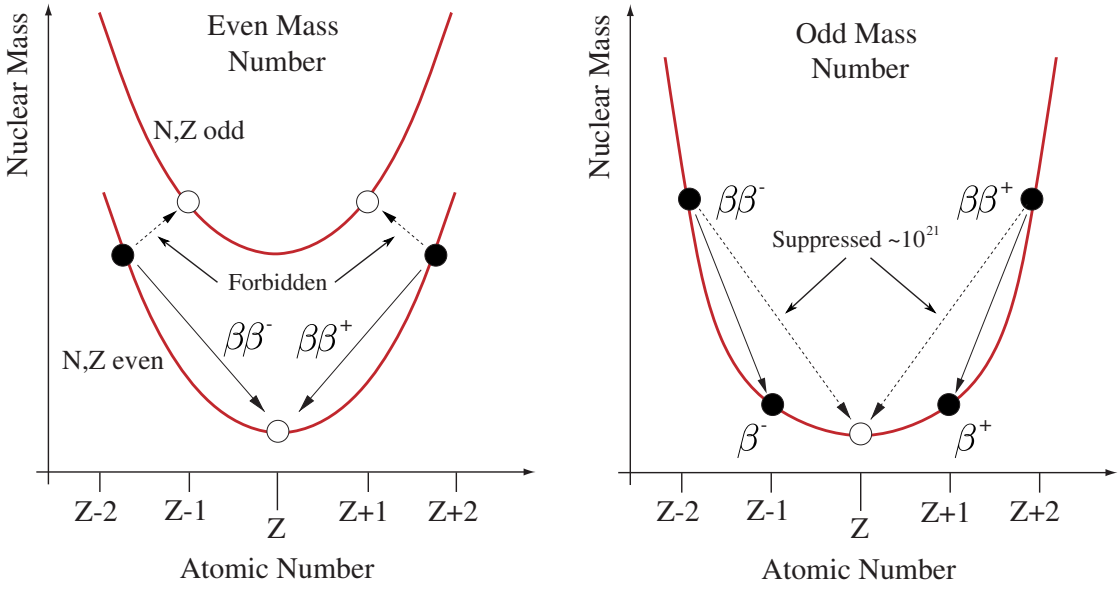

Figure 1.5: Nuclear mass as a function of the atomic number Z in the case of an isobar isotopes with even (left) and odd (right) mass number.

Table 1.6: Isotopic abundance, Q-value ($Q_{\beta\beta}$) and $2\nu\beta\beta$ half-life of the most relevant $\beta\beta$ emitters [44]. The first uncertainty reported is statistical while the second one systematic.

Isotope	i. a. (%)	$Q_{\beta\beta}$ [MeV]	$T^{2\nu}_{1/2}$ [y]	Experiment
^{48}Ca	0.187	4.263	$(6.4\ ^{+0.7}_{-0.6}\ ^{+1.2}_{-0.9}) \cdot 10^{19}$	NEMO-3 (2016) [45]
^{76}Ge	7.8	2.039	$(1.84\ ^{+0.09}_{-0.08}\ ^{+0.11}_{-0.06}) \cdot 10^{21}$	GERDA (2015) [46]
^{82}Se	9.2	2.998	$(9.6 \pm 0.1 \pm 1.0) \cdot 10^{19}$	NEMO-3 (2005) [47]
^{96}Zr	2.8	3.348	$(2.35 \pm 0.14 \pm 0.19) \cdot 10^{19}$	NEMO-3 (2010) [48]
^{100}Mo	9.6	3.035	$(6.90 \pm 0.15 \pm 0.37) \cdot 10^{18}$	CUPID (2017) [49]
^{116}Cd	7.6	2.813	$(2.74 \pm 0.04 \pm 0.18) \cdot 10^{19}$	NEMO-3 (2016) [50]
^{130}Te	34.08	2.527	$(8.2 \pm 0.2 \pm 0.6) \cdot 10^{20}$	CUORE-0 (2016) [51]
^{136}Xe	8.9	2.459	$(2.165 \pm 0.016 \pm 0.059) \cdot 10^{21}$	EXO-200 (2013) [52]
^{150}Nd	5.6	3.371	$(9.34 \pm 0.22\ ^{+0.62}_{-0.60}) \cdot 10^{18}$	NEMO-3 (2016) [53]

a lepton violating interaction and a mechanism to flip from right-handed anti-neutrino to left-handed neutrino. Since this required *chirality flip* is less probable the lower the neutrino mass is, the $0\nu\beta\beta$ decay is strongly suppressed with respect to the $2\nu\beta\beta$.

The $0\nu\beta\beta$ processes associated to the $2\nu\beta\beta$ ones listed in Eq. 1.37 are:

$$(A, Z) \rightarrow (A, Z+2) + 2e^- \qquad (\beta^-\beta^-) \tag{1.43}$$
$$(A, Z) \rightarrow (A, Z-2) + 2e^+ \qquad (\beta^+\beta^+) \tag{1.44}$$
$$(A, Z) + 2e^- \rightarrow (A, Z-2) \qquad (EC - EC) \tag{1.45}$$
$$(A, Z) + e^- \rightarrow (A, Z-2) + e^+ \qquad (EC - \beta^+) \tag{1.46}$$

In the following discussions only the $(\beta^-\beta^-)$ process will be considered. In all the other cases the Coulomb barrier reduces the Q-value below 2 MeV, where the natural background is higher.

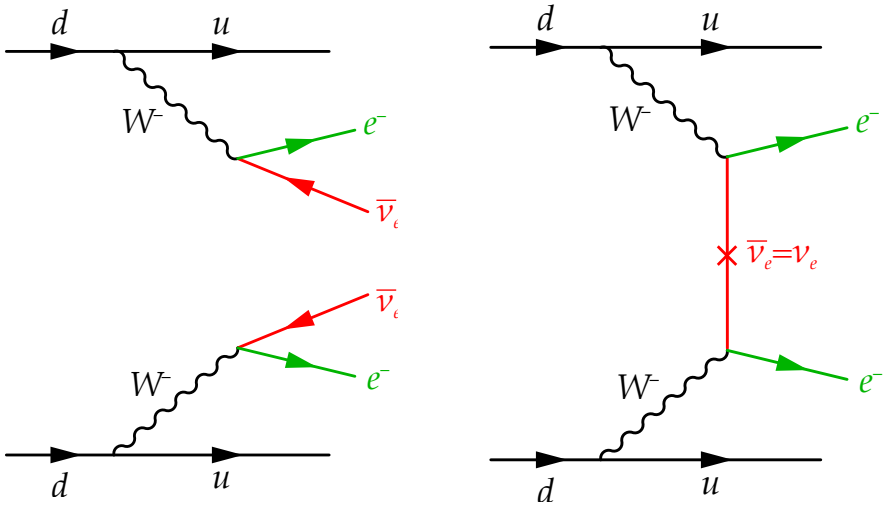

(a) Ordinary $\beta\beta$ decay (b) Neutrinoless $\beta\beta$ decay

Figure 1.7: Feynman diagrams for $2\nu\beta\beta$ decay (a) and hypothesized $0\nu\beta\beta$ decay (b), assuming in the latter case a light Majorana neutrino exchange (one of several theorized possibilities).

The $0\nu\beta\beta$ decay is a powerful tool to investigate the Dirac/Majorana nature of the neutrino but it is also an example of Lepton Number Violation (LNV) an interesting portal toward new physics beyond the SM and finally it can also add crucial informations in the mass sector.

1.4.1 The effective Majorana mass

The half-life of the $0\nu\beta\beta$, mediated by the Majorana neutrino exchange, can be written as [43]

$$\frac{1}{T^{0\nu}_{1/2}} = G^{0\nu}(Q,Z)\left|\mathcal{M}^{0\nu}\right|^2\left(\frac{m_{\beta\beta}}{m_e}\right)^2, \tag{1.47}$$

where $G^{0\nu}$ is the Phase Space Factor (PSF), it can be calculated with high precision from the Q-value of the decay and the nuclear charge in the final state, $\mathcal{M}^{0\nu}$ is the Nuclear Matrix Element (NME), it contains the information on the nuclear structure and its value changes depending on the adopted nuclear model; finally $m_{\beta\beta}$ is the *effective Majorana mass* defined as a linear combination of the neutrinos masses weighted with the electronic coefficients of the PMNS matrix,

$$m_{\beta\beta} = \left|\sum_{j=1}^{3} m_j U^2_{ej}\right| = \left|U^2_{e1}m_1 + U^2_{e2}e^{i\alpha}m_2 + U^2_{e3}e^{i\beta}m_3\right| \tag{1.48}$$

where the Majorana phases α and β appear in the mass definition. The experimental measure of $T^{0\nu}_{1/2}$ allows to estimate $m_{\beta\beta}$ but only combining the results from different isotopes it is possible to overcome the NME uncertain and obtain a trusted value. The results combination is also able to uncover other mechanisms behind the $0\nu\beta\beta$ different from the light Majorana neutrino exchange, as pointed out in [54].

The $0\nu\beta\beta$ has not yet been observed, only lower limits on its half-life have been obtained, that result in an upper limits for $m_{\beta\beta}$ as reported in Tab. 1.8.

Table 1.8: Recent best limits on $0\nu\beta\beta$ decay half-life and $m_{\beta\beta}$ at 90% C.L. .

$\beta\beta$ emitter	$T^{0\nu}_{1/2}$ [y]	$m_{\beta\beta}$ [meV]	Experiment
^{48}Ca	$> 2.0 \cdot 10^{22}$	< 6-26	NEMO-3 [45]
^{76}Ge	$> 8.0 \cdot 10^{25}$	< 0.15-0.33	GERDA [55]
^{82}Se	$> 3.2 \cdot 10^{23}$	< 0.94-2.5	NEMO-3 [56]
^{100}Mo	$> 1.1 \cdot 10^{24}$	< 0.33-0.62	NEMO-3 [57]
^{116}Cd	$> 1.9 \cdot 10^{23}$	< 1.2-1.8	AURORA [58]
^{130}Te	$> 1.5 \cdot 10^{25}$	< 0.14-0.40	CUORE [59]
^{136}Xe	$> 1.1 \cdot 10^{26}$	< 0.061-0.165	KamLAND-Zen [60]
^{150}Nd	$> 2.0 \cdot 10^{22}$	< 1.6-5.3	NEMO [53]

1.4.2 Nuclear Matrix Elements

The main source of theoretical uncertain to convert a given value of $T^{0\nu}_{1/2}$ into a value of $m_{\beta\beta}$ is the one that affects the NME. It involves the hadronic current of the weak

Hamiltonian and depends on the structure of the initial and the final nuclear state. There are different models to calculate the NME: the Interactive Shell Model (ISM) [61, 204], the Quasiparticle Random Phase Approximation (QRPA) [63, 64] and the Interactive Boson Model (IBM-2) [65]. The error on $\mathcal{M}$ within each model is $\lesssim 20\%$ [66–68] but the main issue is the understanding of the differences in the results among the different models and thus give an overall systematic error. Other processes, as single β-decay, electron capture and $2\nu\beta\beta$ are used to compare the measured rates with the theoretical predicted one, but the differences are much larger than 20% [68].

The common parametrization for the NME is the following [69]:

$$\mathcal{M} \equiv g_A^2\, \mathcal{M}_{0\nu} = g_A^2 \left(M_{GT}^{(0\nu)} - \left(\frac{g_V}{g_A} \right)^2 M_F^{(0\nu)} + M_T^{(0\nu)} \right) \tag{1.49}$$

where $M_{GT}^{(0\nu)}$ is the Gamow-Teller operator (spin-spin interaction), $M_F^{(0\nu)}$ is the Fermi contribution (spin independent interaction) and $M_T^{(0\nu)}$ is the tensor operator. g_V and g_A are the axial and vector coupling constants of the nucleon, respectively. It is not yet clear which is the correct value of the axial coupling in the nuclear medium. Usually $g_A \simeq 1.269$, which applies to free nucleons, is used but also quark value $g_A = 1$ is been considered. In the framework of the IBM-2, a comparison among the predicted and measured $2\nu\beta\beta$ decay half-lives was performed to understand which value of g_A is the correct one: assuming $g_A \simeq 1.269$ results in predicted half-lives systematically greater then the measured ones. Fitting the $2\nu\beta\beta$ decay half-lives as a function of the mass number A, the following trend for g_A was found [68]

$$g_A \;=\; g_{A,\,\text{phen.}} = g_{A,\,\text{nucleon}} \;\cdot\; A^{-0.18}. \tag{1.50}$$

This hypothesis is usually called g_A **quenching** but to date it should be considered simply as an effective description, motivated by the approximate nature of the calculation as the omission of the non-nucleonic degrees of freedom (i.e. Δ, N*). If the g_A quenching suggested by the $2\nu\beta\beta$ holds also for the $0\nu\beta\beta$ or not is the crucial open issue; as a metter of fact, from the experimental point of view, a decreasing by 10(20) % of the axial coupling needs of an exposure 2.3 (6) times larger to obtain the same experimental sensitivity in terms of half-life. To clarify this contorted scenario, measurements of relevant cross sections of some specific double charge exchange reactions are recently proposed [70]. A further step towards solving the g_A problem is based on the study of the forbidden non-unique β-decays as suggested in β-decays [71].

1.4.3 Complementary measurements to solve the neutrino mass puzzle

The $m_{\beta\beta}$ alone is not enough to get the values for the neutrino masses. That's because also assuming to know the mass splittings, it involves not only the lightest neutrino mass but also the two Majorana phases as a free parameters. There are other two physical quantities experimentally measurable but they does not involve the Majorana phases: the effective mass of the electronic neutrino, i.e. m_β from the single β-decay and the

sum of the three neutrinos mass Σ from the cosmology, the formulae 1.51 recall their definition.

$$\begin{cases} m_{\beta\beta} = \left| U_{e1}^2 m_1 + U_{e2}^2 e^{i\alpha} m_2 + U_{e3}^2 e^{i\beta} m_3 \right| \\ m_\beta = \sqrt{U_{e1}^2 m_1^2 + U_{e2}^2 m_2^2 + U_{e3}^2 m_3^2} \\ \Sigma = m_1 + m_2 + m_3 \end{cases} \tag{1.51}$$

Oscillations: global fit. As already discussed in Sec. 1.3 the future oscillations experiments will be able to solve at least the hierarchy issue. In global analysis of the data collected so far, NH appears to be somewhat favored with respect to IH at the level of 1.9-2.1 σ, mainly by neutrino oscillation data (especially atmospheric), corroborated by cosmological data [72].

Kinematic measurement of the single β-decay. m_β is the only parameter among the three considered to be model independent, so that it is the natural candidate to directly achieve the neutrino mass. It can be measured from the end-point of the single β-decay spectrum that is slightly shifted respect to the Q-value being the neutrino a massive particle. In particular the shift is exactly given by m_β. The best limit on m_β is of about 2 eV [73, 74] and comes from the spectrometric searches of the ^{3}H β-decay. The next generation spectrometers is expected to lower this limit by a factor of ~ 10 [75] and the use of new detection technologies in the next future is also foreseen. These are based on ^{3}H sources (microwave antennas, [76]) and on the electron capture of ^{163}Ho (micro-calorimeters, [77–79]) and could achieve a sensitivity well below the eV.

Cosmology. From the cosmological point of view, neutrinos are an abundant big-bang relics, so that they can strongly affect the large-scale structure and dynamics of the Universe by means of their gravitational interactions, despite their very small mass. In the ΛCDM cosmology (Cold Dark Matter with a cosmological constant Λ), the scale dependence of clustering observed in the Universe can indeed be used to set an upper limit on Σ. The most stringent limits on Σ are obtained combining data from different galaxy surveys and data on Baryon Acoustic Oscillations (BAO) with the Plank measurements of the CMB [80]. Upper bounds of the order of $\Sigma < (120 - 180)$ meV at 2 σ C. I. [81–86] are the most recent results, although this value is strongly model-dependent. The most strict approach would be to use the neutrino masses as a input parameters to constrain the parameters of the cosmological model, not the opposite.

The formulae 1.51 can be used to transfer the experimental bounds from one variable to the other ones. This can be done writing the masses as a function of the lightest neutrino mass m_l and of the oscillation mass splittings, in the case of NH one gets:

$$\begin{cases} m_1 = m_l \\ m_2 = \sqrt{m_l^2 + \delta m^2} \\ m_3 = \sqrt{m_l^2 + \Delta m^2 + \delta m^2/2} \end{cases} \tag{1.52}$$

while, in the case of IH:

$$\begin{cases} m_1 = \sqrt{m_l^2 + \Delta m^2 - \delta m^2/2} \\ m_2 = \sqrt{m_l^2 + \Delta m^2 + \delta m^2/2} \\ m_3 = m_l \end{cases} \tag{1.53}$$

From the formulae 1.51, 1.52 and 1.53, exploiting the knowledge of the oscillation parameters and propagating the uncertainties the results showed in Figs. 1.9 and 1.10 can be obtained. The predictions for m_β and Σ from oscillations as a function of the lightest neutrino mass are affected only by the propagation of the oscillation parameters uncertainties while for $m_{\beta\beta}$ the dominant uncertain is due to the unknown Majorana phases. The key message of this plots is that the strong limit on Σ from the cosmology disfavors the IH at 1 σ C. L. but as already pointed out this limit is strongly model dependent, so has to be taken with care.

In a recent work [87] the probability distribution for the $m_{\beta\beta}$ as a function of mass m_l is computed via a random sampling from the distributions of the involved mixing angles, squared mass and Σ, assuming a flat prior for the Majorana phases in the range [0,2π]. It show that with the present knowledge, values of $m_{\beta\beta}$ close to the degenerate region are favored both for the IH and the NH.

This approach is very effective to understand how the favored region moves changing the bounds on the parameters but is affected by the lack of informations on the Majorana phases. The values $m_{\beta\beta} \sim 0$ seem to be disfavored because there are only few configurations (determined just by the Majorana Phases) that allow to enter in this region, so it is not related to the experimental measures or physical bounds of the involved parameters.

This discussion pointed out the difficulty of the neutrino properties investigation, in particular in the $0\nu\beta\beta$ decay sector. Even if the mechanisms behind this process is unknown, the prize for observing $0\nu\beta\beta$ decay is to discover lepton-number violation or the Majorana nature of neutrinos, regardless of the actual mechanism.

1.5 Experimental search of $0\nu\beta\beta$

The search for a $0\nu\beta\beta$ signal consists in the detection of the two electrons emitted in the final state. Being the nucleus recoil energy negligible, the sum of the electrons energy corresponds to the Q-value ($Q_{\beta\beta}$) of the decay,

$$Q_{\beta\beta} = M_m - (M_d + 2m_e), \tag{1.54}$$

where M_m is the mass of the parent nucleus, M_d the one of the daughter nucleus. As depicted in Fig. 1.11 the $0\nu\beta\beta$ decay is expected as a monochromatic peak at $Q_{\beta\beta}$, while the $2\nu\beta\beta$ shows a continuum spectrum with $Q_{\beta\beta}$ as end-point.

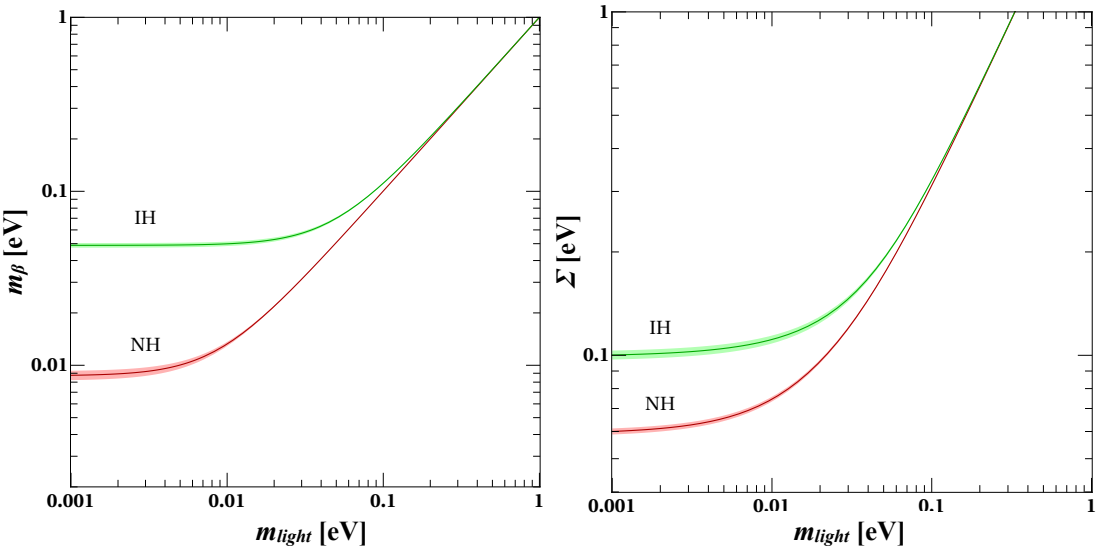

Figure 1.9: Predictions on m_β (Left) and Σ (Right) from oscillations as a function of the lightest neutrino mass (m_{light})in the two cases of NH and IH. The shaded areas correspond to the 3-σ regions due to error propagation of the uncertainties on the oscillation parameters. Figure and caption reprinted from [88].

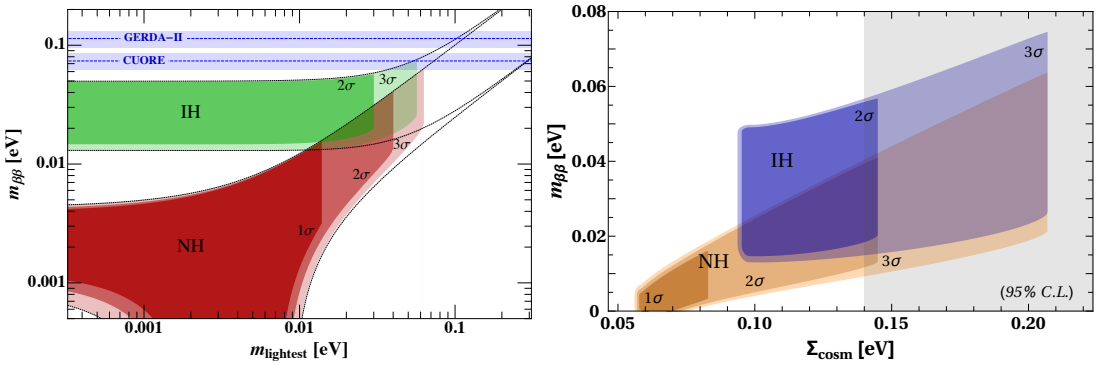

Figure 1.10: Left. Allowed region for $m_{\beta\beta}$ as a function of the lightest neutrino mass (m_{light}). The dotted contours represent the 3 σ regions allowed considering oscillations only. The shaded areas show the effect of the inclusion of cosmological constraints at different C. L. . The horizontal bands correspond to the expected sensitivity for current running experiments. Notice that the 1-σ region for the IH case is not present, being the scenario disfavored at this confidence level. **Right.** Allowed region for $m_{\beta\beta}$ as a function of the sum of the three neutrino masses (Σ). The shaded gray area show the cosmological constraint at 95 % C. L., also in this case the 1-σ region for the IH case is not present. Figure reprinted from [91].

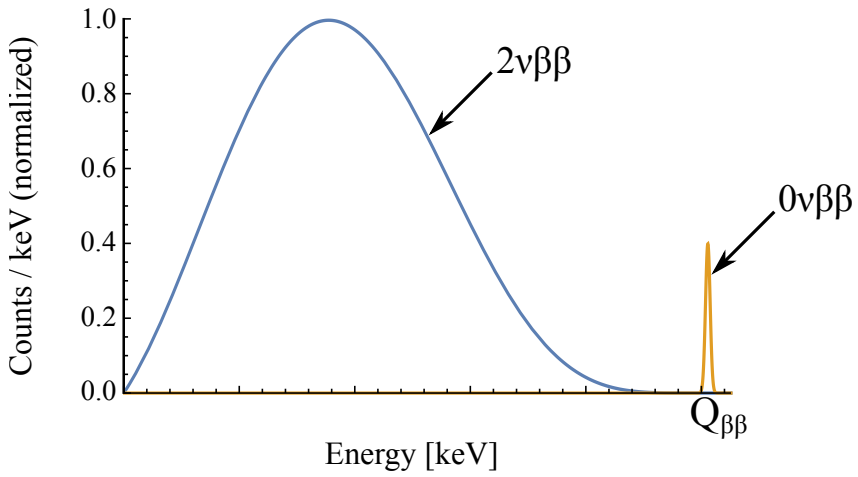

Figure 1.11: Energy spectra of $2\nu\beta\beta$ decay and $0\nu\beta\beta$. The shape of the $2\nu\beta\beta$ decay spectrum follows the Primakoff-Rosen approximation [89]. The monochromatic line of the $0\nu\beta\beta$ decay is smeared to include the experimental energy resolution and increased in magnitude. Figure reprinted from [90].

1.5.1 Experimental challenges

The fundamental parameters for $0\nu\beta\beta$ experiments are three: the Background Index (BI, i.e. the counting rate due to the background in the region of interest), the energy resolution (ΔE) and the exposure (i.e. the mass M multiplied by the live-time T). A very sensitive experiment demands for a large exposure, an extremely low BI and an excellent energy resolution. Achieving these goals depends mainly on the isotope choice and the experimental technique.

Very low background. The main contributions to the background arise from *natural radioactivity*, from *cosmic rays* and eventually from the $2\nu\beta\beta$ itself.

An underground location of the experimental apparatus reduces by several orders of magnitude (e.g. 10^6 at LNGS) the cosmic ray contribution. Hadrons, electrons and γ-rays interact immediately with the rock and are quickly absorbed After a few tens of meters of rock, only high energy muons ($E > 500$ GeV) can penetrate with a rate of the order of 1 $\mu/(\mathrm{m}^2 \cdot h)$ at LNGS. They can be efficiently tagged exploiting the anti-coincidence technique among different detectors or a muon veto.
With respect to the environmental natural radioactivity the most prominent γ-line is the 2615 keV γ emitted by the ^{208}Tl (^{232}Th decay chain). Above this energy there are only a limited number of very rare γ-line (branching ratio lower than 0.014 %) of the ^{214}Bi (^{238}U decay chain) with a maximum energy of con 3270 keV.

Given these numbers, the best solution would be to have a Q-value far from the radioactivity peaks and above 3.3 MeV. Unfortunately the isotopes that fulfill this second requirement have very low isotopic abundance (e.g. ^{48}Ca) or they are not suitable

for detector construction. Furthermore the specific features of the different experimental techniques play a crucial role. For example, the $Q_{\beta\beta}$ of ^{76}Ge is lower than 2615 keV (Tab. 1.6), but this is not a concern thanks to the excellent γ-rejection capability that can be achieved with special configurations of the electrical contacts in germanium diodes. The specific background rejection depends on the isotope and on the detector technique. For example, macro-calorimeters are affected by surface α-events while Ge diodes, due to the low $Q_{\beta\beta}$ of ^{76}Ge, by γ-events. Nevertheless radio-pure materials for the detector and the surrounding parts, as well as proper passive and/or active shielding are mandatory for all the experiments to reduce the environmental radioactivity. Conversely the $2\nu\beta\beta$ contribution, since it is originated by the $\beta\beta$-emitter itself, is unavoidable and not separable but its effect can be reduced at a negligible level by an excellent resolution.

Good energy resolution. This is an important parameter for several reasons. First of all it is the only protection against the intrinsic background induced by the tail of the $2\nu\beta\beta$ spectrum. As shown by the Monte Carlo simulations in Fig. 1.12, considering the ^{136}Xe as $\beta\beta$-emitter, an energy resolution of 1% guarantees to reduce the $2\nu\beta\beta$ events in a FWHM-wide region of interest to a negligible level.

To understand the role of the involved parameters, the signal ($0\nu\beta\beta$) to background ($2\nu\beta\beta$) ratio can be written as [92]:

$$\frac{S}{B} = \frac{m_e Q_{\beta\beta}^5}{7\delta^6}\frac{\Gamma_{0\nu}}{\Gamma_{2\nu}} = \frac{m_e Q_{\beta\beta}^5}{7\delta^6}\frac{T_{1/2}^{2\nu}}{T_{1/2}^{0\nu}}. \tag{1.55}$$

where δ is the energy resolution. The Eq. (1.55) clearly indicates that good energy resolution is fundamental, but also an higher $Q_{\beta\beta}$ allows to increase the signal-to-background ratio. Moreover, it suggests to prefer greater values of $T_{1/2}^{2\nu}$. Indeed the ratio of $T_{1/2}^{2\nu}$ to $T_{1/2}^{0\nu}$ is a parameter which characterizes each isotope, but its (predicted) value is affected by the uncertainty on the nuclear matrix element calculation and it is also model dependent. Eventually a good energy resolution is useful in the background reconstruction to disentangle the different contributions with high precision as shown in Fig. 1.13.

Large exposure. Present experiments have masses of the order of some tens of kg up to a few hundreds kg, but thousands of kilograms of $\beta\beta$ source will be required to cover the inverted hierarchy of neutrino masses [94]. Several collaborations in the $0\nu\beta\beta$ community are studying a future tonne-scale versions of their experiments. The scalability of each experimental technique will be, therefore, the key point for the evaluation of these proposals, together with the detector performance at the 100-kg stage. With the exception of ^{130}Te, which represents the 34% of the natural tellurium, the isotopic abundance of the other $\beta\beta$-emitters is around or below 10%, requiring isotopic enrichment in order to obtain large masses in a limited volume. Large-scale production of the $\beta\beta$ isotopes and the their enrichment are the most important technical challenge, as well as the main fraction of the experiment's budget. Separation by centrifugation is the most effective technique for the isotopic enrichment, but it is only possible for elements with a stable gas compound, so that elements as ^{48}Ca or ^{150}Nd are excluded. Several

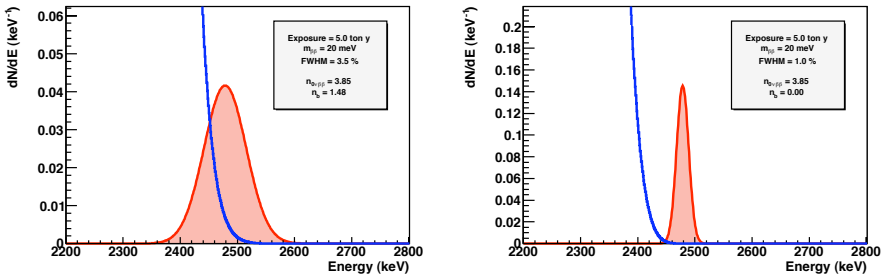

Figure 1.12: Signal (red) and $2\nu\beta\beta$ background (blue) in the ROI around $Q_{\beta\beta}$ of ^{136}Xe with an exposure of 5 tonnes · y and a FWHM resolution of 3.5% (left) and 1% (right). Signal are simulated assuming $m_{\beta\beta}$ =20 meV. n_b is the number of events produced by the $2\nu\beta\beta$ tail in a FWHM-wide region of interest around $Q_{\beta\beta}$. Figure from [93].

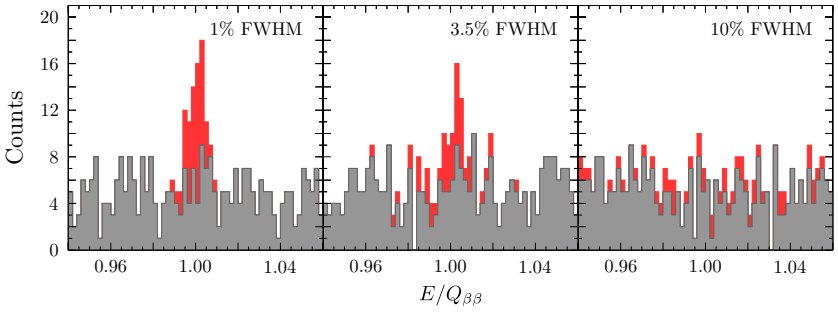

Figure 1.13: Signal (red) and background (gray) in the ROI around $Q_{\beta\beta}$ for 3 Monte Carlo experiments with the same signal strength (50 counts) and background rate (1 count/keV), but different energy resolution: 1% FWHM (left), 3.5% FWHM (center), 10% FWHM (right). The signal is distributed normally around $Q_{\beta\beta}$, while the background is assumed flat. Figure from [93].

isotopes (^{76}Ge, ^{82}Se, ^{100}Mo, ^{136}Xe) are currently used in the enriched form to validate both the purification and the experimental techniques themselves, but further efforts are needed for the next-generation tonne-scale detectors.

1.5.2 Sensitivity

The experiments searching for the $0\nu\beta\beta$ have the goal to measure its half-life, $T^{0\nu}_{1/2}$. If an excess of events at the $Q_{\beta\beta}$ energy shows up in the spectrum, this parameter can be evaluated following the law of radioactive decay:

$$T^{0\nu}_{1/2} = \ln 2 \cdot T \cdot \varepsilon \cdot \frac{N_{\beta\beta}}{N_{\text{signal}}} \tag{1.56}$$

where T is the live-time of the measurement, ε is the detection efficiency, $N_{\beta\beta}$ is the number of $\beta\beta$ emitters, and N_{signal} is the signal counts. Neglecting the small uncertainties on the detector features (i.e. the number of decaying nuclei, the efficiency and the time of measurement) the uncertainty on $T^{0\nu}_{1/2}$ is only given by the statistical fluctuations of the counts:

$$\frac{\delta T^{0\nu}_{1/2}}{T^{0\nu}_{1/2}} = \frac{\delta N_{\text{signal}}}{N_{\text{signal}}}. \tag{1.57}$$

Conversely, if no signal events are detected a lower limit on $T^{0\nu}_{1/2}$ can be established. It is usually defined as the process half-life corresponding to the maximum signal that could be hidden by the background fluctuations (at a given statistical C.L.). Namely it represents the sensitivity of the experiment, $S^{0\nu}$, and can be written as a function of the experiment parameters. It is sufficient to require that the $\beta\beta$ signal N_{signal} exceeds the standard deviation of the total counts in the interesting energy window. At the confidence level n_σ, this means that one can write:

$$N_{signal} \geq n_\sigma \sqrt{n_B} \tag{1.58}$$

where Poisson statistic for counts is assumed, n_B is the background counts.

Assuming the background counts n_B scale linearly with the detector mass,

$$n_B = B\Delta MT \tag{1.59}$$

where B is the background level per unit mass, energy, and time, M is the detector mass, Δ is the Full Width Half Maximum (FWHM) energy resolution. From Eq. (1.56) it is easy to find an expression for $S^{0\nu}$:

$$S^{0\nu} = \ln 2 \cdot T \cdot \varepsilon \cdot \frac{N_{\beta\beta}}{n_\sigma \cdot \sqrt{n_B}} = \ln 2 \cdot \varepsilon \cdot \frac{1}{n_\sigma} \cdot \frac{x\,\eta\,N_A}{\mathscr{M}_A} \cdot \sqrt{\frac{M \cdot T}{B \cdot \Delta}} \tag{1.60}$$

where $N_{\beta\beta}$ is written as a function of the stoichiometric multiplicity of the element containing the $\beta\beta$ candidate (x), the $\beta\beta$ candidate isotopic abundance (η), the Avogadro number (N_A) and, finally, the compound molecular mass ($\mathscr{M}_A$). Despite its simplicity, Eq. (1.60) has the advantage of emphasizing the role of the essential experimental parameters.

When the background level B is so low that the expected number of background events in the ROI along the experiment life is close to zero, the expression of Eq. (1.60) is no more valid. It is the so called "background free" condition and it is identified by the condition:

$$M \cdot T \cdot B \cdot \Delta \leq 1. \tag{1.61}$$

In this case, N_{signal} is given by the maximum number of counts n_L compatible with no observed counts at a given C.L., and the expression for the sensitivity becomes:

$$S_{0B}^{0\nu} = \ln 2 \cdot T \cdot \varepsilon \cdot \frac{N_{\beta\beta}}{n_L} = \ln 2 \cdot \varepsilon \cdot \frac{x\,\eta\,N_A}{\mathscr{M}_A} \cdot \frac{M\,T}{n_L}. \tag{1.62}$$

Reaching the zero background condition is a goal of the experimental searches since, in this case, the sensitivity grows much more rapidly than in presence of background, as it can be seen by comparing Eqs. (1.60) and (1.62).

1.5.3 Current generation of $0\nu\beta\beta$ decay experiment

The interest in the $0\nu\beta\beta$ decay search has grown considerably over the past ten years, many experiments are running, under construction or proposed. The $2\nu\beta\beta$ decay have been observed in 12 isotopes (^{48}Ca, ^{76}Ge, ^{82}Se, ^{96}Zr, ^{100}Mo, ^{116}Cd, ^{128}Te, ^{130}Te, ^{136}Xe, ^{150}Nd, ^{238}U and ^{130}Ba). The updated half-lives are reported in Tab. 1.6.

CUORE [95], GERDA [96], NEMO-3 [97] and KamLAND-ZEN [60] experiments established the recent best limits. A brief description of these (and some other) experiments are provided in the following.

The *Cryogenic Underground Observatory for Rare Events* (CUORE) has started in March 2017 and will take data for 5 years. It will search for the $0\nu\beta\beta$ decay of ^{130}Te using TeO_2 crystal calorimeters [95]. When these crystals are cooled to 10 mK, their heat capacity becomes so small that the energy deposited by interacting particles is measurable as a rise in temperature. The crystals, therefore, work as highly sensitive calorimeters. This technique was used for the first time in $0\nu\beta\beta$ decay searches by the MiDBD [98], Cuoricino [99] and CUORE-0 [100] experiments.

CUORE consists of 988 calorimeters arranged in 19 vertical towers held by a copper frame. The basic detector element is a $5 \times 5 \times 5$ cm^3 TeO_2 crystal of 750 g instrumented with a temperature sensor and a resistive heater. The total mass of the detector is 741 kg, of which 206 kg are ^{130}Te. The towers housed in a cryostat composed of six nested copper vessels (see Fig. 1.14). Two shields protect the calorimeter from radiation: a 6 cm thick layer of ancient Roman lead located between the two middle copper vessels shields the detectors from radioactivity in the outer vessels, a 31 cm thick disc made of modern and Roman lead and located below the mixing chamber plate shield the detectors from the overhead apparatus radioactivity. The cryostat is surrounded by a 73-tonnes octagonal external shield designed to screen the detector from environmental γ rays and neutrons. The shield has three layers: an 20 cm thick outermost layer consisting of a floor and sidewalls of polyethylene to thermalize neutrons; a 2 cm thick side layer of boric-acid powder to absorb neutrons; and an innermost layer of lead bricks of at least 25 cm thickness to absorb γ rays.

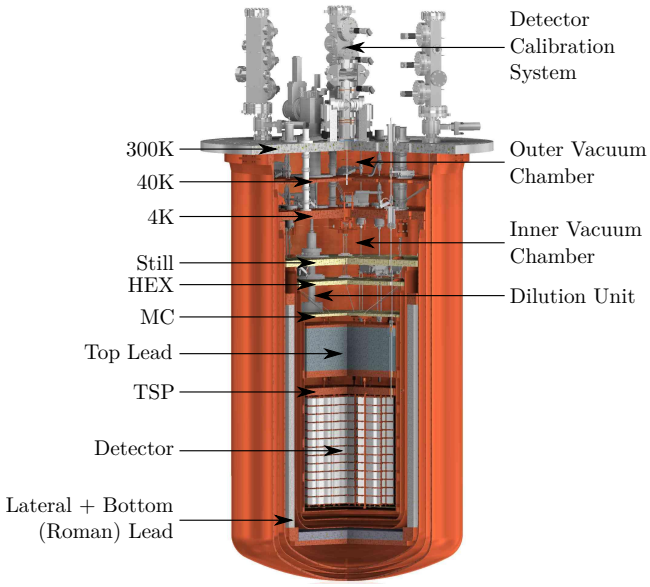

Figure 1.14: CUORE cryogenic calorimeters inside the cryostat, consisting of six nested copper vessels at 300 K (outer vacuum chamber), 40 K, 4 K (inner vacuum chamber), 0.6 K (still), 0.05 K (heat exchanger), and 0.01 K (mixing chamber). Several layers of radio-pure lead shield the calorimeters from external radiation. Figure adapted from [95].

CUORE aims at improving the sensitivity of CUORE-0, its predecessor, by more than a factor of 30 by operating a larger, cleaner, better-shielded detector.

The results of the first Scientific Run are presented in [59]. Examining a total TeO_2 exposure of 86.3 kg $\times$ y, characterized by an effective energy resolution of (7.7 ± 0.5) keV FWHM and a background in the region of interest of (0.014 ± 0.002) counts/(keV $\times$ kg $\times$ y), no evidence for neutrinoless double-beta decay are founded. The median statistical sensitivity of this search is 7.0×10^{24} yr. Including systematic uncertainties, one places a lower limit on the decay half-life of $T^{0\nu}_{1/2}(^{130}\mathrm{Te}) > 1.3 \times 10^{25}$ yr (90% C.L.). Combining this result with those of two earlier experiments, Cuoricino and CUORE-0, one obtains $T^{0\nu}_{1/2}(^{130}\mathrm{Te}) > 1.5 \times 10^{25}$ yr (90% C.L.), which is the most stringent limit to date on this decay. Interpreting this result as a limit on the effective Majorana neutrino mass, it is $m_{\beta\beta} < (140 - 400)$ meV, where the range reflects the nuclear matrix element estimates employed.

The *GERmanium Detector Array* (GERDA) experiment, located in Hall A of the Laboratori Nazionali del Gran Sasso (LNGS), is searching for the $0\nu\beta\beta$ decay of ^{76}Ge using bare high-purity germanium (HPGe) diodes immersed in a cryogenic bath of liquid argon (LAr) [101]. The HPGe detectors are arranged in strings and mounted in special low-mass holders made of ultra-pure copper and PTFE. The strings are suspended inside a vacuum-insulated stainless steel cryostat (4.2 m diameter and 8.9 m height) filled with liquid argon. A copper 6 cm thick lining covers the inner cylindrical shell of the cryostat.

Figure 1.15: Artist's view (HPGe strings not to scale) of the GERDA detector at LNGS. Reprinted from [102].

The cryostat is placed in a 590-m^3 water tank instrumented with PMTs which serves as a Cherenkov muon veto as well as a gamma and neutron shield. A drawing of the entire system is shown in Fig. 1.15.

Since December 2015 the GERDA experiment is taking data with the up-graded apparatus (Phase II) exploiting both coaxial and BEGe detectors. The BEGe detectors (20 kg of ^{enr}Ge) are organized in three strings of eight and one string of six detectors, the coaxial detectors (15.6 kg of ^{enr}Ge) are organized in three strings of three detectors, plus one coaxial in a BEGe string.

The energy resolution at $Q_{\beta\beta}$ integrated over six months is 3.00 $\pm$0.08 keV (4.03 $\pm$ 0.12 keV) for BEGe (coaxial) detectors. The background at $Q_{\beta\beta}$ for the BEGe detectors is $(0.7^{+1.1}_{-0.5}) \cdot 10^{-3}$ counts/(keV $\cdot$ kg $\cdot$ y). The GERDA Collaboration has recently published a limit to the $0\nu\beta\beta$ half-life, $T^{0\nu}_{1/2} > 8.0 \cdot 10^{25}$ y (90% CL) [55].

The NEMO-3 detector [97] had been operating in the Modane Underground Laboratory from 2003 to 2010. It used a tracking calorimeter technique in order to investigate double beta decay processes for different $\beta\beta$-isotopes: thin foils made out of seven $\beta\beta$ emitters were located in a drift chamber with a magnetic field. Outside of the drift region there was a calorimeter made of large blocks of plastic scintillator coupled to low radioactivity photomultipliers (PMTs). The tracking detector was used to identify electron tracks and was able to measure the delay time of any tracks up to 700 s after the initial event. The main advantage of this technology is the possibility to study with the same apparatus a huge number of isotopes, reconstructing also the topology of the two

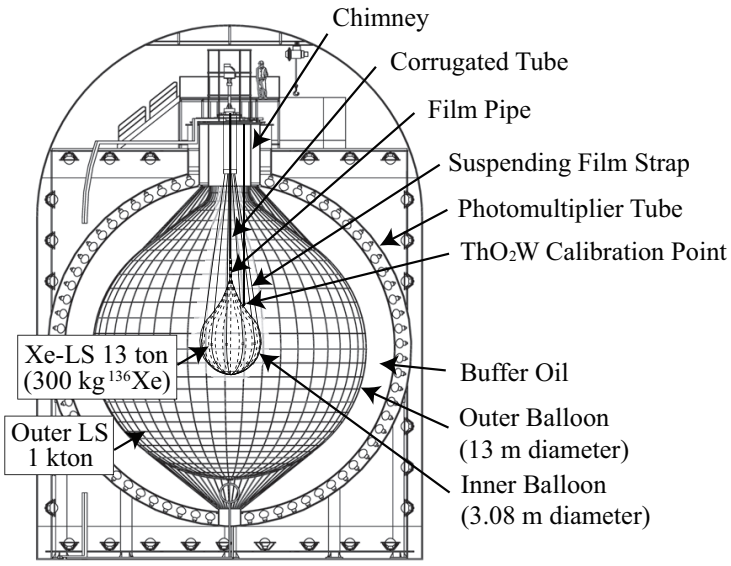

Figure 1.16: Schematic drawing of the KamLAND-Zen detector. Figure reprinted from [105].

electrons. Recent published limits (at 90% C.L.) for the $0\nu\beta\beta$ half-life are $T^{0\nu}_{1/2} > 1.1 \cdot 10^{24}$ y for ^{100}Mo [57], $T^{0\nu}_{1/2} > 2.0 \cdot 10^{22}$ y for ^{48}Ca [45], $T^{0\nu}_{1/2} > 2.0 \cdot 10^{22}$ y for ^{150}Nd [53] and $T^{0\nu}_{1/2} > 1.0 \cdot 10^{23}$ y for ^{116}Cd [50].

The KamLAND-Zen experiment is searching for the $0\nu\beta\beta$ decay of ^{136}Xe using enriched xenon dissolved in liquid scintillator, a technique first proposed by R. Raghavan in 1994 [103]. The experiment reuses the neutrino KamLAND detector [104], located at the Kamioka Observatory, Japan. The KamLAND-Zen detector, shown in Fig. 1.16, is composed of two concentric transparent balloons. The inner one, 3.08 m diameter and fabricated from 25 μm thick nylon film, contains 13 tonnes of Xe-loaded liquid scintillator. The outer balloon, 13 m in diameter, containing pure liquid scintillator, and serves as an active shield for external gamma background as well as a detector for internal radiation from the inner balloon. Buffer oil between the outer balloon and an 18 m diameter spherical stainless-steel containment tank shields the detector from external radiation. Scintillation light is recorded by 1325 17-in and 554 20-in photomultiplier tubes mounted on the stainless-steel tank, providing 34% solid-angle coverage. The containment tank is surrounded by a 3.2-ktonne water-Cherenkov outer detector. The Xe-loaded scintillator consists of 82% decane and 18% pseudocumene by volume, 2.7 g/liter of the fluor Diphenyloxazole (PPO), and 2–3% by weight of enriched xenon gas [105], corresponding to approximately 350 kg of ^{136}Xe.

KamLAND-Zen, which has been collecting physics data since late 2011, has published a measurement of the half-life of the $2\nu\beta\beta$ decay of ^{136}Xe, 2.38 ± 0.02 (stat) $\pm$ 0.14 (syst) $\cdot 10^{21}$ y [105], and a limit to the half-life of the $0\nu\beta\beta$ decay, $1.07 \cdot 10^{26}$ y (90% CL) [60], the best result ever published in this field. The energy resolution of the detector

is 10.9% FWHM at the Q value of ^{136}Xe. The achieved background rate in the region of interest is approximately $1.4 \cdot 10^{-4}$ counts/(keV $\cdot$ kg $\cdot$ y), thanks to a tight selection cut in the fiducial volume and the identification of ^{214}Bi events via Bi-Po tagging [60].

The *Neutrino Experiment with a Xenon TPC* (NEXT) [106] will search for the neutrinoless double beta decay of ^{136}Xe using a high-pressure xenon gas time projection chamber. Such a detector provides several valuable features: a) excellent *energy resolution*, close to 0.3% FWHM at $Q_{\beta\beta}$; b) a *fully active and homogeneous* detector with no dead regions; and c) *scalability* to large detector masses. Following ideas introduced in [107], the design of the NEXT-100 detector is optimized for energy resolution by using proportional electroluminescent (EL) amplification of the ionization signal. The detection process involves the use of the prompt scintillation light from the gas as start-of-event time, and the drift of the ionization charge to the anode by means of an electric field (~ 0.3 kV/cm at 15 bar) where secondary EL scintillation is produced in the region defined by two highly transparent meshes, between which there is a field of ~ 20 kV/cm at 15 bar. The detection of EL light provides an energy measurement using photomultipliers (PMTs) located behind the cathode (the *energy plane*) as well as tracking through its detection a few mm away from production at the anode, via a dense array of silicon photomultipliers (the *tracking plane*).

The R&D phase of the experiment was carried out with the large-scale prototypes NEXT-DEMO and NEXT-DBDM. NEXT-DEMO is as a 1:5 scale prototype of NEXT-100. It is a 1.5 kg volume TPC filled with natural xenon. It employs an array of 19 PMTs as an energy plane and of 256 SiPMs as a tracking plane with the TPC light tube and SiPM surfaces being coated with tetraphenyl butadiene (TPB) which acts as a wavelength shifter for the scintillation light produced by xenon.

The detector has been operating successfully since 2011 and has demonstrated: (a) very good operational stability, with no leaks and very few sparks; (b) 5.5% FWHM energy resolution at 30 keV, extrapolates to 0.6% FWHM at the $Q_{\beta\beta}$; (c) track reconstruction with PMTs and with SiPMs coated with TPB; (d) excellent electron drift lifetime, of the order of 20 ms.

In addition of excellent energy reconstruction, NEXT has a topological signature, not available in most $0\nu\beta\beta$ detectors. Double beta decay events leave a distinctive topological signature in HPXe: a continuous track with larger energy depositions (*blobs*) at both ends due to the Bragg-like peaks in the $\mathrm{d}E/\mathrm{d}x$ of the stopping electrons. In contrast, background electrons are produced by Compton or photoelectric interactions, and are characterized by a single blob and, often, by a satellite cluster corresponding to the emission of 30-keV fluorescence X-rays by xenon.

The *Enriched Xenon Observatory* (EXO) is an experimental program searching for neutrinoless double beta decay using ^{136}Xe. The first phase of the experiment, EXO-200 [108], consists in a 200-kg liquid xenon (LXe) time projection chamber that has been taking physics data at the Waste Isolation Pilot Plant (WIPP), in New Mexico, USA, since early May 2011. The results produced so far by the experiment include the first

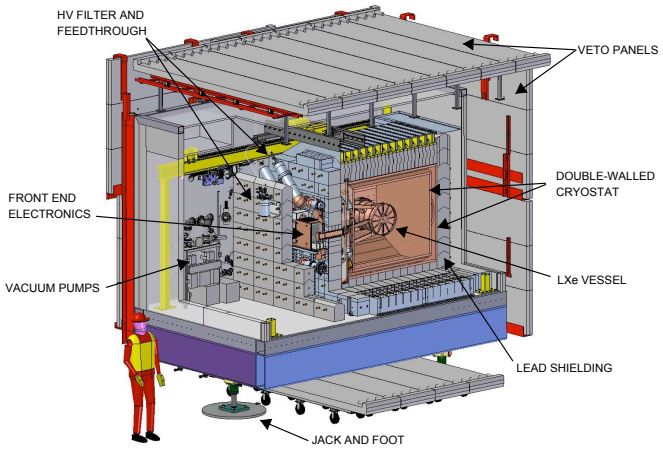

Figure 1.17: Drawing of the EXO-200 detector, cryostat and shielding. Figure reprinted from [108].

observation of the $2\nu\beta\beta$ decay of ^{136}Xe [109] and some of the most stringent limits so far on the effective Majorana neutrino mass [110, 111].

The EXO-200 detector is a cylindrical TPC, about 40 cm in diameter and 44 cm in length, with two drift regions separated in the centre by a transparent cathode. The TPC measures the 3D coordinates and energy of ionization deposits in the LXe by simultaneously collecting the scintillation light and the charge. Charge deposits spatially separated by about 1 cm or more are individually observed with a position accuracy of a few millimeters. A pair of crossed wire planes collects the ionization charge and measures its amplitude and transverse coordinates, and arrays of avalanche photodiodes (APDs) located behind the wire planes measure the scintillation light. The sides of the chamber are covered with teflon sheets that act as reflectors improving the light collection. The xenon, enriched to 80.6% in ^{136}Xe, is held inside a thin copper vessel immersed in a cryogenic fluid that also shields the detector from external radioactive backgrounds. The fluid is maintained at $\sim$167 K inside a vacuum-insulated copper cryostat. Further shielding is provided by at least 25 cm of lead in all directions. The entire assembly is housed in a clean-room located underground at WIPP. Four of the six sides of the clean-room are instrumented with plastic scintillator panels recording the passage of cosmic ray muons. Fig. 1.17 shows the overall detector and shielding arrangement.

The fiducial volume selected in the data analysis contains a 76.5 kg mass of ^{136}Xe. Signal detection efficiency is estimated to be 84.6%. Thanks to the simultaneous measurement of the ionization and scintillation signals, EXO-200 reaches an energy resolution of 3.6% FWHM at the Q value of ^{136}Xe. The last published analysis [110], analyzes an exposure of 100 kg y (736 mol y). The estimate of the background in a $\pm 2\sigma$ window around $Q_{\beta\beta}$ is $31.1 \pm 1.8\,(\text{stat}) \pm 3.3\,(\text{syst})$ counts, or $(2.1 \pm 0.3) \cdot 10^{-3}$ counts/(keV $\cdot$ kg $\cdot$ y). The dominant backgrounds arise from the thorium series (16.0 counts), the uranium series (8.1 counts) and ^{137}Xe (7.0 counts). This amount of ^{137}Xe is consistent with estimates from studies of the activation of ^{136}Xe in muon-veto-tagged data. The EXO Collab-

oration reports a 90% CL lower limit on the half-life of ^{136}Xe of $1.1 \cdot 10^{25}$ y. This corresponds to an upper limit on the Majorana neutrino mass of 190–450 meV.

SNO+, the follow-up of the *Sudbury Neutrino Observatory* (SNO) [113], is a multipurpose liquid scintillator experiment housed in SNOLAB (Ontario, Canada). The detector reuses many of the components of its predecessor, replacing the heavy water by 780 tonnes of liquid scintillator in order to obtain a lower energy threshold. The detector consists of a 12 m diameter acrylic vessel surrounded by about 9500 8-in photomultiplier tubes that provide a 54% effective photocathode coverage. The acrylic vessel is immersed in a bath of ultra pure water that fills the remaining extent of the underground cavern, attenuating the background from external media such as the PMTs and surrounding rock. The density of the liquid scintillator (0.86 g/cm^3) being lower than that of the surrounding water leads to a large buoyant force on the acrylic vessel. To keep it in place, a hold-down rope net has been installed over the detector and anchored to the cavity floor.

The physics program of SNO+ includes the search for neutrinoless double beta decay in ^{130}Te, which will be loaded into the liquid scintillator in the form of (non-enriched) telluric acid. A loading of 0.3%, equivalent to 780 kg of ^{130}Te, is planned for the first phase of the experiment.

The energy resolution of the SNO+ detector is expected to be 10.5% FWHM at the Q value of ^{130}Te [114]. Consequently, the $2\nu\beta\beta$ spectrum will be an important source of background. The expected levels of uranium and thorium in the liquid scintillator can also result in substantial activity near the $0\nu\beta\beta$ endpoint, mostly from the decays of ^{214}Bi and ^{212}Bi. Nevertheless, these can be, in principle, actively suppressed via Bi-Po α tagging [114]. External backgrounds (not originating in the liquid scintillator) can be suppressed with a tight fiducial volume selection, which will cut, however, about 70–80% of the signal.

1.5.4 Future perspectives

The goal of the next generation of $0\nu\beta\beta$-decay experiments is to probe effective Majorana neutrino masses down to 10–20 meV, fully covering the inverted hierarchy region. Such future detectors will involve tonne or multi-tonne scale in $\beta\beta$ emitter mass. Most collaborations are already discussing possible designs for a tonne-scale upgrade of their experiments. Nevertheless, some experimental approaches currently used will not be viable for the next generation, given the cost and difficulty associated; only a few approaches, most likely based on different isotopes, will go ahead.

- GERDA and MAJORANA plan to merge their efforts towards a tonne-scale germanium experiment, called LEGEND (Large Enriched Germanium Experiment for Neutrinoless Double beta decay). In order to reach in a reasonable time $m_{\beta\beta}$ sensitivities in the range 10–20 meV, at least a tonne of enriched material are required, i.e. 20–25 times more mass than that deployed at present by the two experiments. Besides, the background rate would have to be reduced by a factor of

10 with respect to the target rate of the current-generation experiments, reaching 10^{-4} counts/(keV · kg · y).

- The two large liquid-scintillator calorimeters, SNO+ and KamLAND-Zen, are planning future phases to explore the inverse neutrino hierarchy. KamLAND-Zen intends to dissolve about 1000 kg of enriched xenon in the liquid scintillator. SNO+ can, in principle, increase the concentration of telluric acid in the liquid scintillator by a factor of 10 without affecting the detection and optical properties of the mixture [114]. The energy resolution of both detectors may be improved from the current 10% FWHM to values close to 6% FWHM with the use of a brighter liquid scintillator and an enhancement of the light collection efficiency. SNO+ would have to suppress the background level respect to its present target rate, 10^{-4} counts/(keV · kg · y), by an order of magnitude. KamLAND-Zen would require an even higher suppression factor to compensate for the lower deployed mass and the differences between the $\beta\beta$ sources. The sensitivity of these experiments will be limited, ultimately, by irreducible backgrounds such as the $2\nu\beta\beta$ spectrum or the solar neutrino flux.

- The EXO Collaboration has started the design of a 5-tonne liquid xenon TPC called nEXO. In order to fully probe the inverted-hierarchy region, nEXO would require a background rate approximately two orders of magnitude better than that achieved in EXO-200. Self-shielding would help suppressing the external backgrounds, even though at the cost of reducing the fiducial mass. In addition, the detector will require neutron shielding to mitigate the activation of ^{136}Xe.

- The NEXT Collaboration is considering a xenon gas detector with a mass in the range of 1 to 3 tonnes, energy resolution close to 0.5% FWHM at 2.5 MeV, and a background rate of the order of $5 \cdot 10^{-5}$ counts/(keV · kg · y). Besides possible improvements in the radioactivity budget of the detector (more radio-pure photosensors, for example), the target background rate can be attained enhancing the discrimination power of the tracking signature with a moderate magnetic field. A single energetic electron should produce a clear single spiral with radius indicative of its momentum, and a double-electron track with the same energy will produce two spirals each with much less momentum and originating from a common vertex. This information provides an additional way of separating single-electrons arising from background processes from double electrons produced in $0\nu\beta\beta$ decays, in spite of the large multiple scattering that the electrons suffer in the dense gaseous xenon.

- SuperNEMO has, by far, the lower mass-to-volume ratio among the techniques considered for $0\nu\beta\beta$ searches: a SuperNEMO module houses 5–10 kg of $\beta\beta$ isotope in approximately 53 m^3, whereas, for example, the NEXT-100 pressure vessel, with a volume of about 3 m^3, contains 100 kg of enriched xenon in its active volume. Considering this and the limited underground space available, a tonne-scale version of the SuperNEMO experiment seems very unlikely without a more compact design.

Nevertheless the NEMO approach remains the only one able to investigate with high precision the topology of the $\beta\beta$ decay, measuring the two electrons separately.

- An upgraded version of CUORE would require isotopically-enriched TeO_2 calorimeters and a background rate two orders of magnitude smaller than the one measured in the current version. Several techniques are under investigation in the framework of CUPID (CUORE Upgrade with Particle IDentification). The activities carried out within CUPID will be detailed in the next chapters, being the object of the present work.

Chapter 2

Dual-readout cryogenic calorimeters

In the framework of CUORE and CUPID, crystals with $\beta\beta$-emitters embedded are operated as calorimeters at cryogenic temperatures ($\leq$ 20 mK). The additional feature of CUPID, with respect to the well established technique used in CUORE, is particle identification. If the chosen crystals are scintillators, the energy released therein by an interacting particle (αs, β/γs, neutrons) is shared among two channels: heat and light. Most of the energy is deposited as heat, resulting in a temperature increase of the crystal that can be measured with high accuracy by dedicated sensors. The remanent part of the energy (a few %) gives rise to scintillation processes in the crystal with the subsequent emission of light. Thanks to the simultaneous read-out of the heat signal and the scintillation signal a very low background can be obtained. Since the crystals and the light detectors are both working as cryogenic calorimeters, the chapter starts describing their working principle and then details the achieved performances and the future perspectives of this experimental technique in the $0\nu\beta\beta$ decay search.

2.1 Detector model

The most widely used particle detectors measure ionization or scintillation signals produced by the interacting particles. The energy detectable via these channels, however, constitutes only a very small fraction of the total energy deposit, as the largest part is converted in lattice vibrations (i.e. heat) and escapes detection. A possible solution to increase the sensitivity consists in using a detector able to measure the phonons produced by an interaction: a *cryogenic calorimeter*.

In a very simplified model, a cryogenic calorimeter can be sketched as an absorber (with heat capacity C), in which the energy from the interacting particle is deposited, and a phonon sensor (i.e. thermometer) that converts this energy (i.e. the phonons) into a measurable signal.

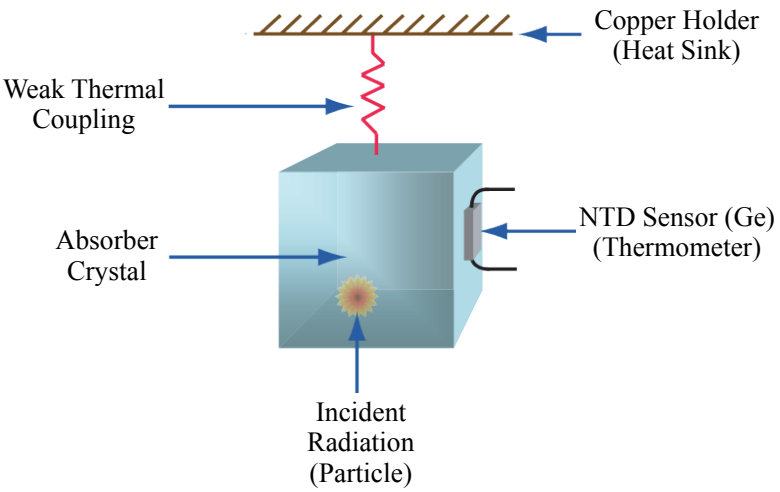

Figure 2.1: Schematics of a cryogenic calorimeter (absorber and sensor). The heat deposited in the absorber is dissipated via a heat sink, that keeps the calorimeter at the steady temperature of about 15 mK.

2.1.1 Absorber response

The absorber with heat capacity C is connected to a heat bath (with constant temperature T_0) through a thermal conductance G.

If a certain amount of energy E is released in the absorber, this will produce a change in temperature ΔT equal to the ratio between E and C. Of course the reasonable condition that the temperature increase ΔT is negligible in respect to T_0 is assumed, so that C and G can be considered constant quantities.

Then, the temperature variation can be described by the time evolution equation:

$$\Delta T(t) = \frac{E}{C}\, \mathrm{e}^{-t/\tau} \quad \text{with} \quad \tau \equiv \frac{C}{G}. \tag{2.1}$$

The value of the time constant τ can be very long, from milliseconds up to a few seconds, depending on the values of C and G. From Eq. (2.1), the fundamental role of the heat capacity appears: to get a large signal amplitude, C has to be as small as possible. In order to minimize C, very low-temperatures are needed and a suitable material for the absorber has to be chosen. In particular, non-magnetic dielectric crystals or superconductors (below the transition) are preferred, so that the main contribution to C is the one from the crystal lattice. In this case, the Debye law for the specific heat c at low-temperatures can be applied:

$$c \propto \left(\frac{T}{\Theta_\mathrm{D}}\right)^3 \tag{2.2}$$

where Θ_D is the Debye temperature which is a property of the material. This parameter depends on the mass number A and on the material density ρ as $\Theta_\mathrm{D} \propto A^{-1/3}\, \rho^{-1/6}$ [115],

so that low atomic mass and low density should be preferred for high Θ_D. Moreover a high Z provides a larger detection efficiency for β radiation, while a high Z/A ratio results in a larger detection efficiency for γs. A naive calculation of the absorber contribution to the theoretical resolution of the cryogenic calorimeter can be done starting from the following considerations: when an interaction releases energy in the absorber, the interactions with the nuclei or the electrons of the material convert the energy deposit into vibrational excitation of the lattice (phonons). If an energy deposition E produces N phonons, each one with energy $\epsilon = k_B T$, one can write:

$$E = N \cdot \epsilon = \int_{T_i}^{T_f} C(T) dT \simeq C(T) \cdot T, \tag{2.3}$$

where both the initial and final temperature can be considered equal to the calorimeter working temperature ($T_f \simeq T_i \simeq 10$ mK). The transport across the thermal link is affected by random thermal fluctuations which traslate in intrinsic energy resolution:

$$\Delta E = \sqrt{N} \cdot \epsilon = \sqrt{k_B \cdot C(T) \cdot T^2}. \tag{2.4}$$

Using typical values of well known crystals (750 g TeO_2 crystals used in CUORE), a thermal capacitance C$\sim 10^{-9}$ J/K at T$\sim$10 mK, providing a temperature increase of ~ 100 μK for an energy deposit of 1 MeV. According to the Eq. 2.4, the expected energy spread would be of the order of 10 eV, well below the measured resolution, of a few keV.

In order to explain this discrepancy, a deeper analysis of the **energy release processes** that occur before the conversion in phonons and the **phonons thermalization** itself is needed (for a detailed description see reference [116]).

Energy release in the absorber. Energy can be transferred to the absorber via two main channels: the *electronic* and the *nuclear channel* [117]. A particle interaction with the electrons of the absorber (electronic channel) produces electron-hole (e-h) pairs all along the particle path (few μm in case of heavy particles or mm in case of electrons) that spread quickly from the interaction point to the rest of the detector. These carriers reach a quasi-equilibrium condition by interacting with each other (*recombination*) and start transferring energy to the lattice as vibrational excitations. In this channel, many phenomena can give rise to a worsening of the energy resolution, like trapping of the carriers in impurity sites or lattice defects, radiative recombinations of electron-hole pairs or non radiative recombinations on very long time scales.

On the other hand, when the particle interacts with the nuclei of the absorber (nuclear channel), part of the energy could be trapped in the structural defects of the lattice. The fraction of energy that leaves the crystal without being detected, as well as the one stored in stable or metastable states, are almost irreducible sources of resolution worsening.

Thermalization of phonon. In order to (qualitatively) understand the phonon thermalization process inside the crystal absorber, let us refer to the mono-dimensional representation of the phonon dispersion curves shown in Fig. 2.2. The e-h pair recombination across conduction and valence bands produces high energy-low momentum *athermal phonons* in the *optical branch* (out-of-phase movements of the atoms in the lattice).

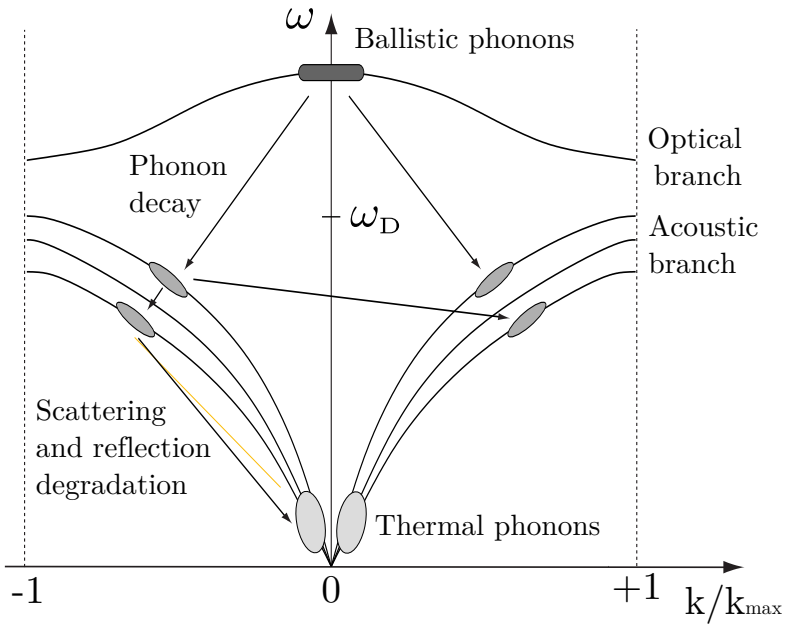

Figure 2.2: Athermal model for the phonons thermalization. The abscissa k/k_{max} is the module of the crystal momentum normalized to the maximum allowed value.

These primary phonons propagate from the particle interaction region and decay in a very short time, $(10 - 100)$ ps. Usually two phonons are created, each with half of the original energy. The decays, mainly in the *acoustic branch* (coherent movements of atoms of the lattice), result in a phonon cascade. The average phonon energy is of the order of $E_D = \hbar\omega_D$, where ω_D is the Debye cut-off frequency of the crystal, the theoretical maximum frequency of vibration for the atoms of the crystal. This energy is much higher than the average energy of *thermal phonons* that, at the calorimeter working temperature, is of some μeV.

At this point, phonon-phonon scattering, mass-defect impurity scattering and boundary scattering phenomena occur, leading to the final phonon energy degradation. In particular, the decay chain proceeds until the mean free path of the phonons becomes larger than crystal dimensions, in other word there is a ballistic propagation of phonons until they reach the crystal surfaces. At that point a fraction of the phonons is directly thermalized while another fraction is reflected. These phonons can suffer other decay processes and, at the end, interact with other thermal phonons with a final thermalization.

A real calorimeter is much more complicated than the simple model here described. In particular the parameters C and G cannot be considered as global quantities, but rather as the sum of many contributions, each with different behavior. Also the role of the thermal sensor is not negligible in the development of the signal [120, 121]. However, this simple description gives a qualitative idea of the signal generation in cryogenic calorimetric detector.

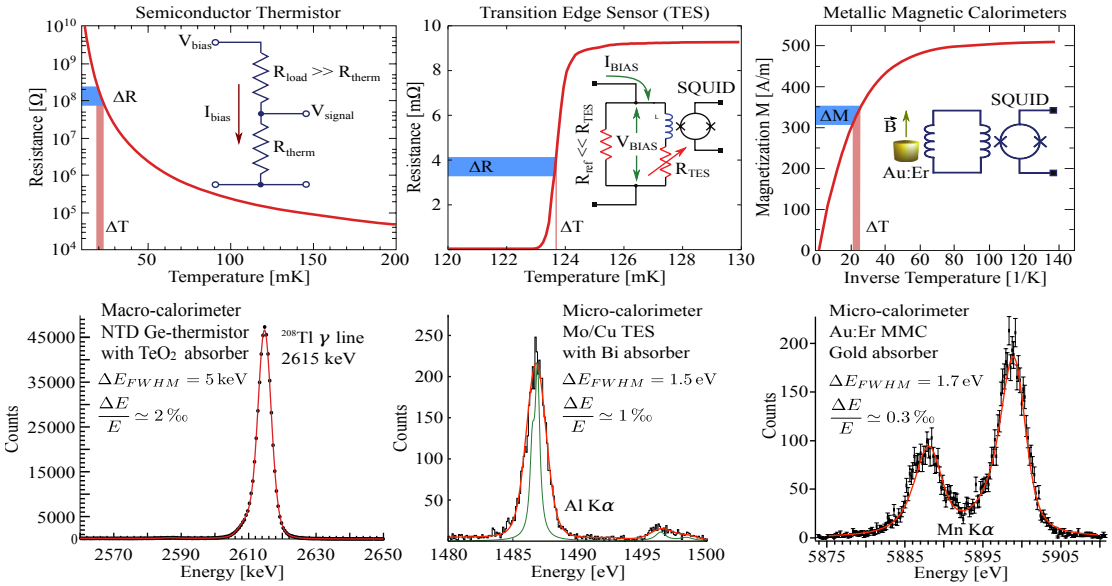

Figure 2.3: Temperature behavior (resistance vs,. temperature), biasing circuit and energy resolutions of different thermal sensors used in the neutrino sector: Ge-NTD (Germanium Neutron Transmutation Doped thermistors), TES (Transition Edge Sensors) and MKID (Mediated Kinetic Inductance Detectors). The TES spectrum (middle column) is courtesy of NIST. Figure reprinted from [118].

Recalling the discussion reported in Sec. 1.5.1, the choice of the material that constitutes the absorber of a cryogenic calorimetric detector is driven by three main considerations. The first one comes from the $\beta\beta$-emitter that has to be studied. If the crystal operated as calorimeter is grow starting from the isotope of interest, indeed, the detector and the source of the experiment coincide, providing a high detection efficiency on the decay. However, it is not always possible to grown a radio-pure crystal based on $\beta\beta$ emitters that shows good mechanical, cryogenic and calorimetric performances. The second constraint comes from the heat capacity of the absorber, that has to be very small in order to ensure that the temperature increase produced by an energy deposit is large enough to be measured (see Eq. 2.1). In the absorber selection, crystals with specific properties that allow to improve background suppression are clearly favored. From this point of view, scintillating crystals, being capable of identifying the nature of the interacting particle, are very interesting devices.

2.1.2 Thermal sensors

The temperature variations in the absorber are converted into electrical signals using dedicated sensors whose impedance shows a steep dependence on temperature. The per-

formance of the thermal sensor matters significantly achieve a high energy resolution in low-temperature calorimetric measurements. In the last decade, different sensors suitable for different energy scales have been developed: Transition Edge Sensors (TESs), Mediated Kinetic Inductance Detectors (MKIDs) and Germanium Neutron Transmutation Doped thermistors (Ge-NTDs). The common feature is the very high energy resolution ($\sim$ ‰) but in different energy ranges. In particular Ge-NTDs were born to operating on macro-calorimeters (hundreds grams and more) in the MeV region while TESs and MKIDs on micro-calorimeter (grams or less) in the eV/keV region, as shown in Fig. 2.3. Ge-NTDs did demonstrate to be suitable for tonne scale $0\nu\beta\beta$ experiment, the other ones require some further efforts.

Transition Edge Sensors. They are thin-film superconducting devices operated at the critical temperature T_c of the superconductor. In transition region, TES devices have a large positive temperature coefficient, which provides a sensitive measurement of temperature: particle interactions in the crystals modify the TES resistance and the current consequently. TES sensors have typically very low impedance, in the range of a few mΩ to an Ω. The large bandwidth offers several advantages: pulse shape sensitivity is significantly improved, and time resolution better than 1 ms can be achieved, reducing pileup due to $2\nu\beta\beta$ decay and background events. The very low-current noise of the SQUID amplifiers and the high signal amplitude makes them very suitable for high-resolution bolometric applications. TES-SQUID based detectors with eV-scale resolutions were operated by the dark matter project CRESST [119].

Mediated Kinetic Inductance Detectors. Their working principle is based on the property of kinetic inductance in superconducting materials. The kinetic component of the impedance depends on the density of Cooper pairs[1], which can be modified by an energy release able to break them apart. If the inductive element is part of a resonant circuit with a high quality factor, the density variation of Cooper pairs generates changes in the transfer function of the circuit. The signal is obtained by exciting the circuit at the resonant frequency, and measuring the phase and amplitude variations induced by energy releases. The main advantage of the KID technology persists in the ability to arrange parallel readout (multiplexing) using room temperature electronics, thus overcoming technical issues related to the operation of TES. Many MKID sensors can be independently coupled to the same excitation line by making them resonate at slightly different frequencies. This feature allows using a small number of wires in the cryostat, simplifying the installation. The potential of MKIDs has been already demonstrated in astrophysical applications where they successfully replaced the TES technology.

Ge thermistors. Intrinsic semiconductors (i.e. not doped) at cryogenic temperatures behave as insulators, since the thermal generation of electrons and holes across the band gap is frozen. On the contrary, the lattice impurities induced by the doping process create new energy levels slightly above the valence band or below the conduction

[1] In superconductive materials, under the critical temperature T_c, the electrons are coupled in boson quasi-particles, named Cooper pairs.

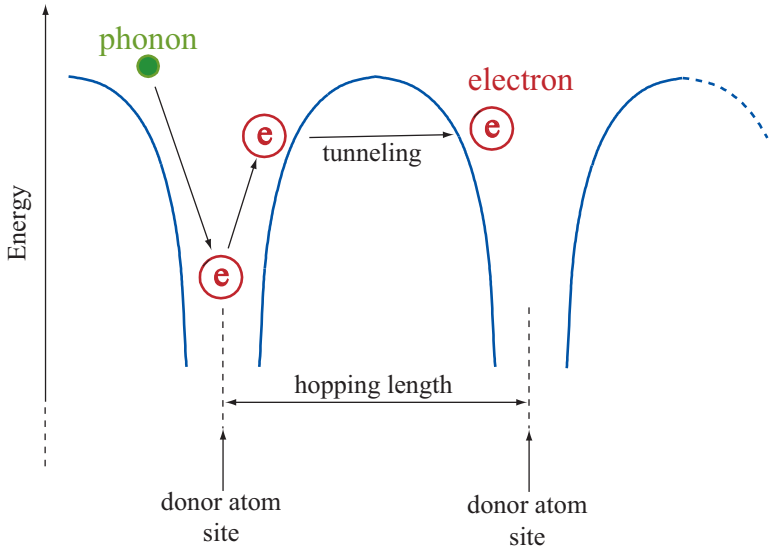

Figure 2.4: Schematic representation of the hopping conduction mechanism.

one (depending on the type of dopant). Conduction for such doped semiconductors occurs when electrons hop between dopant atoms, tunneling through the potential barrier which separates the two dopant sites. The conduction is activated by phonon mediation, as schematically depicted in Fig. 2.4. The tunneling probability is exponentially dependent on the inter-impurity distance and this is why an extreme homogeneity of the dopant distribution is fundamental. In particular, if the dopant concentration is slightly lower than N_c [2], the resistivity strongly depends on temperature. This is why usually semiconductor thermistors are operated just below the MIT region. The conduction mechanism under such conditions is related to the so-called *Variable Range Hopping*, since at low-temperatures the carriers can travel to far sites that have energy close to the Fermi one.

Semiconductor thermistors are intrinsically slow sensors, mainly sensitive to thermal phonons; their signals give information about the system in thermal equilibrium. Usually, a semiconductor thermistor consists of a small Ge (or Si) crystal with a doped region. A very uniform and large dopant distribution and a very accurate net dopant concentration are usually obtained through the Neutron Transmutation Doping (NTD) [122]. Melt-doped Ge crystals cannot achieve the necessary uniformity due to a variety of dopant segregation effects. The only technique available for producing a uniform doping is to produce the dopant by bombarding the Ge crystal with thermal neutrons. The most important aspect of this process is that ^{70}Ge transmutes into ^{71}Ga, an acceptor, and ^{74}Ge transmutes into ^{75}As, a donor, the primary active dopants in NTD Ge. The optimization of the detector performance is strictly related to the characteristics of the NTDs. Indeed the variation of resistance as function of temperature of such heavily doped thermistors

[2] Critical concentration of impurities that define the Metal Insulator Transition (MIT).

is well represented by the formula,

$$R(T) = R_0 \exp\left(\frac{T_0}{T}\right)^{\gamma}, \tag{2.5}$$

where the parameters R_0 and T_0 depend on doping level and donors/acceptors compensation. The exponential γ in the Mott model for a 3-dimensional crystal is equal to 1/4 for low compensation values [123]. It becomes 1/2 for large values of compensation, where the Coulomb repulsion among the electrons leads to the formation of a gap in the electron state density near the Fermi energy [124]. For the thermistors used in this work the following values apply: $\gamma \sim 1/2$, $T_0 \sim 3.3$ K and $R_0 \sim 1.2\ \Omega$.

2.1.3 Detector operation of Ge-NTD

In order to obtain a voltage signal, a steady current $I_{\rm bol} = I_B$ (bias current) is sent through the thermistor by means of the bias circuit shown in the left panel of Fig. 2.5. A bias voltage V_B is produced by a voltage generator closed on a load resistor R_L that is put in series with the thermistor $R_{\rm bol}$, whose resistance is negligible in comparison to R_L ($R_L \gg R_{\rm bol}$, therefore $I_{\rm bol}$ is independent from $R_{\rm bol}$). Once a working point is set by fixing a bias current, a voltage drop $V_{\rm bol}(T) = I_B\, R_{\rm bol}(T)$ is established across the thermistor. The consequent power dissipation $P = I_B\, V_{\rm bol}$ produces a temperature rise and acts back on the resistance $R_{\rm bol}(T)$ until an equilibrium is reached:

$$T_{\rm base} = T_{hs} + \frac{P}{G} \tag{2.6}$$

where G is the thermal conductance between the detector and the heat sink T_{hs}.

This phenomenon makes the V-I relation deviate from linearity and leads to a non-ohmic behavior. It is often referred to as *electrothermal feedback*. For a given I_B, the *static resistance* is simply the ratio $V_{\rm bol}/I_{\rm bol}$ while the *dynamic resistance* is the inverse of the tangent to the V-I curve. By further increasing I_B, the dynamic resistance crosses the so-called *inversion point* and becomes negative. The intersection of the V-I curve, usually called *load curve*, with the load line imposed by the biasing system determines the working point of the sensor (right graph of Fig. 2.5). It is typically chosen before the inversion point in order to maximize the signal amplitude and the signal-to-noise ratio. By a combined fit of load curves measured at different base temperatures, it is possible to evaluate the thermistor intrinsic parameters R_0, T_0 and γ.

In first approximation, the thermal pulse (reported in Fig. 2.6) produced by an energy release in the absorber is characterized by a very fast rise time (instantaneous if one assume the model described in Sec. 2.1 and a negligible thermalization time). The fall time, instead, follows an exponential decay whose time constant depends on the physical characteristic of the detector (recall Eq. (2.1)). Despite the specific time development of each detector, the main pulse features are common to most cryogenic macro-calorimeters. In particular the excellent signal-to-noise ratio and the very slow decay time (several seconds).

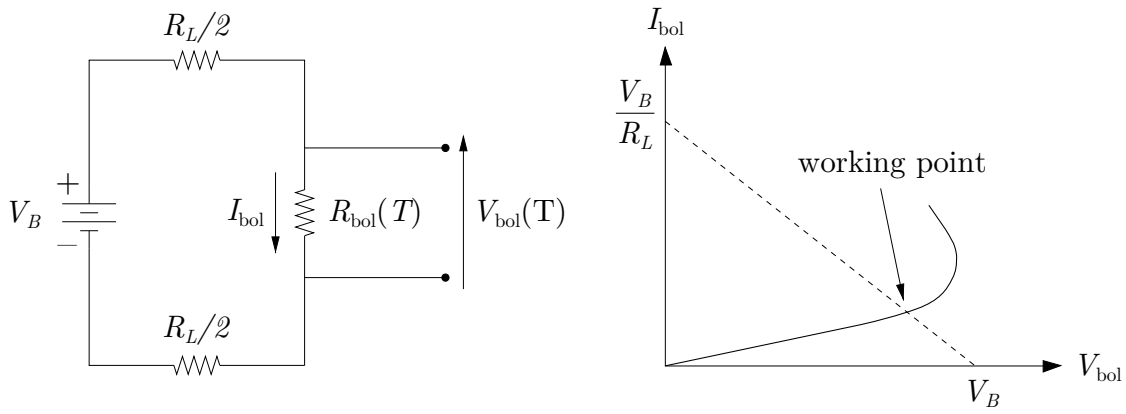

Figure 2.5: (Left) Schematics of the biasing system used for the NTD read-out. (Right) typical load curve of a semiconductor thermistor. The working point is set as the intersection between the V-I characteristic curve and the load line $V_{\rm bol} = V_B - I_{\rm bol}\, R_L$.

2.1.4 Thermal gain stabilization of Ge-NTD sensors

As the gain of a cryogenic calorimeter strongly depends on its operating temperature, its working temperature must be stabilized against low frequency temperature fluctuations from the cryogenic set-up, and any residual temperature drift must be precisely tracked and compensated for offline. In order to stabilize the detector artificial heater pulses are periodically injected using a resistive heater during the whole data-taking. Such heater is attached directly on the crystal surface using epoxy resin. Steady resistances to be uses as heaters are realized through a heavily doped semiconductor, well above the MIT region, so that a low-mobility metallic behaviour is exhibited. The stabilization signal is a square pulse having a width (T) much shorter than the detector response time, typically ∼100 ms for large calorimeters. The square pulses are triggered, allowing to generate them with a selectable rate and easily tag them for the data analysis. While the power consumed on the heating resistor is controlled by the pulse parameters, the energy injected to the calorimeter is proportional to the thermal coupling between the heating resistor and the crystal. This constant is not known a priori and changes from crystal to crystal. The efficiency of this method has already been demonstrated in the Cuoricino and CUORE-0 experiments where a high-stability pulse generator has been longer used. A detailed discussion on the use of heaters for stabilization cryogenic calorimeters can be found in [125] and reference therein.

2.2 The CUORE experience

The understanding of bolometric detectors and their performances improvement have been possible thanks to decades of development. The milestones and main achievements over the past 30 years in cryogenic calorimeters for $0\nu\beta\beta$ studies are explained in detail in [88] and summarized in Tab. 2.7.

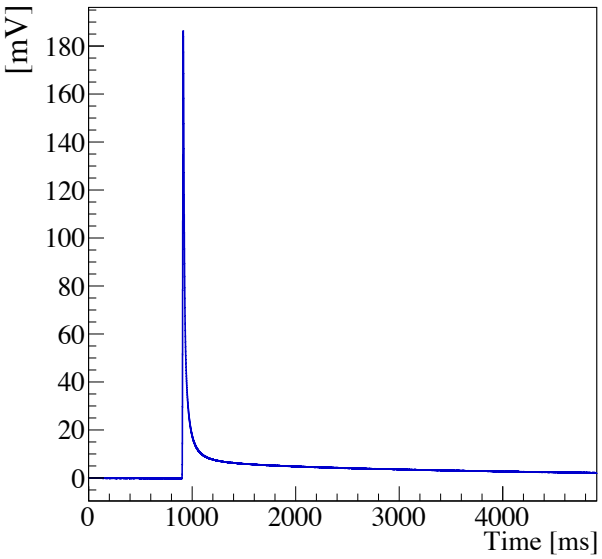

Figure 2.6: Bolometric pulse due to the energy deposition of 2615 keV in a ZnSe crystal.

The ^{130}Te choice for the $0\nu\beta\beta$ emitter was dictated by its large isotopic abundance (33.8%), that allows to operate a large source mass without enriching the material. In addition, even if its $Q_{\beta\beta}$ (2527 keV) is not among the highest, it lies between the peak and the Compton edge of the 2615 keV line of ^{208}Tl, which is a rather clean window to look for $0\nu\beta\beta$.

While a very good energy resolution ($< 1\%$) was already achieved by Cuoricino and the mass scalability has now been demonstrated by CUORE, obtaining a low background requires further work. The results of the efforts to reduce the dominant α-background are detailed in the next section.

Table 2.7: List of the TeO_2 bolometric experiments searching for the $0\nu\beta\beta$ of ^{130}Te performed at LNGS. The main characteristics are reported. The sensitivity in terms of $\beta\beta$ half-life is the combined value with the previous experiments. Table reprinted from [88].

Experiment	Running period	Crystals	Mass [kg]	Exposure [kg y]	Bkg in the ROI [counts/(keV · kg · y)]	FWHM @ $Q_{\beta\beta}$ [keV]	$S^{1/2}_{0\nu}$ (90% C. L.) [y]
6 g crystal, [126]	Jan 1991 - Apr 1991	1	0.006	0.0002	123	50	$4.0 \cdot 10^{19}$
21 g crystal, [127]	May 1991 - Jun 1991	1	0.021	0.0004	88	20	$5.3 \cdot 10^{19}$
34 g crystal, [128]	Jul 1991 - Oct 1991	1	0.034	0.0041	79	30	$4.4 \cdot 10^{20}$
73 g crystal, [129]	Nov 1991 - Aug 1992	1	0.073	0.020	35 (Run I) / 17 (Run II)	7	$2.7 \cdot 10^{21}$
334 g crystal, [130, 131]	Jan 1993 - Aug 1994	1	0.334	0.40	3.4	15	$2.1 \cdot 10^{22}$
4 crystal array, [132]	Oct 1994 - Oct 1995	4	1.32	0.73*	4	$\lesssim 12$	$3.3 \cdot 10^{22}$
MiDBD, [98]	Apr 1998 - Dec 2001	20	6.8	4.25	0.6 (Run I) / 0.3 (Run II)	$5 - 15$	$2.1 \cdot 10^{23}$
Cuoricino, [99, 133]	Mar 2003 - Jun 2008	62	40.7	71.4	0.20 (Run I) / 0.15 (Run II)	5.8 ± 2.1	$2.8 \cdot 10^{24}$
CUORE-0, [100, 133]	Mar 2013 - Mar 2015	52	39.0	35.2	0.058 ± 0.004	4.9 ± 2.9	$4.0 \cdot 10^{24}$
CUORE (first release), [59]	2017 - 2023	988	742	86.3	0.014 ± 0.002	7.7 ± 0.5	$1.5 \cdot 10^{25}$
CUORE (expected), [134]	2017 - 2023	988	742	3705	0.01	5	$9.5 \cdot 10^{25}$

2.2.1 Alpha mitigation from Cuoricino to CUORE

The α-particles produced by ^{238}U, ^{232}Th chains and their daughter nuclei are not of concern when the contaminations are present in crystal's bulk, since the full energy of the decay is measured (> 4 MeV, far from $Q_{\beta\beta}$ of the usual $\beta\beta$-emitters). If the α-emitters are on the crystals surfaces or in the surrounding materials, a variable fraction of their energy can be lost in the inactive material, thus producing a flat background from the energy of the decay down to the region of interest for $0\nu\beta\beta$.

A dedicated study of the α-background mitigation was started already during the Cuoricino data-taking. In Cuoricino, the background rate in the ROI was 0.153 ± 0.006 counts/(keV $\cdot$ kg $\cdot$ y). Three main contributions were identified [134]: $(30 \pm 10)\%$ of the measured background was attributed to multi-Compton events of the 2615 keV γ-quantum produced by ^{232}Th contaminations in the cryostat shields; $(10 \pm 5)\%$ was due to surface contaminations of the crystals (primarily degraded αs from the natural decay chains); and $(50 \pm 20)\%$ is ascribed to similar surface contamination of inert materials surrounding the crystals, most likely copper.

On the basis of this result, the R&D for CUORE has pursued two major complementary lines: the reduction of surface contamination and the selection of extremely radiopure construction materials. A new design for the detector structure was proposed, which reduced the amount of copper and the copper surfaces facing the TeO_2 crystals by a factor ~ 2. The bulk and surface contaminations were also checked, in order to validate a new production and treatment protocol for CUORE [135]. All the crystal surface treatments for CUORE were performed in the clean room at LNGS.

A new copper cleaning techniques led to a reduction of a factor ~ 2 of the background in the $(3 - 4)$ MeV region, the one dominated by surface contaminations. The copper cleaning procedure consisted of 4 steps: tumbling, electro-polishing, chemical etching and magnetron plasma cleaning [136].

In view of CUORE all the operations related to the detector assembly were standardized and automatized. Moreover, to avoid recontamination of all the parts due to direct contact with less radiopure materials and exposure to radon in the atmosphere, the whole assembly process was confined into hermetic volumes constantly flushed with nitrogen.

All these new procedures as well as the radiopurity of materials for the CUORE experiment were tested through the first tower produced with the CUORE assembly line, called CUORE-0. It was run as independent experiment in the same cryostat of Cuoricino from March 2013 up to April 2015 (see Ref. [133, 138] for more details on the CUORE-0 results).

The comparison of the background spectra of CUORE-0 and Cuoricino, depicted in Fig. 2.8, clearly shows an important reduction. It is less prominent up to 2.6 MeV, since the source of this background was mostly located in the outer shields of the cryostat, which was the same for both detectors. In the continuum region (2.7 - 3.9) MeV the

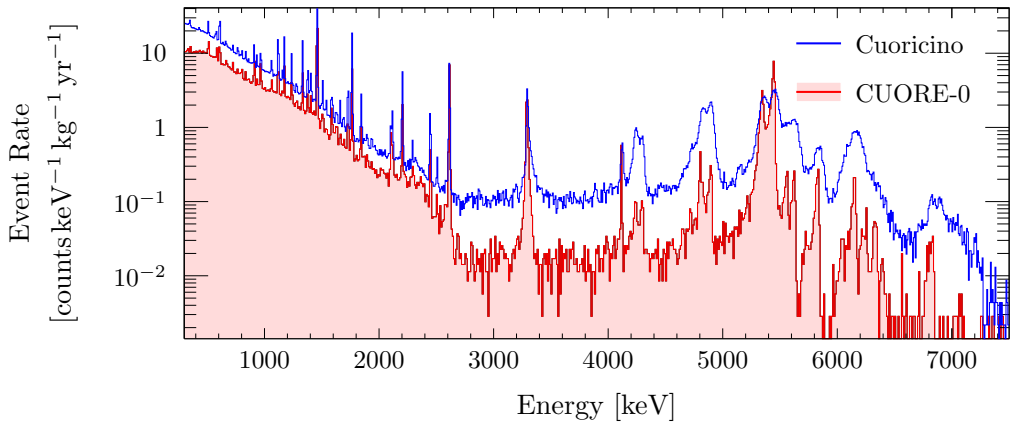

Figure 2.8: Final spectra of Cuoricino and CUORE-0 in the (750 - 7500) keV region. The reduced background rate in CUORE-0 is clearly visible, especially in the α-region, where it is about a factor 7 reduced in comparison to Cuoricino [138].

background is dominated by smeared αs, with an almost flat distribution. The only exception is the ^{190}Pt peak ($Q_\alpha = 3249\,\text{keV}$), which is a bulk contamination of the TeO_2 due to the platinum crucible used for the crystal growth.

In CUORE-0, a rate of (0.016 ± 0.001) counts/(keV $\cdot$ kg $\cdot$ y) was measured for this flat background [100], a value about a factor 7 smaller than the one obtained in Cuoricino, which was of (0.110 ± 0.001) counts/(keV $\cdot$ kg $\cdot$ y) in the same energy region [99].

In the region of interest, the background rate measured by CUORE-0 was $(0.058 \pm 0.004\,\text{(stat.)} \pm 0.002\,\text{(syst.)})$ counts/(keV $\cdot$ kg $\cdot$ y) [100]. This value corresponds to an improvement of a factor 3 with respect to the Cuoricino one, which was (0.169 ± 0.006) counts/(keV $\cdot$ kg $\cdot$ y) [99].

A further background reduction in the continuum region is instead expected for CUORE, thanks to the improved material selection for its custom-made cryostat and thanks to self-shielding effects. Nevertheless the dominant α-background at the level of 10^{-2} counts/ (keV $\cdot$ kg $\cdot$ y) still remains the limiting factor of the CUORE sensitivity. Only an active α-particles rejection tool will allow to reduce the background in a next-generation experiment. Before addressing this crucial topic in Sec. 2.3 it is worth to discuss how to reduce the background exploiting the features of a large-scale detector.

The modular design of the bolometric detectors provides several advantages to study and mitigate environmental backgrounds. First, the granularity of the detector can be exploited to divide the whole array in different clusters (i.e. towers, floors) and localize background sources in Monte Carlo simulations. It also allows to remove from the analysis crystals that show higher level of contaminations or bad performances without spoiling global detector efficiency.

Furthermore several background sources, such as multi-Compton, muon-induced elec-

tronic showers or external βs, deposit energy in multiple crystals within the response time of the detector. On the contrary $\beta\beta$ decay events are usually confined within the crystal they originate from. This feature is used in the analysis by forming multiplets of events that occur within a certain coincidence window (usually ranging from 5 to 20 ms) in different crystals. Since the event rate is approximately 1 mHz, the probability of accidental (i.e. causally unrelated) coincidences is extremely small ($\sim 10^{-5}$).

Finally the self-shielding provided by the external detector layers to the inner ones allows to further reduce the β/γ background coming from the external shields. The different fraction of background removed following these procedures and the final counting rate in the different regions of interest (under/above the 2.6 MeV line) will be calculated exploiting the background models of CUORE and CUPID-0.

2.3 Active background reduction

Being fully active and sensitive to all types of radiation, the background reduction in bolometric detectors is a difficult goal to be achieved. General prescriptions for low-background experiments were introduced in Sec. 1.5.1 while the already implemented strategies to reduce the background in cryogenic calorimeters were discussed in the previous section. Now it is to be investigated how overcome the CUORE background limit.

Tab. 2.9 summarizes the final results of the CUORE projected background detailed in [139], highlighting each single contribution. The elements of the experimental setup are grouped in *External*, *Farl* and *Near*.

The label *External* is referred to the environmental γs, neutrons and cosmic ray muons.

The label *Far* collects all the cryostat compounds that do not *see* directly the crystals. Their contaminants can be considered distributed in the bulk of the material. The surface contaminations in far elements are negligible, since their αs cannot reach the crystals (due to their short path) while β/γs can be considered as produced in the material bulk. This category includes copper parts such as external shields (*CuOFE*), superinsulation layers (*SI*), Roman lead shield (*RomanPb*), Modern lead shield (*ModernPb*), stainless steel rods (*Rods*) and the 300K steel flange (*300KFlan*).

Finally the label *Near* indicates components in the vicinity to TeO_2 detectors, for which the contribution of surface contaminations can not be neglected (mainly smeared-α). This includes TeO_2 crystals (TeO_2), Si heaters (*heaters*), NTD Ge thermistors (*NTDs*), PEN-Cu cables [3] (*PEN*), copper wire pads (*pads*), PTFE (teflon) supports (*PTFE*) and copper parts such as the detector holder and the 10 mK shield (*CuNOSV*).

The total projected BI in the region of interest of CUORE is equal to $[1.02 \pm 0.03(\text{stat}) \, ^{+0.23}_{-0.10}(\text{syst})] \cdot 10^{-2}$ counts/(keV $\cdot$ kg $\cdot$ y). This number is obtained by summing all the contributions listed in Tab. 2.9 (i.e. sources with an upper limit are excluded). The BI is by far dominated by the near copper contribution (i.e. the detector holder), mainly ascribed to degraded α-particles from surface contaminants as already discussed above. It is worth to stress that also assuming to remove the whole α-component, it is not obvious that the present configuration of the CUORE structure can meet the requirements for a next-generation experiment. Indeed, as reported in [140], the BI for a next generation bolometric experiment in a FWHM-wide region centered around the $Q_{\beta\beta}$ has to be lower than 0.1 counts/(tonne $\cdot$ y).

Referring to the last column of Tab. 2.9 and considering a fully α-background rejection, only the two last contributions in the *Near* contaminations panel would be reduced (< 2 counts/(tonne $\cdot$ y)) [141], all the other ones still remains unchanged. Instead nothing can be said about the present upper limits, unless more sensitive measurements will be done in order to lower them. Of course the full background reconstruction of CUORE will give us more informations about the most critical limits (*RomanPb, CuOFE*). However

[3] Cu-insulator tapes having PEN (Polyethylene 2.6 Naphthalate) substrate going from the detectors to the mixing chamber, the coldest stage at which the array is thermally and mechanically anchored, and from the mixing chamber to room temperature.

it is clear that the environmental and superinsulation contributions are not compatible with a next-generation experiment. Further reduction of the environmental background can be obtained by implementing a muon veto and by using thicker lead and polyethylene shields, as investigated in the framework of CUPID (CUORE Upgrade with Particle IDentification, introduced in Sec. 2.5) project [142]. Finally the superinsulation can be removed and replaced with a cleaner low-temperature insulator.

Table 2.9: Main background indexes expected for the various components of CUORE (limits are 90% C.L.), more details in the text.

Region	Source	Background Index [counts/(keV · kg · y)]	Background Index FWHM 5 keV [counts/(tonne · y)]
External	Environmental γ	$<3.6 \cdot 10^{-4}$	<2
	Environmental n	$(8\pm6) \cdot 10^{-6}$	$\sim5 \cdot 10^{-2}$
	Environmental μ	$(1.0\pm0.2) \cdot 10^{-4}$	$\sim5 \cdot 10^{-1}$
Far	*Rods* and *300KFlan*: natural radioactivity	$(7\pm3) \cdot 10^{-5}$	$(3.5\pm1.5) \cdot 10^{-1}$
	SI: natural radioactivity	$(2.2\pm0.4) \cdot 10^{-4}$	1.1 ± 0.2
	ModernPb: natural radioactivity	$<1.8 \cdot 10^{-4}$	<0.9
	RomanPb: natural radioactivity	$<2.9 \cdot 10^{-3}$	<14.5
	CuOFE: natural radioactivity	$<1.7 \cdot 10^{-3}$	<8.5
Near	TeO_2 : cosmogenic activation	$<6.7 \cdot 10^{-5}$	$<3.4 \cdot 10^{-1}$
	CuNOSV: cosmogenic activation	$<2.2 \cdot 10^{-6}$	$<1.1 \cdot 10^{-2}$
	CuNOSV: natural radioactivity	$(8.7\pm0.3) \cdot 10^{-3}$	44 ± 2
	TeO_2 : natural radioactivity	$(1.2\pm0.1) \cdot 10^{-3}$	6.0 ± 0.5

2.3.1 Event-by-event α identification

Cryogenic calorimeters based on scintillating crystals are called *scintillating calorimeters* and provide a natural solution for α-background identification. The amount of the scintillation light produced by an interacting particle in the absorber depends on the nature of the particle itself. In particular α-particles, being charged and massive, release their whole energy in few μm with an high ionization density. In this way they saturate all the scintillation centers in the vicinity to the interaction point, the excess energy is lost in non radiative channels causing the suppression of the light output. On the contrary electrons have a small energy loss per path length, therefore can reach more scintillation centers without saturating them. A phenomenological description of this phenomenon was proposed by Birks[4] in 1951 [143] in differential form:

$$\frac{dL}{dx} = \frac{A\frac{dE}{dx}}{1 + k \cdot B\frac{dE}{dx}} \tag{2.7}$$

[4]Birks' law has mostly been tested for organic scintillators. Its applicability to inorganic scintillators is debated but it is not a concern for our discussion.

where the *absolute scintillation factor A* is assumed to be independent on the energy and on the type of interacting particle [144], k accounts for the saturation while $B \cdot \frac{dE}{dx}$ is the density of luminescent centers along the particle track. Usually the product $k \cdot B$ is treated as one constant factor, called *Birks factor* and indicated with k_B. From the previous formula, one can calculate the total light output:

$$L(E) = \int_0^E \frac{AdE'}{1 + k_B \frac{dE'}{dx}} \tag{2.8}$$

whence, plugging in the right $\frac{dE}{dx}$ one can calculate for every particle the scintillation response. k_B is a free parameter defined once for each material, then it is the same for all the particle.

Dividing the light produced from ions/alphas by the light from electrons at the same energy one can define the **quenching factor**:

$$QF^{\alpha}(E) = \frac{L_{\alpha}(E)}{L_e(E)} = \frac{\int_0^E \frac{AdE'}{1+k_B(\frac{dE'}{dx})_{\alpha}}}{\int_0^E \frac{AdE'}{1+k_B(\frac{dE'}{dx})_e}}. \tag{2.9}$$

It is independent of A but it depends on energy and on k_B which is assumed to be constant.

The bigger is the QF_{alpha}, the easier is the particle discrimination achievable by measuring the light output. Usually $QF^{\alpha} < 1$ as from the above equations, $L(E)_e > L(E)_{\alpha}$. ZnSe crystals show a particular behavior, as the $L(E)_{\alpha}$ is greater than $L(E)_e$ (see Fig. 2.10). As discussed in [145] this phenomenon is related to the internal structure of ZnSe crystal and the defects therein, showing the QF could be tuned by a thermal treatment of the crystal. In principle, this does not prevent separating the two populations. However, if part of the scintillating light of an α event is lost this could leak in the signal band. If $L(E)_{\alpha} < L(E)_e$, it could make a cut on the detected light and completely eliminate the entire α background, losing efficiency on the signal.

It is difficult to give an absolute measurement of LY and QF of a given compound, as several factors are involved:

- the QF depends on the characteristics of the crystal and the temperature and measuring it accurately requires a good knowledge of light collecting efficiency and a trustable calibration source for the light detector;
- the QF depends on the presence of impurities and defects in the crystals in case of ZnSe;
- the scintillation signal is made by several components, whose time-development usually depends on the interacting particle; the choice of an algorithm to evaluate the amplitude of these pulses, as well as the optimization of certain technical parameters like the signal collection time, can affect the evaluation of the QF [146, 147].

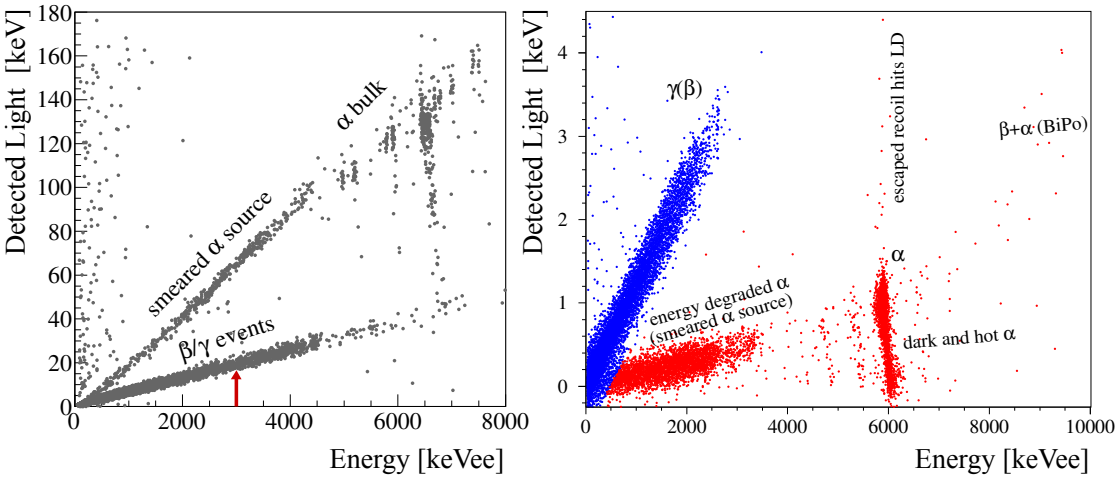

Figure 2.10: Scatter plots of light-versus-heat signals of ZnSe (left) and $ZnMoO_4$ (right) scintillating calorimeters. $ZnMoO_4$ crystals show the expected quenching factor since the α-particles produce lower light then β/γs [49]. On the contrary in ZnSe crystals the two bands (α and β/γ) are inverted. Both ZnSe and $ZnMoO_4$ crystals are faced to a smeared α-source, while in ZnSe there is also an AmBe neutron source (high energy γs in the lower band). The arrow points to the ^{82}Se $Q_{\beta\beta}$ (2998 keV).

2.3.2 Background sources and tagging in scintillating calorimeters

Isotopes suitable for scintillating calorimeter such as ^{116}Cd, ^{82}Se and ^{100}Mo have a $Q_{\beta\beta}$ at $\sim$3 MeV. In this region the natural radioactivity contribution is lower then in the region below the 2.6 MeV peak of ^{208}Tl, where the Compton plateau of this line plays a crucial role. The relevant contributions to the background from ^{238}U and ^{232}Th in the crystals (internal) and in the cryostat (external) are depicted in Fig. 2.11.

Internal contaminations can be efficiently removed exploiting the knowledge of the decay chains. ^{214}Bi decays with a branching ratio (BR) of 99.98% in ^{214}Po, which α-decays with a Q-value of 7.8 MeV. The half-life of ^{214}Po, which is about 160 μs, is extremely short compared to the time development of bolometric signals, which is hundreds of ms. For this reason the β/γ-emission of ^{214}Bi, simultaneously followed by a 7.8 MeV α-particle, does not represent a problem for the background, as the superimposition of the two signals lies at much higher energies than the region of interest. When evaluating the background due to the ^{214}Bi also its decay in ^{210}Tl has to be considered, which occurs via α-emission (BR of 0.02 %). This contribution, however, can be easily suppressed: ^{210}Tl β-decays with a Q-value of 5489 keV and a half-life of 1.30 min. The background induced by the β-emission can be rejected using the delayed coincidences on the α of ^{214}Bi. In this case, the dead time induced by the delayed coincidences is almost negligible, as the half-life of ^{210}Tl is very short and the BR for this decay is extremely small.

Another dangerous background source is the one due to the internal contamination of ^{208}Tl, that belongs to the ^{232}Th chain and β-decays with a Q-value of 5001 keV. In 36% of the ^{208}Tl decays, two γs are emitted in cascade (i.e. 2615 keV and 583 keV). Their

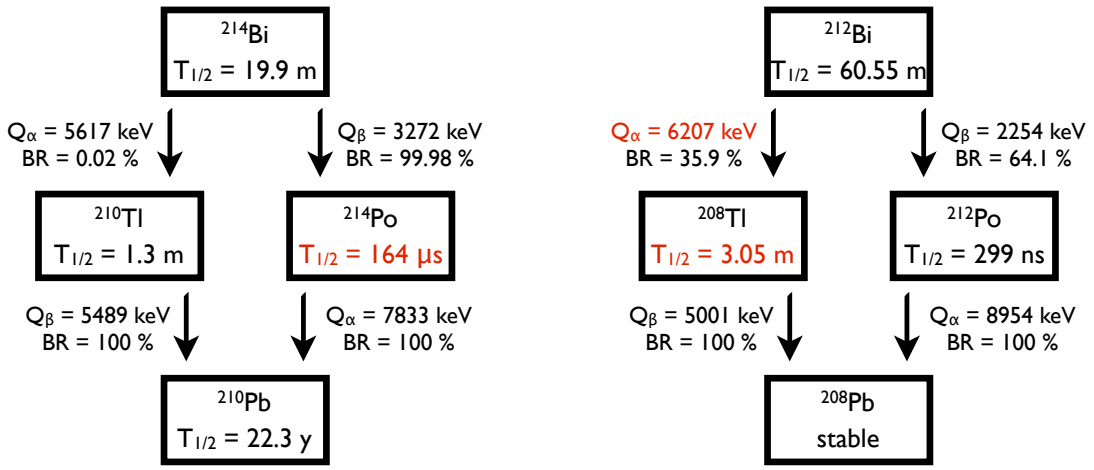

Figure 2.11: Left. Decay scheme of ^{214}Bi. The short life of its daughter, ^{214}Po, causes the superimposition of the β emitted by ^{214}Bi and the α particle produced by ^{214}Po. **Right.** Decay scheme of ^{208}Tl. The delayed coincidences with the α particle produced by its parent, ^{212}Bi, allows to suppress this background source. Figure and text reprinted from [149]

occurrence in the same crystal produce a pile-up event in the $Q_{\beta\beta}$ energy region, if a fraction of their energy escapes the detection. This contribution to the background can be suppressed using the coincidence with its parent, ^{212}Bi. Also in this case one would obtain a negligible dead-time.

The efficiency of this tagging technique, usually called *delayed veto*, spoils when the contaminations are on the crystals surface, since the α can escape from crystals (details in [157]). For this reason the crystals surface treatment was addressed with particular care (see Sec. 3.1.5). On the contrary when the background sources are in the detector holder or in the shielding they cannot be tagged. However even in this case the higher $Q_{\beta\beta}$ helps: the 2615 keV and 583 keV γ-lines pileup are geometrically favored only if coming from elements very close to the detector (i.e. inner shield, holder), while the 2615 keV multi-Compton can be a concern also if produced in the far elements (i.e. thermal insulation).

2.3.3 $2\nu\beta\beta$ pile up

The background sources described above could theoretically be reduced to zero, even though the technical challenges would be substantial. However there is a background source for any $0\nu\beta\beta$ search that is always present: the $2\nu\beta\beta$ decay of the candidate isotope itself. The end point of the $2\nu\beta\beta$ spectrum can contribute substantially to the background in the ROI when the energy resolution is significantly larger. However, as already shown in Sec. 1.5.1, in detectors with good energy resolutions like calorimeters, the ratio of $2\nu\beta\beta$ to $0\nu\beta\beta$ event rate, assuming $|m_{\beta\beta}|$ in the inverted hierarchy region,

Table 2.12: $2\nu\beta\beta$ pile-up induced background in a 5 keV ROI around the $Q_{\beta\beta}$ for experiments based on the four $\beta\beta$ candidates discussed in [141]. The pile-up rate is evaluated for a 90% enrichment, a $5 \cdot 5 \cdot 5$ cm^3 crystal and for a minimum pulse separation time $\Delta t = 1$ ms.

Isotope	Crystal	$N_{\beta\beta}$ [n/crystal]	$T^{2\nu}_{1/2}$ [y]	Bkg in ROI [5 keV] [counts/(tonne · y)]
^{82}Se	ZnSe	$2.5 \cdot 10^{24}$	$9.2 \cdot 10^{19}$	$2.7 \cdot 10^{-2}$
^{116}Cd	$CdWO_4$	$1.5 \cdot 10^{24}$	$2.8 \cdot 10^{19}$	0.07
^{100}Mo	$ZnMoO_4$	$1.3 \cdot 10^{24}$	$0.7 \cdot 10^{19}$	1.5
^{130}Te	TeO_2	$2.5 \cdot 10^{24}$	$68 \cdot 10^{19}$	$0.5 \cdot 10^{-3}$

is negligible.

Nevertheless, a drawback using calorimeters comes from their slow response time. Accidental pile-up of $2\nu\beta\beta$ events can produce a background contribution in the ROI, thus limiting the sensitivity of the experiment [150, 151]. Two events produced in the same detector by two random $2\nu\beta\beta$ decays within a time window smaller than the rise time of the detector ($\sim$ 10 ms) can produce a signal that mimics a $0\nu\beta\beta$ decay. Pile-up occurrences that produces two distinct pulses in the same acquisition window are easily discharged by pulse shape analysis.

The analysis described in [141] shows that standard pulse shape analysis cuts, already developed for CUORE, give a pile-up rejection efficiency of 100% down to $\Delta t \sim 5$ ms and, for the best performing detectors, down to $\Delta t \sim 1$ ms. In Tab. 2.12 the $2\nu\beta\beta$ pile-up-induced background for the main $\beta\beta$ candidates are summarize. The pile-up rate is evaluated for 90% enrichment, a $5 \times 5 \times 5$ cm^3 crystal, and for a minimum pulse separation times of $\Delta T = 1$ ms. The background is expressed in counts/(tonne · y) in a ROI of 5 keV around the respective $Q_{\beta\beta}$.

Further improvement could be obtained by exploiting the faster time response of light detectors; the pulse rise time of bolometric light detectors is already a factor $\sim$5 smaller than the rise time of bolometric signals. For example, the case of ^{100}Mo, which is the most problematic among the isotopes in Tab. 2.12, given the relatively small $T^{2\nu}_{1/2}$, has been extensively studied in [151]. There, it is shown that the pile-up discrimination on light signals can reduce the background induced by $2\nu\beta\beta$ in ^{100}Mo to well below 1 counts/(tonne · y).

In principle a pile-up can occur not only among two $2\nu\beta\beta$ decays but also among two radioactive background pulses or among a $2\nu\beta\beta$ decay and a radioactive decay. Both these additional contributions can result in spurious pulses in the ROI. While the $2\nu\beta\beta$ pile-up rate, is irreducible, the pile-up rate from background and background plus $2\nu\beta\beta$ depends on the radioactive background rate and can therefore be limited to a certain extent. Assuming a radioactive background rate of 0.14 mHz (CUORE

estimate), the resulting pile-up background in the ROI from radioactive sources and radioactive sources plus $2\nu\beta\beta$ is negligible for all isotopes. However, considering the additional background reduction foreseen for a future bolometric experiment with respect to CUORE, the only source of pile-up background in the ROI that has to be taken into account is the $2\nu\beta\beta$ decay.

2.3.4 Natural radioactivity reduction for CUPID

The active background rejection techniques, on which next-generation detector developments are focused, aim at reducing to negligible levels the effect of surface contaminations from detector materials. As mentioned, this background source is identified as the dominant contributor to Cuoricino and CUORE-0 counting rates and is the limiting factor for CUORE sensitivity. Further background reduction is needed to ensure the achievement of a background level three orders of magnitude lower than CUORE (i.e. 0.1 counts/(tonne · y)). Indeed, also bulk contaminations can contribute to the ROI counting rate at levels of 10 counts/(keV · tonne · y) [139]. Among these, the most dangerous are certainly the radioactive contaminations of the detector elements: crystals, copper, lead shield, and the "small parts" as glue, detector heaters, bonding wires or flat cables and pads etc. In the CUORE background budget [139], no positive indication of the presence of contaminants in the different detector elements have been obtained, with the exception of surface contaminations. However, in most cases, the available upper limits on materials contamination translate to potentially dangerous counting rates for the CUPID goal (see Tab. 2.14 of the next chapter about CUPID). For this reason, an improvement of the presently attained sensitivities is mandatory.

Two techniques will be explored in the CUPID program:

- **Pre-concentration of radio-contaminants through chemical treatment of materials.** When coupled to Nuclear Activation Analysis (NAA), Inductively Coupled Plasma Mass Spectrometry (ICPMS), or High Purity Germanium (HPGe) screening this will allow to increase the present achieved sensitivity. As an example, in the case of copper both NAA and HPGe spectroscopy achieve a similar sensitivity of about 1 μBq/kg on ^{232}Th. In both cases the sensitivity is ultimately limited by the mass of the copper sample that can't be increased ad libitum[5]. A pre-concentration of the contaminant is equivalent to an increase in the mass of the sample resulting therefore in a sensitivity increase. The technique is often used in ICPMS measurements but can also be successfully applied for NAA and HPGe measurements. However, it requires a dedicated study for each material, where the achievement of the required concentration as well as the control of systematics have to be proven.

- **Development of a bolometric detector for the measurement of surface/bulk contamination of small samples and foils.** In a number of cases the aforementioned screening techniques can't be applied either because the available mass

[5]Increasing the mass of a sample measured with HPGe is often not effective due to the self-absorption of the gamma lines inside the sample

sample is too small (HPGe spectroscopy require large mass samples to reach high sensitivity) or because the material properties are inappropriate (NAA and ICPMS have restrictive conditions on the chemical elements that can be analyzed). For CUORE this was true in the case of small parts or materials used in the form of foils (superinsulation, flat cables, etc). In these cases, the use of surface alpha spectroscopy through Si surface barrier diodes has been shown to reach competitive sensitivities on shorter time scales. The same kind of screening, implemented through the use of bolometric detectors, will achieve a sensitivity that is between 10 and 100 times higher thanks to the better energy resolution of these devices as well as to their higher radiopurity. Si wafers or TeO_2 slabs can be used for this purpose realizing a sandwich-like detector where samples are inserted in-between such thin calorimeters.

If successful, the improvement reached with the development of these two technologies will allow us to reach a sensitivity on U and Th concentrations of about one to two orders of magnitude higher than what is obtained today, which would fit the goal for CUPID materials.

As deeply discussed above the efforts needed for a next generation detector are mainly focused on the background reduction. The technology based on scintillating calorimeters, allows for an active rejection of α-particles and a lower β/γ-background due to the higher $Q_{\beta\beta}$. A similar result can be obtained also with TeO_2 measuring the Cherenkov light ($\sim$100 eV), but more sensitive light detectors are required. On the contrary the technology for the scintillation light detection is already available, as discussed in the next section.

2.4 Cryogenic light detectors

The light detectors (LDs) used for scintillating calorimeter, similar to the one reported in Fig. 2.13, are disk-shaped pure Ge crystal (ϕ 44 mm $\times$ 180 μm) grown by UMICORE using Czochralski technique, etched on one side and polished on the other one. A SiO_2 layer is deposited on the side that faces the scintillating calorimeter, in order to increase the light absorption [152]. These crystals are operated as calorimeters, because standard LDs (like photo- multipliers, photodiodes) show many technical problems when cooled at 10 mK. Therefore, when scintillating photons escape the crystal, they are absorbed by the LD and eventually converted into phonons. The heat signal is then detected via a $3 \times 1.5 \times 0.4$ mm^3 NTD Ge thermistor, thermally coupled to the etched side of the crystal with 6 epoxidic glue spots of $\sim$600 μm diameter and $\sim$50 μm height.

As mentioned before, only a few % of the energy deposited by interactions in scintillating calorimeters is emitted in the form of light. Accounting also for the collection efficiency a small light signal is expected, only $\sim$3.5 keV for Li_2MoO_4 and $\sim$10 keV for ZnSe when an energy release of 3 MeV occurs in the scintillating crystal. For this reason, usually all the LDs were permanently exposed to a ^{55}Fe source that, emitting two X-rays at 5.9 and 6.5 keV, provides the energy calibration in the region of interest. In addition,

the fit performed on the X-rays doublet, reported in Fig. 2.13, allows to evaluate the energy resolution achievable with this device. This spectrum, obtained operating the detector in standard conditions, shows a FWHM energy resolution lower than 170 eV, which is much better than the required one. Finally, it should be highlighted that the shape of signal acquired with such LDs shows a strong dependance on the working point. Since the time development of the light signals can be used to enhance the particle discrimination (as shown in the next chapters), the working point of the thermistor is set by compromising between a good energy resolution and a fast detector response. Other interesting features of the LDs, like their characterization in terms of signal amplitude, energy resolution and signal development, can be found in reference [153].

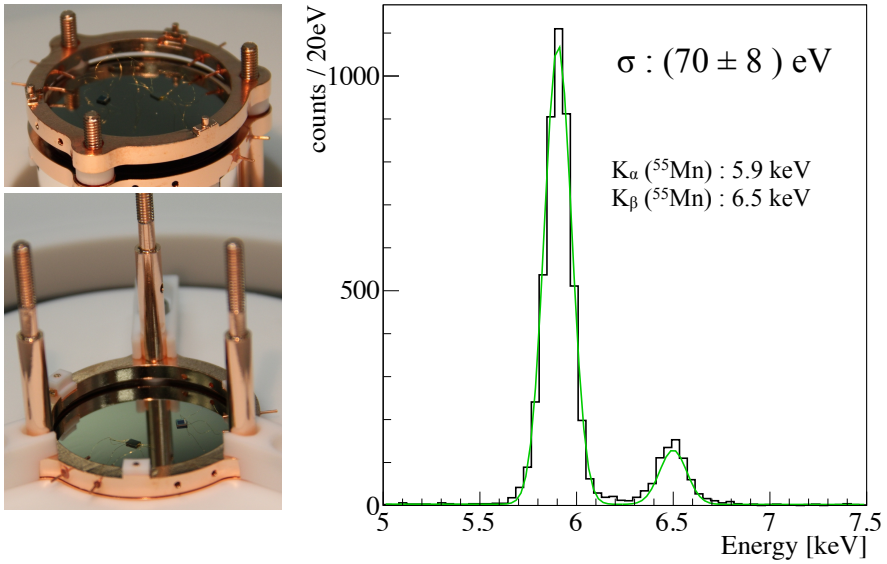

Figure 2.13: Left. Bolometric light detector: a pure Ge wafer is fixed in a copper frame by means of teflon clamps. Temperature sensor and heater were glued directly on the Ge-disk. **Right.** Energy spectrum of a ^{55}Fe X-ray source obtained with such detector.

2.5 CUPID: a next generation experiment

CUPID is a proposed future bolometric $0\nu\beta\beta$ experiment which aims at a sensitivity to the effective Majorana neutrino mass on the order of 10 meV, covering entirely the so-called inverted hierarchy region of the neutrino mass patterns ($\sim$ 15-50 meV). CUPID will be designed to observe $0\nu\beta\beta$ with a sufficiently high confidence level ($> 3\ \sigma$). This sensitivity level corresponds to a $0\nu\beta\beta$ lifetime of $10^{27} - 10^{28}$ y, depending on the isotope. This primary objective poses a set of technical challenges: the sensitive detector mass must be in the range of several hundred kg up to a tonne of the isotope, and the background must be close to zero at the tonne $\cdot$ year exposure scale in the ROI around the $0\nu\beta\beta$ transition energy.

2.5.1 CUPID milestones

The scientific goals outlined above can be achieved with a bolometric experiment like CUORE running at LNGS, including crucial upgrades. The required improvements concern:

- isotopic enrichment;
- active rejection of αs and surface backgrounds in detector materials;
- further reduction (compared to CUORE) in the γ backgrounds by careful material and isotope selection and an active veto for multi-site events;
- further reduction in cosmogenically generated radioactive backgrounds.

The successful start of CUORE in 2017, as well as the CUORE experience in ultra-clean assembly of calorimeters and the cryostat system, paved the ground for the viability of a future experiment. Groups in both Europe and the US are engaged in an active R&D program [142] along all the directions outlined above. The cost and purity of bolometric crystals highly enriched in ^{130}Te as well as other potential isotopes (^{82}Se, ^{100}Mo, and ^{116}Cd) are under investigation, studying background rejection with scintillation, Cherenkov radiation, ionization, and pulse-shape discrimination, and testing novel materials and sensor technologies. Experience with the CUORE assembly allows to further refine and optimize the process of putting together a 1-tonne scale detector. CUORE is now operational so that the intensive R&D program is ramping up, with the goal of preparing a full proposal for an upgraded bolometric experiment with $\mathcal{O}(10$ meV) Majorana mass sensitivity. This requires a detector with a mass of active isotopes on a tonne-scale and a background level of $\lesssim 10^{-1}$ counts/(tonne $\cdot$ y) in the ROI. While this extremely low background level cannot be verified directly before CUPID is in operation, the chosen technology should prove convincingly that this target can be achieved, by means of dedicated experimental tests and dedicated simulations. Key performance parameters, such as radioactivity contaminations, α/β and surface/bulk event rejection capability, α-backgrounds above 2.6 MeV, cosmogenic backgrounds and energy resolution are to be taken into account.

One of the key features of the bolometric technology is the excellent energy resolution. It is important that this feature is maintained in CUPID, to keep the $2\nu\beta\beta$ background on a very low level (see Sec. 1.5.1). Ideally, the CUPID energy resolution should not be worse than that achieved by CUORE ($\sim$ 7 keV). This needs to be verified in dedicated experimental tests with crystals of the size to be used for CUPID.

A tonne-scale bolometric detector will imply $\mathcal{O}(1000)$ single detectors. An appealing feature of the bolometric technology is its scalability: from single-module devices to a full-tower demonstrator and finally to the full CUORE-sized array.

The chosen technology must demonstrate reproducibility in terms of technical performance (energy resolution, pulse shape, noise features). The detector behavior should therefore be tested with an array of at least 8 modules and operated underground in

conditions as similar as possible to those expected in the final experiment in terms of base temperature, vibration level, read-out, and electronics configuration.

CUPID technology should be as compatible as possible with the existing CUORE infrastructure, in terms of mechanical coupling, cryogenics, readout, and DAQ features.

In the next two years, the R&D activities [142] will proceed vigorously. CUORE operation and background measurements already give precious information to improve the detector technology.

A summary on the goals of the CUPID program, depending on the (ultimate) isotope of choice, are listed in Tab. 2.14. The efforts towards CUPID can be divided into two main categories: those which focus on TeO_2 calorimeters (and therefore the isotope ^{130}Te) and those which study alternative compounds, moving to other isotopes (see Fig. 2.15). All the R&D activities carried out in the framework of CUPID by the different groups are detailed in [142]. In the following the most recent advances are summarized, focusing on the activities carried out within this Ph.D. work.

TeO_2. Large scale production of high quality TeO_2 crystals was already demonstrated by CUORE. However, the enrichment procedure and crystal growth with enriched material still has to be validated in order to certify the energy resolution as well as the internal contamination and to avoid losses of enriched material due to the crystal growth. This work already started: two highly-enriched TeO_2 crystals were tested at LNGS. The crystals, 435 g each, show an energy resolution, evaluated at the 2615 keV γ-line of ^{208}Tl, of 6.5 and 4.3 keV FWHM. The only observable internal radioactive contamination arises from ^{238}U (15 and 8 μBq/kg, respectively). The internal activity of the most problematic nuclei for neutrinoless double beta decay, ^{226}Ra and ^{228}Th, are both evaluated as $<$3.1 μBq/kg and $<$2.3 μBq/kg respectively. Thanks to the readout of the weak Cherenkov light emitted by β/γ particles by means of Germanium Neganov-Luke[6] bolometric light detectors it is possible to perform an event-by-event identification of β/γ events with a 95% acceptance level, while establishing a rejection factor of 99.99 % for α particles [154]
.
MKIDs-based light detectors demonstrated a baseline resolution of 30 eV with a 2 $\times$ 2 cm^2 prototype. Full size ones (i.e. 5 $\times$ 5 cm^2) are planed to be tested with a CUORE-like TeO_2 crystal. Silicon Neganov-Luke amplified light detectors were successfully tested on a 1 $\times$ 1 $\times$ 1 cm^3 TeO_2 crystal, obtaining a fully rejection (4.6 σ) of the α-particles [155]. Also in this case a full-size test is on schedule. Even assuming a total rejection of the αs, the γ-background at the ^{130}Te $Q_{\beta\beta}$ is not negligible for a next generation experiment. Therefore further improvement in screening and selecting the materials are required. The CUORE background model will help to understand which are the dominant sources of events in the ROI. In this way only the contaminated parts (of the cryostat, the shielding of the detector support) will have to be re-treated or replaced.

Li_2MoO_4. Large mass ($\sim$1 kg), high optical quality, radiopure ^{100}Mo-containing

[6]Signal amplification technique based on the application of an electric field in the absorber of the light detector.

zinc and lithium molybdate crystals have been produced and used to develop high performance single detector modules based on 0.2 - 0.4 kg scintillating calorimeters. In particular, the energy resolution of the lithium molybdate detectors at the $Q_{\beta\beta}$ of ^{100}Mo (3034 keV) is 4–6 keV FWHM. The rejection of the α-induced dominant background above 2.6 MeV is better than 8σ. Less than 10 μBq/kg activity of ^{232}Th (^{228}Th) and ^{226}Ra in the crystals is ensured by boule recrystallization. The potential of ^{100}Mo-enriched scintillating calorimeters to perform high sensitivity double-beta decay searches has been demonstrated with 10 kg $\cdot$ day exposure: $2\nu\beta\beta$ decay half-life of ^{100}Mo has been measured with the up-to-date highest accuracy as $T_{1/2} = [6.90 \pm 0.15(\text{stat.}) \pm 0.37(\text{syst.})] \cdot 10^{18}$ y. Both crystal production and detector technologies favor lithium molybdate to zinc molybdate, which has been selected for the ongoing construction of the CUPID-0/Mo demonstrator, containing several kg of ^{100}Mo [49].

ZnSe. It was deeply investigated within the LUCIFER (Low Background Installation For Elusive Rates) program, establishing from scratch the ZnSe powder synthesis and purification protocols. The crystals growth was refined, studying by means of cryogenic tests the properties of dozens of ZnSe samples [147,156,157]. Finally 24 ZnSe crystals, 95 %-enriched in ^{82}Se were produced and mounted in CUPID-0. The CUPID-0 demonstrator is currently taking data. Details about its construction, commissioning, operation as well as the most recent results are reported in the following. CUPID-0 is the object of this Ph.D. work, dealign with detector construction, operation and final data analysis.

Table 2.14: CUPID sensitivity goals in terms of $m_{\beta\beta}$ and $0\nu\beta\beta$ lifetime.

Parameter	Projected value and/or range	
Readiness for construction	2018	
Construction time	5 years	
Total fiducial mass (kg)	TeO_2	750
	$ZnMoO_4$	540
	ZnSe	670
Isotope fiducial mass (kg)	^{130}Te	543
	^{100}Mo	212
	^{82}Se	335
Energy resolution at endpoint (FWHM)	< 5 keV	
Event selection efficiency in fiducial volume	75-90%	
Background within FWHM of endpoint	< 0.02 counts/(tonne $\cdot$ y)	
90% C.L. $0\nu\beta\beta$ lifetime limit for 10 year run (10^{27} ys)	^{130}Te	5.1
	^{100}Mo	2.2
	^{82}Se	4.2
90% C.L. $m_{\beta\beta}$ limit for 10 year run (90% C.L.) (meV)	^{130}Te	6–15
	^{100}Mo	6–17
	^{82}Se	6–19
$0\nu\beta\beta$ lifetime discovery sensitivity (3σ) in 10 years	^{130}Te	4.9
	^{100}Mo	2.1
	^{82}Se	4.0
$m_{\beta\beta}$ discovery sensitivity (3σ) in 10 years	^{130}Te	6–15
	^{100}Mo	7–17
	^{82}Se	6–19

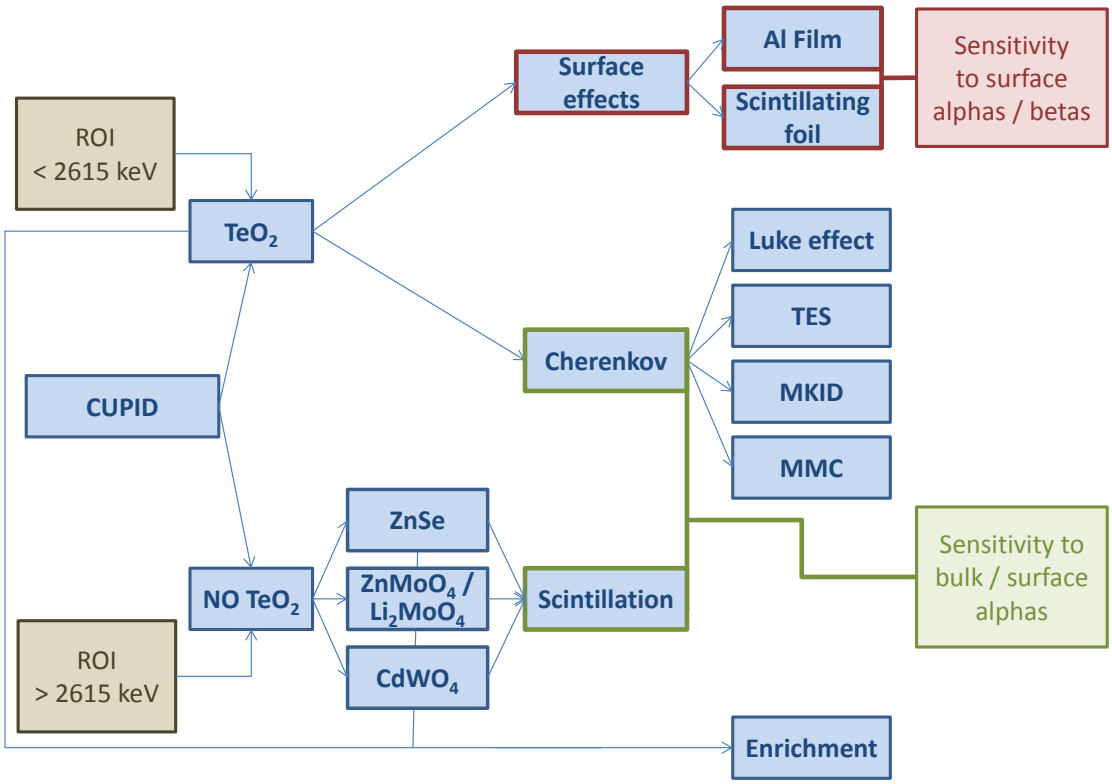

Figure 2.15: Scheme of the R&D detector activities for CUPID [142].

Chapter 3

The CUPID-0 demonstrator step by step

The CUPID-0 detector at the Laboratori Nazionali del Gran Sasso (Italy) is the first large array of enriched scintillating cryogenic detectors for the investigation of ^{82}Se neutrinoless double-beta decay ($0\nu\beta\beta$). CUPID-0 aims at measuring a Background Index (BI) in the Region of Interest (ROI) for $0\nu\beta\beta$ at the level of 10^{-3} counts/(keV $\cdot$ kg $\cdot$ y), the lowest value ever measured using cryogenic calorimeters. This is the BI order of magnitude measurable in the current experimental setup (i.e. cryostat and shielding). A dedicated Monte Carlo simulation will be performed to estrapolate the final CUPID-0 result to a tonne-size experiment housed in the CUORE cryostat. In this way it will be possible to

This result can be achieved by the current technology for background suppression and thorough protocols and procedures for detector preparation and construction. In this chapter, the various phases of the detector design and realization are presented, from the material selection for the calorimeter production to the new and innovative detector structure. In the framework of my Ph.D. thesis I have addressed several activities reported in this chapter: cryogenic tests of the ZnSe crystals (Sec. 3.2), detector assembly (Sec. 3.5), cryostat refurbishment installing new wiring and thermalization system (Sec. 3.6), detector commissioning (Sec. 3.9) and characterization (Sec. 3.10).

3.1 ZnSe enriched crystals: production and processing

Zinc selenide is rarely found in nature and the synthesis of ZnSe compound can be made in different forms (powder, bulk pieces or thin layers) by different methods and starting from different raw materials, depending on the use that is given to the final product. ZnSe can be produced also in form of crystals which are grown by different methods and can be made in both hexagonal (wurtzite) and cubic (zincblende) crystal structure. Zinc selenide is a II-VI semiconductor with a relatively large band-gap (about 2.70 eV at 25 °C, value strongly dependent on the production conditions) which is used as an infrared optical material because of its wide range of transmission (0.45 μm to 21.5 μm).

The material is also used as LED medium or scintillator, especially in X-ray and γ-ray detectors in which case can also be doped for increased scintillating performance. Tab. 3.1 gives the general properties of ZnSe crystal. Although it has several applications in IR

Table 3.1: General physical properties of ZnSe (Zinc Selenide) crystal developed for CUPID-0.

Crystal type	cubic
Lattice constant	a=5.657Å
Density	5.27 g/cm^3 at 25 °C
Melting point	1525 °C
Refractive index (n)	2.417 - 2.385 at 8-13 μm 2.40272 at 10.6 μm
dn/dT	$+61 \cdot 10^{-6}$/°C at 10.6 μm at 298K
Transmission range	0.45 to 21.00 μm
Band gap (at 10K)	2.82 eV (direct)
Bulk absorption coefficient	$5 \cdot 10^{-4}$ cm-1 at 10.6 μm
Reflection loss	29.1% at 10.6 μm (2 surfaces)
Young's Modulus	$6.72 \cdot 10^9$ dynes/mm^2
Specific Heat at 25 °C	356 J/kg/°C
Linear thermal expansion	7.57 $\cdot 10^{-6}$ / °C at 20 °C
Hardness (Knoop)	105-120 kg/mm^2
Solubility	0.001g/100g water
Molecular Weight	144.37 (8.73 % ^{82}Se, natural) 147.25 (95 % ^{82}Se, enriched)

optics and optoelectronic devices, ZnSe is quite seldom produced in the form of large (single) crystals. For an effective $0\nu\beta\beta$ experiment based on the cryogenic calorimeter technique, crystals of relatively large dimensions ($>$ 400 g) are needed. The Chemical Vapor Deposition (CVD) technique (the most efficient method for obtaining large samples at a convenient price) was discarded in early phases of our project due to the poor scintillation and bolometric performance of ZnSe samples grown by this method. Such samples, in spite of their good optical aspect (transparent, homogeneous, no visible bubbles or inclusions) generally have a polycrystalline structure which causes the deterioration of the bolometric performance and the quenching of scintillation at low-temperatures. The adverse effect of polycrystalline structure and extended defects was observed also in crystals grown from melt by different versions of the Bridgman technique. The growth of large ZnSe crystals from the melt is very difficult due to the high melting point (1525 °C) and total vapor pressure (0.2 MPa at 1525 °C) and is further hampered by the high volatility of the components Zn and Se, which in addition have different vapor pressures leading to a deviation from the stoichiometric composition of the melt during the growth process. The very narrow homogeneity range in the ZnSe phase diagram [158, 159] and the solid-solid phase transition from hexagonal wurtzite to cubic sphalerite (zinc blende)

occurring in the cooling phase of the grown crystal at 1425 °C [160, 161] are additional problems to be solved when the melt growth option is considered to obtain large, homogeneous ZnSe crystals. All crystals discussed in this work were grown from the melt in graphite crucibles using a modified Bridgman technique.

3.1.1 Specific requirements for rare events physics application

As deeply discussed in Sec. 2.1 the crystal absorber is the core of a cryogenic calorimeter, being at the same time the source of the $0\nu\beta\beta$ decay and the radiation detector. A high level of crystal perfection and homogeneity are requested for high sensitivity calorimeters because the presence of bulk defects like bubbles and metallic inclusions or any other inhomogeneity like veils and cracks may drastically reduce the signal amplitude and the energy resolution of such detectors. There are several studies dedicated to the perfection of ZnSe crystals [162–164]. The crystals grown in this work were subject to a special thermal regime aimed at reducing the presence of such defects. The crystal cooling process was conducted under conditions that did not alter the crystal perfection during the phase transition from wurtzite to sphalerite symmetry. The capability of the cryogenic technique to identify the DBD signal is limited by the presence of environmental radioactivity and radioactive contaminants in the detector. Therefore the detector has to be free of any contaminant that can mimic or deface the DBD signal by producing an energy deposit in the region of interest for the $0\nu\beta\beta$. The contamination may come from long-lived, naturally occurring isotopes, such as ^{238}U, ^{232}Th, ^{40}K and their daughters and from cosmogenic activation of the detector materials and surroundings. In the case of $Zn^{82}Se$ crystals, this means a detailed monitoring of all materials, tools and facilities used for the synthesis of $Zn^{82}Se$ powder and the crystal growth, the chemical and mechanical processing of grown crystals, their handling, packing and storage before mounting in the experimental setup. Land transport and underground storage of raw materials and finished crystals are necessary in order to minimize cosmogenic activation [165]. Another important feature required for scintillating calorimeters is a good optical transmittance. Highly transparent crystals are needed in order to avoid reabsorption of scintillation light. Zinc selenide is a direct gap semiconductor in which the normal band-to-band optical absorption is strongly perturbed by absorption on excitons and impurities. The concentration of impurities has to be reduced (typically below ppm levels) also because they may alter the transmission in the IR region of the spectrum usually dominated by the absorption on free carriers. A reduced IR transmission may alter the propagation of phonons with consequent reduction of bolometric performance of the crystal.

3.1.2 High purity material production/procurement

The different steps of $Zn^{82}Se$ crystal production starting from elemental zinc and selenium are illustrated in Fig. 3.2. The elemental ultra-pure Zn was produced by the National Science Center Kharkov Institute of Physics & Technology (KIPT) in Kharkov Ukraine while the enriched Se was delivered by the URENCO Stable Isotopes unit based at Almelo in the Netherlands. The synthesis of ZnSe powder and its conditioning for

crystal growth (steps 11, 12 and 14 in Fig. 3.2) were made at ISMA Kharkiv, Ukraine and the processing of the crystal ingots at LNGS, Italy. The certification process was developed and performed in INFN laboratories. The measurement methods for radiopurity certification as well as the protocols applied for each production phase including handling, cutting and polishing of $Zn^{82}Se$ crystals in the following are similar to those described in [166] for the TeO_2 crystals produced for the CUORE experiment. Given the very high price of the material used, in particular for the enriched selenium, additional measures have been taken to minimize the loss of material in all stages of production. Recovery of the material loss at cutting and polishing was also foreseen (step 17 in Fig. 3.2). The elemental ultra-pure Zn was produced at KIPT Kharkov in Ukraine [167] starting

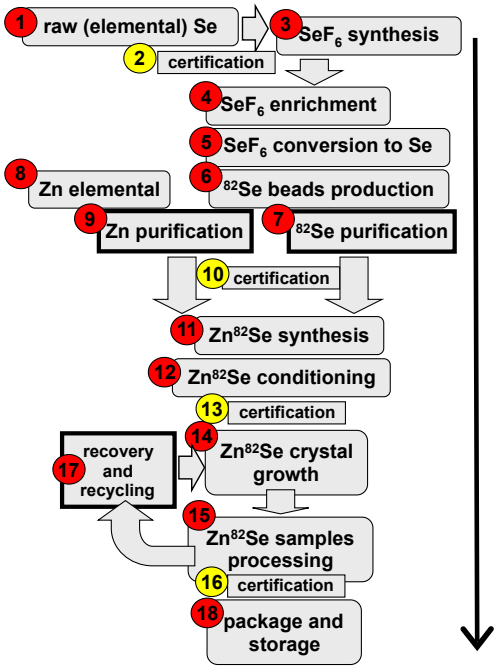

Figure 3.2: Diagram of $Zn^{82}Se$ crystal production protocol developed for CUPID-0.

from Zn metal which is commercially available and by applying a dedicated purification process using multi-stage vacuum distillation. The final Zn metal product was delivered in form of beads.

The production of ^{82}Se-enriched selenium starting from elemental selenium turned into SeF6 for enrichment by gas centrifugation and further converted into selenium was described elsewhere [168, 169]. Supplementary purification of the enriched Se (step 7 in Fig. 3.2) was applied at the URENCO production site using a distillation procedure which cannot be disclosed. The chemical purity of the enriched ^{82}Se from URENCO are given in Tab. 3.3 together with the purity of Zn produced at KIPT. Besides the reduction of sodium and sulfur concentration which was the main purpose of the supplementary

Table 3.3: Chemical purity as measured by ICP-MS on samples of enriched ^{82}Se and Ze randomly chosen from regular production at URENCO and at KIPT respectively.

Element	Se initial [ppb]	Se distilled [ppb]	Zn initial [ppb]	Zn purified [ppb]
Na	500000	<1000	1000	30
Mg	<1000	<100	-	-
Al	-	<200	4000	35
Si	-	18000	7000	40
S	1140000	130000	-	-
K	<2500	<2000	3000	35
Ca	-	5000	2000	70
V	<20	<40	<200	<9
Cr	100	<100	<200	<90
Mn	<100	<10	<200	<90
Fe	700	110	30000	56
Co	<10	<4	<200	<10
Ni	400	64	<300	<90
Cu	250	<10	10000	110
Mo	<300	<10	<2000	4
Cd	-	<4	20000	4300
Sn	-	-	15000	<300
Tl	-	-	<2000	180
Pb	-	<6	<3000	290
Bi	-	6	<1000	<2
Th	<0.4	<0.1	<2000	<0.2
U	<0.2	<0.1	<2000	<0.2

purification of ^{82}Se, the reduced concentration of Cr, Fe, Ni and Cu is to be noted. In the case of Zn, a decrease of almost two orders of magnitude is noticed for all the concentrations of contaminants. The isotopic concentration of the enriched Se beads delivered by URENCO and used in CUPID-0 are given in Tab. 3.4. The radio-purity of Zn and enriched Se (before and after the distillation) was measured by HPGe gamma spectroscopy at LNGS and the results are given in Tab. 3.5. The extremely low-background conditions in which the measurement was carried out and the high radio-purity of the ^{82}Se allowed us to establish for the double- beta decay of ^{82}Se to excited states of ^{82}Kr the most stringent lower limits on the half-lives of the order of 10^{22} y, with a 90% C.L. [171].

3.1.3 ZnSe syntesis

The synthesis of Zn^{82}Se powder and its conditioning for crystal growth were made using ultraclean fused quartz reactors. The whole process consisted of three distinct steps which are described in the following. In the first step (primary synthesis: S1), the synthesis of Zn^{82}Se is made in vapor phase by evaporation of Zn and enriched ^{82}Se in Ar atmosphere at 950 °C. The analysis of the ZnSe powder obtained in this first step (S1), showed that not all the material reacted. Roughly 222 g of enriched ^{82}Se and roughly 178 g of Zn

Table 3.4: Isotopic abundance of natural [170] and enriched selenium. Values for the enriched isotope are averaged over 70 gas-to-metal conversion processes, weighted for their relative mass.

	^{74}Se	^{76}Se	^{77}Se	^{78}Se	^{80}Se	^{82}Se
Natural Se [%]	0.87	9.36	7.63	23.78	49.61	8.73
Enriched Se [%]	<0.01	<0.01	<0.01	<0.01	3.67±0.14	96.33±0.31

Table 3.5: Internal radioactive contamination for 2.5 kg of 96.3% enriched ^{82}Se metal beads and for 2.5 kg of ^{nat}Zn. Limits are computed at 90% C.L.. The measurements were carried out on October 2014 [171].

Chain	Nuclide	^{82}Se Activity [μBq/kg]	^{nat}Zn Activity [μBq/kg]
^{232}Th			
	^{228}Ra	< 61	< 95
	^{228}Th	< 110	< 36
^{238}U			
	^{226}Ra	< 110	< 66
	^{234}Th	< 6200	< 6200
	^{234m}Pa	< 3400	< 4700
^{235}U	^{235}U	< 74	< 91
	^{40}K	< 990	< 380
	^{60}Co	< 65	< 36
	^{56}Co	–	80±20
	^{65}Zn	–	5200±600

are processed in a large ampule to make the first step. Approximately 90% of the crop is selected as first quality material (containing 95% $Zn^{82}Se$ and 5% not fully reacted material). The remaining 10% (containing approximately 70% $Zn^{82}Se$ and 30% material not fully reacted) is collected separately as second quality material.

The material resulted from several S1 runs is re-processed in a so-called Vertical Thermal Treatment (VTT) aimed at completing the synthesis of material not fully reacted in S1. In the VTT procedure the powder collected in several S1 crops (first and second quality) is conveniently put together in a dedicated ampoule and thermally treated at 950 °C in Ar atmosphere. The yield of the VTT process is of the order of 99.60% first quality material. The remaining 0.40% of unreacted (waste) material is recovered and thermally treated in the following VTT run. The material (first quality) resulted after the VTT proved to be still not suitable for efficient crystal growth because it still contains parts of not fully reacted Zn and ^{82}Se. During the crystal growth process, possible elemental Zn will evaporate and escape the crucible.

Elemental selenium instead if present, will react with the graphite crucible and give Carbon Diselenide (CSe_2) which is then imbedded in the crystal as impurity. In order to avoid this problem and guarantee a good quality powder for the crystal growth, the powder resulted after VTT was subject to a third treatment, so called Horizontal Thermal Treatment (HTT). The HTT is performed in a dedicated reactor with two different chambers allowing for a gas flow to flush away (or let them further react) free Zn and Se. The scheme of the reactor used for HTT is given in Fig. 3.6. The presence of two different reactor volumes prevents the contamination of the purified material by the unreacted material flushed away by the gas flow. During a HTT run roughly 530 g of $Zn^{82}Se$ resulting from the VTT process is treated. The treatment consists of slowly heating the powder under hydrogen flow up to 650 °C. During the heating, starting at 300 °C, $H_2{}^{82}Se$ will form and will be partially purged (in gaseous form) out of the small ampoule. Note that the H_2 flow is rather weak avoiding the extraction of all the free selenium. After a few tens of minutes, the temperature is increased enough and reaches 500 °C when a new reaction will take place:

$$H_2^{82}Se + Zn \longrightarrow Zn^{82}Se + H_2 \tag{3.1}$$

This regime is maintained at 650 °C (the temperature that maximize the reaction) in order to ensure an exhaustive synthesis of Zn and ^{82}Se. In fact, other mechanisms enter in the reaction. Selenium melts at 221 °C and boils at 685 °C. This means that during the reaction part of the selenium will evaporate and escape the ampoule. Once all the free selenium is completely escaped (or reacted) one has to eliminate the residual zinc. In order to remove the residual Zn from the $Zn^{82}Se$ powder, the temperature is slowly raised just above the boiling point of Zn. During this procedure, argon is purged in the system instead of Hydrogen. The atomic mass of Ar is much closer to the one of Zn which makes it more efficient as scavenger for the Zn to be taken out from the ampoule. Moreover, argon is preferred for being much less dangerous than H_2. The control of different gas flux in the system is made through a network of pipes and valves illustrated in Fig. 3.6. The inner ampoule (containing the $Zn^{82}Se$ powder) is continuously rotated

by a step motor. A dry vacuum pump (Edwards nXDS6i 100) is used to pump the whole reactor before starting the thermal treatment. The transfer of the $Zn^{82}Se$ powder inside and outside the reactor is made in argon atmosphere through a system which avoids the contact of the powder to free atmosphere. The yield of the HTT process is of the order of 99.40% first quality material, ready for crystal growth. The total yield of the process of $Zn^{82}Se$ powder synthesis and conditioning for crystal growth was 98.35% (99.55% at S1, 99.40% at VTT and 99.40% at HTT).

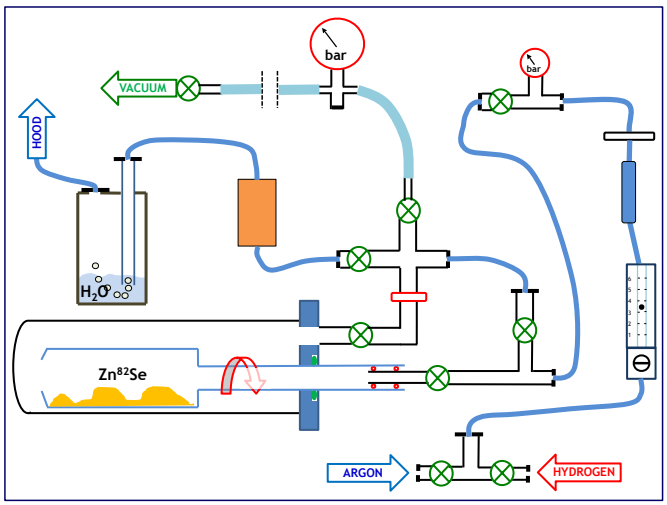

Figure 3.6: Schematic view of the system used for the Horizontal Thermal Treatment (HTT).

3.1.4 Crystals growth

All the CUPID-0 crystals were grown from the melt, in graphite crucibles using the Bridgman technique. Loading crucibles with $Zn^{82}Se$ powder was performed in controlled atmosphere (ultra-pure Ar, relative humidity $<1\%$) using a glove box and other dedicated equipment, previously certified for radio-purity (gloves, containers, plastic bags, jars and pestles, etc). The crystal growth was performed in a vertical furnace kept in argon atmosphere (up to 15 MPa).

The furnace [172] was composed of two heaters giving a temperature gradient designed to go from 1575 °C to 900 °C in the melt zone and further to insure a temperature of about 900 °C in the thermalization zone. The growth rate was typically 1 mm/hour and the accuracy of temperature control ± 3 °C. The whole process (temperature control and crucible movement) was computer controlled using a software of ISMA Kharkiv property. The thermalization in the isothermal region of the heater at about 900 °C, followed by gradual cooling to room temperature was applied to reduce the residual thermal stresses in the crystal. $Zn^{82}Se$ crystal growth process was prone to big difficulties due to technical problems arising from the need of growing large ZnSe crystals with a low coefficient of

material loss. Losses during crystal growth is due to thermal dissociation and due to diffusion through the walls of the graphite crucible. Further complication comes from the fact that evaporation and diffusion are different for the two elements, Zn and Se:

- evaporation of the decomposed melt (Zn and Se_2) is different due to the fact that partial pressure of Zn is twice as much as the partial pressure of Se_2;
- the diffusion through the walls of graphite crucible is different due to the larger dimension of the Se_2 molecule with respect to Zn atom.

In order to minimize $Zn^{82}Se$ loss the graphite crucibles were longer than usual (about 250 mm including the seed compartment) and sealed with a screwed cap. The evaporated material deposited inside the crucible on the upper side of the walls (approximately 12% of initial charge) as well as the material evaporated and condensed in powder form on the cold parts of the furnace (about 5% of initial charge) was carefully collected for future recycling. The as-grown ingot represented typically 78% of the initial charge, i.e. the total yield in terms of mass balance was approximately 95%.

Fig. 3.7 gives a typical $Zn^{82}Se$ crystal ingot ready for mechanical processing (cutting, shaping and polishing).

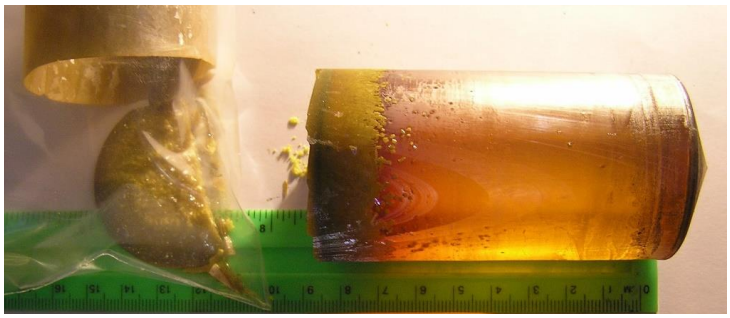

Figure 3.7: Typical $Zn^{82}Se$ crystal ingot as grown by ISMA Kharkiv. On the left side (collected in a plastic bag) is the evaporated material deposited inside the crucible on the upper side of the walls.

3.1.5 Crystals cutting, surface processing and handling

The as-grown $Zn^{82}Se$ crystal ingots were cut and polished to the standard dimensions: 45 mm diameter, 55 mm length or less, depending on the quality of the ingot. The remaining material after ingot cut is to be recycled as indicated in Fig. 3.2 (steps 15-17-14). The expected mass of a $Zn^{82}Se$ crystal with standard dimensions is 470 g, which corresponds to 248 g content of ^{82}Se. The ingots were found particularly brittle when heated by the friction of mechanical operation, implying that operations like cut and polishing are extremely delicate.

The cutting was made using a precision diamond wire saw model STX-202A with three-dimensional digital control. The yield of the cutting process (taking into account

the recovery of the scraps) was 96.72 %. Cutting, shaping and optical polishing of the crystals was made in normal laboratory conditions (above ground) using commercial waterproof abrasive paper of different roughness. The above-ground operations were concluded in clean-room by a chemical etching made using 10 % diluted HCl and ultra-clean packaging.

Afterwards, all the crystals were treated in the underground clean room of the Princeton University (class 1000, radon activity <5 mBq/m^3). The purpose of this step is to clean the surfaces, through the following processes:

- polishing of the whole surface applying the polishing technique used for the TeO_2 crystals in CUORE and described in [166];
- washing with ultra-pure water to remove the impurities mixed with the polishing powder;
- second polishing and final washing.

The targeted number of atomic layers to be taken away by this final polishing is on the order of 10^5 to eliminate all impurity atoms that may have been adsorbed on the surface and further diffused in its bulk. Finally, the polishing removed at least 12μm from the surfaces, which makes more than 10^5 atomic layers. This procedure is also intended to bring the crystal dimensions as close as possible to the nominal values and to improve the surface quality by removing possible extended defects induced by chemical etching.

The polishing suspension was prepared on site using SiO_2 powder (Admatechs product Admafine SO-E5) and ultra-pure water added directly inside the plastic bags in which the SiO_2 was delivered. In this way, the crystals arrived in the clean room, came into direct contact only with materials previously certified for their radio-purity: ultra clean gloves, ultra-pure water (with Rn stripped by N_2 fluxing), polishing suspension, polishing pads, cleaned and conditioned polyethylene sheets and vacuum plastic bags. The abrasive powder was selected for CUORE experiment based on dedicated research on the radiopurity and mechanical characteristics of different materials available on the market. The Admatechs product Admafine SO-E5 (average particle diameter 1.5 μm) was selected for having the best radio-purity, even though it has moderate material removal efficiency. A special package made in a dedicated clean area and using certified polyethylene bags is guaranteed at the production site in Nagoya (Japan). The package consists of two successive bags. After removal of the outer bag in the clean room, the inner bag was used for the preparation of the polishing slurry by adding ultra-pure water.

At the end of clean room operation, crystals were packed in a triple vacuum package and stored in polyethylene vacuum boxes similar to those used for CUORE experiment [166]. The yield of the surface processing procedures (shaping and polishing) was 99,80%. An improvement of the global yield of the mechanical processing (cutting and polishing) is expected due to the foreseen recovery of ^{82}Se from the waste which was carefully collected and stored at LNGS. Since not all crystals were grown in the same type of crucible and some of the as-grown ingots were not homogeneous a compromise was necessary in order to get the maximum possible of experimental mass. As a result, only a few crystals have

a perfect cylindrical shape (Fig. 3.8 a) while other have a special geometry aimed at fitting the copper frames (Fig. 3.8 b) and some of them were subject to a dedicated cut in order to extract the largest possible mass from the as-grown ingot (Fig. 3.8 c). Also in some cases very short crystals were extracted from the ingot due to cracks occurred during the cutting process (Fig. 3.8 d).

Figure 3.8: $Zn^{82}Se$ crystals of different shape ready for mounting: a) perfect cylindrical shape; b) collar and lateral strip aimed at fitting the copper frames; c) dedicated cut for maximum mass; d) short crystal.

3.1.6 Quality checks: EM scanning, optical and cryogenic tests

The radio-purity of $Zn^{82}Se$ crystals is a parameter of crucial importance for $0\nu\beta\beta$ application. Given the rareness of this hypothetical process, the experimental conditions have to ensure a background level below $1 \cdot 10^{-3}$ counts/(keV $\cdot$ kg $\cdot$ y) which asks for extremely low (ppt and less) acceptance limits of radioactive contamination elements in the crystal. Tab. 3.9 gives the concentration limits (ICP-MS measurement) for radioactive isotopes requested for the materials used in the production of $Zn^{82}Se$ crystals. The limits were fixed according to a background goal of $1 \cdot 10^{-3}$ counts/(keV $\cdot$ kg $\cdot$ y) for the CUPID-0 detector.

The high purity of raw materials and the careful conditioning of $Zn^{82}Se$ powder in view of crystal growth were the main reasons that have allowed us to achieve the

Table 3.9: Concentration limits (ICP-MS certified) for radioactive isotopes requested for raw materials, reagents, consumables and intermediary products used for the production of $Zn^{82}Se$ crystals.

Material	contamination limits [ppb]
elemental Zn and Se	$^{238}U < 0.2$ $^{232}Th < 0.2$
water and solvents for cleaning	$^{238}U < 2 \cdot 10^{-3}$ $^{232}Th < 2 \cdot 10^{-3}$
ZnSe powder	$^{238}U < 0.2$ $^{232}Th < 0.2$
ZnSe crystal, ready-to-use	$^{238}U < 3 \cdot 10^{-4}$ $^{232}Th < 3 \cdot 10^{-4}$
SiO_2 powder and polishing pads	$^{238}U < 4 \cdot 10^{-3}$ $^{232}Th < 4 \cdot 10^{-3}$
Handling tools and package	$^{238}U < 4 \cdot 10^{-3}$ $^{232}Th < 4 \cdot 10^{-3}$

production of $Zn^{82}Se$ crystals with a high crystal perfection in a relatively large scale production process. Special efforts were devoted to avoid the presence of very small (100 μm) black-colored inclusions or larger ($\sim$1 mm) dark clouds. The total absence of such inclusions and possible bubbles was guaranteed by the thermal regime (thermal gradients and lowering speed) applied during the whole growing process. Finally, the cleaning procedure and conditioning of the crucible has been fundamental to avoid the contamination of the melt by material condensed on the crucible walls. The modified geometry of the crucible mentioned above was also made for this purpose.

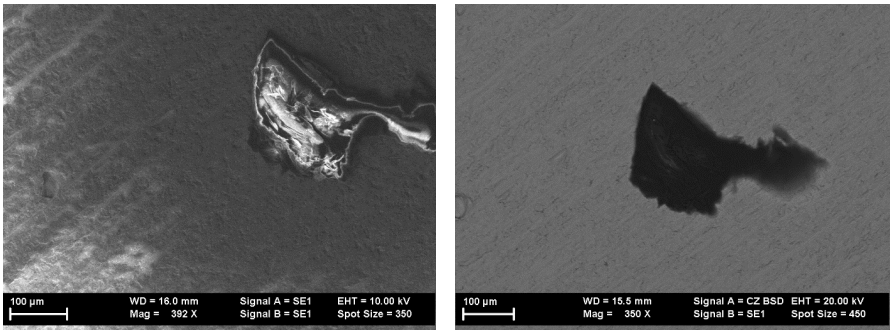

Figure 3.10: Scanning Electron Microscope (SEM) images of a typical small inclusion in ZnSe crystals. On the left, the black point visible also with naked eye proves to be a small (100-200 μm) chop of impurity which was embedded in the crystal during the growth process. The image on the right is obtained with the Back-Scatter Detector and proofs the homogeneous elemental composition of the inclusion.

Fig. 3.10 shows the Scanning Electron Microscope (SEM) images of a typical inclusion when present as very small isolated dust grain. The image at the right side of the figure is obtained with the Back-Scatter Detector (BSD). The BSD characterization permits the differentiation between different elements (different atomic number) and allows to perform a qualitative evaluation of composition. The image proofs the homogeneous constitution of the grain. The precise composition of it measured by Energy Dispersive

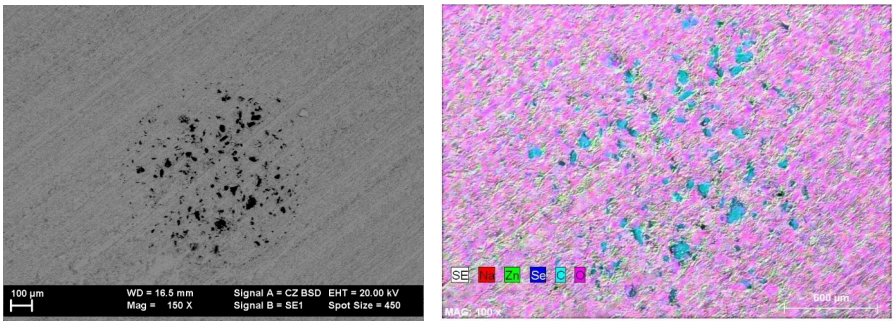

Figure 3.11: Scanning Electron Microscope (SEM) image (left) of a relatively large (800 μm) *dark cloud* inclusion. On the right, the Energy Dispersive X-ray Analysis (EDX) element mapping image showing that the dark cloud is in fact a cluster of small inclusions mainly composed of carbon.

X-ray Analysis (EDX) shows that the inclusion is composed mainly of carbon (61%) and oxygen (30%). Carbon comes from elemental Se and Zn reaction with grafite crucible during the crystal growth. Conversely the oxygen was not present in the as-grown crystal, so that it is due to the diffusion during the preparation of the very thin sample used for this measurement. Other impurities detected inside the grain are zinc (3%), chlorine (2%), indium (2%), sulfur (1%) and other (<1%). The values measured outside the grain are: zinc (56.60%), selenium (41.54%), other (<1%). Values in parenthesis are normalized concentration in weight percent of the element. When present in the form of relatively large dark clouds (hundreds of micron typically), the inclusions proved to be in fact clusters of small inclusions mainly composed also of carbon. Fig. 3.11 gives the SEM images together with the EDX element mapping image of a typical dark cloud inclusion.

The crystals grown for CUPID-0 were subject to a special thermal regime aimed at reducing also the presence of veils and other extended inhomogeneities leading to cracks. Crystals homogeneity was guaranteed by the very high stability of the thermal regime during the crystal growth and the post-growth thermal regime. The thermal stability is also responsible for the absence of cracks. The start of the growth process was also tuned in order to avoid twinning and further development of a multiple-crystal ingot. Finally the crystal cooling process was conducted under conditions that did not alter the crystal perfection during the phase transition from wurtzite to sphalerite symmetry. The Fig. 3.12 shows the uniform orientation of crystalline plans of the as-grown $Zn^{82}Se$ crystals.

As already mentioned, ZnSe crystals have a very large transmission range, broader than silicon and germanium, extending from visible to the infrared (IR) region of the spectrum. Nevertheless, optical absorption in ZnSe crystals can be strongly perturbed by impurities. Also, in the case of crystals grown from melt, due to the relatively high temperature, inhomogeneities may appear in the crystal bulk which are source of random wavering of the fundamental absorption edge.

Fig. 3.13 illustrates the transparency of an optically polished 50 mm long, 50 mm

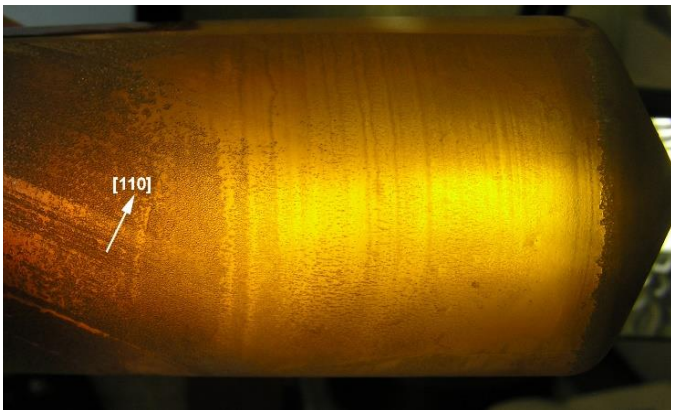

Figure 3.12: As-grown $Zn^{82}Se$ crystal ingot showing uniform orientation of crystalline plans (arrow indicates the direction perpendicular to the 110 plane of the ZnSe crystal).

Figure 3.13: Optically polished $Zn^{82}Se$ crystal.

diameter $Zn^{82}Se$ crystal produced for CUPID-0. In Fig. 3.14 is given the transmission spectrum in the visible region for different ZnSe crystals grown in the phase of tuning of the production parameters. Characteristic for a crystal with a high concentration of defects is the crooked shape of the fundamental absorption edge at typically 550 nm. The presence of impurities also may harm the transmittance in the infrared region of the absorption spectrum, usually dominated by the absorption on free carriers [173]. Impurities of carbon compounds and selenium can be identified by the vibrational absorption bands in the infrared spectra [173]. Particularly, the iron impurities proved to worsen the bolometric performance of ZnSe crystals due to 3.3 μm characteristic absorption band in the IR region of the absorption spectrum and consequent damping of phonon transport i.e. worsening of bolometric signal. The concentration of iron can be calculated from the absorption band at 3.3 μm (Fig. 3.14) and values of $<$1ppm were found to be compatible with a good bolometric performance. Fig. 3.14 gives the optical transmission spectra of

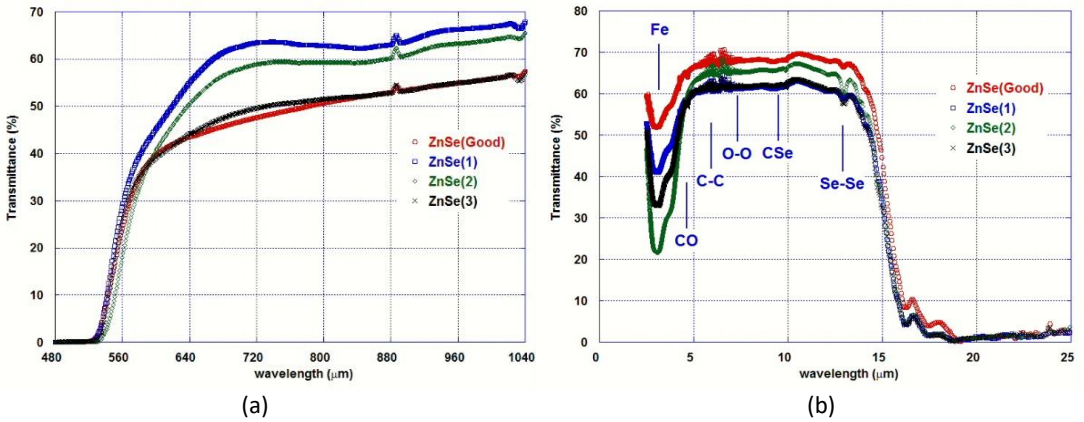

Figure 3.14: Visible (a) and infrared (b) spectra of ZnSe crystals ϕ 50 mm, L 50 mm. The nature of defects (b) responsible for the absorption bands in the infrared region of the spectrum are indicated with arrows.

the preliminary series of ZnSe crystals with different types of defects and degrees of point defect concentration.

3.2 First bolometric test of $Zn^{82}Se$ crystals

For a preliminary test of the crystals produced for CUPID-0, three enriched $Zn^{82}Se$ crystals of the first production batch were operated as scintillating calorimeters in the cryogenic facility of the Hall-C of LNGS.

The crystals, surrounded by 3M VM2002 reflecting foils, were assembled in a single array, interleaved by cryogenic light detectors (for a complete detector description see [157]). For technical reasons during the test, the cryostat was operated at a temperature of slightly above 20 mK, limiting the performances of the temperature sensor of the crystal (bolometric signal). At this temperature, indeed, the working resistance of sensors ranged from 0.17 to 0.22 MΩ, while the electronics is optimized for sensor resistances of tens of MΩ, corresponding to a temperature of about 5-10 mK. The electronic noise produced by the higher temperature dominated each detector baseline resolution that was characterized by different values according to the sensor resistance.

Table 3.15: Detector baseline resolutions and light yield (LY) of the scintillating calorimeters made from three $Zn^{82}Se$ crystals.

Crystal ID	Baseline Resolution [keV FWHM]	Resolution at $Q_{\beta\beta}$ [keV FWHM]	LY (β/γ) [keV/MeV]	LY (α) [keV/MeV]
$Zn^{82}Se$ - 1	7.0	30.1 ± 1.7	5.2	14.1
$Zn^{82}Se$ - 2	14.1	29.7 ± 1.4	3.3	9.1
$Zn^{82}Se$ - 3	18.6	30.2 ± 1.7	4.6	13.7

Tab. 3.15 gives the detector baseline resolutions (i.e. the resolution at zero energy) and light yield (LY) of the scintillating calorimeters built using the data of the three $Zn^{82}Se$ crystals. In spite of the not most suitable operation conditions, the energy resolution in the region of interest for the expected $0\nu\beta\beta$ of ^{82}Se, was the same among the three crystals, proving the reproducibility of the bolometric performance. The energy resolution of the crystals is expected to further improve with a lower base temperature of the cryogenic apparatus [153,156]. The scintillation light emitted by each $Zn^{82}Se$ calorimeter was measured using two cryogenic Ge light detectors (see Sec. 2.4), placed on the top and bottom surface of the cylindrical crystals as in CUPID-0. The light measured by the two light detectors ranges from 3.3 to 5.2 keV/MeV for electrons and from 9.1 to 14.4 keV/MeV for αs [1]. Moreover, the different time development of light pulses produced by electrons and αs interactions allows to completely disentangle and reject the αs background: Fig. 3.16 shows the α vs. β/γ discrimination obtained with TVR (Test Value Right) shape parameter of the light. All the pulse shape parameters are defined and deeply discussed in Sec. 4.4. The cryogenic test allowed to assess the radioactive contaminations of the crystals bulk with high sensitivity. The activities of the most dangerous isotopes obtained by analyzing the counting rate of the α-peaks (see Fig. 3.17) are

[1] These value are obtained calibrating the light output with a ^{55}Fe X-ray source and the heat output (i.e. the energy deposited in the absorber) by ^{232}Th source.

reported in μBq/kg in Tab. 3.18. Projecting the counting rate in the region of interest due to the measured internal contaminations, they are expected to produce a background of $1 \cdot 10^{-3}$ counts/(keV $\cdot$ kg $\cdot$ y) which is in compliance with the CUPID-0 requirements. Details on the results of the cryogenic tests are given in [157].

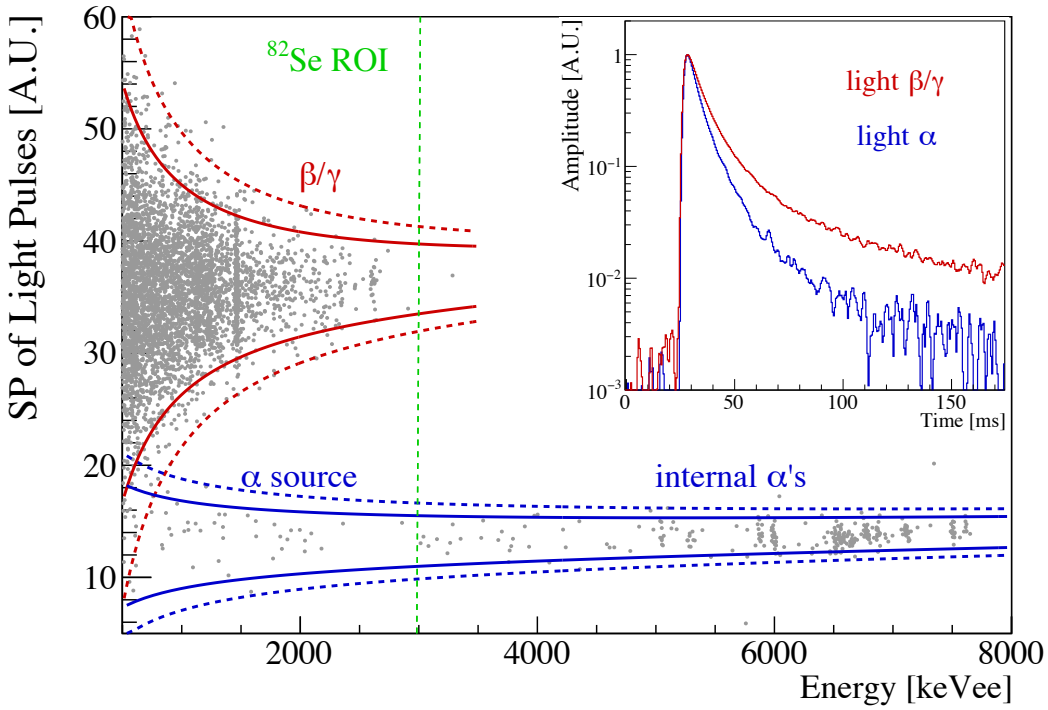

Figure 3.16: Shape parameter (SP) of a light pulses as a function of the energy released in $Zn^{82}Se$-1. The red and blue lines indicate the 2σ (continuous) and 3σ (dotted) β/γ and α bands respectively. α-events produced by the smeared Sm source (below 3 MeV) and by contaminations of the crystal bulk (above 5 MeV) can be easily rejected. Inset: time development of light pulses produced by β/γ (blue) and α (red) interactions with energy of about 2.6 MeV.

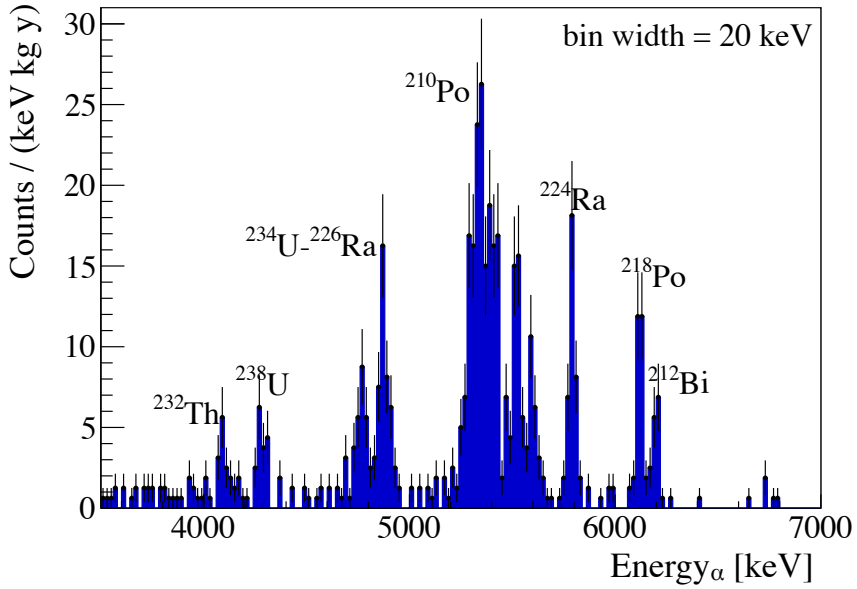

Figure 3.17: α-region of the $Zn^{82}Se$ array collected in 530 h. The spectrum was energy-calibrated using the nominal energy of the most prominent α peaks.

Table 3.18: Crystal contaminations in the isotopes of ^{238}U and ^{232}Th chains derived from the analysis of the α region (see Fig. 3.17). The same analysis is performed on the energy spectrum of each $Zn^{82}Se$ calorimeter to highlight differences among crystals. Isotopes with long half-lives, that can break the secular equilibrium, are highlighted in bold type.

	$Zn^{82}Se$ -1 [μBq/kg]	$Zn^{82}Se$ -2 [μBq/kg]	$Zn^{82}Se$ -3 [μBq/kg]	Array [μBq/kg]
^{232}Th	13 ± 4	13 ± 4	<5	7 ± 2
^{228}Th	32 ± 7	30 ± 6	22 ± 4	26 ± 2
^{224}Ra	29 ± 6	26 ± 5	23 ± 5	27 ± 3
^{212}Bi	31 ± 6	31 ± 6	23 ± 5	29 ± 3
^{238}U	17 ± 4	20 ± 5	<10	10 ± 2
^{234}U+^{226}Ra	42 ± 7	30 ± 6	23 ± 5	33 ± 4
^{230}Th	18 ± 5	19 ± 5	17 ± 4	18 ± 3
^{218}Po	20 ± 5	24 ± 5	21 ± 5	21 ± 2
^{210}Pb	100 ± 11	250 ± 17	100 ± 12	150 ± 8

3.3 Design of the CUPID-0 detector array

CUPID-0 detector is completely different from any other previously designed bolometric experiments due to its high degree of complexity: large number of channels, extremely compact structure and the different absorber dimensions [2]. This forced the collaboration to the design of a detector structure which had to be reliable, flexible and light at the same time. CUPID-0 is an array of 26 ZnSe crystals, 24 highly enriched in ^{82}Se at a level of 95 % and 2 naturals [3]. All the crystals are arranged in a tower like structure and in total there are 5 towers, four containing 5 crystals and one with 6 crystals. The position of the crystals inside the different towers is done in a way such that each tower has about the same weight of about 2 kg. The overall number of $\beta\beta$ nuclei included in the CUPID-0 detector is $3.8 \cdot 10^{25}$ (natural + enriched crystals). Tab. 3.20 shows the masses of the crystals and the total mass used in the analysis. The enriched crystals CG-28 and CG-29 are not used in the analysis due to their poor signal amplitude and energy resolution. Maybe some contaminants (e.g. Fe) were accidentally embedded in the ZnSe powder during the crystal growth, since they are red (see Fig. 3.21) while ZnSe crystals are usually orange.

Figure 3.19: Picture of the two enriched crystals (CG-28 on the left and CG-29 on the right) not used in the analysis due to their poor bolometric performances. Usually ZnSe crystals are orange while they are red.

Each tower is about 30 cm tall, ZnSe crystals are interleaved with Ge-LD. As it is shown in Fig. 3.21, each ZnSe is faced to two LDs, one on the top and one on the bottom, so that there is redundancy in the light signal read-out in case of any issue related to their performance.

[2] ZnSe and LD have different dimensions, but also all the ZnSe crystal have different heights

[3] The natural isotopic abundance of ^{82}Se is 8.82 % [170].

Table 3.20: Masses of the crystals after cutting, shaping and surface treatment.

Channel ID	Name	Tower	Type	Mass [g]
1	CG-01	1	Enriched	439.40
2	CG-13	1	Enriched	427.86
3	CG-28	1	Enriched	427.00
4	NAT-1	1	Natural	418.39
5	CG-26	1	Enriched	408.22
6	CG-02	2	Enriched	441.29
7	CG-15	2	Enriched	469.64
8	CG-29	2	Enriched	480.90
9	CG-14	2	Enriched	470.59
10	CG-16	2	Enriched	260.52
11	CG-03	3	Enriched	438.65
12	CG-20	3	Enriched	214.62
13	CG-23	3	Enriched	174.89
14	Xtra-4	3	Enriched	409.88
15	CG-18	3	Enriched	410.31
16	CG-22	3	Enriched	418.92
17	CG-04	4	Enriched	442.32
18	Xtra-2	4	Enriched	442.43
19	CG-17	4	Enriched	474.22
20	NAT-2	4	Natural	431.21
21	CG-21	4	Enriched	233.08
22	CG-10	5	Enriched	440.47
23	CG-08	5	Enriched	431.00
24	CG-24	5	Enriched	429.62
25	CG-25	5	Enriched	434.51
26	CG-27	5	Enriched	431.18
Total				10501.12
			Natural	849.60
			Enriched	9651.52
Used			Natural	431.21
			Enriched	8743.62

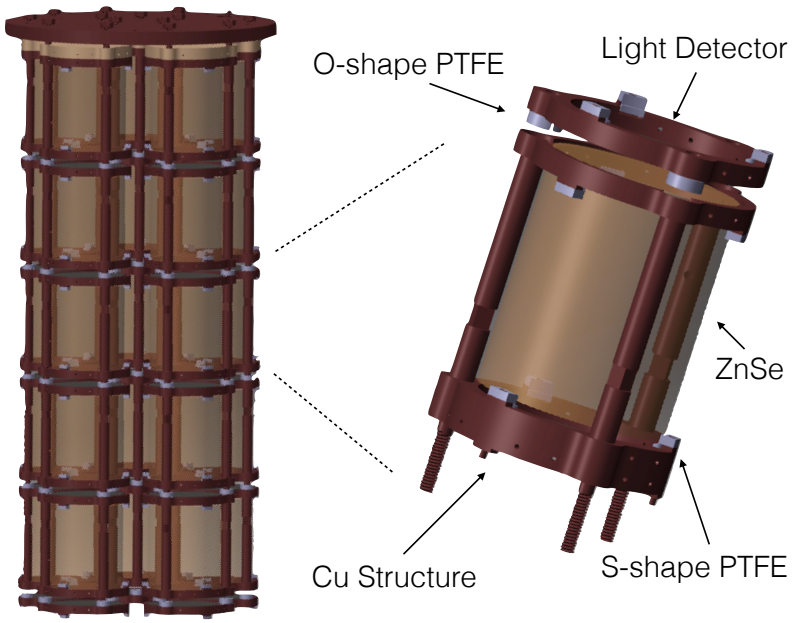

Figure 3.21: Rendering of one CUPID-0 tower and a single module.

In order to minimize the amount of passive material next to the detector, which may induce a β/γ background in the RoI due to their internal radioactive contaminations, the only components selected for the detector construction are: copper, PTFE and light reflectors (VIKUITI-3M). All these materials were selected for their radiopurity, information about material assay can be found in [138].

The copper structure is composed by copper frames and columns. The innovative idea for making the structure the simplest possible was to use a single copper frame both as ZnSe and LD holder, as it is shown in Fig. 3.21. In fact the top part of the circular copper component on its upper part holds the crystal, while the bottom part acts on the LD. Progressively on the top of the crystal there is a second frame (like the previous one, but rotate upside-down) where on its top part a new LD is set in place. Using this new type of design for each ZnSe and its adjacent LD only two copper frames are needed. The frames are kept together by means of 3 copper columns, which lengths is specifically defined by each crystal height. The overall amount of copper in the detector structure was pushed down to 22% of the overall detector mass, an unprecedented value compared to any previous bolometric experiment.

The second material employed for the detector construction was PTFE, which was used to secure in place the two absorbers. This was machined in two sets of pieces: one with a S-shape for the ZnSe and one with a O-shape per the LD. The ZnSe are supported with 3 S-shaped PTFE on the bottom and 3 on the top, while the LD are clamped by 3 O-shape holders by means of a narrow slit made on the perpendicular axis of the holder. The overall fraction of PTFE in the structure amounts to 0.1%. After the machining all the PTFE small components are deeply cleaned with soap, citric acid and nitric acid to

remove the surface contamination and stored under nitrogen atmosphere.

The last component used for the realization of the CUPID-0 detector is the light reflector VIKUITI from 3M. This plastic foil was shaped in cylinders and placed around each crystal, so to maximize the light collection efficiency on the two LDs. Secondly the reflecting foil serves also as thermal radiation shielding for the detector. The reflector was completely surrounding the crystals preventing any line of sight between the absorbers and the closer radiation shield at 50 mK. This prevented us from installing a massive copper shield around the detector, reducing by a large fraction the copper mass next to the detector. Reflecting foils are shaped and cut under a controlled atmosphere maintaining the protective films and stored in a nitrogen fluxed box; protective films are removed just before the assembly.

3.4 Detector components

Each component employed for the detector construction was specifically selected for its intrinsic radiopurity. After material screening for each item a dedicated cleaning and purification technique was adopted, the final goal was to mitigate and prevent any recontamination. All the protocol developed for the ZnSe crystals are already deeply discussed. In the following subsection there will be a detailed description of how each detector component was selected and handled before its final installation in CUPID-0.

3.4.1 Ge light detectors

Operating reliable and robust LDs is of paramount importance, given the fact that particle identification relies on the performance of these devices. LDs are composed by a high-purity Ge substrate, a thermal sensor of the same type used for the ZnSe and a holding structure made of Cu and PTFE.

The Ge substrate/absorber, purchased at UMICORE Electro-Optic Material (Geel, Belgium), is a double side polished wafer of $\oslash = 44.5$ mm of diameter and an average thickness of 170 μm, with an impurity concentration $< 2 \cdot 10^{10}$ atoms/cm^3.

All the long-standing experience in the development of cryogenic LDs [137] helped in defining the critical issues for an efficient particle identification and rejection, above all: energy resolution and signal amplitude. The former is strongly dependent on the operating conditions of the thermal sensor, as it is thoroughly discussed in [153]. The latter mostly depends on the detector design and on the ability to maximize the light detection efficiency. For this reason a dedicated procedure for the enhancement of the light collection efficiency using an anti-reflective coating was developed at CSNSM (Orsay, France). Furthermore, a reflecting foil was employed for focusing on the LD the scintillation light coming from the ZnSe crystal.

Antireflective coating

A way to significantly improve the light detector performance is to increase the light collection by minimizing its reflectivity. Such improvement can be obtained by using a special anti-reflective coating on the side of the light detector which is facing the scintillating calorimeter.

One of the simplest ways to reduce the reflection is the so called *refractive index matching method*. In the approximation of normally incident light from a transparent to an absorbing medium, the absorbed fraction can be calculated by the following formula:

$$R = \frac{(n_0 - n_1)^2 + k^2}{(n_0 + n_1)^2 + k^2} \tag{3.2}$$

where n_0 is the real refraction index of the transparent medium and n_1 (k) is the real (imaginary) part of the complex refraction index of the absorbing medium, i.e. germanium. Considering a simple vacuum-germanium interface, the fraction of absorbed light is only 51%. On the contrary, if a thin coating layer with refractive index n_i, with value between n_0 and n_1 is placed between the two media, one should evaluate first the R value for the vacuum-coating interface, then for the coating-germanium transition. The optimum value for anti-reflective material to be placed in between vacuum and Ge is $\sim$2.4 which leads to a gain on the light absorption of about 35% with respect to bare Ge, depending on the wavelength.

The best thickness for the layer can be determined by fulfilling the conditions for an optimal anti-reflective coating in the approximation of single-layer interference. The coating thickness should be $d = \lambda/4$, where λ is the wavelength of the incident light. This method works well for monochromatic light sources. It can takes λ=645 nm, which corresponds to the maximum of the intensity emission for ZnSe scintillation, even though the wavelength distribution is rather broad [174]. The optimal thickness results to be around 65 nm, for $n_i \sim 2.4$ and considering the refraction index of SiO, which is $\sim$2.5, so the wavelength in SiO is reduced by this factor.

Several cryogenic tests on anti-reflective coatings were performed at LNGS and at CSNSM during the past years [174, 175]. The best results were achieved with a SiO coating, which has a refractive index of $\sim$ 2.5, close to the optimum value previously computed. The increase of the absorbed light fraction was 34%, in agreement with the expectations. For these reasons a SiO coating of about 50 nm was deposited on CUPID-0 LDs.

Forty Ge absorbers were prepared at CSNSM for CUPID-0 detector. Before the SiO deposition each Ge wafer was previously etched with a mixture of nitric (HNO_3 70%), acetic (CH_3COOH 100%) and hydrofluoride (HF 40%) acids in proportion 5:3:3. This mixture is aggressive enough to react with the Ge surface. The thickness of the removed surface layer was $\approx$ 10 μm with an etching time of about 1 min. After the chemical etching the surface was also treated with an Ar ion bombardment. The gas was ionized with an electron gun, the Ar pressure during the bombardment was $3 \cdot 10^{-3}$ mbar. These procedures remove any possible residual oxides and improves the surface quality for the coating process. The deposition is performed using a tantalum box, where the SiO is

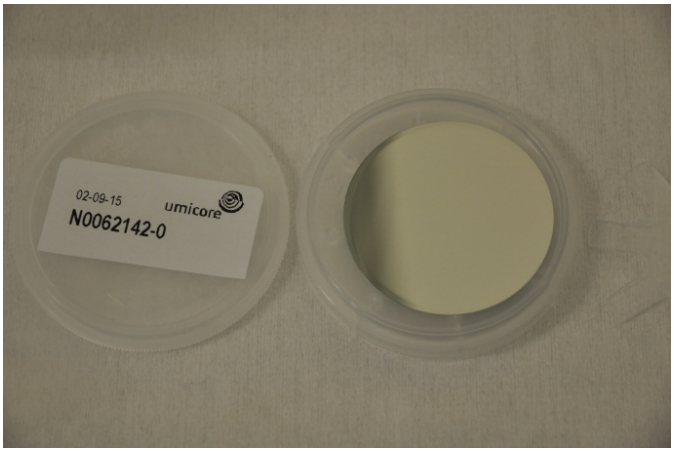

Figure 3.22: A high purity Ge slab before applying any procedures.

heated up to T $\sim$ 1000 ^oC. The deposition is performed under vacuum: the pressure in the evaporation camera is P$< 10^{-7}$ mbar.

The evaporation rate was tuned to be in the range of 0.5-1 nm/s. The deposition thickness is controlled with a high precision ($<$ 0.1 nm) piezoelectric quartz crystal, its frequency depends on the deposited mass.

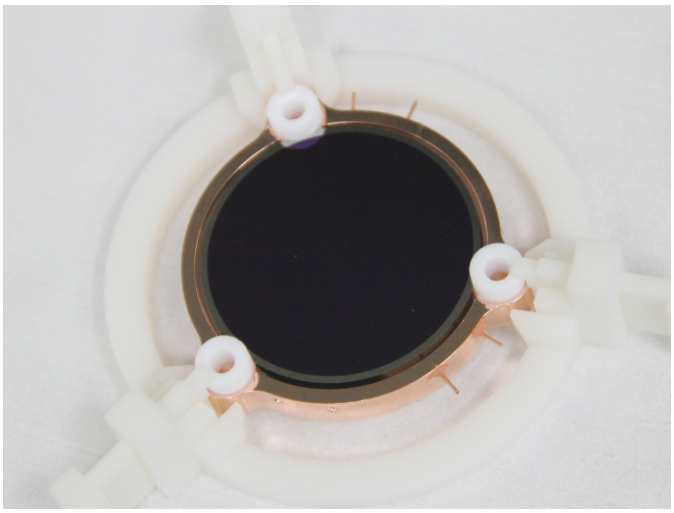

Figure 3.23: Light detector before mounting, side with antireflective coating.

The average final thickness of the SiO coatings was between 70-80 nm. This is a good approximation of the value required by the single-layer interference anti-reflective coating, as previously discussed.

3.4.2 VIKUITI light reflector

The light reflector foil installed around the crystal is a VIKUITI multi-layer specular reflector produced by 3M. The foil has been characterized at different temperatures and it ensures a reflectivity greater than 98% for wavelengths between 400-800 nm [176] over a wide temperature range, from 300 K to 20 K.
The emission spectrum of ZnSe at 10 K has three main components at: 645 nm, 610 nm and 460 nm [177], thus ensuring an excellent light collection efficiency.

The reflector radiopurity was investigated with ICP-MS at the LNGS employing an innovative mineralization procedure for the sample preparation [178]. The measured concentration of the elemental Th and U were 10 ± 3 and 8 ± 2 ppt, respectively. The reflecting foil is on average more contaminated than crystals but the effect is expected to be negligible due to the small amount used in the whole (i.e. $\sim$17g / 0.21 m^2). To avoid Rn re-contaminations reflecting foils are handled under controlled atmosphere (i.e. clean room with Rn abatement system) and stored in a nitrogen fluxed box.

3.4.3 Ge-NTD thermal sensor

The CUPID-0 thermal sensor production started on March 2012. Nine wafers of high-purity Ge, $\oslash$ = 65 mm and thickness 3.25 mm, were irradiated at the MIT Nuclear Reactor Laboratory, Boston (MA, USA), see Fig. 3.24. The exposure to high neutron fluxes is needed in order to uniformly dope the wafers, the required dopants concentration to enable the operation of the Ge as thermal sensor is at level of 10^{16} atom/cm^3. Such high and uniform doping level will take the semiconductor close to the metal-to-insulator region. The electrical conductivity of these heavily doped semiconductors has an exponential dependence on the temperature, making these sensors the most suitable technology for our purposes [179]:

$$\rho(T) = \rho_0 \, e^{(T_0/T)^{0.5}}, \tag{3.3}$$

where T_0 depends on the Ge-NTD doping level and ρ_0 on the doping level and on the sensor geometry. As a consequence, a fluctuation of the doping level will strongly affect the sensitivity of the thermometer, the target value are T_0=4.66 and ρ_0=1.1 Ω, having a sensor sensitivity of about 1 MΩ/μK.

An accurate and precise measurement of the flux and neutron dose to which the Ge wafers are exposed is of paramount importance for the success of the experiment, since on these values will depend the detector response and resolution. The entire neutron dose should not exceed 2% of the nominal value, which is estimated to be $4 \cdot 10^{18}$ n/cm^3. To achieve such high accuracy and precision nominal neutron dose, several Ge wafers are irradiated as follows: 3 wafers at $\pm$7% of the target dose, 2 wafers at $\pm$3%, 1 wafer at +2% and 3 wafers at the nominal value. This choice was driven by the fact that the Nuclear Reactor facility could ensure dose within 5% of the target value. After each irradiation the total fluence was evaluated by measuring the activity of witness samples that underwent the same irradiation of the wafers. At last a final fine tuning of the neutron dose was carried out at the LENA Nuclear Research Reactor Laboratory, where the most intense

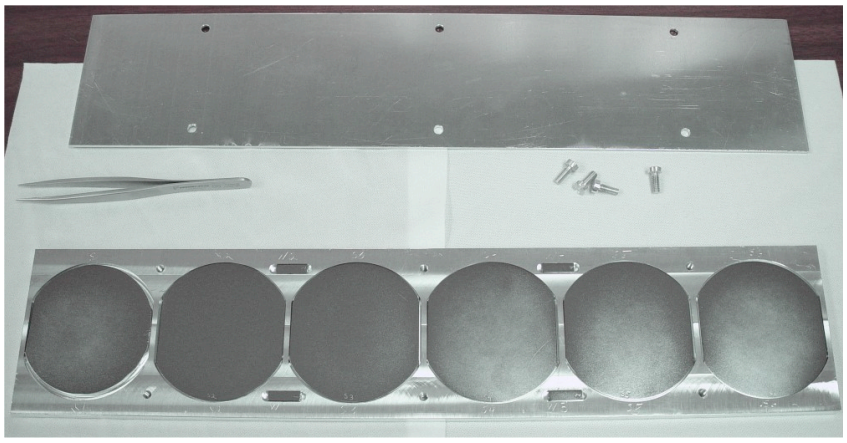

Figure 3.24: Six out of 9 Ge wafers, ⌀ =65 mm and thickness 3.25 mm, installed in an Al holder before neutron irradiation at the MIT Nuclear Reactor Laboratory (MA, USA).

neutron flux is about 3 orders of magnitude lower than the MIT one, thus allowing a more accurate neutron irradiation. A detailed mapping of the LENA reactor neutron fluxes was performed [180, 181] before irradiating the sensors, this allowed us to select the irradiation channel more suitable for our purpose, thus with a ratio thermal/fast neutron flux of about 20.

After the irradiation a cool-down time of about 3 years has elapsed. On two wide area sides of the Ge wafer a 4000 Å gold layer is deposited, which serves as sensor Ohmic contacts. After the deposition the wafer is diced in sensors of the desired size, the final sensor dimensions for the ZnSe and LDs are $3 \times 2.8 \times 1$ mm^3 and $2 \times 2.8 \times 0.5$ mm^3, respectively, see Fig. 3.25.

Sensors gluing

The mechanical and thermal coupling of the sensors to the crystal absorbers (referred as gluing) is a well-known concern in the construction of calorimeters, because it influences the quality of the detector performance. In particular, the R&D towards the Cuoricino experiment [99] established stringent requirements to this delicate process, involving the geometry of the glue interface between sensor and absorber, the selection of glue, and the environmental conditions in which the operation has to be performed.

According to these constraints, it is preferable to deposit the glue in a matrix of dots, in order to compensate for the different thermal contractions at low-temperatures. The optimal number of dots for a 2.8×3 mm^2 surface NTD is 9. These dots must have a

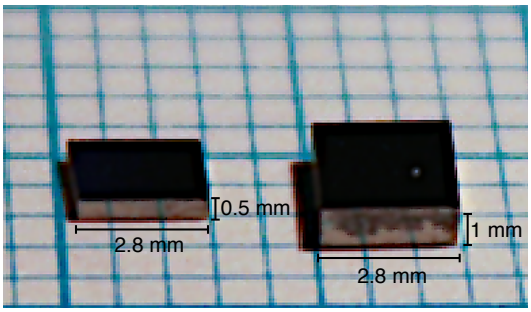

Figure 3.25: Ge Neutron Transmutation Dope sensors for ZnSe (right) and light detector (left).

diameter of 0.7 mm, while their height is determined by imposing a 0.05 mm gap between the crystal and the absorber, see Fig. 3.26.

Moreover, the glue is deposited on the sensor surface instead of on the crystal, because the former is easier to reprocess in case of gluing failure, while the cleaning of the crystal surface may require an entire crystal surface polishing treatment.

The glue used for the process must have a density high enough to avoid the merging of the dots after their deposition. Besides that, it has to work at cryogenics temperatures and through several thermal cycles and it must fulfill the radiopurity constraints required by the experiment. The selected glue is the bi-component epoxy Araldite Rapid by Huntsman Advanced Materials [182]. It has a viscosity of 30 Pa·s, a very quick pot life of about 3 min, but also a very short curing time of about 1 h and low radioactivity, less than $8.9 \cdot 10^{-4}$ Bq/kg for ^{232}Th and $1.0 \cdot 10^{-2}$ Bq/kg for ^{238}U [138].

To improve the reproducibility of the detector performance, a R&D was carried on to develop a semi-automated system for the sensor-to-absorber coupling of the CUPID calorimeters, similar to the one developed for the CUORE experiment [95]. The CUPID-0 gluing system was developed starting from the previously acquired knowledge [183].

Our system is based on a pneumatic dispenser held to a x-y-z Cartesian for the glue deposition and a six-axis robotic arm to handle the detector component. The introduction of automated elements reduces the variability induced by manual work and gives the advantage of precise timing, which is useful considering the short time window of epoxy life-time. The result was a semi-automated system in which the dots are performed through a matrix of spring-loaded tips applied to a x-z Cartesian robot.

As last remark, the gluing procedure must be performed in controlled atmosphere. to avoid unexpected glue reaction given the fact that the glue intrinsic properties (especially viscosity, curing time and transparency) have a strong dependence on the temperature and humidity of the environment.

The gluing procedure is divided in three steps: the tool preparation, the glue dispensing and the crystal deposition. Among the three, only the second one is automated. Firstly, the Cartesian robot is equipped with the correct spring-loaded tip matrix accord-

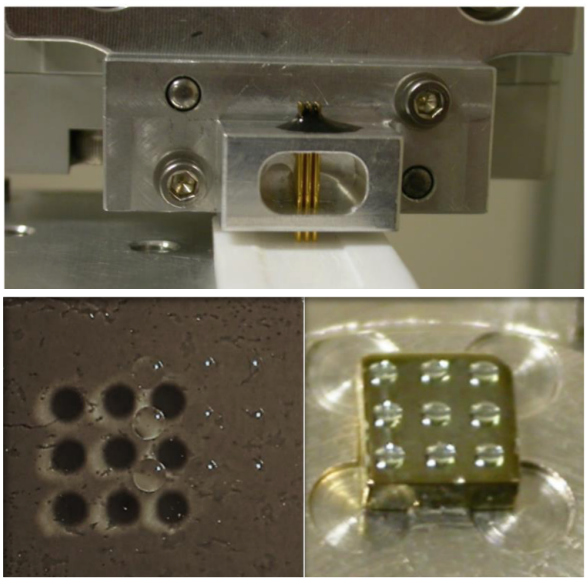

Figure 3.26: Picture of the matrix system for the glue deposition (top), test of glue dots deposited on a transparent substrate (left) and glue dots deposited on the $Zn^{82}Se$ thermal sensor (right).

ing to the kind of NTD to be glued (a nine tip matrix for the $2.8 \times 3 \times 1$ mm^3 NTDs for ZnSe crystals and a six tip matrix for the $2.8 \times 2 \times 0.05$ mm^3 NTDs for LDs). Then the sensor is placed on a positioning device on the Cartesian robot, where it is held in place by vacuum. In parallel, the crystal is prepared in a dedicated PTFE holder that will be inserted onto the sensor positioning device after the glue handling phase. This begin with the mixing of the two epoxy components through a dispensing gun provided with a disposable static mixer; the mixed glue is poured and then leveled in a small PTFE container placed on the Cartesian robot. The x-z arm dips the tip matrix in the glue container and then presses it onto the sensor surface to deploy the glue dots. The correct size of the single glue dot is determined by choosing a proper diameter of the tip (0.53 mm) in combination with the depth of the glue container (0.70 mm). The fact that the tips are spring-loaded ensures a uniform collection/deposition of the glue by each tips. Finally, the crystal is lowered on the glue dots thanks to the PTFE crystal holder in which it was previously hosted, that ensures a gap of 0.05 mm between the crystal and NTD surfaces. This, together with the fact that the sensor is held by vacuum for all the glue curing time prevents the dots to merge in a layer, preserving the shape of the dot matrix.

The gluing activity of CUPID-0 was performed inside a radon-free cleanroom to ensure low radioactive conditions and a very stable environment in terms of temperature and humidity.

3.4.4 Ultra-high cleaning copper protocol

CUPID detector structure is mainly composed by copper, it makes about 22% of the overall detector mass. Minimizing the concentration of radioactive impurities, especially from the surface of the detector structure is important for suppressing possible background sources, namely ^{232}Th which may induce pile-up events from γs. For this reason a dedicated cleaning procedure was developed for the abatement of surface contamination in copper, similar to the one described in [184].

The frames that hold the crystals are made of electrolytic tough pitch copper, also known as NOSV copper. Some impurities, including decay products of ^{232}Th and ^{238}U decay chain can accumulate of the material surface following an exposure to a uncontrolled atmosphere. Additional impurities are deposited also during the production process, in fact several mechanical machining steps were needed to produce the copper holders. Their concentration is usually modeled as a gradient from the first external layer to the inner bulk, caused by the diffusion of contaminations in the material. The radioactive contaminants of ^{232}Th and ^{238}U are usually present on copper surfaces to a depth of about 20 μm [185], see Fig. 3.27.

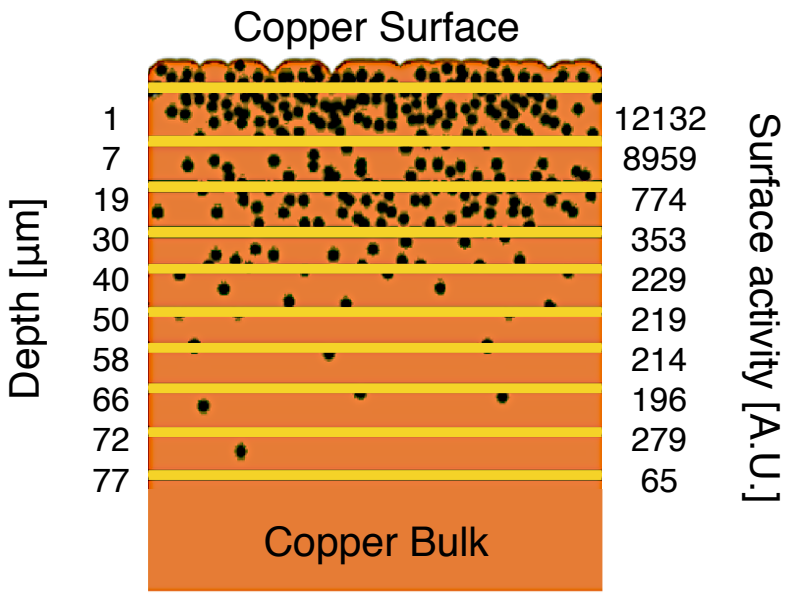

Figure 3.27: Schematic view of radioactive impurity distribution on copper surface and bulk.

All the copper NOSV components were cleaned within a period of 6 months. The cleaning protocol consists of 5 general macro steps divided in sub-steps for a total of 61 single processes, the time required for cleaning one set was about 10 days. The total number of pieces cleaned was 268, divided into 78 columns (with 26 different lengths), 70 frames two large copper plates for the tower installation and several spare parts.

Cleaning process protocol to reduce the radioactive contamination levels in Cu components

The cleaning procedure, developed at the Legnaro National Laboratories (LNL) of INFN. consists on a sequence of the successive treatments: Tumbling, Electropolishing, Chemical etching and Magnetron plasma etching (T+E+C+M). The storage of the copper parts between cleaning steps were performed in a clean room to avoid possible re-contamination of the surface.

- Pre-cleaning process: The pre-cleaning is performed for removing any lubricant residues deposited on the copper surfaces and it directly affect the efficiency of the electropolishing process. It is performed wiping the copper surface using specific wipes and a sequence of three different solvents: tetrachlorethylene, to solve organic materials, acetone to degrease and remove tetrachloroethylene and ethyl alcohol to dissolve the acetone from the copper surface. Later, the copper pieces are cleaned in ultrasound baths (33 kHz) at 40^{o}C for 10 minutes with deionized water and NGL1740PSP powder soap. Right after the bath, the copper pieces are dried with alcohol and nitrogen taking precautions to avoid re-contamination.

- Chemical etching pre-electrochemical process: The surface must be prepared for the electropolishing process. Tumbling was used for CUPID-0 pieces but some delicate parts cannot undergo the tumbling process, due to their fragility and small thickness (less than 1 mm). The tumbling step cleaning protocol is substituted for some components by an ammonium persulfate chemical treatment with a concentration of 20 g/L for 2 hours.

- Electrochemical process: The electropolishing remove a surface layer up to 50 μm for the frames and 100 μm for the other parts. To avoid the removal of the cooper in certain segments of the pieces, PTFE protections were used. The copper pieces are placed inside an electrochemical solution of 40% of butanol - 60% of phosphoric acid, following a designed specific anode cathode configuration for each type of copper piece. During the process, all parameters and the copper surface quality is controlled. After the electrochemical treatment, residual electro-polishing solution is removed with ultrasonic cleaning.

- Chemical etching process and Passivation: The chemical etching is applied to reduce the radioactive contaminants from the areas screened with the PTFE protections. The erosion rate is about 2 μm/min. This chemical etching is performed using deionized water heated at 72$\pm$4^{o}C with a recipe of sulfamic acid, ammonium citrate in powder form adding hydrogen peroxide and butanol in liquid form, named SUBU. The copper pieces are fixed to a sample holder through a copper wire and drawn in the SUBU solution for 5 min, the pieces rotate to enhance the reaction rate. After the SUBU process, the copper pieces are passivated in sulfamic acid solution at a concentration of 20 g/L for 5 minutes and cleaned in ultrasonic bath to finally be dried and packed.

- Plasma cleaning: The plasma cleaning constitutes an important step because it is carried out in a vacuum system and is the last phase before the assembly of the detector. The erosion rate during plasma cleaning is about 1μm/h. The plasma cleaning is a process based on DC magnetron sputtering technique which consists in the erosion of a target (copper pieces) through the impact ions of argon inert gas (plasma). The copper pieces are fixed on a different sample holder for each kind of component, inside of a class 100 cleanroom in order to handle the copper pieces in a controlled environment. The holder is placed into the vacuum chamber and before the plasma cleaning, 12 hours of baking at 100^{o}C is performed in order to degas adsorbed chemical substances and humidity. After the baking, a uniform magnetic field of $1.5 \cdot 10^{-2}$ T is generated and a 30 W power is supplied for 5 minutes.

After the cleaning procedure the frames are stored under vacuum and shipped in triple plastic bags to LNGS, where they are prepared for the assembly. The plastic bags are opened in clean room under controlled atmosfere and the frames are stored in nitrogen atmosphere for several weeks.

3.5 Detector assembly

All activities for the construction of CUPID-0 detector were carried out in an underground Rn-suppressed clean room, with a Rn contamination of less than 5 mBq/m^3 located in the Hall C of the LNGS. The cleanroom contained two separate workstations: one for gluing the sensors to the ZnSe crystals and to the Ge wafers (see Fig. 3.28, left), and one for building and instrumenting the towers (see Fig. 3.28, right). A nitrogen-flushed storage container was also installed in the clean room for hosting the detector after its assembly. The first step in the CUPID-0 tower construction was the pre-assembling of the light detectors: each Ge wafer equipped with NTD was hold in its copper frame using three PTFE O-shape holders. Since the Ge wafers are 170 μm thick specific assembly tools were developed in order to avoid accidental damage and recontamination of the copper frame during the assembly procedures. These tools were realized with a ENVISIONTEC ULTRA 3SP 3D printer using a high radio-pure plastic resin (see Tab. 3.29). These tools consisted of a mounting template and of a handling system (see Figs. 3.30 a and 3.30 c respectively). The assembly procedure for the 31 LDs of the CUPID-0 detector consisted in the following steps: positioning of the Ge wafer with the PTFE O-shape holders on the mounting template, positioning of the copper holder and connection of the Ge-NTD gold wires for the sensor read-out, fitting and tightening of the handling tool and removal from the mounting template and finally their storage of the assembled light detectors in a vacuum box, see Fig. 3.30.

The second step in assembling the CUPID-0 towers was to physically assembly them using Cu, PTFE, 26 crystals and 31 pre-assembled LDs. The towers were manually built, one floor at the time [4], starting from the lower one. In order to maintain a suitable operational working height, the towers were assembled in an automatically adjustable

[4] A floor is defined as a single module, this is composed by a $Zn^{82}Se$ and its most adjacent LD.

Figure 3.28: Photos of the two working areas inside the cleanroom. On the left is shown the station where the Ge-NTD thermal sensors are glued to the absorbers, on the right is shown the area where the tower are assembled and stored.

table, named garage. After the assembly of the first floor, the detector is lowered by the height of this floor, in this configuration the operator always works at the same level. The main steps for the assembly of a single tower are shown in Fig. 3.31. The first operation is the positioning of the first pre-assembled LD on the bottom copper holder of the tower and installation of the first three columns that will host the ZnSe crystal, then the positioning of the ZnSe crystal on the bottom copper frame equipped with three S-shaped PTFE clamps. The third step is the installation of the VIKUITI-3M reflector and the top copper holder equipped with three S-shaped PTFE clamps. At this point the electrical connections between the gold-wire and the mechanical structure are made. Finally the second LD is installed on the top from of the previously installed ZnSe. All these procedure are repeated until a tower of 5 floors is completed. After the completion of the detector assembly the 5 towers are hosted on a copper plate which acts as support structure and connection between the cryogenic system and the detectors, see Fig. 3.32.

3.6 Cryostat

CUPID-0 cryostat is the same cryogenic infrastructure that hosted the Cuoricino [99] and CUORE-0 [100] experiments. This system was upgraded in order to meet our stringent requirements in terms of low vibrational environment and increase number of read-out channels. The cryostat was commissioned at the LNGS in 1988 and it is a top loading Oxford TL400 with a copper He dewar. The ^{3}He/^{4}He dilution unit has a cooling power at 100 mK of about 400 μW, this ensures the possibility to install in the system a large number of read-out channels without spoiling the cryostat performance in terms of

Table 3.29: Radioactive contamination of the polymer-resin used for the 3D-printing of the detector assembling tools (3SP WHITE D7).

Chain	Nuclide	Activity [mBq/kg]
^{232}Th		
	^{228}Ra	< 9.3
	^{228}Th	< 10.3
^{238}U		
	^{226}Ra	< 3.8
	^{234}Th	< 73
	^{234m}Pa	< 0.25
^{235}U	^{235}U	< 5.3
	^{40}K	81 ± 35

cooling power.

In Fig. 3.33, the cryogenic system where the CUPID-0 detector is installed is shown. The detector is installed right below a Roman Pb shield by means of a spring and it is thermally coupled to the Mixing Chamber stage (MC) by means of a oxygen-free high conductivity copper foil of 50 μm thickness. The MC, which is the coldest point of the system ensures the detector cooling down to the designed base temperature of 7.5 mK.

Two major upgrades were implemented in the system compared to the previous configuration: increasing the number of read-out channels and installing a vibrational dump system. Upgrading the number of read-out channels was a mandatory step given the fact that for each ZnSe crystal there is also a LD, this doubles the number of wires from room temperature down to the detectors. The cryostat when it was hosting the CUORE-0 experiment was able to read-out up to 52 calorimeters, now the system can handle up to 136 detectors, irrespectively if they are ZnSe or LDs. For CUPID-0 67 channels are used: 26 for ZnSe, 31 for LDs and 10 thermometers for monitoring the stability of the detectors and of the system. The remaining available channels might be employed for a future upgrade of the detector.

The signals are extracted from the detectors using NbTi-NOMEX [5] ribbon cables. The NbTi-NOMEX cable run from room temperature down to the MC, while from the MC to the detectors there are constantan wires, see Fig. 3.34. All the cables are thermalised at the different temperature stages of the cryostat, and on the MC they are plugged into custom-made junction boards, which connect the ribbon to the constatan wires, as shown in Fig. 3.35 and Fig. 3.32.

The NbTi-NOMEX ribbon cables are made of 13 twisted pairs of twisted 100 μm

[5] Registered trademark of Du Pont.

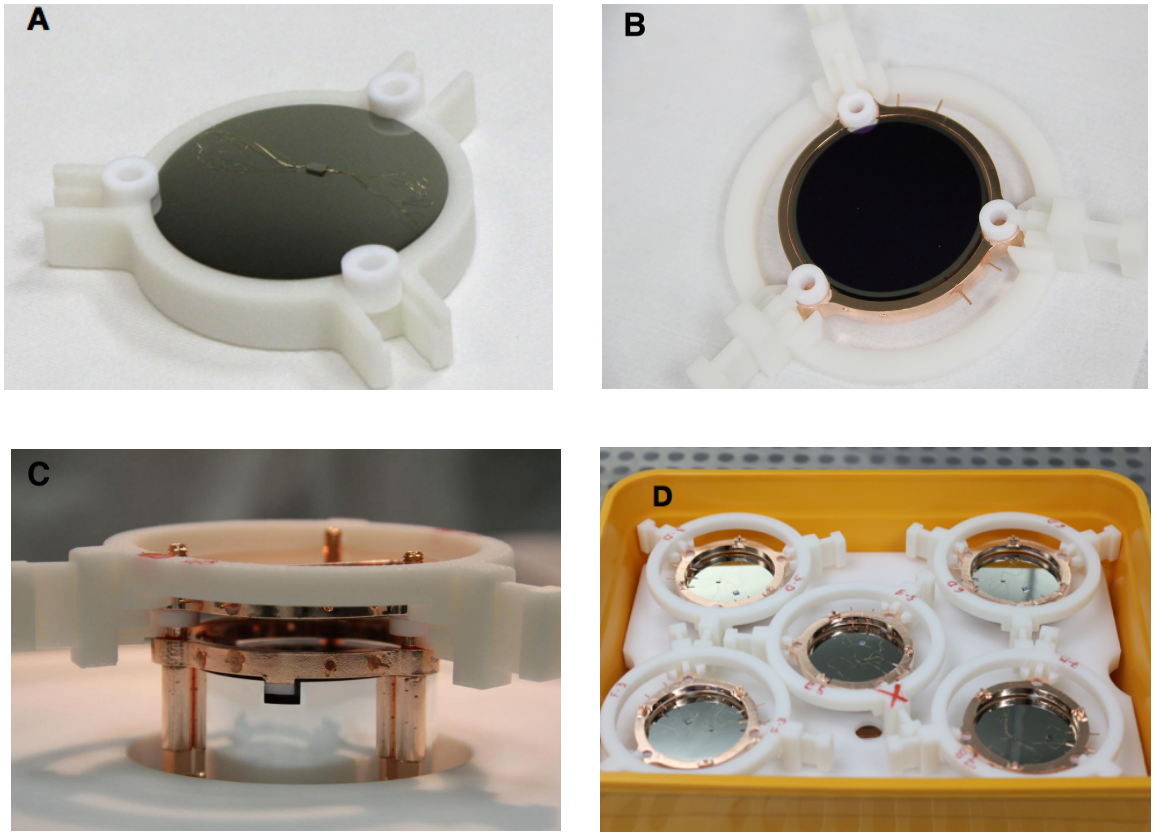

Figure 3.30: Light detectors assembly: A) Positioning of the Ge wafer with the PTFE O-shape holders on the mounting template. B) Positioning of the copper holder and connection of the Ge-NTD gold wires for the detector read-out. C) Fit and tighten of the handling tool and removal from the mounting template. D) Storage of the assembled light detectors in a vacuum box.

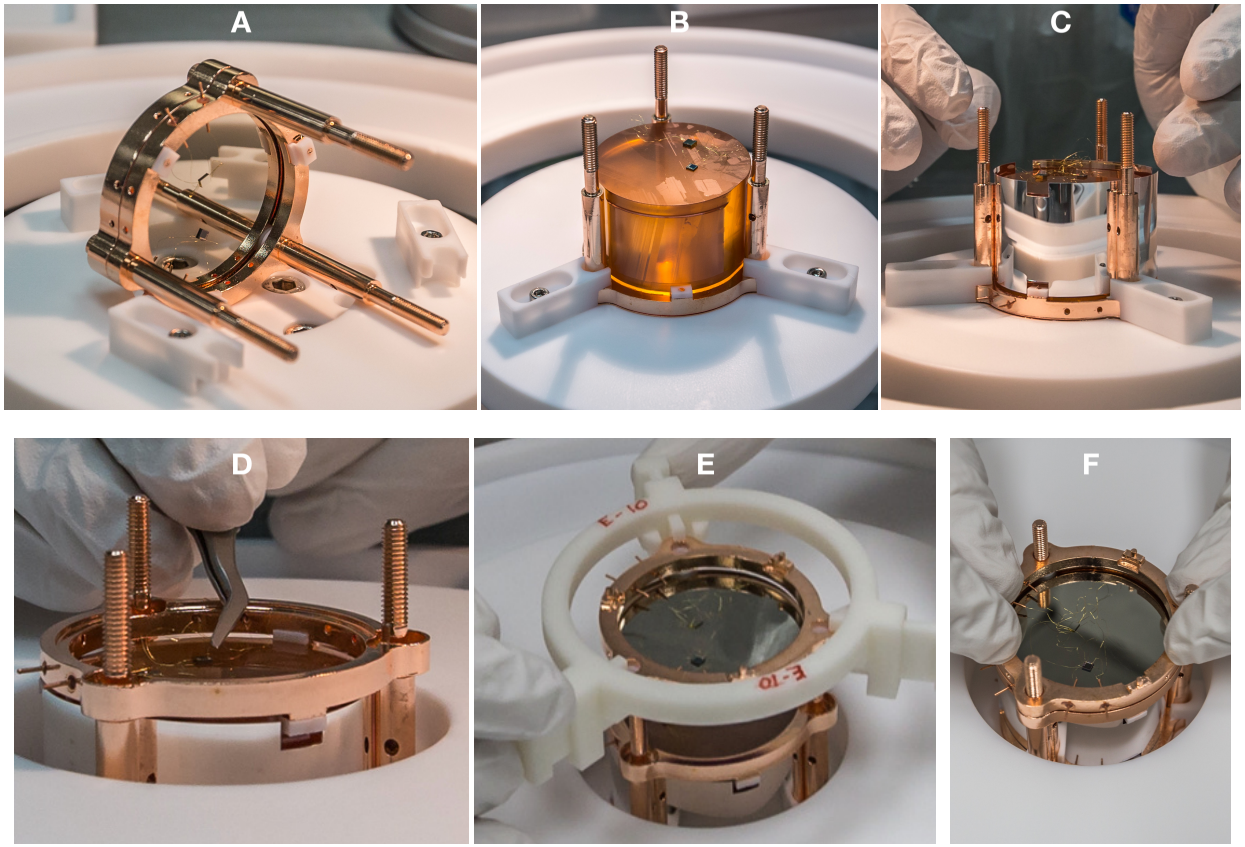

Figure 3.31: Single tower assembly: A) Positioning of the first pre-assembled LD on the bottom copper holder of the tower; installation of the first three columns that will host the ZnSe crystal. B) Positioning of the ZnSe crystal on the bottom copper frame equipped with three S-shaped PTFE clamps. C) Positioning of the VIKUITI-3M reflective foil. D) Positioning of the top copper holder equipped with three S-shaped PTFE clamps; connection of the Ge-NTD gold wires in the inner copper pins. E) Positioning of the top pre-assembled LD. F) Coupling of the pre-assembled LD with the top ZnSe copper holder.

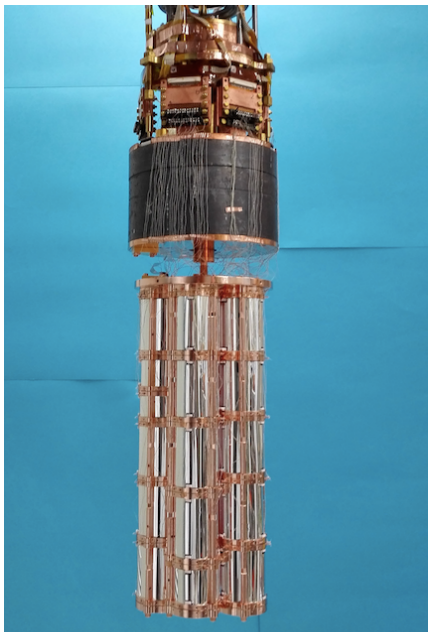

Figure 3.32: CUPID-0 detector installed on the cryogenic system, just below the 10 cm thick Roman Pb shielding.

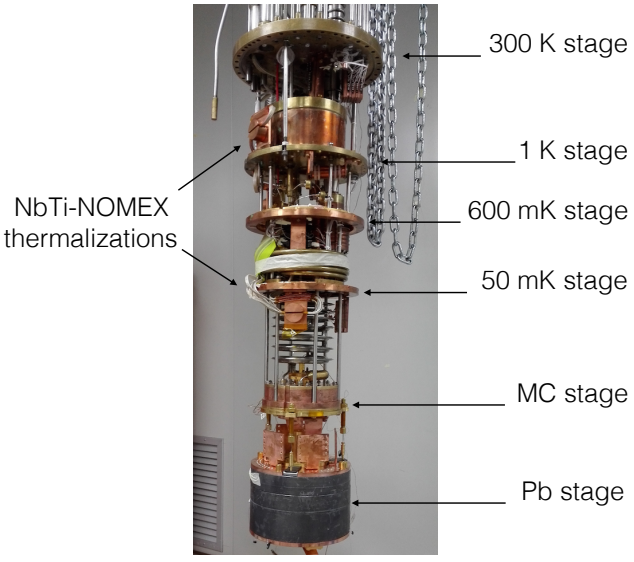

Figure 3.33: Picture of the dilution unit. The different thermalization stages are identified by the arrows. A Roman Pb shield is anchored to the MC stages by means of a vibrational dumping system. On the Pb stage are installed the junction board shown in Fig. 3.35.

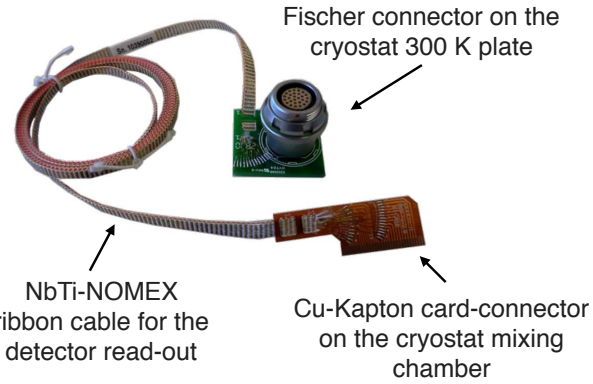

Figure 3.34: NbTi-NOMEX cable from 300 K to the mixing chamber. On the room temperature side they are soldered to Fischer 27-pin connectors on the other hand they are soldered to Cu-Kapton cards.

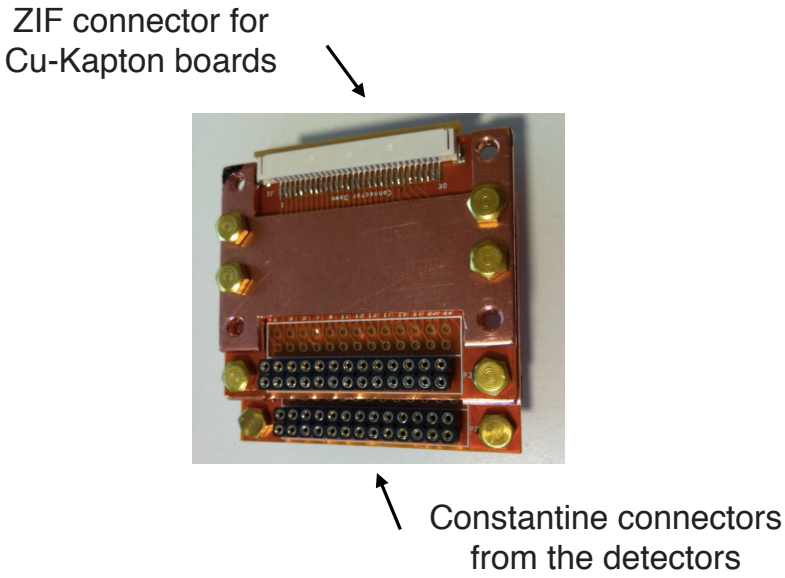

Figure 3.35: Junction boards on the MC for connecting the NbTi-NOMEX cables to the constantine wires from the detectors.

NbTi wires. Their low radioactivity and electrical properties [186] make them the best choice for the detector read-out. They are characterised by low thermal conductivity, becoming superconducting below 10 K, low parasitic capacitance (100 pF/m) and a negligible cross-talk level, 500 twisting/m.

The second major upgrade of the cryogenic system consisted in a mechanical double stage anti-vibrational decoupling system, similar to the one developed in [187]. The main purpose for the development and installation of such system was driven by the fact that any microphonic noise source has to be minimized, in order to prevent any spoiling of the LD bolometric performance. In fact the LDs, having a higher sensitivity compared to the ZnSe crystals, requires a much lower vibrational environment compared to a system where only a massive crystals are operated.

In Fig. 3.36 is shown a scheme of the mechanical decoupler which is directly anchored to the MC using the top brass ring. The circular brass piece holds in place the 10 cm thick Roman Pb shield by means of three custom-designed wires made of harmonic steel (red color of Fig. 3.36, where just one wire connector is shown). The Roman Pb shield is connected to the harmonic steel wires by means of three harmonic steel wings mechanical anchored on the Pb (purple color of Fig. 3.36). The characteristic longitudinal resonance frequency of this first decoupling stage is about 12 Hz. On the top of the Pb shield is encapsulated a steel spring which is mechanical connected to the detectors by means of Cu cylinder housed inside the Pb shield. The Cu connector is mechanical decoupled from the the Pb acting as second mechanical decoupling system, and it is characterized by longitudinal resonance frequency of about 5 Hz.

3.7 Electronics readout

The readout system of CUPID-0 shares the same general structure as that of the CUORE experiment [188]. Many of the operating parameters were optimized for CUPID-0. Fig. 3.37 shows the block diagram of the readout chain for a single detector, valid for both crystals and LDs. The thermistor R_B is biased with a DC current through a pair of load resistors $R_L = 30\ G\Omega$ (10 GΩ). The bias generator V_L can be set between $-25\ V$ and $25\ V$ with 16-bit resolution. The voltage across the thermistor is amplified by the two-stage amplifier A_1 and A_2. The total gain can be set between 27 V/V and 10000 V/V with 12-bit resolution. The input stage of A_1 is based on a JFET differential pair. We designed two different options: a) low parallel noise, less than 100 fA below 50 $°C$, and about 3.5 $nV/\sqrt{Hz}$ series white noise (twice this value at 1 Hz); and b) low series noise, 1.2 $nV/\sqrt{Hz}$ (twice this value at 1 Hz), with larger parallel noise. In principle, the choice depends on the value of detector impedance. In practice we observed that in both cases this stage was not limiting the resolution, and option a) was found adequate for all detectors. The thermal parallel noise of the load resistors R_L, whose maximum value and temperature of operation are constrained by practicality.

In Fig. 3.38, the noise (in nV/$\sqrt{Hz}$) at 5 Hz is shown for the ZnSe crystals and the LD, respectively. The measured noise in the present setup is larger than expected considering Johnson noise of R_{load}, Johnson noise of R_{bol} and contributions from the

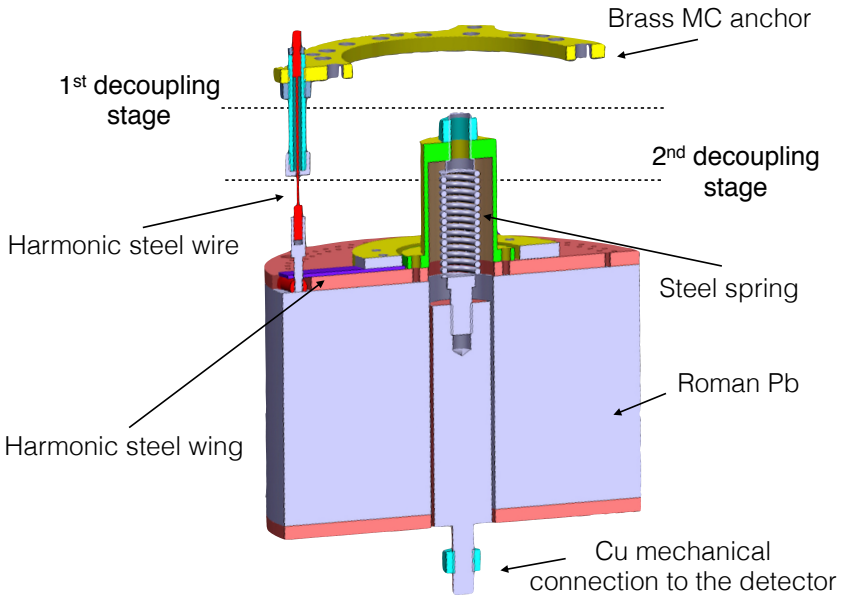

Figure 3.36: Rendering of the double stage mechanical decoupling system. This is installed directly on the cryostat mixing chamber with the top brass anchor and on the bottom part there is a Cu mechanical connection for the detector installation.

front-end amplifier (JFET). In particular a greater noise is measured for the ZnSe crystals operated over the invention point (red dots in Fig. 3.38). This is not a usual working condition but it was chosen by optimizing the signal-to-noise ratio, indeed it was proved to be irrelevant for the detectors performance (i.e. baseline resolution). LDs show a more uniform noise and also the spread with respect to the calculated noise is lower. This different behavior of ZnSe crystals and LDs indicate that the excess of noise could be related to ZnSe crystals features. Future optimization and investigation will be focused on further reducing the observed noise, attempting to reach the electronics limit.

The amplified signals are routed out of the Faraday cage to the antialiasing filters (Bessel-Thomson, 6 poles) and the data acquisition system (DAQ) [190]. The cutoff frequencies, settable in 4 steps, are $15, 35, 100, 120$ Hz for the crystals and $15, 100, 140, 220$ Hz for the LDs.

The Pulser board is used to generate voltage pulses, which are injected onto the detector by resistor R_H [191]. The pulses are triggered and tagged by the DAQ, and used for relative calibration during data taking. Their noise is negligible, typically at the order of 10 ppm RMS, and their thermal stability is better than 1 ppm/$^\circ C$, reducing the need for calibration runs with radioactive sources. Similar boards are also used to stabilize the temperature of the mixing chamber and of the detector holder through PI (proportional-integral) control loops. The power supply is provided by a two stage system: a commercial floating AC/DC generator with a custom filtering solution [192], followed by two custom linear power supplies with low noise (1.6 μV peak to peak between

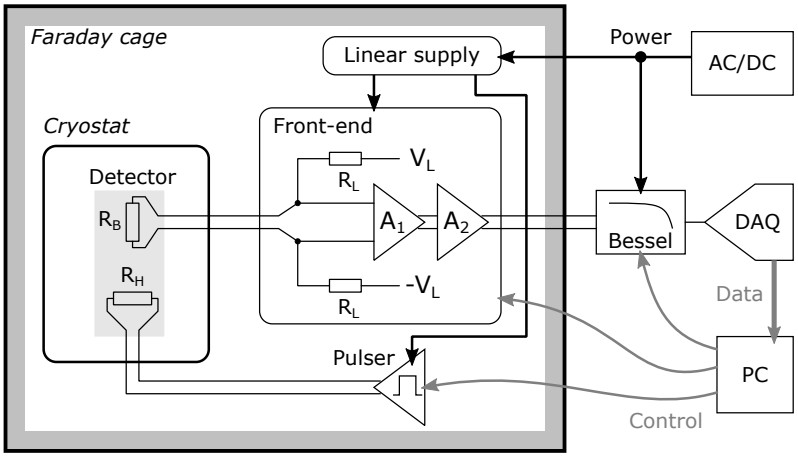

Figure 3.37: Block diagram of a readout channel, from the detector to the DAQ.

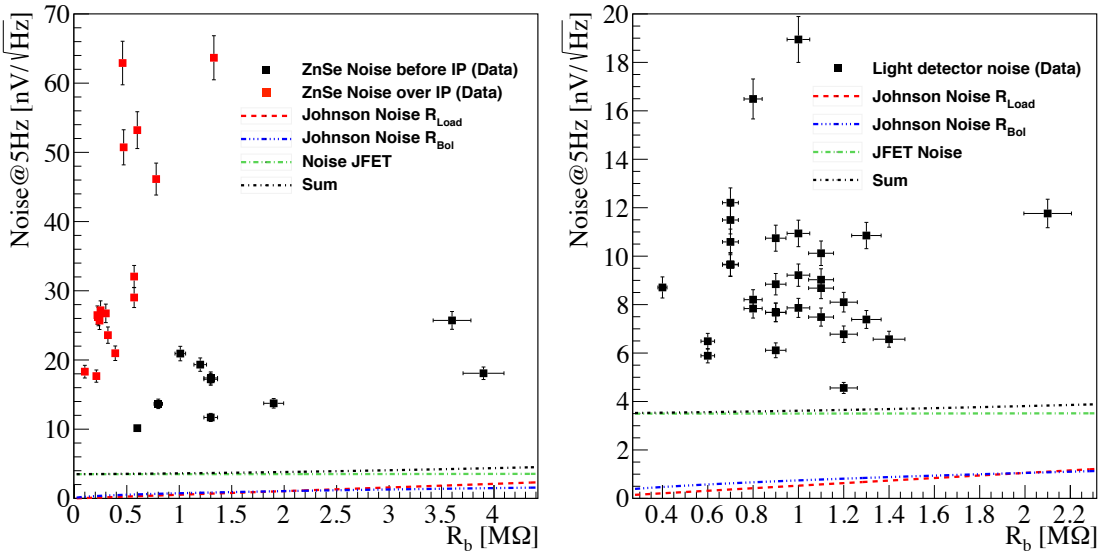

Figure 3.38: Detectors noise at 5 Hz as a function of the Ge-NTD dynamic impedance for ZnSe crystals (left) and the LD (right). The measured noise in the present setup is larger than expected considering the Johnson noise of R_{load} (red), the Johnson noise of R_{bol} (blue) and the contributions from the front-end amplifier (JFET, green). The black curve is the quadratic sum of all the contributions. ZnSe are noisier then the expected, in particular if operated over the invention point (IP) while the LDs noise is lower and quite uniform. Functions for the noise are detailed in [189].

0.1 Hz and 100 Hz) and high stability (about 1 ppm/$^\circ C$), which serve also as reference voltages for the front-end amplifier and the bias generator [193]. In this way the entire system is able to maintain a stability better than 10 ppm/$^\circ C$. The front-end and the Pulsers are housed in 19" 6U and 19" 3U standard racks respectively. A total of 66

channels are available, which are also used to read out diagnostic thermometers. Two Pulser boards (4 channels each) are used for stabilization, and one (two channels) is used for PI control. The entire system is remotely controlled by a PC through an optically coupled CAN bus.

3.8 DAQ system

The data acquisition (DAQ) system is based on commercial digitizer boards from National Instruments, NI-PXI628x. These boards feature 18-bit ADCs, configurable sampling frequency up to 500 kHz, configurable input range up to ± 10 V, digitization of up to 16 analog signals in differential input configuration. The DAQ boards are contained in a PXI chassis controlled remotely via computer. The data link between the DAQ chassis and computers is made through optical fiber connection providing a proper data transmission bandwidth and a complete electrical decoupling between the computers and the detectors. The calorimeter waveforms are digitized with sampling frequencies of 1 kHz for ZnSe and 2 kHz for the light detectors. The complete data stream is transferred from the PXI chassis to the computers; triggers are implemented via software. This approach allows to implement arbitrarily complex signal detection algorithms, the only constraint being the computing resources. The CUPID-0 raw data consist in Root NTuples files containing the continuous data stream of all channels recorded by the DAQ at the proper sampling frequencies. Triggers are implemented via software and saved in a custom format based on the ROOT data analysis framework. Each event contains the waveform of the triggering calorimeter plus some ancillary information. The non event-based information is stored in a PostgreSQL database that is also accessed by the offline data analysis software. The data taking is arranged in runs, each run lasting about two days. Raw data are transferred from the DAQ computers to the permanent storage area at CNAF and LNGS. A full copy of data is preserved also on tape.

3.9 Detector operation

After four months dedicated to the optimization and debugging of the cryogenic apparatus, the detector was cooled down in February 2017 and the first operation to be performed was the evaluation of the detector temperatures. This consists in measuring the resistance of the Ge-NTD sensors on all the detectors. According to the sensor design we are expecting a base resistance (R_{base}) of hundreds of MΩ on the ZnSe and one at least order of magnitude larger values for the LD, given the reduced sensor mass. The spread in the distribution of the base temperature provides information on the uniformity of the absorber properties, namely the heat capacity of the system: ZnSe + Ge-NTD. This discrepancy can be stressed if looking at the distribution of the working resistance (R_{work}) of the detectors, the value of the resistance (or temperature) once the operational condition of the detector are set.

In Fig. 3.39, the distributions for the R_{work} for the ZnSe and LD are shown. The distribution of the LD confirms that the production of such detectors is highly reproducible

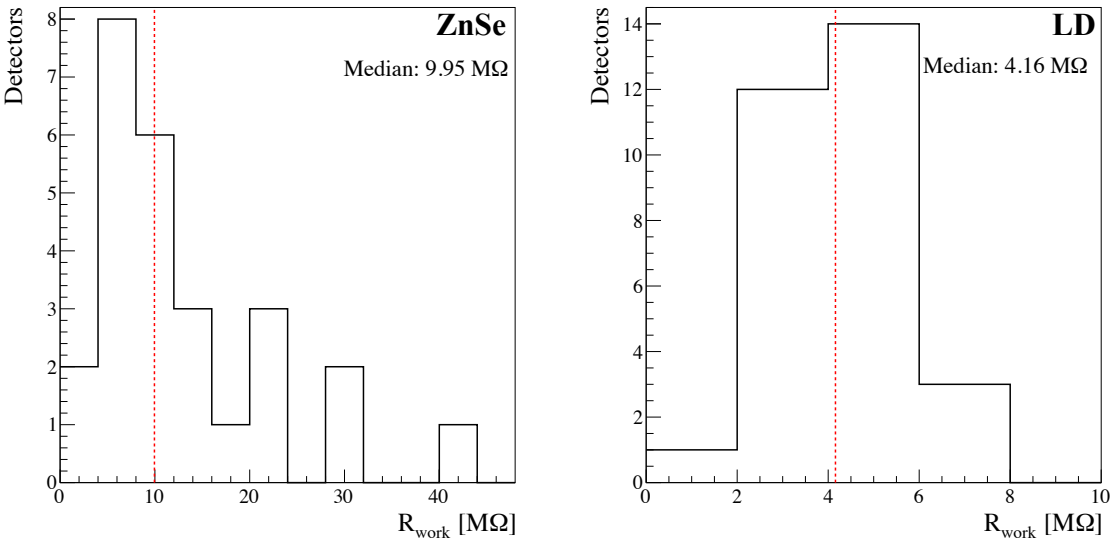

Figure 3.39: Distribution of the Ge-NTD sensor resistances for ZnSe (left) and LD (right) at the operating conditions, once the biasing voltage of the thermistor is set.

and there is a robust control of the critical aspect for the detector production. For the ZnSe, on the other hand the spread of the distribution is large and this is due to two different aspects: the first is because the crystal have different masses, hence different heat capacities, and the second because there is limited control of the ferromagnetic impurities inside the absorber. The first point is corroborated by looking at the high value outliers which are the crystals with the smaller masses, and the second by the fact that the other crystals which have similar masses have a rather large spread of R_{work}. A bias scan is performed in order to evaluate the best operating condition of each detector, this was done varying the biasing voltage of each detector and evaluating the best signal-to-noise ratio for each configuration. Fig. 3.40, shows how the signal amplitude varies as a function of the detector biasing voltage for a ZnSe detector. The signals in the detectors are generated by a Si resistor coupled to the crystal operated as Joule heater. This chip is coupled to the crystal with a procedure similar to the one adopted for Ge-NTDs.

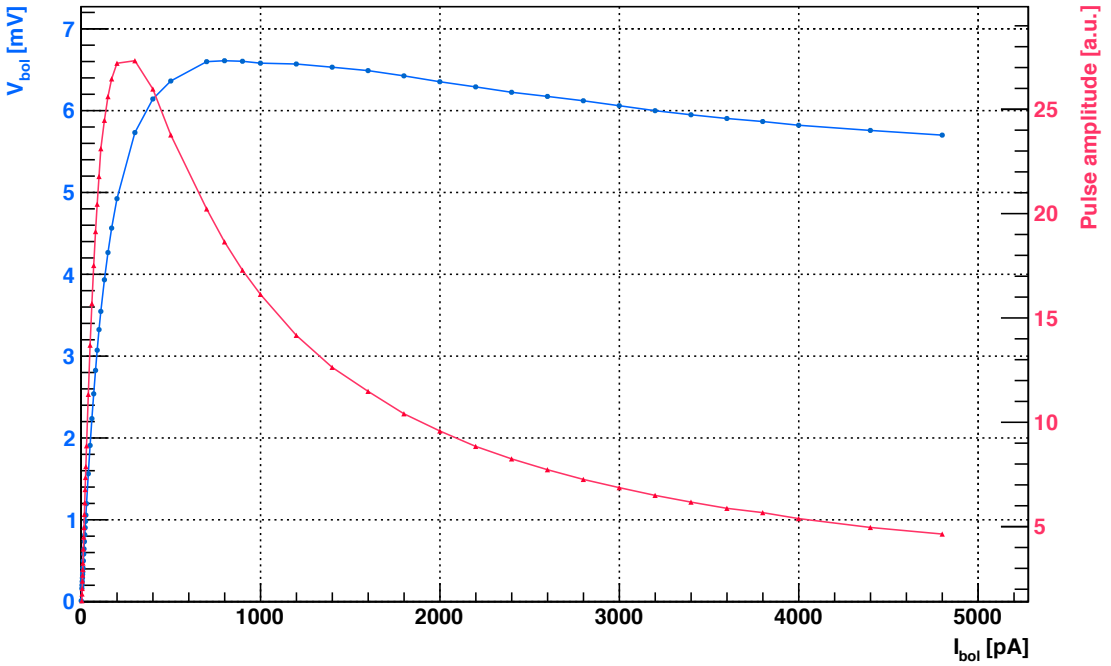

Figure 3.40: Characteristic load curve of a CUPID-0 ZnSe crystal operated with a Ge-NTD thermal sensor. The figure shows how varying the detector biasing voltage acts on the signal amplitude (red) and the voltage drop in the sensor (blue).

In order to better estimate the best operating conditions of the detectors the signal-to-noise ratio is the key parameter to be optimized. In fact, also the noise amplitude has to be taken into account, especially the parallel Johnson noise that develops across the resistances of the biasing circuit, which becomes more relevant at high value of the Ge-NTD resistance, hence lower temperature. A compromise between low noise condition - higher temperature - and large signal amplitudes - lower temperature - must be established. A reference pulse (i.e. heater pulse) is generated on each detector dissipating the same amount of energy through the Si resistors. While varying the biasing voltage it is monitored how the amplitude of the reference signal varies and how the detector noise changes. In Fig. 3.41 the signal-to-noise ratio for a set of measurements at different detector operating bias for ZnSe and LD's is reported. The signal amplitudes are estimated filtering the acquired pulses by means of the Optimum Filter technique [195]. Summarizing, for each detector load curves measurements are performed for evaluating the configurations that maximize the signal amplitudes, see Fig. 3.40. Then, a narrower scan in proximity of these defined working operation is carried out, aiming at defining the best signal-to-noise ratio for each detector, see Fig. 3.41.

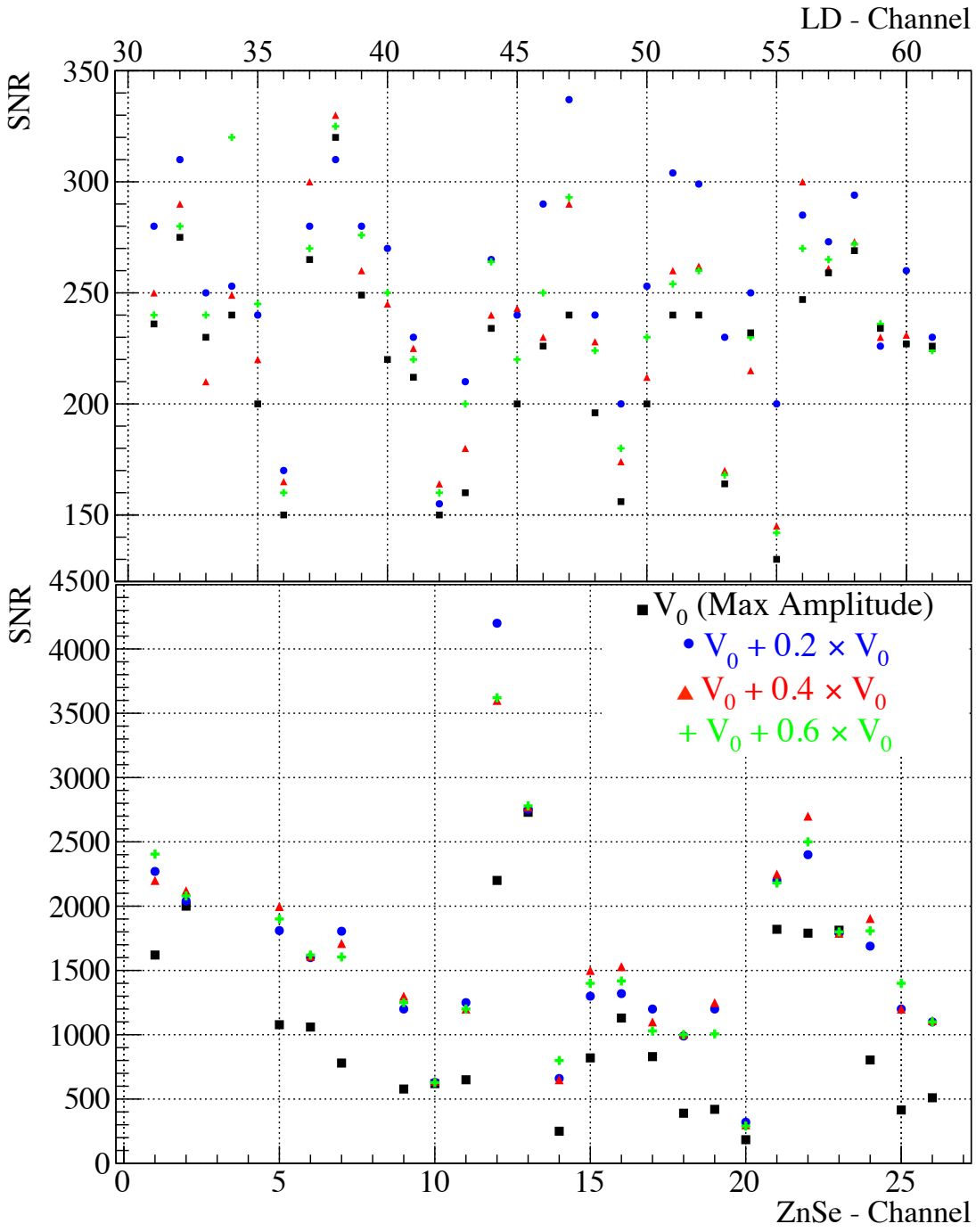

Figure 3.41: Signal-to-noise ratio (SNR) scan for LDs (top) and ZnSe crystals (bottom) varying the voltage bias. It is calculated as the ratio of the filtered pulser amplitude to the $\sigma_{baseline}$. V_0(Max Amplitude) represents the biasing voltage which gives the maximal pulse amplitude. The scan is performed at bias higher than V_0(Max Amplitude) because we expect a stronger reduction of the noise compared to the signal amplitude.

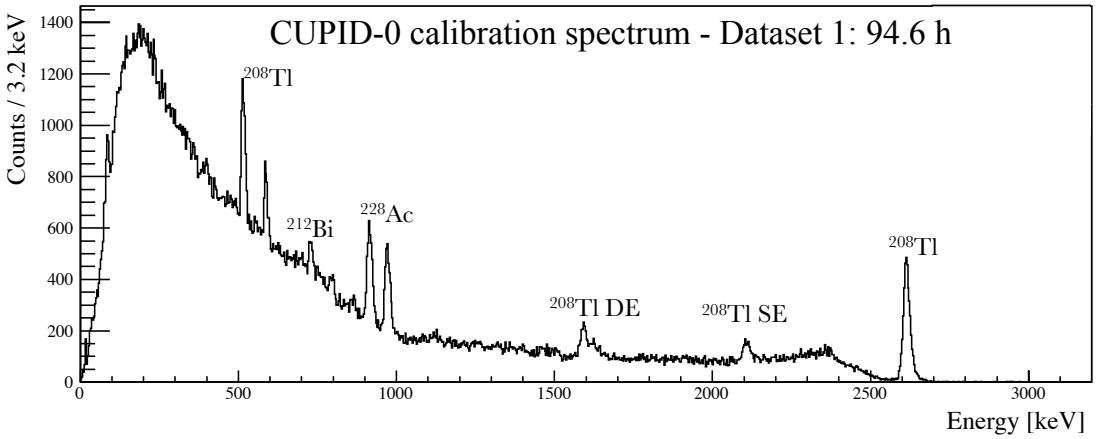

Figure 3.42: ^{232}Th calibration spectrum collected over 94.6 hours during the Dataset 1, only enriched detectors are considered. Calibration peaks due to ^{208}Tl and ^{228}Ac are labeled; ^{212}Bi peak, single and double escape (SE, DE) are not used for the detector calibration.

3.10 Detector performance

The overall detector performance are benchmarked by means of a ^{232}Th calibration source deployed next to the detector. Global calibration spectrum of CUPID-0 is reported in Fig. 3.42. This is used to calibrate the energy response of the detector and to evaluate the detector energy resolution at the ROI but also at 0 keV (i.e. $\sigma_{baseline}$). Unfortunately, only ZnSe crystals are calibrated and not the LD's, due to their low mass. The best method to calibrate such small devices would be to place a permanent X-ray source on the detector, as it was already done in [157]. In CUPID-0 there are not permanent sources on the detector because of the ultra-low background condition in which the measurement is carried out.

In Fig. 3.43, shows the distribution of the detector FHWM resolutions for the ZnSe detectors at 0 keV (FWHM$_{baseline}$) and at 2.6 MeV (FWHM$_{2615}$), the high energy and high intensity γ-line produced by the ^{232}Th source.

The detector FWHM$_{baseline}$ ranges from 0.96 keV and 6.1 keV (only 22 working enriched ZnSe are considered) with a median value is <FWHM$_{baseline}$ > = 3.47 keV, compatible with the values obtained by CUORE-0 detector operated in the same infrastructure [194]. It is worth recalling that CUORE-0 had a mass of about 40 kg (4 times the one of CUPID-0, without considered the copper holder), which provided a self-attenuation of the vibrations while in CUPID-0 this effect is given by the new double stage dumping system. The detector FWHM energy resolution at 2.6 MeV, which is considered as a preliminary proxy of detector response, shows a median value of 21.5 keV, ranging from 14 keV and 35 keV. The spread in the energy resolution is driven by the limited crystal quality, in fact while an ideal bolometer is supposed to be a crystal with a single-crystalline structure, the ZnSe used in CUPID-0 have polycrystalline structures. This characteristic strongly affects the thermalization of phonons inside the

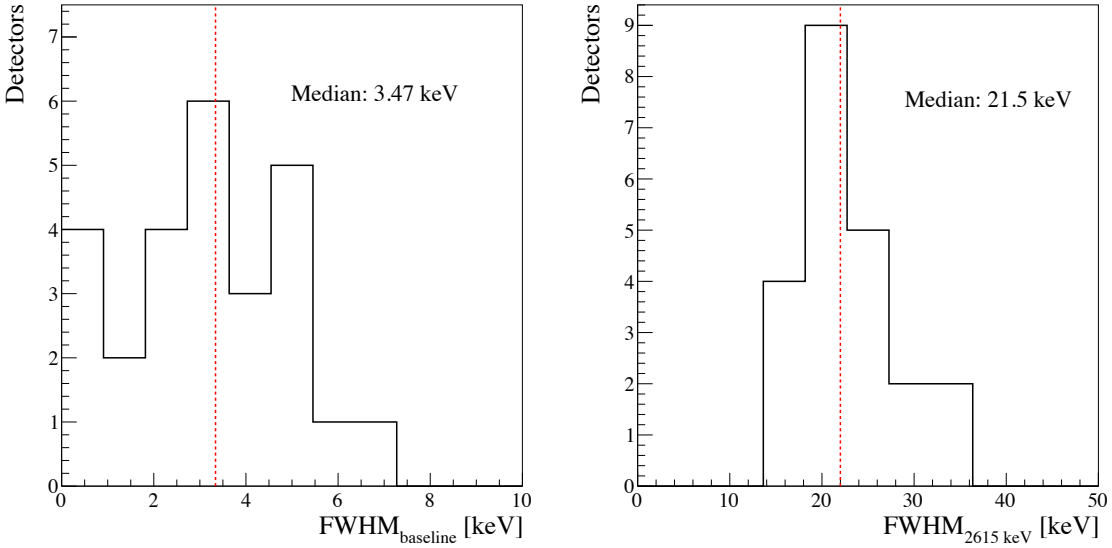

Figure 3.43: Distribution of the ZnSe energy resolutions. On the left is shown the FHWM resolution at 0 keV, which is defined as the detector baseline noise. On the right the distribution for the 2615 keV γ-line energy response is shown.

crystal, hence the detector response function. It is worth underlining the fact that there are still effective rooms for improving the detector energy resolutions, and the most important ones consists in taking advantage of the heat-light correlation in ZnSe crystals and a more affective response model. By exploiting the de-correlation of heat and light signals one can improve the detector energy resolution by a 25% as already demonstrated in [156], even if in CUPID-0 detectors the correlation seems to be less evident then the one observed in the past. A major improvement can come out using a different function to model the response of our detector, since the line-shape of the calibration peaks shows a pronounced non-gaussianity (see Sec. 4.2).

In Fig. 3.44, the distribution of the signal amplitudes for the $Zn^{82}Se$ crystals is reported. The median value of the distribution is 59.3 μV/MeV, which is a value comparable with other large mass bolometers like $^{nat}TeO_2$ [138].

Concerning the light detectors, this is the first time that a such large number (i.e. 31) of LDs is operated. Their performance were never probed in such a large scale. Due to the lack of a calibration source for the LDs, their performances are investigated by means of the pulses generated by Si resistor coupled to the absorber. The energy dissipated on each detector is the same within an error of few ‰ and the energy scale is comparable to the scintillation light signal induced by the ZnSe crystals. In Fig. 3.44, the distribution of the signal-to-noise ratio of the heater pulses recorded on each LD is shown. The detector performance are extremely good and these are demonstrated by the narrow distribution which has a spread of 43 and a median value of 138.

Finally in Tab. 3.45, the overall operating and performance parameters of the detectors are shown. The rise-time and the decay time are computed as the time interval

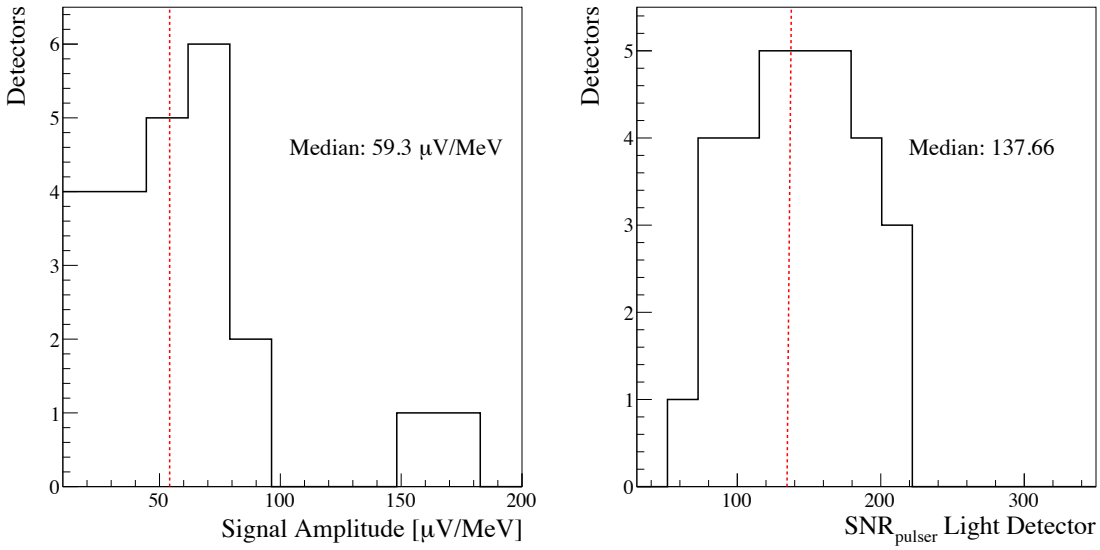

Figure 3.44: Performance of the CUIPD-0 single detectors. **Left.** Distribution of the ZnSe absolute signal amplitudes. **Right.** Distribution of the LD SNRs.The signal amplitude is evaluated on test pulses generated by Si resistor coupled to each LD. The amount of dissipated energy is the same for each detector.

between the 10% and 90% of the leading edge of the pulse amplitude and as the 90% and 30% of the trailing part of the pulse amplitude, respectively. Furthermore the noise amplitude are evaluated at 5 Hz which is within the signal bandwidth. This shows that the detector resolution is limited not by the electronics noise (see Sec. 3.7), but by the detector theirselves. As already anticipated in Sec. 3.3 the crystals CG-28 and CG-29 are not performing from the bolometric point of view: signal amplitude cannot be assigned the these detector being impossible identify any peaks in the detector, also exploiting monochromatic calibration source (i.e. ^{40}K). For this reason they are not considered in analysis.

It is worth to underline that the energy calibration of the LD it is not needed in order to perform the particle identification and rejection, because this is carried out on the relative signal amplitude. Moreover, in Tab. 3.45 given the reproducibility of the LD performance we only show the median value for the different parameters.

Table 3.45: Summary of the main operating parameters of the CUPID-0 detectors. For the LDs only the median values are reported, given the small spread in the performance. Three detectors (Channel ID 3, 4, 8) have a reduced signal amplitude which prevented us from evaluating the detector energy resolution.

Channel ID	Name	Tower	Type	Mass [g]	R_{base} [MΩ]	R_{work} [MΩ]	Noise@5Hz [nV/$\sqrt{Hz}$]	Signal Amplitude [μV/MeV]	Rise time [ms]	Decay time [ms]	$FWHM_{baseline}$ [keV]	$FWHM_{2615}$ [keV]
1	CG-01	1	Enriched	439.40	10	4.17	11.7	40	10.1	24.7	2.59	21
2	CG-13	1	Enriched	427.86	54	14.71	25.7	81	12.0	37.6	2.58	35
3	CG-28	1	Enriched	427.00	29	9.63	18.1	-	9.5	17.3	-	-
4	NAT-1	1	Natural	418.39	34	11.28	26.3	-	5.5	20.7	-	-
5	CG-26	1	Enriched	408.22	7	3.94	20.9	51	11.1	33.1	3.22	19
6	CG-02	2	Enriched	441.29	16	4.90	19.3	46	9.3	23.6	3.86	22
7	CG-15	2	Enriched	469.64	25	11.25	17.2	47	12.6	26.2	2.88	20
8	CG-29	2	Enriched	480.90	23	6.42	17.7	-	8.5	13.7	-	-
9	CG-14	2	Enriched	470.59	27	9.56	26.5	66	10.3	21.5	3.57	20
10	CG-16	2	Enriched	260.52	2	1.22	10.1	13	9.2	26.4	6.09	19
11	CG-03	3	Enriched	438.65	11	4.34	13.7	23	10.3	27.4	4.84	22
12	CG-20	3	Enriched	214.62	14	6.42	21.0	179	18.1	48.3	0.96	15
13	CG-23	3	Enriched	174.89	33	9.85	25.7	156	12.0	34.2	1.47	14
14	Xtra-4	3	Enriched	409.88	63	12.69	23.6	26	11.5	26.7	6.85	25
15	CG-18	3	Enriched	410.31	77	18.13	29.0	57	14.5	33.3	3.17	24
16	CG-22	3	Enriched	418.92	65	21.26	50.7	68	15.1	47.5	3.84	18
17	CG-04	4	Enriched	442.32	150	30.78	46.1	69	15.8	40.4	4.10	25
18	Xtra-2	4	Enriched	442.43	101	23.63	62.9	73	14.4	35.7	5.05	25
19	CG-17	4	Enriched	474.22	73	20.76	32.1	36	14.0	36.6	5.11	29
20	NAT-2	4	Natural	431.21	216	41.40	63.7	38	15.9	32.9	8.41	38
21	CG-21	4	Enriched	233.08	23	10.06	27.2	61	14.6	58.1	2.40	20
22	CG-10	5	Enriched	440.47	14	6.91	17.2	68	14.4	39.3	1.94	19
23	CG-08	5	Enriched	431.00	79	28.19	53.2	84	18.1	44.0	3.36	17
24	CG-24	5	Enriched	429.62	42	14.33	26.7	62	11.9	26.1	3.06	29
25	CG-25	5	Enriched	434.51	14	5.32	18.3	35	9.7	20.5	4.84	26
26	CG-27	5	Enriched	431.18	11	5.77	13.7	21	10.6	26.8	5.36	25
ZnSe Median					28	9.95	24.6	59.3	13.5	35.7	3.47	22
LD Median					6.1	4.16	6.5	-	3.5	7.1	-	-

Chapter 4

Data analysis methods used for CUPID-0

The CUPID-0 raw-data consist of voltage measurements on the thermistor of each individual calorimeter, digitized and sampled every 1 ms (0.5 ms for the light detectors). The data are collected using a custom designed DAQ software package, called Apollo, which was used in CUORE-0 and currently is used for CUORE. It reads data from ADC (analog to digital converter) and stores them in data buffer, than it looks for triggers and sets flags in data buffer. Finally it reads data from shared memory and dumps them to file. The derivative trigger parameters are set individually for each calorimeter according to the signal amplitude and the noise level. For each trigger, a time-flag to identify the event is recorded. Each event on the ZnSe contains 5000 (1000 for the LDs) samples encompassing the 5 (0.5) second window, 1 (0.1) second (i.e pre-trigger) before to 4 (0.4) seconds after the trigger fired. Additionally, the channel number, trigger time, and a unique event number are saved for each event.

The CUPID-0 data are organized into *runs*, each lasting approximately two days, which are further grouped into *datasets*, each lasting approximately one month. A dataset is an ensemble of runs which have the same calibration. Ideally, a dataset consists of one or more initial **calibration runs**, followed by a series of **physics runs (background)**, followed by one or more final calibration run to cross check the stability. The final calibration of one dataset is used also as the initial calibration of the next one; therefore, calibration runs belong always to two datasets.

The raw data are processed to compute quantities such as energy, pulse shape parameters, and coincidence information for each event. A custom C++ based analysis software called Diana and developed within the CUORE collaboration is used for data processing in CUPID-0. Further features to handle the additional light signal were developed during the long R&D phase on scintillating calorimeters (i.e LUCIFER) and implemented in the CUORE software for CUPID. The Diana framework provides a standardized event class and data storage format, as well as a system for running analysis code in a modular fashion controlled by plain-text configuration files. Indeed Diana is

organized in sequences, each consisting in a packages of modules that scan the events in the ROOT files sequentially, evaluate some relevant quantities and store them back in the events.

Once the data-taking has started I have become member of the analysis team (5 people). As a first analysis shifter I defined the signal processing protocol reported in Sec. 4.1, establishing also a set of analysis tools to check the data quality. Then I have taken care of pulse shape analysis detailed in Sec. 4.4, fundamental step for the data selection discussed in Sec. 4.5.

4.1 Data Processing

The first-level data processing takes the data from a series of triggered waveforms to a calibrated energy spectrum. The data processing procedure for CUPID-0 follows that of CUORE-0, outlined in [133], but with several options newly developed for the scintillating calorimeters within LUCIFER and CUPID R&D.

In order to estimate the energy of each event i, the time-waveform $V_i(t)$ of each calorimeter is modeled as the sum of a known detector response function $S_i(t)$ and an unknown additive noise term $N_i(t)$,

$$V_i(t) = B_i \cdot S_i(t) + N_i(t), \tag{4.1}$$

where B_i is the amplitude of the signal response. $S_i(t)$ is usually approximated with the *average pulse* obtained averaging a selected sample of signal pulses (detailed description in the following). The amplitude B_i can be decomposed as

$$B_i = G_i(T) \cdot A_i(E), \tag{4.2}$$

where the amplitude $A_i(E)$ depends only on the energy deposited into the calorimeter E, and $G_i(T)$ is a bolometric gain which depends on the operating temperature T of the calorimeter.

The first-level data processing performs the following steps on each triggered waveform in order to extract the deposited energy of the event:

1. produce the basic parameters of the waveform (*Preprocess*);
2. measure the amplitude of the signal B_i while minimizing the effect of the noise term in order to maximize the detector energy resolution (*Amplitude Evaluation*);
3. stabilize the temperature-dependent gain term $G_i(T)$ against temperature drifts of the detector (*Thermal Gain Stabilization*);
4. determine an energy calibration that models the form of $A_i(E)$, allowing us to extract the energy for each event (*Energy Calibration*);
5. offline trigger and synchronize the two light pulses associated to each main event in the ZnSe crystal (*Side-pulses Production and Processing*).

1. Preprocess: In this stage Diana first measures the value of the baseline, averaging the pre-trigger samples (i.e. the 1 s region before the trigger). The software evaluates also the slope and the RMS of the pre-trigger data to determine the detector behavior before the event occurs. Then, it counts the number of pulses in the event: after differentiating the pulse and determining the RMS of the derivative, each local maximum in the differentiated waveform is counted as a pulse if the value exceeds 5 times the RMS. Finally other basic parameters of the pulse are calculated (e.g. *MaxBaseline* as the difference among the maximum of the pulse in the window and the baseline).

2. Amplitude Evaluation: Since the $V_i(t)$ involves both the signal and the stochastic noise, the above defined *MaxBaseline* would not provide an optimal estimate of the pulse amplitude. In turn, this would not give the best achievable energy resolution. Therefore, the *Optimum Filter* (OF) technique [195] is used for the analysis of CUPID data.

The underlying idea of the OF is to build a filter that, when applied to the raw-pulse, produces a pulse with the maximized signal to noise ratio. The filtered pulse is then used to evaluate the signal amplitude. In the frequency domain, the OF transfer function $H(\omega)$ is given by

$$H(\omega) = K \frac{S^*(\omega)}{N(\omega)} \mathrm{e}^{-\mathrm{j}\,\omega\, t_{\max}} \tag{4.3}$$

where $S(\omega)$ is the Fourier transform of the average pulse, which represents the response of the system to an energy deposition, $N(\omega)$ is the noise power spectrum (PS), while $t_{\max}$ is the delay of a given pulse with respect to the reference one. An appropriate normalization factor K is needed to obtain the correct event energy.

The role of the OF is to weight the frequency components of the signal in order to suppress those frequencies that are more affected by the noise. As it can be seen from Eq. (4.3), the waveform filtering requires the knowledge of both the reference pulse and the noise PS $N(\omega)$.

For each detector, the average pulses are built by selecting β/γ events in the energy region from 1800 keV and 2700 keV in the calibration runs. The averaging process consists of two steps: the alignment of the pulses and the actual averaging. Diana measures the peak position (in time) of each pulse. This is determined by differentiating the pulse and interpolating where the derivative crosses from positive to negative. Then, all the pulses are aligned so that the maxima occur at the same time. After the alignment, the pulses are linearly averaged together.

The noise PS is obtained by acquiring many detector baselines in the absence of thermal pulses and averaging the corresponding square modulus of the Fourier transform (Wiener-Khinchin theorem). In fact, apart from triggered events, the DAQ software also collects random triggers intended to be stochastic noise samples. These triggers are fired at evenly spaced intervals of 200 s.

In Fig. 4.1, an example of average pulses (left panel) and noise PS (right panels) before and after the filtering process are shown both for a ZnSe (top panels) and a light detector (bottom panel).

Once filtered, the amplitude of each pulse is determined by interpolating the three

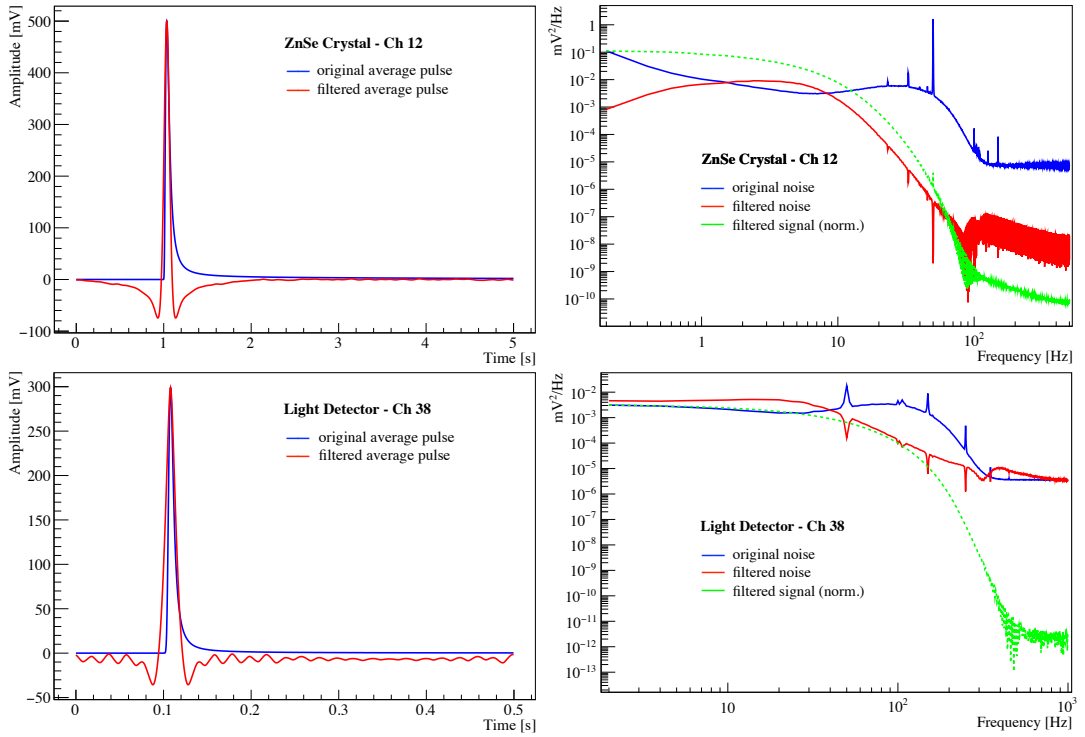

Figure 4.1: Example of average pulses (left) and noise PS (right) before and after the filtering with the OF for a ZnSe (top panels) and a light detector (bottom panels). The peaks in the in the noise spectra are due to the vibrations of the readout wires (i.e. microphonic noise).

data points around the peak of the filtered pulse and evaluating the maximum of that parabola, in order to reduce rounding errors. The amplitude is defined as the global maximum of the parabola, and the time of the peak position as the time of this maximum.

3. Thermal Gain Stabilization: The thermal gain stabilization (TGS) compensates slow variation in the gain of the calorimeters $G_i(T)$ due to drifts of the operating temperature of the detector. The TGS technique is the same used for Cuoricino, CUORE-0 and CUORE and it is described in [196]. This approach uses the heater attached to each calorimeter to inject fixed-energy heater pulses every 300 s during each run. The Joule heating in the chip heats the crystal, simulating a particle event. Since the energy of the heater pulse is constant, any variation in its measured amplitude B_i^{ref} is due to a change in the bolometric gain $G_i(T)$.

The value of the baseline, obtained averaging the 1 s pre-trigger samples of each pulses, is used as a proxy for the calorimeter temperature at the time of the event. By regressing the reference amplitude B_i^{ref} as a function of the baseline value, one can determine $G_i(T)$ (up to a multiplicative constant that can be folded into $A_i(E)$). Once this relationship is known for each channel, the amplitude of all the pulses is corrected accordingly.

4. Energy Calibration: For each dataset, the energy response of each calorimeter

$A_i(E)$ is calibrated using the reconstructed positions of at least four of the seven strongest γ-lines of the ^{232}Th decay chain in the calibration runs. This consists of fitting each peak using a Gaussian line-shape and performing a fit on the expected energies of the calibration peaks against their reconstructed positions using a second-order polynomial with zero intercept.

The same procedure is exploited to calibrate the α-events, using a Gaussian line-shape for each α-peak due to the internal contaminations (see Sec. 5.2) and performing a second order polynomial fit on the obtained mean values. The correct low-energy extrapolation of this calibration is verified by checking the peak position of the natural occurring ^{147}Sm (nominal energy 2310.5 keV), that is a common contaminant of ZnSe crystals. The energy calibrated in this way is labeled with E_α in the following.

5. Light pulses triggering and processing: For each pulse triggered by a ZnSe detector, two waveforms are sampled offline in the continuum data-stream of the associated light detectors. The same procedure described above is applied to process these data. However the amplitude of the light signal is estimated from the value of the filtered waveform at a fixed time delay with respect to the signal in the heat calorimeter, as explained in [197]. The time delay among heat and light can be considered a feature of the detector setup (depended mainly on the rise time of light and heat detectors), so that it is calculated at high energy (i.e. 1800- 2700 keV) and applied to each waveform. Furthermore the light detectors are too thin to absorb high energy γs emitted by the ^{232}Th, thus they are not calibrated; just a re-scaling of the light signal amplitude is performed to set the light yield of the β/γ to 1, making the response of the different detectors uniform.

4.2 Detector energy response

The energy calibration described in Sec. 4.1 exploit a Gaussian line-shape to find the mean amplitude of the pulses induced by γs of the calibration source. This procedure allows for a very effective energy calibration, nevertheless the Gaussian line-shape does not provide a perfect fit to the reconstructed peak shape, as depicted in Fig. 4.2, where the ^{208}Tl line at 2615 keV is fitted as an example exploiting the function:

$$f_i(E; N^{sign}, \mu^i, \sigma^i, a) \equiv \text{Gauss}(E; N^{sign}, \mu^i, \sigma^i) + \text{Exp}(E; a). \tag{4.4}$$

This model seems to be unable to reproduce the peak line-shape, especially the right tail. Also the exponential decay does not allow for a good description of the background, that seems to be quite constant on the left flank and absent in the right one.

Several checks are performed to understand the nature of this non-Gaussian behavior, excluding every kind of bias introduced in the signal processing as detector miscalibration. The presence of this substructure is unaffected by the choice of pulse filtering technique or TGS algorithm and it is present on all channels. It is not clustered in time or a result of pile-up of events. A detailed shape inspection of pulses selected from the primary and secondary peaks reveals no obvious difference in the pulse shape. Also the

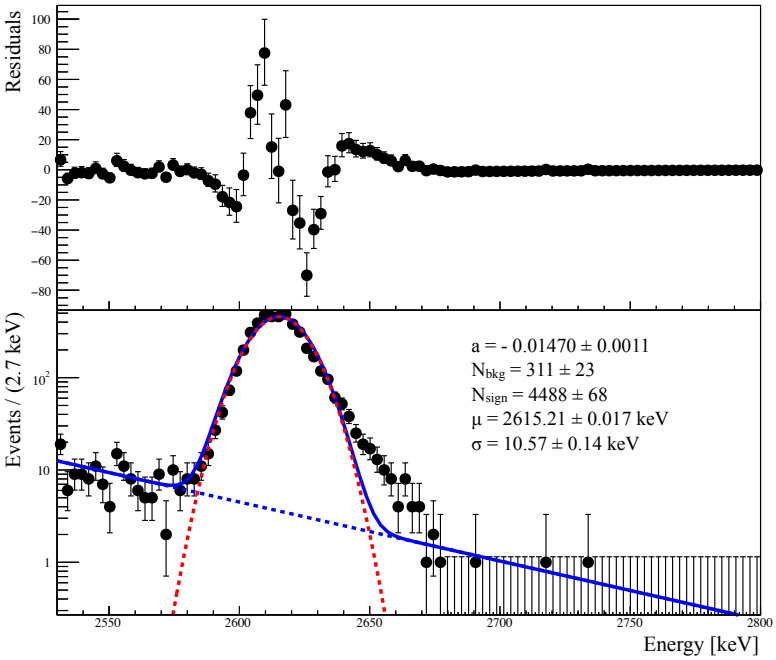

Figure 4.2: Fit of the 2615 keV γ-line of ^{208}Tl obtained using the single-Gaussian model plus an exponential decaying background. Data are from the calibrations runs of the first dataset and include all enriched ZnSe channels.

Cuoricino data shows a hint of an asymmetric line shape and the improved resolution of the CUORE-0 detector has made this effect clear [133].

Ultimately, the energy detector response is modeled using the functional form:

$$\rho(E;\mu_1,\sigma_1,\eta,\delta,\lambda) \equiv \eta \cdot \text{Gauss}(E;\mu_1,\sigma_1) + (1-\eta) \cdot \text{Gauss}(E;\delta\cdot\mu_1,\lambda\cdot\sigma_1). \quad (4.5)$$

For each calibration peak this function produces a primary Gaussian centered at μ_1^i with resolution σ_1^i and a secondary Gaussian at a slightly higher energy $\delta\cdot\mu_1$ with resolution $\lambda\cdot\sigma_1$. Given that double-Gaussian is not needed to fit the α-peaks (see Fig. 5.3), it could be a good indication that the broadening of the γ spectrum (and the requirement to use double-Gaussian response function) is due to differences in heat capacity or phonon propagation/collection in different parts of the ZnSe crystal. Since α-particles have shorter ranges compare to γs, most of the energies for α-events are deposited locally (while multiple Compton scattering are possible for γs). This possible origin of the smaller secondary Gaussian will be investigated using different Si-resistor (i.e. heaters) glued in different positions on the crystal surface and comparing the resolution at the same energy.

The best-fit detector response for each dataset is estimated by fitting the intense ^{208}Tl 2615 keV calibration peak. This fit is over the range 2530–2730 keV and includes two more elements to describe the underlying background: a smeared step function, modeled as an Erfc function, to model γ-rays that scatter in the shields before interacting with a

crystal or scatter multiple times in a single detector before exiting and a flat background. The final model obtained is:

$$f^{\mathrm{Tl}}(E) = N^{\mathrm{Tl}}\rho(E;\mu_1,\sigma_1,\mu_2,\sigma_2,\eta) + r_{\mathrm{Scatter}}N^{\mathrm{Tl}}\mathrm{Erfc}\left(\frac{E-\mu_1}{\sqrt{2}\sigma}\right) + b^{\mathrm{flat}} \tag{4.6}$$

where N_i^{Tl} represents a detector dependent ^{208}Tl number of signal counts, which is a free parameter in the fit. The event rate of the scattered γ-rays is given as fractions of the peak event rate, r_{Scatter}, left unconstrained in the fit. The final parameter b^{flat} is a global flat background rate, also unconstrained.

A simultaneous Unbinned Extended Maximum Likelihood (UEML) fit of the ^{208}Tl line (summed over all the detectors) is performed to each dataset using the RooFit fitting package [198], thus allowing for setting the value of the parameters η, δ and λ. It is calculated once (in each dataset) using the ^{208}Tl line and used to fit the other calibration peaks (results in Tab. 4.5) and in the ROI fit. Fig. 4.3 shows the resulting best-fit model to the summed calibration data for all detectors of a single dataset. A strong corroboration of the model goodness is given by the fact that the values obtained for μ_1, μ_2, σ_1,σ_2 are almost constant over all the datasets, as reported in Tab. 4.4.

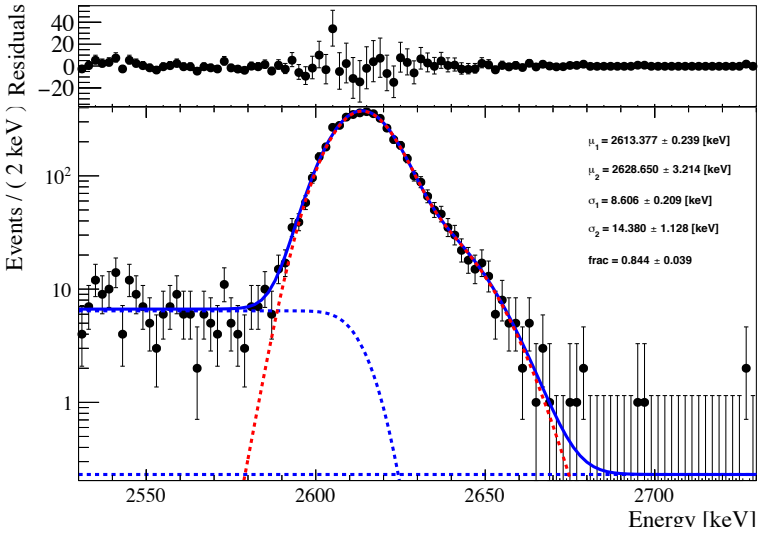

Figure 4.3: Best-fit model to the ^{208}Tl calibration peak for all detectors of a single dataset. The solid line shows the full summed model, and the dashed lines show the individual components: the sum of the primary and secondary peaks of the detector response (red); the smeared step-function and a flat background (blue).

4.2.1 Extrapolation at $Q_{\beta\beta}$

The CUPID-0 target is to exploit in the near future a ^{56}Co calibration source, whose γ-lines at 2598.5 keV (B.R. 17.28 %), 3009.6 (B.R. 1%) and 3253.4 (B.R. 7.93%) will provides a perfect calibration tool nearby the region of interest. The information obtained

Table 4.4: Results of the fit of the 2615 keV peak in different datasets. The last column reports the percentage variation of the parameter.

Parameter	Dataset 1 [keV]	Dataset 2 [keV]	Dataset 3 [keV]	Dataset 4 [keV]	[%]
μ_1	2613.9 ± 0.2	2613.0 ± 0.2	2612.7 ± 0.2	2613.4 ± 0.2	<1
μ_2	2629.6 ± 2.3	2627.85 ± 2.1	2626.2 ± 2.5	2628.7 ± 3.2	<1
σ_1	8.8 ± 0.2	8.7 ± 0.2	8.5 ± 0.2	8.6 ± 0.2	∼ 2.7
σ_2	16.8 ± 0.8	16.2 ± 0.7	14.8 ± 0.8	14.4 ± 1.1	∼ 13
η (frac)	0.845 ± 0.025	0.841 ± 0.03	0.818 ± 0.039	0.844 ± 0.039	∼ 4

from a ^{56}Co calibration will be used also to test the consistency of the results discussed in this thesis, since the resolution at $Q_{\beta\beta}$ can be only extrapolated at the current stage.

For this purpose each calibration peak in the energy spectrum is fitted with the model in Eq. 4.5, considering the parameters that characterize the detector response at 2615 keV (η, δ and λ), as fixed. Each fit also includes a background model that is either a 1st or 2nd-degree polynomial. The resolution of the most prominent Gaussian is taken as estimator of the energy resolution at the energy of the considered peak, the resulting value for a selected dataset a reported in Tab. 4.5. The extrapolation of the energy resolution at the $Q_{\beta\beta}$ was performed with the following functions,

$$\Delta E = E_0 + aE, \tag{4.7}$$

$$\Delta E = E_0 + aE + bE^2, \tag{4.8}$$

$$\Delta E = \sqrt{E_0^2 + aE^b}, \tag{4.9}$$

$$\frac{\Delta E}{E} = a + \frac{b}{\sqrt{E}} + \frac{c}{E}. \tag{4.10}$$

Since the resulting fits, reported in Fig. 4.6, show a quite linear behavior and the energy resolution at $Q_{\beta\beta}$ obtained in the different fits are compatible, the function in Eq. 4.7 was chosen to extrapolate the energy resolution at $Q_{\beta\beta}$. The results for ΔE in the different dataset are reported in Tab. 4.7, where the final energy resolution is given by the following weighted sum:

$$FWHM = \frac{\sum_i FWHM_i \cdot M_i \cdot T_i}{\sum_i M_i \cdot T_i} \tag{4.11}$$

being $M_i \cdot T_i$ the exposure of the dataset i and FWHM$_i$ the resolution at $Q_{\beta\beta}$ extrapolated separately for each dataset i.

Table 4.5: Results of the double-Gaussian fit of the secondary calibration peaks. The function in Eq. 4.5 plus an exponential decaying background is used. The free parameters are μ_1 and σ_1 and the background decaying constant. Only the dominant peak is considered.

Peak [keV]	μ_1 [keV]	σ_1 [keV]
511	511.95 ± 0.14	3.45 ± 0.14
583	583.63 ± 0.21	3.40 ± 0.19
911	910.47± 0.13	4.35 ± 0.13
968	966.98 ± 0.17	5.24 ± 0.18
Double Escape	1586.16 ±0.47	6.57 ± 0.48
Single Escape	2014.9 ± 0.72	7.35 ± 0.70

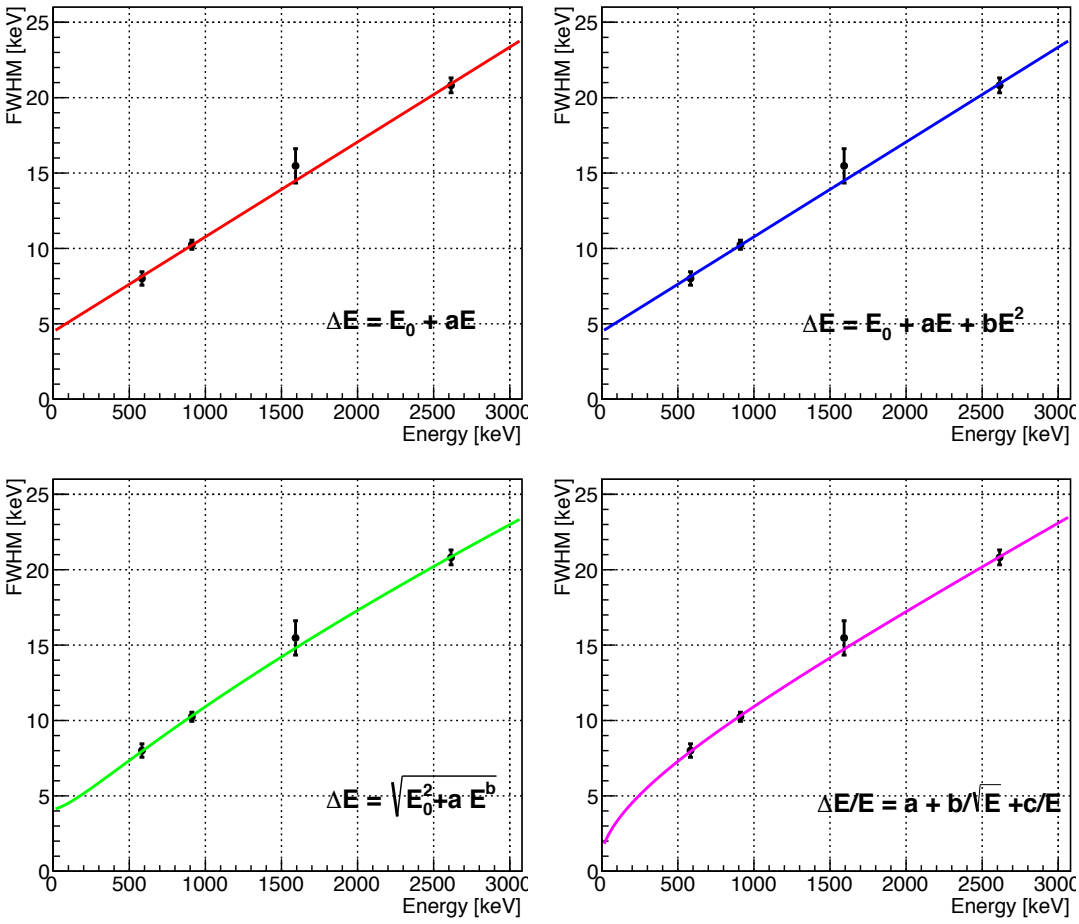

Figure 4.6: Comparison among different extrapolation functions to extend the energy resolution to the $Q_{\beta\beta}$ region.

Table 4.7: Extrapolated resolution at $Q_{\beta\beta}$ for all dataset obtained exploiting the function in Eq. 4.7.Only enriched crystals are considered.

Dataset	Exposure [kg · y]	FWHM$_i$ [keV]
1	0.606	23.05 ± 0.51
2	0.944	22.95 ± 0.53
3	0.817	22.64 ± 0.64
4	1.076	23.14 ± 0.59
Final	3.443	22.95 ± 0.57

4.3 Energy threshold

The energy threshold of each ZnSe channel is estimated through a dedicated multi-pulser run. In this measurement the heaters on the heat channels, usually biased with a fixed voltage to provide the stabilization pulse, are biased with five different voltages in turns to range the pulser energy within the 3 – 200 keV interval. In this way it is possible to study the energy threshold and the trigger efficiency as a function of the energy, being known the number of the injected pulses at a given energy.

The energy-dependent trigger efficiency $\epsilon(E)$ is modeled by the Gaussian cumulative density function:

$$\epsilon(E) = \frac{1}{2}\,\mathrm{erf}\left(\frac{E-\theta}{\sqrt{2}\sigma_{\mathrm{OF}}}\right) + \frac{1}{2}, \tag{4.12}$$

where σ_{OF} is the baseline noise resolution after the optimum filter and θ is the energy corresponding to a 50 % trigger efficiency. Fig 4.8 shows the threshold fit of a selected channel. Considering all the channels θ ranges from 17 keV to 164 keV, while σ_{OF} spans from 3 keV to 20 keV pointing out a good agreement (∼5%) with the value reported in Tab. 3.45. Nevertheless some of these numbers are affected by a huge uncertainty due to the few points sampled in step region. A second optimized multi-pulser run is already scheduled.

4.4 Pulse shape parameters

The goal of the pulse shape analysis is to remove spurious pulses, i.e. events that trigger the data acquisition, but are not due to a particle interaction in the calorimeter absorber (for example electronic spikes or events in the thermal sensor) and deformed pulses, which may be due to a particle interaction, but are degraded by noise or pileup such that the amplitude cannot be accurately evaluated.

For each triggered waveform the following shape parameters are calculated:

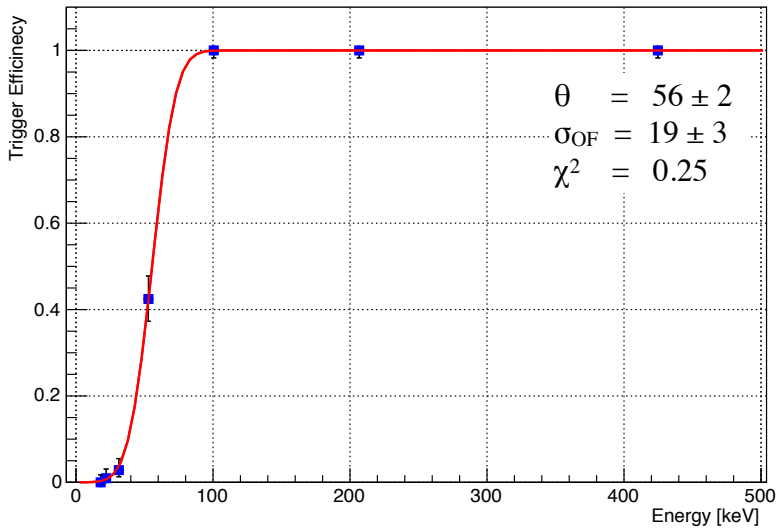

Figure 4.8: An example of the trigger efficiency obtained from Eq. 4.12 as a function of energy (line) and data obtained from low energy pulser measurements (square).

- **RiseTime** as the time span required for the output signal to rise from 10% to 90% level.
- **DecayTime** as the time span required for the output signal to drop from 90% to 30% level.
- **Delay** as the position of the maximum of the filtered pulse in the acquisition window.
- **BaselineSlope** as the slope of the linear fit of the baseline trend before the trigger fires (pre-trigger region).
- **TVR and TVL (Test Value Right/Left)** defined as

$$TVR = \frac{1}{Aw_r}\sqrt{\sum_{i=i_M}^{i_M+\omega_r}(y_i - A \cdot S_i)^2} \tag{4.13}$$

$$TVL = \frac{1}{Aw_l}\sqrt{\sum_{i=i_M}^{i_M-\omega_l}(y_i - A \cdot S_i)^2} \tag{4.14}$$

where y_i is the sampled pulse, A and i_M its amplitude and maximum position, S_i the average pulse scaled to unitary amplitude and aligned to y_i, w_r (w_l) the right (left) width at half maximum of S_i. The TVR and TVL are χ^2 test-variables that evaluate how similar the filtered pulse is to the average) pulse on the left and right side of the maximum, respectively. They are very sensitive parameters to compare the shape of the

single pulse with respect the shape of the average pulse (i.e. the response function of the calorimeter) before and after the maximum. All these parameters are calculated both for the heat pulse and the side light pulses of each triggered events. Cuts on the *heat shape* parameters are used to remove the non-physical events, while a cut on the light TVR are used to identify also the nature of the interacting particles (α, β/γ or high energy neutrons).

4.4.1 Shape parameters linearization and normalization

The pulse shape parameters of bolometric signals have in general an evident dependence on the energy of the event. It happens because the detector response is itself energy dependent. An high energy deposition in the absorber changes a bit the detector temperature, so the working point. In other word heating up the detector it becomes slightly slower. A further energy dependence is introduced by the optimum filter: since it is made with a fixed average pulse S_i, the small variation of the detector response with the energy is not taken into account.

For example the TVR and TVL introduced above are well described by a parabolic function with the minimum centered at the energy of the average pulse. In general, these variables can be used only to set an energy-dependent cuts, that would be very awkward for the cut optimization over a wide energy range. Furthermore the evaluation of their efficiency is a very difficult task, in particular if there are not visible peaks close to the ROI.

This problem can be avoided by removing the energy dependence of the shape parameters through a linearization and normalization algorithm, described in the following. In the first step the energy spectrum (channel by channel) is divided in slices, for each of them the median (μ) and the MAD (median average deviation, δ) of the considered shape parameter are calculated. The error on the median is taken as the MAD itself.On the contrary the uncertainty on the MAD is not easy to calculate and after several tests it was decided to set it constant and exploit a fit based on the Ordinary Least Squares method.

The values obtained for each slice are interpolated to get the functions μ(E) and δ(E) in the whole energy range. Fig. 4.9 shows the resulting fits for the TVL of a single channel. In the second step the normalized value $\bar{p_i}$ is associated to the event i as

$$\bar{p_i} = \frac{p_i - \mu(E_i)}{\delta(E_i)} \tag{4.15}$$

where p_i is the value of the parameter before the normalization, E_i is the energy of the event while μ(E) and δ(E) are the functions obtained in the first step. This procedure is applied to each shape parameter of the heat pulses. The effect of the TVL and TVR normalization are shown in Fig. 4.10. It allows to set cuts corresponding to a given confidence level. A dedicated AmBe calibration source is periodically deployed close to the CUPID-0 cryostat to provide a set of data with the γ-band populated up to 4 MeV, useful to study the detector behavior and in particular to perform the first shape parameters normalization.

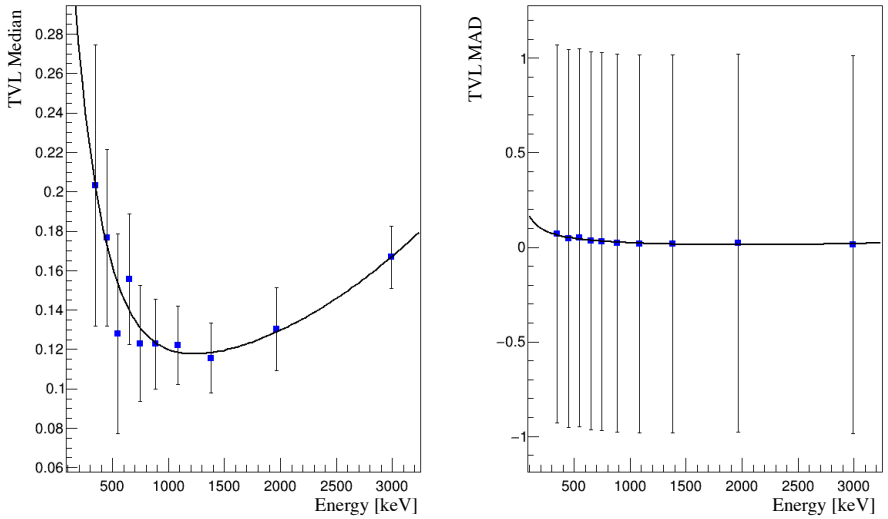

Figure 4.9: Fit of the median (left) and the median average deviation (MAD, right) of the shape parameter Test Value Left (TVL, analytically defined in Eq. 4.14) of a selected channel. The blue point are the values obtained in the different slices of the energy spectrum.

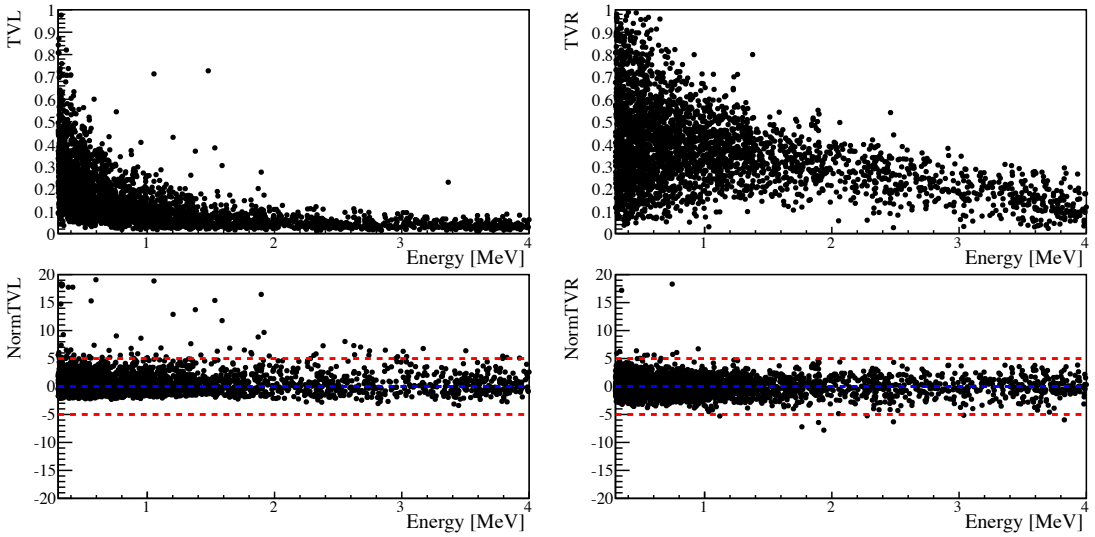

Figure 4.10: Heat pulse shape parameters, TVL (left) and TVR (right), of a selected channel before (top) and after (bottom) the normalization as a function of the energy. Data are from the AmBe neutron calibration used to fit the median and the Median Average Deviation (MAD) trends of each parameter as a function of the energy. Red dashed lines delimit the symmetric 5 MAD interval while the blue dashed line is centered in zero.

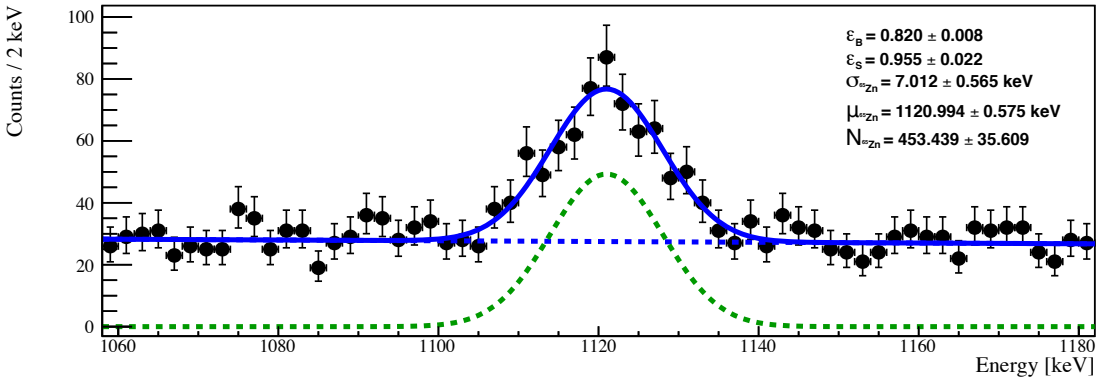

Figure 4.11: Fit of the ^{65}Zn peak of the last dataset. It is exploited to calculate signal (ϵ_S) and background (ϵ_B) efficiency applying the all the selection cuts. The events in the ^{65}Zn peak are taken as signal while the events in the peak flanks as background.

4.5 Data selection and efficiency

Once the first level data processing, including the shape parameter normalization, is completed the events of interest are selected with a set of event cuts. These cuts fall into three types:

1. Time-based cuts that remove periods of time where the data quality was poor or the data processing failed due to cryostat instabilities, noise of the electrical network or human activities close to the experimental area (*RejectBadIntervals*).

2. Anti-coincidence cuts that remove events that occur in multiple calorimeters (in a time-window of 20 ms) and are thus unlikely to come from a $0\nu\beta\beta$ decay (*Anti-coincidence*).

3. Alpha-coincidence cuts that remove events in the β/γ region (E$<$ 4000 keV) if they occur after a ^{212}Bi events (2000 keV $<$ E$_\alpha$ $<$ 6500 keV)[1] in a time-window of $3\tau^{Tl-208}=$ 9.1 min, following the decay scheme of ^{212}Bi reported in Fig. 2.11 (*Delayed veto*).

4. Event-based cuts that remove poorly reconstructed and non-signal-like events to maximize sensitivity to $0\nu\beta\beta$ decay (*Pulse Shape*).

For the last category only the shape parameters of the heat pulses are considered. The efficiency of each cut is calculated on the ^{65}Zn peak ($\sim$ 1120 keV), the most prominent one in background spectrum, as reported in Fig. 4.11. ^{65}Zn in the crystals is due to cosmogenic activation of natural Zn. It decays by electron capture to the 1115 keV excited level and by electron capture and β^+ decay to the ground state of ^{65}Cu.

[1]The lower limit of the ^{212}Bi selection interval is chosen to take into account also surface contaminations, whose energy could be partially lost in the reflecting foil.

The efficiency are calculated as the ratio of the events in the peak (i.e. the area of the Gaussian) first and after the cut are applied. While the efficiency on the continuum is calculated as the ratio of the events in the peak flanks with and without the cut. The cut efficiency in the peak in comparison with the continuum is not so different since most of the events in the peak flanks are due to the $2\nu\beta\beta$. The shape parameters normalization as a function of the energy ensures that efficiency calculated at 1 MeV is constant up to the ROI at 3 MeV. Furthermore a cross check was performed by calculating the efficiency also on the M2 spectrum [2]. This class of event is a good candidate for efficiency calculation since the probability to have a spurious pulse in coincidence with a signal event within 20 ms is very small given the low counting rate.

The energy spectrum of the M2 events is divided in 200 keV wide bins from 300 keV up to 2900 keV and the efficiency in each bin is calculated as the fraction of the signal that passes the cuts. A linear regression as a function of the energy returns the global efficiency, as reported in Fig 4.12. The check is repeated on each dataset, obtaining the values summarized in Tab. 4.13. A fully consistency among the two methods is attested.

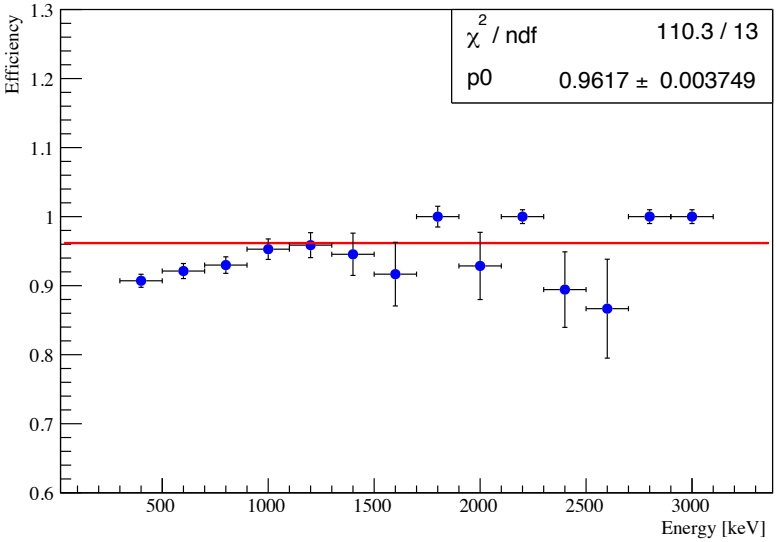

Figure 4.12: Selection efficiency of Dataset 1 calculated bin by bin in the M2 (Multiplicity = 2) spectrum and relative linear regression. The global efficiency obtained in the fit is compared with the one obtained from the Zn peak fit.

The fit of the ^{65}Zn peak is also exploited to optimize the heat pulse shape cuts. The value of each single cut on the *heat shape* parameters was chosen by optimizing the score function $\frac{\epsilon_S}{\sqrt{\epsilon_B}}$ (see Fig. 4.14), where ϵ_S and ϵ_B are the signal and background efficiency respectively. The events in the ^{65}Zn peak are taken as signal while the events in the peak flanks as background. When the efficiency of a cut is calculated all the other cuts are removed (except *RejectBadIntervals* above defined). The optimization is performed using 50% of randomly sampled ^{65}Zn peak events, the other ones are used for the efficiency

[2]It is obtained by requiring that two crystals have coincidence signals in a 20 ms long time window.

Table 4.13: Comparison among the two different methods to calculate the selection efficiency, on the Zn peak and on the M2 (Multiplicity = 2) spectrum. The total efficiencies are calculated as average weighted on the dataset exposure.

Dataset	Efficiency M2	Efficiency Zn
1	96.2 ± 0.4%	97 ± 2%
2	93.2 ± 0.4%	93 ± 2%
3	94.1 ± 0.4%	94 ± 2%
4	95.8 ± 0.3%	98 ± 2%
Total	94.8±0.4%	95.5 ± 2%

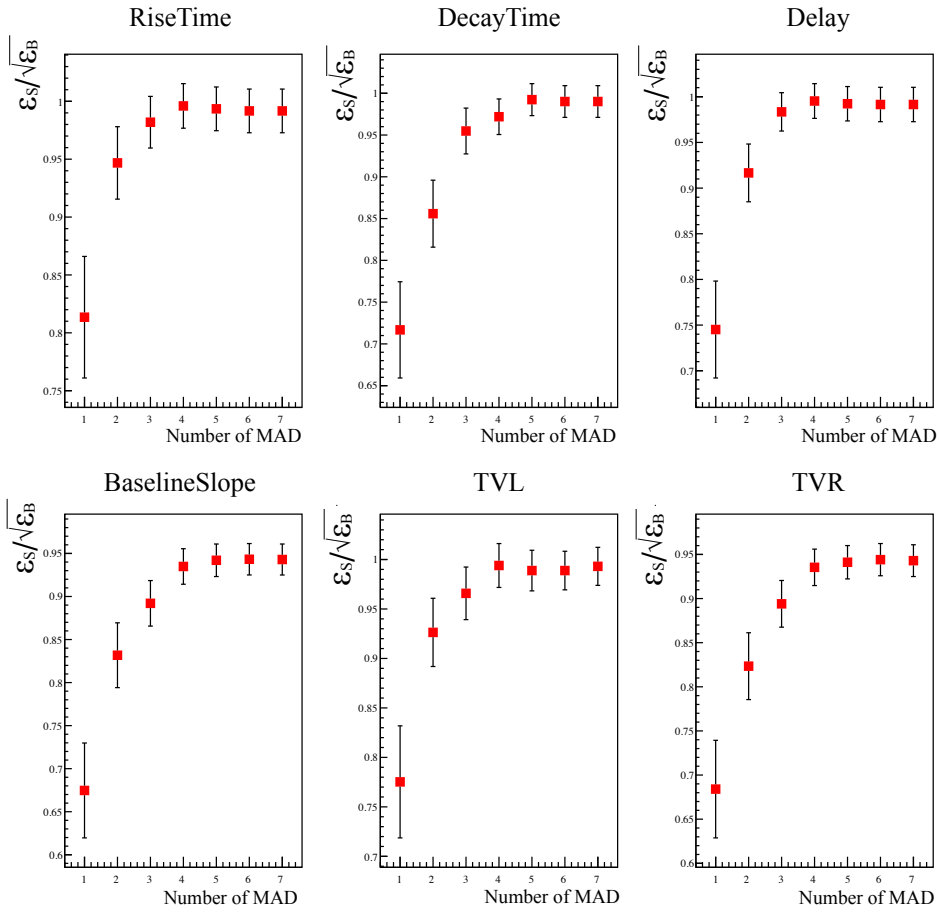

Figure 4.14: Optimization of the cut values performed in the last dataset on each *heat shape* parameter. It is done by maximizing the score function $\frac{\epsilon_S}{\sqrt{\epsilon_B}}$ where ϵ_S and ϵ_B are the signal and background efficiency respectively. They are calculated for different values of the cut (applied one at time) in the ^{65}Zn fit (Fig.4.11). The x-axis reports the value of the cut in number of Maximum Average Deviations (MADs).

estimate. The outcome of this procedure is that the efficiency reaches a plateau at 5 MAD for all the shape parameters. Finally a conservative cut at 6 MAD was chosen to increase the efficiency on the signal.

Alpha rejection cut

The main feature of scintillating calorimeters is the α-identification achieved measuring the light output. Usually the amplitude of the light signal is an effective parameter for this purpose. This is not the case of ZnSe, where the QF_α>1 makes possible an αs dropping in β/γ band due to light leakage. Usually the cryogenic light detectors used in past were calibrated exploiting an X-ray sources in order to associate an energy to the light pulses (i.e. E_{light}). In this way the light yield (i.e. LY) was defined as

$$LY = \frac{E_{light}}{E_{heat}}, \tag{4.16}$$

where E_{heat} is energy measured in the ZnSe crystals. Their typical values are $LY_{\beta/\gamma}$ ∼4 keV/MeV and LY_α ∼12 keV/MeV. In CUPID-0, since the light detectors are not calibrated, the light pulse amplitude is re-scaled in order to have $LY_{\beta/\gamma} = 1$, as shown in Fig. 4.15 (top). The β/γ cluster is centered at <LY>=1, conversely the α-particles have an average light yield of <LY>=3 but they spread in the lower LY region. Since this light leakage is more evident for the ^{210}Po, the only contamination with an evident surface contamination contribution, it can be ascribed to lower scintillation yield of the surfaces or non fully light collection.

In order to avoid particle misidentification, the α-selection is based on the light shape, exploiting the different time-development of the light produced by α-events in the ZnSe crystals with respect to the one produced by βs. The parameters suitable for α/β discrimination are mainly decay time and TVR of the light pulses. The latter one was chosen as it is the most sensitive one. The TVR of the light pulses does not require a normalization as a function of the energy, since it is almost flat in a wide range of energy (including the ROI). To tune the selection, coincident events with an energy release in at least five crystals are required. These events are generated only by electromagnetic showers induced by the passage of a high energy cosmic muon in the surrounding shielding and their energy extends up to 5 MeV. The cut LightTVR < 6 (α *rejection* in the following) is chosen to ensure unitary efficiency on signal selection in the ROI. The α-discrimination capability for anti-coincidence events is show in Fig. 4.15 (bottom).

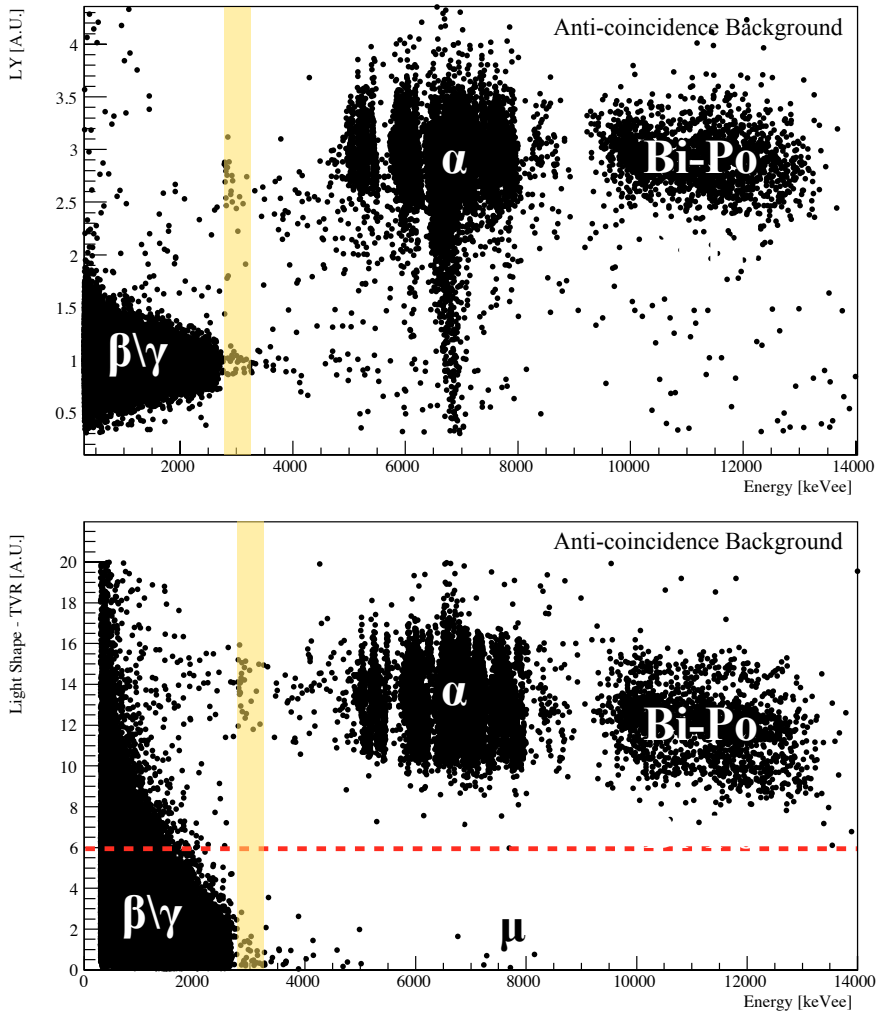

Figure 4.15: The scatter plots show the light yield (LY) and the light shape parameter (TVR) as a function of the energy released by the interacting particle in the ZnSe crystal. All the physics runs (background) of the first four official dataset are included (3.44 kg · y). *Anti-coincidence* cut is applied, therefore most of the muon induces events are removed. *Delayed veto* is not applied. **Top.** LY as a function of the energy. The β/γ cluster is centered at <LY>=1, due to the light inter-calibration that set the light amplitude of the ^{208}Tl at 2615. The α-particles have an average light yield of <LY>=3 but they spread in the lower LY region. **Bottom.** Light TVR as a function of the energy. The α-events are concentrated in the right upper region; β/γ events populate the left lower corner. The red dashed line indicates the acceptance threshold. The shaded vertical band represents the ROI.

Chapter 5

First results of the CUPID-0 experiment

The last part of this thesis deals with the results of the CUPID-0 experiment. A detailed analysis of the internal contaminations is performed to validate the radiopurity of the ZnSe crystals and understand their role in the background budget (see Sec. 5.2). The first physics spectrum obtained with the data collected up to November 2017 is shown and discussed, focusing on the comparison of the spectra obtained adding sequentially *heat shape*, α *rejection* and *delayed veto* cuts. In each of these three cases the BI is calculated by integrating the spectra in the region of interest. A preliminary study of the background is then performed on the single tower and channel spectrum, highlighting differences among different towers/channels (see Sec. 5.3). Finally the first result of the neutrinoless double beta decay ($0\nu\beta\beta$) of ^{82}Se search with CUPID-0 is shown (see Sec. 5.4).

5.1 CUPID-0 exposure and live-time

During the first 8 months of data-taking from March to November 2017, CUPID-0 collected an exposure of 4.51 kg $\cdot$ y. Thanks to the new optimized cryogenic system, helium refills reduce the live-time by only 4% (two hours every two days). The physics runs account for 75% of the live-time, calibration runs almost 10% while the remaining $\sim$11% was spent in system upgrade or lost due to software/hardware debugging. All the information about the collected statistics for each dataset are summarized in Tab. 5.1. The natural crystal contribution in term of decaying isotopes is negligible (< 0.5 %), moreover they show a worse energy resolution. For this reason in the $0\nu\beta\beta$ analysis presented here only the enriched crystals are selected.The first set of data (i.e. Dataset 0) was used for fine tuning of detector parameters and solving ground loop problems that affected several channels. Besides, during this dataset dripping water entered in the Faraday Cage, leading to a possible increased background due to ^{222}Rn. Thus Dataset 0 was discarded from the final analysis due to the detector instabilities, resulting in a worse energy resolution

Table 5.1: Statistics collected by CUPID-0 since March 2017 up to November 2017 for enriched (ENR) and natural (NAT) ZnSe crystals.

		Dataset 0	Dataset 1	Dataset 2	Dataset 3	Dataset 4
E	$Zn^{82}Se$ [kg · y]	0.854	0.606	0.944	0.817	1.077
N	^{82}Se [kg · y]	0.454	0.322	0.501	0.434	0.572
R	^{82}Se [atoms · y]	$3.33 \cdot 10^{24}$	$2.36 \cdot 10^{24}$	$3.68 \cdot 10^{24}$	$3.12 \cdot 10^{24}$	$4.20 \cdot 10^{24}$
N	ZnSe [kg · y]	0.042	0.030	0.0467	0.0403	0.053
A	^{82}Se [kg · y]	0.0021	0.0015	0.0023	0.0020	0.0026
T	^{82}Se [atoms · y]	$1.551 \cdot 10^{22}$	$1.09 \cdot 10^{22}$	$1.70 \cdot 10^{22}$	$1.47 \cdot 10^{22}$	$1.94 \cdot 10^{22}$

and cousin also mis-calibration. Summarizing a total ^{82}Se exposure of 1.83 kg · y (3.44 kg · y of $Zn^{82}Se$) was used in the analysis.

5.2 Radiopurity

In order to achieve an extremely low-background in the ROI for the investigation of $0\nu\beta\beta$ decay, the radiopurity of the detector is of paramount importance. All the materials used for the detector realization were chosen for their ultra-low concentration of radioactive impurities. Nevertheless, the final detector radiopurity can be spoiled if dedicated procedures are not adopted, while producing or handling detector components. To validate the efficiency of the procedures adopted for the detector realization, it is worth analyzing the internal contamination present in the crystals used for CUPID-0. At the same time the study of the internal contaminations of the detector is fundamental for the development of a reliable and robust background model to gain an exact picture on the background sources present in the ROI.

Due to their very short range, α particles can give a clear indication of bulk or surface contaminations. If the α-decaying isotope is located in the crystal bulk, both the α particle and the nuclear recoil are absorbed by the calorimeter, giving rise to a peak at the Q-value of the decay. On the contrary, if the contaminant is located on the crystal surface, α's (and with much lower probability nuclear recoils due to their shorter range) may leave the crystal before being stopped and the event is recorded with an energy lower than the Q-value. Only for very shallow surface contaminations the α-line at about 100 keV below the Q-value becomes visible.

In the energy spectrum reported in Fig. 5.2, the peaks between 4 MeV and 7 MeV are induced by natural radioactive decays occurring in the crystal bulk, while the excess of events at higher energies are induced by pile-up events, usually defined as Bi-Po cascade. In the ^{238}U and ^{232}Th decay chains there are two nuclides which undergo a β decay followed up after few milli-seconds by an α decay. The poor time resolution of the detector does not allow to disentangle these two events which show up a single events with a total energy equal to the Q-value of the two transition reduced by the energy

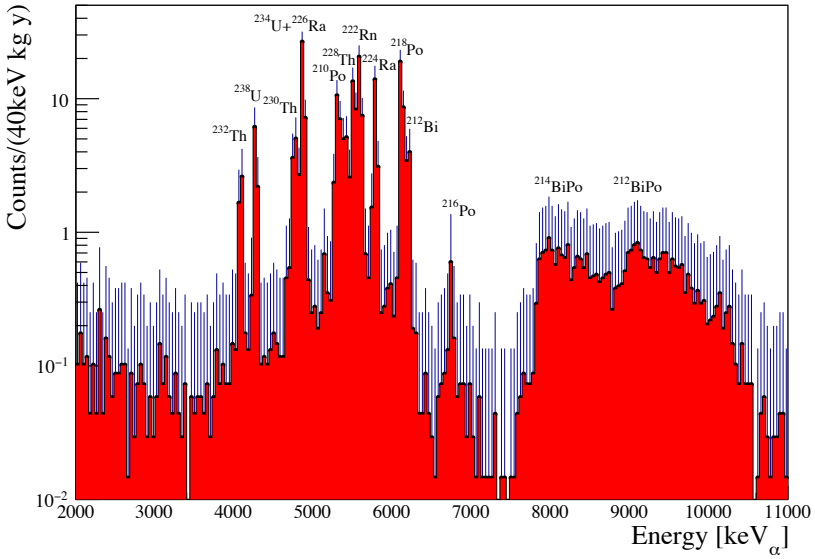

Figure 5.2: Energy spectrum in the α-region 2 – 11 MeV calibrated exploiting the α-lines themselves. All visible peaks from the ^{238}U and ^{232}Th natural decay chains are labelled.

carried away by the neutrino. These cascades are ^{214}Bi$\rightarrow^{214}$Po for the ^{238}U chain and ^{212}Bi$\rightarrow^{212}$Po for the ^{232}Th decay chain.

All the other events in the energy spectrum are mostly ascribed to surface α contaminations [185].

Each α-peak is fitted with a Gaussian line-shape[1] on a flat background and the Gaussian area is taken as estimator of the number of decays, as depicted in Fig. 5.3.

The results are reported in the fourth column of Tab. 5.4. Isotopes with long half-lives, that can break the secular equilibrium, are highlighted (bold type). Looking at Tab. 5.4, the broken equilibrium happens both in the ^{232}Th and the ^{238}U decay chains, for ^{228}Ra and ^{226}Ra respectively. Identify where the equilibrium is broken is easy in the ^{238}U chain, since all the involved isotopes emit a well identifiable α particle. It is less evident in the ^{232}Th chain, where the ^{228}Ra emits only a low energy electron (not included in the table). In this case the equilibrium-break appears only at the ^{228}Th (τ = 1.9 y) level, nonetheless it happens most probably before, among ^{232}Th ($\tau = 1.4 \cdot 10^{10}$ y) and ^{228}Ra (τ = 5.7 y), being different atomic species with a so different half-life. Even if surface contaminations of ^{210}Pb occur in the spectrum (α-line at 5300 keV), it is treated as bulk contamination, summing both the contribution at the Q-value= 5407 keV and the α-line. Indeed, without a detailed background reconstruction the crystals surface contaminations cannot be disentangle from that of the inactive material that surrounds them (i.e. reflecting foil and copper detector holder).

[1]There was no need to use the double-Gaussian model, as the single-Gaussian allows estimating the number of counts effectively. As a further cross-check, the Gaussian area is always compared with the integral of spectrum in [Q-value - 3σ, Q-value + 3σ] where σ is obtained by the gaussian fit of each peak, finding compatibility within the error.

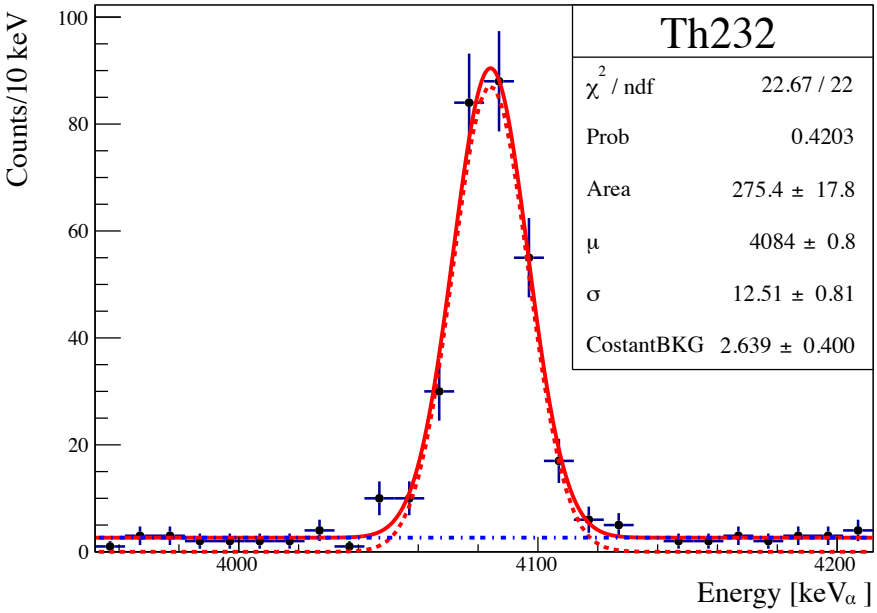

Figure 5.3: Gaussian fit of the ^{232}Th α-line in the CUPID-0 global spectrum. There is no evidence of double-Gaussian shape as used for the γ-line.

The same analysis of the contaminations was performed on the energy spectra of each Zn^{82}Se to highlight possible differences. The results obtained for the most clean and the most dirty crystals are also shown in Tab. 5.4. ^{210}Pb contaminations are quite homogeneous, then only the value of the whole array is reported. In some cases there is no evidence of contaminations, thus a 90% C.L. upper limit is reported. For this purpose, the signal is defined as the number of events falling in the energy region [Q-value - 3σ, Q-value + 3σ] and the background as the average number of events falling in the 3σ side-bands of this interval. Following the Feldman-Cousins approach, the 90% C.L. upper limit is calculated on the number of events and, correcting for the branching ratio of the nuclide, the upper limit on the activity is inferred. The α-lines not quoted in the table are the two $\sim$6 MeV lines of ^{232}Th because they cause a pile-up event rejected as a deformed signal by pulse shape cuts as well as the two α lines that in both chains are summed with the following beta emission (Bi-Po events) producing a continuum above 8 MeV. The contamination level shows a very clear trend as a function of the crystals batch: the crystals produced as first ones are dirtier then the average while the last ones are cleaner. The average contamination of the five most clean crystals (i.e. CG15, CG18, CG21, CG25, Xtra2) and the three most dirty ones (i.e. CG01, CG02, CG04) are reported in second and third column of Tab. 5.4 respectively. The handling procedure developed for ZnSe was improved step by step in each batch production, resulting in a better quality of the crystals.

Table 5.4: Contaminations from different isotopes of the ^{238}U and ^{232}Th decay-chains derived from the analysis of the α-region for most clean, most dirty crystals and the whole CUPID-0 array. Isotopes with long half-lives, that can break the secular equilibrium, are highlighted in bold type. ^{210}Pb is treated as bulk contamination, summing both the line at Q-value= 5407 keV and the α-line at 5300 keV.

Contaminants	ZnSe - most clean [μBq/kg]	ZnSe - most dirty [μBq/kg]	CUPID - 0 [μBq/kg]
^{232}**Th**	< 0.54	8.6 $\pm$1.2	2.5 $\pm$ 0.2
^{228}**Th**	2.3 $\pm$0.8	26.9 $\pm$ 2.2	13.6 $\pm$ 0.4
^{224}Ra	2.1 $\pm$0.6	23.1 $\pm$ 2.0	10.9 $\pm$ 0.3
^{212}Bi	$<$3.7	24.2 $\pm$ 3.5	12.2 $\pm$ 0.6
^{238}**U**	< 1.2	12.7 $\pm$ 1.5	5.1 $\pm$ 0.2
^{234}**U**	1.0 $\pm$ 2.0	14.7 $\pm$ 4.3	5.3 $\pm$ 0.8
^{230}**Th**	< 2.4	16.4 $\pm$ 1.7	5.3 $\pm$ 0.2
^{226}**Ra**	3.8 $\pm$ 0.9	18.4 $\pm$ 1.8	17.0 $\pm$ 0.4
^{218}Po	3.4 $\pm$ 0.6	19.8 $\pm$ 1.9	17.4 $\pm$ 0.4
^{210}**Pb (bulk+surf)**	-	-	18.8 $\pm$ 0.6

5.3 Preliminary background study

The collected statistics is not yet enough to allow for a detail background reconstruction. Comparing CUPID-0 with CUORE-0 there are three main factors that increase the complexity of the background model development. First, the enrichment in ^{82}Se makes the $2\nu\beta\beta$ decay the dominant contribution in the spectrum below 3 MeV. Therefore a quite higher statistics is needed to identify any background peaks in this region. Second, the lower Z reduces the detection efficiency for γ radiation. Finally the reflecting foil, but also the cylindrical shape of the crystals and the subsequence low compactness of the detector, spoil the capability to tag surface contaminations by studying coincidence among close crystals. A detailed background model of CUPID-0 will be possible in the future by increasing the available statistics and exploiting the knowledge of the cryostat contaminations achieved thanks to CUORE-0. Furthermore the knowledge of the internal contaminations reported above and the preliminary study here introduced are the fundamental starting point for the background reconstruction.

The lack of background model of course does not prevent to calculate the BI by integrating the experimental spectrum in the region of interest. Nevertheless defining the region of interest itself without a detailed model could be in general a chancy procedure, but this is not the case. Three are the background contributions close to the $Q_{\beta\beta}$ of the ^{82}Se: pileup in ^{208}Tl decay, high energy βs and γs of ^{214}Bi and eventually muon induced shower that produce single hit events. A good motivated choice for the ROI to estimate the background is 2800–3200, since the ^{208}Tl pileup is due to the sum of 2615 keV and 583 keV γ-lines (i.e. 3198 keV) while the high energy β/γs of ^{214}Bi are

respectively 3272 keV (β endpoint) and 3233.2 keV (γ-line with B.R. $\sim$ 0.0001 %). The lower limit of 2800 keV is chosen to avoid introducing also the tail of the 2615 keV line and $2\nu\beta\beta$ events. In CUORE-0 only 1.5 % of the background in the ROI was induced by muons [139]. In that case the background was dominated by smeared αs, moreover the bigger detector size reduced the muon induced counting rate in the ROI at the level of 10^{-4} counts/(keV $\cdot$ kg $\cdot$ y). CUPID-0 is completely different, since the αs are fully rejected and the detector geometry spoils the tagging efficiency of muon induced events by anti-coincidence cut. Preliminary simulations show that muon contribution in the energy interval 3000–4000 keV in the single hit spectrum is of the order of $(1.5 \pm 0.3) \cdot 10^{-3}$ counts/(keV $\cdot$ kg $\cdot$ y). Being this value of the same order of magnitude of the one expected from ^{208}Tl and ^{214}Bi, it is worth investigating the muon effect in a wider ROI, for example 2800–4600 keV. If the BI in the two regions is the same, one can concludes that the background is dominated by muons secondary interactions, whose contribution is almost constant over a wide energy range, or by internal/surface ^{232}Th contaminations, which can produce a β/γ background up to Q-value(^{208}Tl) = 5001 keV. Conversely, if the background decrease when the ROI increase external near sources of contamination are favored (pileup in ^{208}Tl decay and ^{214}Bi).

Background index

Non-particle events, as cross-talks, electronic spikes and thermal instability as well as a large fraction of pile-up events are removed by cutting on the *heat shape* parameters while the multiplicity of the event (i.e. *anti-coincidence* cut) is used to reject multisite events induced by muons or internal contamination. The energy spectrum obtained applying these preliminary cuts are reported in Fig. 5.5 (gray), while the following BI in the ROI results:

$$2800 - 3200 \text{ keV} \;:\; (3.7 \pm 0.5) \cdot 10^{-2} \text{ counts/(keV} \cdot \text{kg} \cdot \text{y)}, \tag{5.1}$$

$$2800 - 4600 \text{ keV} \;:\; (2.0 \pm 0.2) \cdot 10^{-2} \text{ counts/(keV} \cdot \text{kg} \cdot \text{y)}. \tag{5.2}$$

A similar value was obtained in CUORE-0, where the BI in the region 2700–4000 keV was $1.6 \cdot 10^{-2}$ counts/(keV $\cdot$ kg $\cdot$ y. However the direct comparison of the two results is not so straightforward without a detailed model. In CUORE-0 the anti-coincidence cut removed efficiently surface α-particles that release energy in two close crystals. In CUPID-0 α-particles stop in the reflecting foil when come out of a crystal, so they cannot be tagged in the same way. Adding the α *rejection* cut to remove the α-particles (see Fig. 5.5, red) the BI becomes:

$$2800 - 3200 \text{ keV} \;:\; (1.4 \pm 0.3) \cdot 10^{-2} \text{ counts/(keV} \cdot \text{kg} \cdot \text{y)}, \tag{5.3}$$

$$2800 - 4600 \text{ keV} \;:\; (6.7 \pm 0.1) \cdot 10^{-3} \text{ counts/(keV} \cdot \text{kg} \cdot \text{y)}. \tag{5.4}$$

These counting rates is still dominated by pile-up in the ^{208}Tl decay, which justify the huge difference among the two region of interest: even if ^{208}Tl decay can produce β/γs up to Q-value(^{208}Tl) = 5001 keV the main contribution comes from the sum of 2615

keV and 583 keV γ-lines (i.e. 3198 keV). The ultimate BI in the ROI is obtained by including also the *delayed veto* cut. Since the contamination could be also on the surface, they can release only a fraction of their energy in the crystals. In order to account also this contribution the selection window 2000–6500 keV$_\alpha$ was chosen for the ^{212}Bi parents selection, thus resulting in the follow background index:

$$2800 - 3200 \text{ keV} \quad : \quad (3.4 \pm 1.6) \cdot 10^{-3} \text{ counts/(keV} \cdot \text{kg} \cdot \text{y)}, \tag{5.5}$$

$$2800 - 4600 \text{ keV} \quad : \quad (2.5 \pm 0.6) \cdot 10^{-3} \text{ counts/(keV} \cdot \text{kg} \cdot \text{y)}. \tag{5.6}$$

Fig. 5.5 (blue) shows the final energy spectrum after all selection criteria.

The reduction of the BI in the wider region corroborates the hypothesis of near ^{232}Th or ^{214}Bi source, as explained above. Fig. 5.5 (right) reports the events in the ROI in the different channels and tower. In the narrower ROI 3 events over the final 5 are in Tower 5 while the other 2 are in Tower 3, in the first or the second crystal of starting from the top plate (first floor of the CUPID-0 detector in Fig. 5.6).

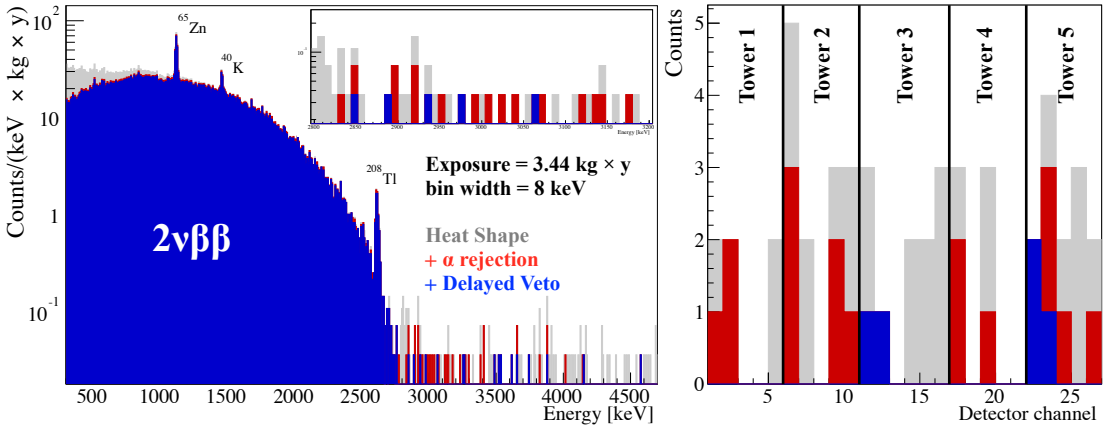

Figure 5.5: Left. Final CUPID-0 energy spectrum obtained applying anti-coincidence and heat pulse shape (gray). *α rejection* cut are then added (red) to remove the α-contribution. Finally the *delayed veto* among ^{212}Bi and ^{208}Tl to remove the pile-up events produced in ^{208}Tl decay are included in the cuts (blue). The insets show spectrum zoom in the ROI 2800–3200 keV used for the $0\nu\beta\beta$ analysis. **Right.** Events in the ROI divided by channel, applying the different selection criteria. 3 events over the final 5 are in Tower 5 (60%) while the other 2 one are in Tower 3 (40%).

Tower and channel spectra

In order to understand if the background measured by CUPID-0 could be due to a near localized source of ^{232}Th, single tower and channel spectra are considered (see Fig. 5.7). Being dominated by the $2\nu\beta\beta$ contribution, the only evident peaks are from ^{65}Zn, due to cosmogenic activation of Zn in the crystals, ^{40}K and ^{208}Tl form the cryostat contamination. Even if there are other tiny excesses of counts they are not consistent with γ-lines from ^{232}Th or ^{232}U decay chains or other known contaminants of ZnSe due

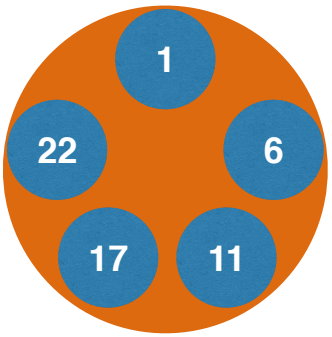

Figure 5.6: Configuration of the first floor of the CUPID-0 detectors.

to a missing match among the peaks counting rate and their branching ratio. Tower 4 shows also the peak of the ^{60}Co at 2505.8 keV given by the sum of the 1173.3 keV and 1332.5 keVγ-lines. ^{60}Co is produced by cosmogenic activation of copper, most probably the one used to made the crystals holder: in the spectrum of Tower 4 only the sum of the γs is visible, indicating that the ^{60}Co source is very close to the detector.

In Tab. 5.8 the counting rates od the ^{208}Tl peak, obtained by integrating each single channel/tower spectrum in the energy region 2590–2650 keV are reported. It is worth to recall that only β/γ events are selected by the α *rejection* cut and ^{208}Tl from ZnSe contamination are removed by *delayed veto* and *anti-coincidence* cuts. The ratio among the $2\nu\beta\beta$ counts in the considered region and the total $2\nu\beta\beta$ events is $2.2 \cdot 10^{-4}$, calculated from Monte Carlo simulation of the $2\nu\beta\beta$ spectrum of CUPID-0. Therefore in the energy region 2590–2650 keV about 20 ± 5 counts due $2\nu\beta\beta$ decay are expected in the 3.44 kg $\cdot$ y of exposure considered, being 169 ± 13 the observed counts. Finally one can conclude that in the selected region external ^{208}Tl is the dominant contribution.

About the tower counting rate one can only state that the Tower 1 one is slightly lower than other towers, that are quite similar among them (neglecting channel 6 in Tower 2). The number related to the single channel spectra are more interesting but difficult to interpret: due to a small number of counts (often less then twelve) the statistical fluctuations become not negligible. The value measured for channel 6 is the only outlier easy to spot but it could be an hint of a localized ^{232}Th source. However, looking at the Fig. 5.6, it is not easy to imagine a configuration where channel 6 measures only the 2615 keV γ-line while channel 11 (close to channel 6) and channel 22 (opposite to channel 22) measure the sum of the 2615 keV and 583 keV γ-lines.

Even if the channels that have counts in the ROI (i.e. 11,12, 22, 23) have a ^{208}Tl counting rate higher then the CUPID-0 average, the difference is to small to claim something. One could think that ^{232}Th contaminations are on top plate of the detector holder, since the counting rate seems to decrease going down along the towers, but channels 15, 17 and 21 contradict this hypothesis. Further cross-checks are performed to clarify the low counting rate of several crystals (i.e. 14, 16, 17, 26) excluding any possible problem due to cut efficiency or signal triggering. Finally, at this stage this preliminary study is not able to clarify the origin of the background measured by CUPID-0.

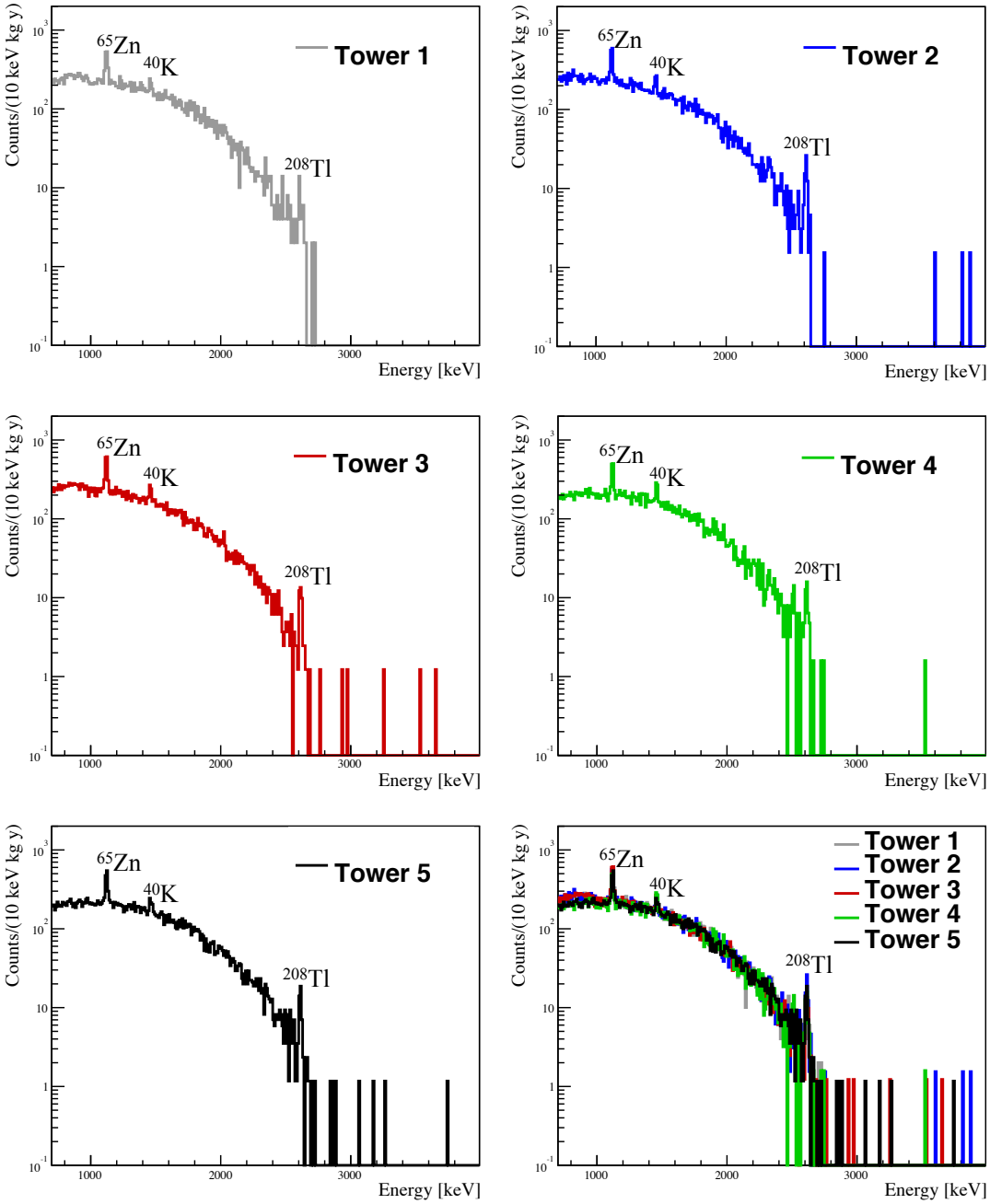

Figure 5.7: Energy spectra of the five towers of the CUPID-0 detector and their comparison in the region 700 – 4000 keV. All the data selection criteria are applied. Being $2\nu\beta\beta$ the dominant component of the spectrum the only evident peaks are from ^{65}Zn due to cosmogenic activation of Zn, ^{40}K and ^{208}Tl form the cryostat contamination. Tower 4 shows also the peak of the ^{60}Co at 2505.8 keV (given by the sum of the 1173.3 keV and 1332.5 keVγ-lines).

Table 5.8: Crystals, towers and total counting rate in the interval 2590–2650 keV, dominated by the external ^{208}Tl contribution. All the data selection criteria are applied.

Crystal	Rate ^{208}Tl region 2590–2650 [μBq/kg]
1	1.1 ± 0.5
2	1.1 ± 0.5
5	1.4 ± 0.5
Tower 1	1.2 ± 0.3
6	3.8 ± 0.8
7	2.2 ± 0.6
9	1.5 ± 0.5
10	1.9 ± 0.8
Tower 2	2.1 ± 0.3
11	2.6 ± 0.7
12	2.6 ± 0.9
13	1.4 ± 0.8
14	0.4 ± 0.3
15	2.2 ± 0.6
16	0.8 ± 0.4
Tower 3	1.4 ± 0.2
17	0.5 ± 0.3
18	1.6 ± 0.5
19	1.9 ± 0.6
20	0.4 ± 0.3
21	2.8 ± 0.9
Tower 4	1.5 ± 0.3
22	1.8 ± 0.6
23	1.9 ± 0.6
24	1.9 ± 0.6
25	1.1 ± 0.5
26	0.9 ± 0.4
Tower 5	1.5 ± 0.2
CUPID-0	1.6 ± 0.1

5.4 Searching for $0\nu\beta\beta$ decay of ^{82}Se

The fit to the ROI follows an analogous process to the other peaks in the physics spectrum. Both the hypothetical $0\nu\beta\beta$ decay signal and a flat background are included. For each dataset the fit comprises the bi-gaussian peak, $\rho(E|Q_{\beta\beta}, \sigma(Q_{\beta\beta}), \eta, \delta, \lambda)$, for the $0\nu\beta\beta$ decay (Eq. 4.5) and a flat component background, b_{ROI}:

$$f_{ROI}(E) = R^{0\nu}\rho(E|Q_{\beta\beta}, \sigma(Q_{\beta\beta}), \eta, \delta, \lambda) + b_{ROI} \tag{5.7}$$

where $\sigma(Q_{\beta\beta})$ is the FWHM energy resolution calculated in Sec. 4.2.1, resulting to be (23.0 ± 0.6) keV, $R^{0\nu}$ is the event rate in counts/(keV · kg · y) for $0\nu\beta\beta$ decay and is assumed to be uniform across the detector. $R^{0\nu}$ can be directly related to the physical ^{82}Se $0\nu\beta\beta$ decay rate $\Gamma_{0\nu}$ through

$$R^{0\nu} = \varepsilon_{0\nu\beta\beta}\frac{a_i N_A}{W}\Gamma_{0\nu}, \tag{5.8}$$

where $\varepsilon_{0\nu\beta\beta}$ is the total signal efficiency, a_i is the isotopic abundance of ^{82}Se (95 ± 1 %), W is the molar mass of ZnSe and N_A is Avogadro's number.

Selection efficiency

The signal efficiency $\varepsilon_{0\nu\beta\beta}$ comprises the probability that $0\nu\beta\beta$ event is confined inside a single crystal, that is triggered and its energy properly reconstructed, and finally that it survives the selection criteria. The probability of a $0\nu\beta\beta$ event to be fully contained in a single crystal is determined from simulation to be on average (80.8 ± 0.2)%, where the uncertainty takes into account the different geometries and density effect. The trigger efficiency is evaluated as the ratio of triggered to flagged heater pulses and the probability of the mono-energetic heater pulse to be reconstructed within three gaussian standard deviations. The combined trigger efficiency, weighted on dataset exposure, is (99.44 ± 0.01)%. The selection efficiency from a a simultaneous fit on both the spectra of accepted and rejected events in the 1120 keV ^{65}Zn peak in the sample not used for the optimization as detailed in Sec. 4.5. The exposure-averaged selection efficiency is (93 ± 2)%. The overall efficiency results in (75±2)%.

Fit to $Q_{\beta\beta}$ energy

The number of $0\nu\beta\beta$ signal events is estimated from a simultaneous UEML fit in the ROI. The position of the $0\nu\beta\beta$ peak is fixed ($Q_{\beta\beta}$) and the detector response function parameters (η, δ and λ) are constrained to estimated ones in calibration data. The efficiency and the energy resolution are dataset dependent. The decay rate $\Gamma^{0\nu}$ and the background index in the ROI are treated as global free parameters. In a total ^{82}Se exposure of 1.83 kg · y 5 events are found, which are ascribed to the background.

The best fit reported in Fig. 5.9 yields a background index in the ROI of $(3.6^{+1.9}_{-1.4}) \cdot 10^{-3}$ counts/(keV · kg · y) .

The systematics due to the uncertainty on the absolute energy scale, the detector response function, the efficiency and the exposure are estimated: for each influence parameter the likelihood is weighted with a gaussian p.d.f. with mean and width fixed to the best estimated values and uncertainties respectively. Then the likelihood is numerically integrated.

The energy offset is derived from the peak residuals distribution in calibration data. A constant fit holds to (0.42±0.05) keV. Any possible difference between calibration and physics data are investigate exploiting the fit to the 2615 keV ^{208}Tl line, the closest peak to the $Q_{\beta\beta}$ in the spectrum. A null residual of (0.1±1.1) keV was found. In order to be conservative the energy scale uncertainty is modeled with a flat distribution between the extremal residuals ±1.4 keV and neglecting the 0.3 keV uncertainty of the measured $Q_{\beta\beta}$ [199].

Decay rate $\Gamma^{0\nu}$ calculation and results

No signal evidence is founded and a 90% C.I. Bayesian upper limit on $\Gamma^{0\nu}$ is set using a uniform prior in the physical region and marginalizing over the nuisance parameters in the fit: $\Gamma^{0\nu} < 0.285 \cdot 10^{-24}$ y^{-1}. This corresponds to a lower limit on the ^{82} Se half life of

$$T^{0\nu}_{1/2} > 2.4 \ \cdot \ 10^{24}\text{y (90\% C.I.)}.$$

The median 90% C.I. lower limit sensitivity is evaluated from toy MC experiments to be: $T^{0\nu}_{1/2} > 2.3 \cdot 10^{24}$ y. The probability to obtain a limit greater than the one reported is 44%, computed via toy MC. The CUPID-0 result surpasses by almost one order of magnitude the previous limit of $T^{0\nu}_{1/2} > 3.6 \cdot 10^{23}$ y [56] obtained by NEMO with a larger ^{82}Se exposure (∼3.5 kg · y). Fig. 5.10 shows the energy spectrum in the analysis window applying all the cuts in series and the fitted spectrum together with a hypothetical signal corresponding to the 90% C.I. limit of $T^{0\nu}_{1/2} = 2.4 \cdot 10^{24}$ y.

In the light Majorana neutrino exchange model for the $0\nu\beta\beta$ decay, the effective neutrino mass $m_{\beta\beta}$ is related to $T^{0\nu}_{1/2}$ by the equation

$$(T^{0\nu}_{1/2})^{-1} = G_{0\nu} \, |\mathcal{M}_{0\nu}|^2 \, m^2_{\beta\beta} \tag{5.9}$$

where $G_{0\nu}$ and $M_{0\nu}$ are the phase space factor of the decay and the dimensionless nuclear matrix element (NME) . Using $G_{0\nu}$ from [200, 201], NME from [202–204] and an axial coupling constant g_a=1.27 one get an upper limit on $m_{\beta\beta} <$ 376-770 meV.

In summary no evidence of ^{82}Se $0\nu\beta\beta$ decay in 1.83 kg · y ^{82}Se exposure are found and the most stringent limit on this decay was set.

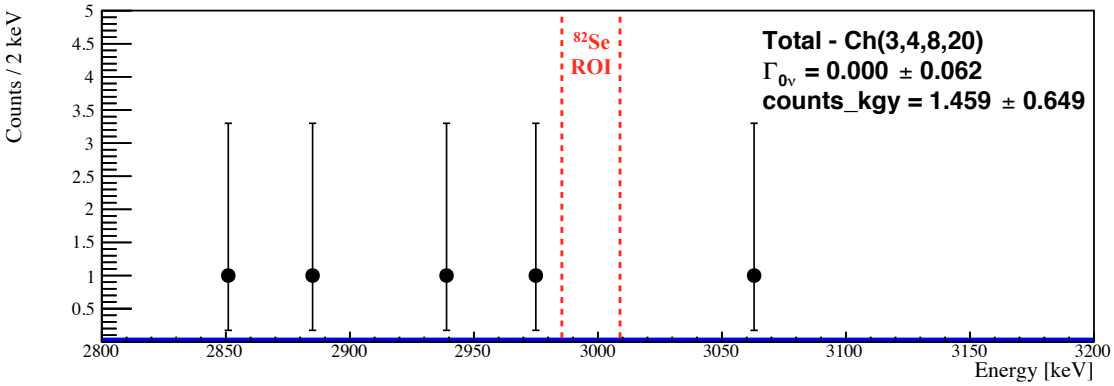

Figure 5.9: The best-fit model (blue line) overlaid on the CUPID-0 energy spectrum (data points) after all the selection criteria. The dash red line indicates the FWHM wide region at which a potential $0\nu\beta\beta$ decay signal is expected.

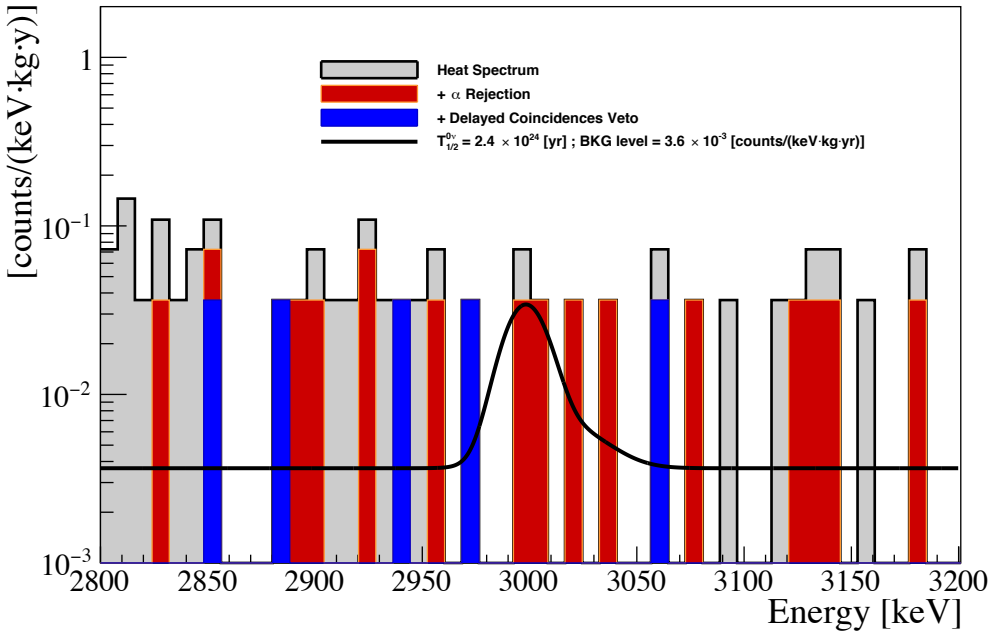

Figure 5.10: The energy spectrum in the analysis window. The filled gray histogram is the spectrum obtained with the selection on Zn^{82}Se thermal pulses. The filled orange histogram includes the α rejection through the LD pulse shape. The filled blue histogram is the final spectrum after the delayed-coincidences veto is applied. The blue line is the fitted spectrum together with a hypothetical signal corresponding to the 90% C.I. limit of $T^{0\nu}_{1/2} = 2.4 \cdot 10^{24}$ y. The detector response function is described in Sec. 4.2.

Conclusions

The CUPID-0 demonstrator at the Laboratori Nazionali del Gran Sasso (Italy) is the first large array of enriched scintillating cryogenic detectors for the investigation of ^{82}Se neutrinoless double-beta decay ($0\nu\beta\beta$). It was born as pilot project, paving the way to a next generation $0\nu\beta\beta$ experiment based on this powerful technique. The main goal is to probe the feasibility of the scintillating calorimeter in reducing the Background Index (BI) in the Region of Interest (ROI) for $0\nu\beta\beta$ at the level of 10^{-3} count/(keV $\cdot$ kg $\cdot$ y). This result can be achieved by current technology for background suppression and through custom protocols for detector preparation and construction.

In the first part of this Ph.D. work all the various phases of the detector design, assembly and commissioning was faced. The successful construction and operation of the detector lead to very promising detector performance. After the first eight months of data taking CUPID-0 features an effective energy resolution of (23.0 $\pm$ 0.6) keV and a background level of $(3.6^{+1.9}_{-1.4}) \cdot 10^{-3}$ count/(keV $\cdot$ kg $\cdot$ y) in the ROI, the lowest value ever measured using cryogenic calorimeters. No signal evidence is found in 1.83 kg $\cdot$ y ^{82}Se exposure and a Bayesian lower limit on the $0\nu\beta\beta$ ^{82}Se half life of $T^{0\nu}_{1/2} > 2.4 \cdot 10^{24}$ y at 90% C.I. is derived. The median 90% C.I. lower-limit half life sensitivity is $T^{0\nu}_{1/2} > 2.3 \cdot 10^{24}$ y. This represents the most stringent limit to date on this isotope. In terms of the effective Majorana neutrino mass the limit achieved is, $m_{\beta\beta} <$ (376-770) meV where the range takes into account the nuclear matrix element calculations. CUPID-0 is expected to run at least for 1 year of live-time and will reach a sensitivity on the ^{82}Se $0\nu\beta\beta$ half life of $T^{0\nu}_{1/2} > 6 \cdot 10^{24}$ y, a remarkable result considering the small mass compared to other experiments [59, 60, 96, 110].

The background study conducted within this thesis suggests contributions from contaminations of the actual cryogenic setup and from muons induced events. A deeper understanding of the CUPID-0 background will be possible with a detailed reconstruction of the single contributions, which I started to work on. Moreover the installation of a muon veto to tag and characterize muon induced showers is also under discussion in the collaboration. In view of a future experiment based on this technique both contributions can be reduced to a negligible level running in a radiopure cryostat equipped with a muon veto. The successful operation of CUPID-0 and the capability to reject the α induced background is a key milestone for a next generation tonne-scale CUORE Upgrade with Particle IDentification.

Acknowledgements

I want to thank F. Bellini, L. Pattavina, S. Pirro, C. Rusconi e K. Schäffner for reading this thesis but especially for supporting me during these years. An other special thanks goes to L. Cardani, N. Casali and L. Gironi for their invaluable help with the data analysis. Finally, I would like to thank all the professors, researchers and technicians of LNGS and GSSI who have contributed directly or indirectly to this work and have turned three years into an opportunity for growth.

Ovviamente i ringraziamenti veri vanno ben oltre le formalità espletate sopra in tre righe. I Laboratori Nazionali del Gran Sasso sono stati casa mia per tre anni e sotto quel tetto ho imparato molto da Stefano, Luca, Karo e Claudia. Conservo bellissimi ricordi del tempo trascorso insieme, siete stati dei fantastici compagni di viaggio!

Questa tesi e CUPID-0 stesso non sarebbero quello che sono (o semplicemente non esisterebbero) se Stefano non avesse dato l'anima come ha fatto in questi anni. Ad una persona normale sarebbe bastato vedere il luogo in cui sono stati cresciuti i cristalli per lasciar perdere. Ma Stefano notoriamente non è normale! Se questo sia sempre un bene non lo so, ma per ora ci ha fatto portare a casa un esperimento e dei risultati.

Luca, Karo e Claudia hanno pazientemente fatto da filtro fra le urla di Stefano e me, insegnandomi molte delle cose imparate al Gran Sasso. Siamo stati una bella squadra e poiché "squadra che vince non si cambia", ora siamo tutti in posti diversi:)

Voglio ringraziare moltissimo anche Fabio, Laura e Nicola...per tutte le volte che non mi hanno mandato al diavolo all'ennesima domanda sulla macro X o sul modulo Y. Grazie per il vostro tempo, per i vostri consigli e per il vostro affetto. Non scorderò mai che per me tutto è cominciato da lì. A Milano, dove sono da poco approdato, voglio ringraziare Luca Gironi, per aver condiviso con me i drammi della PSA e Davide Chiesa per avermi *inizializzato* con JAGS. Nel corso del tempo accumulerò buoni motivi per ringraziare anche tutti gli altri milanesi, ma a quel punto non avrò una tesi da scrivere, quindi li ringrazio ora sulla fiducia.

Grazie anche a tutti gli amici e colleghi del GSSI con cui ho condiviso questo percorso, soprattuto nella fase iniziare. Un ringraziamento speciale a Francesco...che per tutti noi è stato molto più di un coordinatore, oltre che un pilastro del GSSI.

Andrei purtroppo finisce alla fine di questo lungo elenco perché la mia gratitudine nei suoi confronti non riesce ad incasellarsi in alcun modo nelle categorie precedenti. Oltre ad aver colorato le giornate passate insieme in galleria, ora sto scrivendo le ultime pagine di

questa lunga storia sul divano di casa tua, mentre...Mikke si fa una bionda, Laura compie solo X5 anni, Giorgia tresca con il tipo della maglia sobria (Voi non potete capire...!!!), Gaetano dalla Sicilia si spaccia per Andrea da Zurigo...mentre tutti, rigorosamente, vorremo solo essere ad Alghero! E se Giuni Russo voleva andarci con uno straniero, io ci andrei con Tania, magari in viaggio di nozze a settembre! Con questo ultimo gossip ringrazio anche te per essermi accanto e sostenermi praticamente da sempre. Concludo con il ringraziamento più grande, quello alla mia famiglia...anche se non hanno ben capito quello che faccio sanno che a guidarmi sono la passione e la curiosità che loro stessi mi hanno trasmesso.

Bibliography

[1] W. Pauli, Letter to the Physical Institute of the Federal Institute of Technology, Zürich.

[2] E. Fermi, *Trends to a theory of β ray emission (in Italian)*, Ric. Sci. **4**, 491 (1933).

[3] H. Bethe and C.I. Peierls, *The neutrino*, Nature **133**, 3362 (1934).

[4] F. Close, *Half life*, Oneworld Publications (2015).

[5] F. Reines and G. Cowan, *The neutrino*, Nature **178**, 4531 (1956).

[6] G. Danby, J-M. Gaillard, K. Goulianos, L. M. Lederman, N. Mistry, M. Schwartz, and J. Steinberger, *Observation of high-energy neutrino reactions and the existence of two kinds of neutrinos*, Phys. Rev. Lett. **9**, 36 (1962).

[7] M. Goldhaber, L. Grodzins, and A. W. Sunyar, *Helicity of neutrinos*, Phys. Rev. **109**, 1015 (1958).

[8] M. L. Perl *et al.*, *Evidence for anomalous lepton production in e^+e^- annihilation*, Phys. Letter B **35**, 1489 (1975).

[9] K. Kodama *et al.*, *Observation of tau neutrino interaction*, Phys. Letter B **504**, 3 (2001).

[10] S. Schael *et al.*,*Precision electroweak measurements on the Z resonance*, Physics Reports **427**, 257 (2006).

[11] A. Strumia and F. Vissani, *Neutrino masses and mixings and...*, arXiv hep-ph/0606054 (2010).

[12] Z. Maki, M. Nakagawa and S. Sakata, *Remarks on the Unified Model of Elementary Particles*, Prog. Theor. Phys. **28**, 5 (1962).

[13] B. Pontecorvo, *Neutrino Experiments and the Problem of Conservation of Leptonic Charge*, Sov. Phys. Jept. **26**, 5 (1968).

[14] L. Wolfenstein, *Neutrino Oscillations in Matter*, Phys. Rev. D **17**, 2369 (1978).

[15] S.P. Mikheev and A.Yu. Smirnov, *Resonance Amplification of Oscillations in Matter and Spectroscopy of Solar Neutrinos*, Sov. J. Nucl. Phys. **42**, 913 (1985).

[16] F. Vissani, *Neutrino Sources and Properties*, PoSGSSI14, 001 (2015).

[17] J. N. Bahcall, *Solar Neutrinos I. Theoretical*, Phys. Rev Lett **12**, 300 (1964).

[18] R. Davis, D. Harmer, and K. Hoffman, *Search for neutrinos from the Sun*, Phys. Rev. Lett. **20**, 1205 (1968).

[19] J. N. Abdurashitov *et al.*, *Measurement of the Solar Neutrino Capture Rate by SAGE and Implications for Neutrino Oscillations in Vacuum*, Phys. Rev. Lett. **83**, 4686 (1999).

[20] W. Hampel *et al.*, *GALLEX solar neutrino observations: Results for GALLEX IV*, Phys. Letter B **447**, 127 (1999).

[21] G. Bellini *et al.* (Borexino Collaboration), *Neutrinos from the primary proton-proton fusion process in the Sun*, Nature **512** 383-386. (2014).

[22] Q. Ahmad *et al.*, *Direct evidence for neutrino flavor transformation from neutral current interactions in the Sudbury Neutrino Observatory*, Phys. Rev. Lett. **89**, 011301 (2002).

[23] S. Abe *et al.*, *Precision measurement of neutrino oscillation parameters with KamLAND*, Phys. Rev. Lett. **100**, 221803 (2008).

[24] D. Kielczewska *et al.*, *Oscillatory signature in atmospheric neutrinos*, Int. J. Mod. Phys. A **20**, 3102-3105 (2005).

[25] K. Abe *et al.*, *Evidence of electron neutrino appearance in a muon neutrino beam*, Phys. Rev. D **88**, 032002 (2013).

[26] F. An *et al.*, *Improved measurement of electron-anti-neutrino disappearance at Daya Bay*, Chin. Phys. C **37**, 011001 (2013).

[27] K. Soo-Bong *et al.*, *Observation of reactor anti-neutrino disappearance in the RENO experiment*, Phys. Rev. Lett. **108**, 191802 (2012).

[28] Y. Abe *et al.*, *First measurement of θ_{13} from delayed neutron capture on hydrogen in Double Chooz experiment*, Phys. Lett. B **723**, 66-70 (2013).

[29] A. Gando *et al.* (KamLAND Collaboration), *Reactor on-off antineutrino measurement with KamLAND*, Phys. Rev. D **88**, 033001 (2013).

[30] http://www.nu-fit.org

[31] P. Adamson *et al.*, (NOvA), *First measurement of muon-neutrino disappearance in NOvA*, Phys. Rev. D **93** 051104 (2016).

[32] K. Abe *et al.*, (T2K), *Measurement of Neutrino Oscillation Parameters from Muon Neutrino Disappearance with an Off-Axis Beam*, Phys. Rev. Lett. **111** 211803 (2013).

[33] F. An *et al.*, (JUNO), *Neutrino physics with JUNO*, J. Phys. G **43** 030401 (2016).

[34] E. Majorana, *Theory of the Symmetry of Electrons and Positrons (in Italian)*, Nuovo Cim. **14**, 171 (1937).

[35] P. Minkowski, $\mu \to e\gamma$ *at a rate of one out of* 10^9 *muon decays?*, Phys. Lett. B **67**, 4 (1977).

[36] R. N. Mohapatra and G. Senjanovic, *Neutrino Mass and Spontaneous Parity Violation*, Phys. Rev. Lett. **44**, 912 (1980).

[37] T. Yanagida, *Horizontal symmetry and masses of neutrinos*, Prog Theor. Phys. **64**, 3 (1980).

[38] T. Hambye, *Leptogenesis: beyond the minimal type I seesaw scenario*, New J. of Phys. **14**, 125014 (2012).

[39] M. Goeppert-Mayer, *Double Beta-Disintegration*, Phys. Rev. **48**, 6 (1935).

[40] M. G. Inghram and J. H. Reynolds, *On the Double Beta-Process* Phys. Rev. **76**, 1265 (1949).

[41] S. R. Elliott, A. A. Hahn, and M. K. Moe, *Direct evidence for two-neutrino double-beta decay in* ^{82}Se, Phys. Rev. Lett. **59**, 2020 (1987).

[42] W. Furry, *On Transition Probabilities in Double Beta Disintegration*, Phys. Rev. **56**, 1184 (1939).

[43] S. Bilenky and C. Giunti, *Neutrinoless double-beta decay. A brief review*, Mod. Phys. Lett. A **27**, 1230015 (2012).

[44] R. Saakyan, *Two-Neutrino Double-Beta Decay*, Ann. Rev. Nucl. Part. Sci. **63**, 503 (2013).

[45] R. Arnold *et al.* (NEMO Collaboration), *Measurement of the double-beta decay half-life and search for the neutrinoless double-beta decay of* ^{48}Ca *with the NEMO-3 detector*, Phys. Rev. D **93**, 112008 (2016).

[46] M. Agostini *et al.* (GERDA Collaboration), *Measurement of the half-life of the two-neutrino double beta decay of* ^{76} *with the GERDA experiment*, J. Phys. G: Nucl. Part. Phys. **42**, 115201 (2015).

[47] R. Arnold *et al.* (NEMO Collaboration), *First Results of the Search for Neutrinoless Double-Beta Decay with the NEMO 3 Detector*. Phys. Rev. Lett. **95**, 182302 (2005).

[48] A. S. Barabash *et al.*, *Investigation of double beta decay with the NEMO-3 detector*, Phys. Atom. Nucl. **74** (2011) .

[49] E. Armengaud *et al.*, *Development of ^{100}Mo-containing scintillating bolometers for a high-sensitivity neutrinoless double-beta decay search*, Eur. Phys. J. C **77**, 785 (2017).

[50] R. Arnold *et al.* (NEMO Collaboration), *Measurement of the $2\nu\beta\beta$ decay half-life and search for the $0\nu\beta\beta$ decay of ^{116}Cd with the NEMO-3 detector*, Phys. Rev. D **95**, 012007 (2017)

[51] A. Gando *et al.* (KamLAND-Zen Collaboration), *Measurement of the double-β decay half-life of ^{136}Xe with the KamLAND-Zen experiment*, Phys. Rev. C, **85**, 045504 (2012).

[52] N. Ackerman *et al. An improved measurement of the $2\nu\beta\beta$ half-life of ^{136}Xe with EXO-200*, Phys. Rev. C, **89** 015502 (2014).

[53] R. Arnold *et al.* (NEMO Collaboration), *Measurement of the $2\nu\beta\beta$ decay half-life of ^{150}Nd and a search for $0\nu\beta\beta$ decay processes with the full exposure from the NEMO-3 detector*, Phys. Rev. D **94**, 072003 (2016).

[54] M. Doi and T. Kotan, *Neutrinoless modes of double beta decay*, Prog. Theor. Phys. **89** (1993).

[55] L. Pandola's talk at TAUP 2017

[56] A. S. Barabash and V. B. Brudanin (NEMO), *Investigation of double beta decay with the NEMO-3 detector*, Phys. Atom. Nucl. **74**, 312 (2011).

[57] R. Arnold *et al.* (NEMO Collaboration), *Results of the search for neutrinoless double-β decay in ^{100}Mo with the NEMO-3 experiment*, Phys. Rev. D **92**, 072011 (2015).

[58] F. A. Danevich *et al.*, *Search for double beta decay of ^{116}Cd with enriched $^{116}CdWO_4$ crystal scintillators (Aurora experiment)*, J. Phys. Conf. Ser. **718**, 062009 (2016).

[59] C. Alduino *et al.*, *First Results from CUORE: A Search for Lepton Number Violation via $0\nu\beta\beta$ Decay of ^{130}Te*, arXiv:1710.07988, Submitted to Phys. Rev. Lett. .

[60] A. Gando *et al.* (KamLAND Collaboration), *Search for Majorana Neutrinos near the Inverted Mass Hierarchy Region with KamLAND-Zen*, Phys. Rev. Lett. **117**, 082503 (2016)

[61] E. Caurier, G. Martinez-Pinedo, F. Nowacki, A. Poves and A. P. Zuker, *The Shell model as unified view of nuclear structure*, Rev. Mod. Phys. **77**, 427 (2005).

[62] J. Menéndez, A. Poves, E. Caurier and F. Nowacki, *Disassembling the Nuclear Matrix Elements of the Neutrinoless beta beta Decay*, Nucl. Phys. A **818**, 139 (2009).

[63] F. Simkovic, V. Rodin, A. Faessler and P. Vogel, *$0\nu\beta\beta$ and $2\nu\beta\beta$ nuclear matrix elements, quasiparticle random-phase approximation, and isospin symmetry restoration*, Phys. Rev. C **87**, 045501 (2013).

[64] J. Hyvarinen and J. Suhonen, *Nuclear matrix elements for $0\nu\beta\beta$ decays with light or heavy Majorana-neutrino exchange*, Phys. Rev. C **91**, 024613 (2015).

[65] J. Barea, J. Kotila and F. Iachello, *$0\nu\beta\beta$ and $2\nu\beta\beta$ nuclear matrix elements in the interacting boson model with isospin restoration*, Phys. Rev. C **91**, 034304 (2015).

[66] V. A. Rodin, A. Faessler, F. Simkovic and P. Vogel, *On the uncertainty in the $0\nu\beta\beta$ decay nuclear matrix elements*, Phys. Rev. C **68**, 044302 (2003).

[67] V. A. Rodin, A. Faessler, F. Simkovic and P. Vogel, *Assessment of uncertainties in QRPA $0\nu\beta\beta$ nuclear matrix elements*, Nucl. Phys. A **766**, 107 (2006).

[68] J. Barea, J. Kotila and F. Iachello, *Nuclear matrix elements for double-decay*, Phys. Rev. C **87**, 014315 (2013).

[69] F. Simkovic, G. Pantis, J. D. Vergados and A. Faessler, *Additional nucleon current contributions to neutrinoless double beta decay*, Phys. Rev. C **60**, 055502 (1999).

[70] F. Cappuzzello, M. Cavallaro, C. Agodi, M. Bondi, D. Carbone, A. Cunsolo and A. Foti, *Heavy-ion double charge exchange reactions: a tool towards $0\nu\beta\beta$ nuclear matrix elements*, Eur. Phys. J. A **51**, 145 (2015).

[71] J. Kostensalo, M. Haaranen and J. Suhonen, *Electron spectra in forbidden β decays and the quenching of the weak axial-vector coupling constant g_A*, Phys. Rev. C **95**, 044313 (2017).

[72] F. Capozzi, E. Di Valentino, E. Lisi, A. Marrone, A. Melchiorri and A. Palazzo, *Global constraints on absolute neutrino masses and their ordering*, Phys. Rev. D **95**, 096014 (2017).

[73] C. Kraus *et al.*, *Final results from phase II of the Mainz neutrino mass search in tritium beta decay*, Eur. Phys. J. C **40**, 447 (2005).

[74] V. N. Aseev *et al.*, *An upper limit on electron antineutrino mass from Troitsk experiment*, Phys. Rev. D **84**, 112003 (2011).

[75] J. Angrik *et al.* (KATRIN Collaboration), *KATRIN design report 2004* (2005).

[76] P. J. Doe *et al.* (Project 8 Collaboration), *Project 8: Determining neutrino mass from tritium beta decay using a frequency-based method*, arXiv:1309.7093.

[77] L. Gastaldo *et al.*, T*he Electron Capture ^{163}Ho Experiment ECHo: an overview*, J. Low Temp. Phys. **176**, 876 (2014).

[78] B. Alpert *et al.*, *HOLMES - The Electron Capture Decay of ^{163}Ho to Measure the Electron Neutrino Mass with sub-eV sensitivity*, Eur. Phys. J. C **75**, 112 (2015).

[79] M. P. Croce *et al.*, *Development of holmium-163 electron-capture spectroscopy with transition edge sensors*, J. Low. Temp. Phys. **184**, 958 (2016).

[80] P. A. R. Ade *et al.* (Planck Collaboration), *Planck 2015 results. XIII. Cosmological parameters*, Astron. Astrophys. **594**, A13 (2016).

[81] N. Palanque-Delabrouille *et al.*, *Constraint on neutrino masses from SDSS-III/BOSS Lyα forest and other cosmological probes*, J. Cosm. Astropart. Phys. **1502**, 045 (2015).

[82] A. J. Cuesta, V. Niro and L. Verde, *Neutrino mass limits: robust information from the power spectrum of galaxy surveys*, Phys. Dark Univ. **13**, 77 (2016).

[83] E. Di Valentino, E. Giusarma, O. Mena, A. Melchiorri and J. Silk, *Cosmological limits on neutrino unknowns versus low redshift priors*, Phys. Rev. D **93**, 083527 (2016).

[84] E. Giusarma, M. Gerbino, O. Mena, S. Vagnozzi, S. Ho and K. Freese, *Improvement of cosmological neutrino mass bounds*, Phys. Rev. D **94**, 083522 (2016).

[85] N. Palanque-Delabrouille *et al.*, *Neutrino masses and cosmology with Lyman-alpha forest power spectrum*, J. Cosm. Astropart. Phys. **1511**, 011 (2015).

[86] X. Zhang, *Impacts of dark energy on weighing neutrinos after Planck 2015*, Phys. Rev. D **93**, 083011 (2016).

[87] G. Benato, *Effective Majorana Mass and Neutrinoless Double Beta Decay*, Eur. Phys. J. C **75**, 563 (2015).

[88] S. Dell'Oro *Optimization of the CUORE detector during the commissioning phase*, Ph.D. Thesis, Gran Sasso Science Institute (2017).

[89] W. Haxton and G. J. Stephenson *Double Beta Decay* Prog. Part. Nucl. Phys. **12**, 409 (1984).

[90] J. S. Cushman, *A search for neutrinoless double-beta decay in tellurium-130 with CUORE*, Ph.D. Thesis, Yale University (2018).

[91] S. Dell'Oro *et al.*, *The contribution of light Majorana neutrinos to neutrinoless double beta decay and cosmology* J. Cosm. Astropart. Phys **1512**, 12 (2015).

[92] S. R. Elliott and P. Vogel, *Double beta decay*, Ann. Rev. Nucl. Part. Sci. **52**, 115 (2002).

[93] J. J. Gómez-Cadenas and J. Martìn-Albo, *Phenomenology of neutrinoless double beta decay*, PoSGSSI14, 004 (2015).

[94] S. Dell'Oro, S. Marcocci and F. Vissani, *New expectations and uncertainties on neutrinoless double beta decay*, Phys. Rev. D **90**, 033005 (2014).

[95] D. R. Artusa *et al.* (CUORE Collaboration), S*earching for neutrinoless double-beta decay of* ^{130}*Te with CUORE*, Adv. High Energy Phys. **2015**, 879871 (2015).

[96] M. Agostini *et al.* (GERDA Collaboration), *Background free search for neutrinoless double beta decay with GERDA Phase II*, Nature **544**, 47 (2017).

[97] R. Arnold *et al.* (NEMO Collaboration), *Technical design and performance of the NEMO 3 detector*, Nucl. Instrum. Meth. A **536**, 122 (2005).

[98] C. Arnaboldi *et al.* (CUORE Collaboration), *A calorimetric search on double beta decay of Te-130*, Phys. Lett. B **557**, 167 (2003).

[99] E. Andreotti *et al.*, ^{130}*Te neutrinoless double-beta decay with Cuoricino*, Astropart. Phys. **34**, 822 (2011).

[100] K. Alfonso *et al.* (CUORE Collaboration), *Search for Neutrinoless Double-Beta Decay of* ^{130}*Te with CUORE-0*, Phys. Rev. Lett. **115**, 102502 (2015).

[101] K. H. Ackermann *et al.* (GERDA Collaboration), *The GERDA experiment for the search of* $0\nu\beta\beta$ *decay in* ^{76}*Ge*, Eur. Phys. J. C **73**, 2330 (2013).

[102] C. Macolino (GERDA Collaboration), *Search for neutrinoless double beta decay with the GERDA experiment*, Nuovo Cim. C **036**, 13–20 (2013).

[103] R. S. Raghavan, *New approach to the search for neutrinoless double beta decay*, Phys. Rev. Lett. **72**, 1411 (1994).

[104] S. Abe *et al.* (KamLAND Collaboration) *Production of radioactive isotopes through cosmic muon spallation in KamLAND*, Phys. Rev. C **81**, 025807 (2010).

[105] A. Gando *et al.* (KamLAND-Zen Collaboration), *Measurement of the double-*β *decay half-life of* ^{136}*Xe with the KamLAND-Zen experiment*, Phys. Rev. C **85**, 045504 (2012).

[106] J. J. Gomez-Cadenas *et al.* (NEXT Collaboration), *Present status and future perspectives of the NEXT experiment*, Adv. High Energy Phys. **2014**, 907067 (2014).

[107] D. Nygren, *High-pressure xenon gas electroluminescent TPC for* $0\nu\beta\beta$*-decay search*, Nucl. Instrum. Meth. A **603**, 337 (2009).

[108] M. Auger *et al.* (EXO Collaboration), *The EXO-200 detector, part I: Detector design and construction*, J. of Instrum. **7**, P05010 (2012).

[109] J. B. Albert *et al.* (EXO-200 Collaboration), *Improved measurement of the* $2\nu\beta\beta$ *half-life of* ^{136}*Xe with the EXO-200 detector*, Phys. Rev. C **89** 015502 (2014).

[110] J. B. Albert *et al.* (EXO-200 Collaboration), *Search for Majorana neutrinos with the first two years of EXO-200 data*, Nature **510**, 229-234 (2014).

[111] M. Auger *et al.* (EXO Collaboration), *Search for neutrinoless double-beta decay in* ^{136}*Xe with EXO-200*, Phys. Rev. Lett. **109**, 032505 (2012).

[112] J. Albert, *Status and results from the EXO Collaboration*, *EPJ Web Conf.* **66**, 08001 (2014).

[113] J. Boger *et al.* (SNO Collaboration), *The Sudbury neutrino observatory*, Nucl. Instrum. Meth. A **449**, 172 (2000).

[114] S. Andringa (SNO+ Collaboration), *Current Status and Future Prospects of the SNO+ Experiment* , Adv. High Energy Phys. **2016**, 6194250 (2016).

[115] C. Enss and H. Siegfried, *Low-Temperature Physics*, Springer (2005).

[116] Y. Levinson, *Nonequilibrium phonons in nonmetallic crystals*, Modern Problems in Condensed Matter Sciences **16**, 91-143 (1986).

[117] A. Alessandrello *et al.*, *Preliminary results on the performance of a TeO-2 thermal detector in a search for direct interactions of WIMPs*, Phys. Lett. B **384**, 316-322 (1996).

[118] A. Giachero, *Assess the neutrino mass with micro and macro calorimeter approach*, J. Phys. Conf. Ser. **841**, 012027 (2017).

[119] G. Angloher *et al.*, *Results on low mass WIMPs using an upgraded CRESST-II detector*, Eur. Phys. J. C **74** 3184 (2014).

[120] M. Pedretti, *The single module for Cuoricino and CUORE detectors: tests, construction and modeling*, Ph.D. Thesis, University of Insubria (2004).

[121] M. Vignati, *Model of the Response Function of CUORE Bolometers*, Ph.D. Thesis, La Sapienza University of Rome (2009).

[122] E. E. Haller, N. P. Palaio, M. Rodder, W. L. Hansen and E. Kreysa, *NTD Germanium: A Novel Material for Low Temperature Bolometers* In: Larrabee R.D. (eds) Neutron Transmutation Doping of Semiconductor Materials. Springer, Boston, MA.

[123] N. F. Mott, *Conduction in non-crystalline materials*, Philos. Mag. **19**, 835 (1969).

[124] B. I. Shklovskii and A. L. Efros, *Electronic Properties of Doped Semiconductors*, Springer (1984).

[125] P. Carniti, L. Cassina, A. Giachero, C. Gotti, and G. Pessina, *A High Precision Pulse Generation and Stabilization System for Bolometric Experiments*, arXiv:1710.05565v2

[126] A. Alessandrello *et al.*, *Large mass, low-temperature, low background detectors*, Nucl. Instrum. Meth. A **315**, 263 (1992).

[127] A. Giuliani *et al.*, *A low-temperature TeO2 detector to search for double beta decay of 130Te*, Proc. European Phys. Soc. Conf. on High-energy Phys. **670** (1991).

[128] A. Alessandrello *et al.*, *A search for neutrinoless double beta decay of 130Te with a bolometric detector*, Nucl. Phys. B (Proc. Suppl.) **28**, 229 (1992).

[129] A. Alessandrello *et al.*, *Milano experiment on $0\nu\beta\beta$ decay of 130Te with a thermal detector*, Nucl. Phys. B (Proc. Suppl.) **31**, 83 (1993).

[130] A. Alessandrello *et al.*, *A New search for neutrinoless beta beta decay with a thermal detector*, Phys. Lett. B **335**, 519 (1994).

[131] A. Giuliani *et al.*, *The Milano-Gran Sasso experiment on double beta decay using thermal detectors*, Proc. 27th Int. Conf. on High-energy Phys. **943** (1994).

[132] C. Brofferio *et al.*, *Improvements in Te-130 double beta decay search with cryogenic TeO-2 array detectors*, Nucl. Phys. B (Proc. Suppl.) **48**, 238 (1996).

[133] C. Alduino *et al.* (CUORE Collaboration), *Analysis techniques for the evaluation of the neutrinoless double-β decay lifetime in ^{130}Te with the CUORE-0 detector*, Phys. Rev. C **93**, 045503 (2016).

[134] F. Alessandria *et al.* (CUORE Collaboration), *Sensitivity of CUORE to Neutrinoless Double- Beta Decay*, arXiv:1109.0494 [nucl-ex] (2011).

[135] C. Arnaboldi *et al.*, *Production of high purity TeO_2 single crystals for the study of neutrinoless double beta decay*, J. Cryst. Growth **312**, 2999 (2010).

[136] A. De Biasi *et al.*, *Surface Treatments for Ultra-Cleaning of CUORE copper Parts* LNL-INFN (REP) 173/ 2009.

[137] S. Pirro *et al.*, *Development of bolometric light detectors for double beta decay searches* , Nucl. Instrum. Meth. A**559**, 361-363 (2006).

[138] C. Alduino *et al.* (CUORE Collaboration), *CUORE-0 detector: design, construction and operation*, J. Instrum. **11**, P07009 (2016).

[139] C. Alduino *et al.* (CUORE Collaboration), *The projected background for the CUORE experiment*, Eur. Phys. J. C **77**, 543 (2017).

[140] G. Wang *et al.* (CUPID Interest Group) *CUPID, CUORE Upgrade with Particle IDentification*, arXiv:1504.03599 (2015).

[141] D. R. Artusa *et al.* (CUORE Collaboration),*Exploring the Neutrinoless Double Beta Decay in the Inverted Neutrino Hierarchy with Bolometric Detectors*, Eur. Phys. J. C **74**, 3096 (2014).

[142] G. Wang *et al.* (CUPID Interest Group), *R&D towards CUPID*, arXiv:1504.03612 (2015).

[143] J. Birks, *The Theory and Practice of Scintillation Counting*, Oxford Pergamon Press, 1964.

[144] V. Tretyak, *Semi-empirical calculation of quenching factors for ions in scintillators*, *Astropart. Phys.* **33** (2010).

[145] S. Nagorny *et al.*, *Quenching factor for alpha particles in ZnSe scintillating bolometers*, IOP Conf. Ser.: Mater. Sci. Eng. **169**, 012011 (2017).

[146] R. Gwin and R. Murray, *Scintillation process in CsI(Tl). i. comparison with activator saturation model*, Phys. Rev **131** (1963).

[147] C. Arnaboldi *et al.*, *Characterization of ZnSe scintillating bolometers for Double Beta Decay*, Astropart. Phys. **34**, 344 (2011).

[148] T. Tabarelli de Fatis, *Cerenkov emission as a positive tag of double beta decays in bolometric experiments*, Eur. Phys. J. C **65**, 359 (2010).

[149] L. Cardani, *ZnSe and $ZnMoO_4$ scintillating bolometers to search for $0\nu\beta\beta$* Ph.D. Thesis, La Sapienza University of Rome (2013).

[150] J. Beeman *et al.*, *A next-generation neutrinoless double beta decay experiment based on $ZnMoO_4$ scintillating bolometers*, Phys. Lett. B **710**, 318 (2012).

[151] D. Chernyak *et al. Random coincidence of $2\nu2\beta$ decay events as a background source in bolometric $0\nu2\beta$ decay experiments*, Eur. Phys. J. C **72**, 1 (2012).

[152] J. W. Beeman *et al.*, *Effect of SiO_2 coating in bolometric Ge light detectors for rare event searches*, Nucl. Instrum. and Meth. A **709**, 22-28 (2013).

[153] J. W. Beeman *et al.*, *Characterization of bolometric light detectors for rare event searches*, J. of Instrum. **1307**, P07021 (2013).

[154] D.R. Artusa *et al.*, *Enriched TeO_2 bolometers with active particle discrimination: towards the CUPID experiment*, Phys. Lett. B **767**, 321-329 (2017).

[155] L. Gironi *et al.*, *Cerenkov light identification with Si low-temperature detectors with sensitivity enhanced by the Neganov-Luke effect*, Phys. Rev. C **94** 054608 (2016).

[156] J W Beeman, *et al.*, *Performances of a large mass ZnSe bolometer to search for rare events*, J. of Instrum. **8** P05021 (2013).

[157] D. R. Artusa *et al.*, *First array of enriched $Zn^{82}Se$ bolometers to search for double beta decay*, Eur. Phys. J. **C76**, 364 (2016).

[158] H. Okada, T. Kawanaka, S. Ohmoto, *Study on the ZnSe phase diagram by differential thermal analysis*, J. Cryst. Growth **165** (1996).

[159] R.C. Sharma and Y.A. Chang, *The Cd-Se system* J. Phase Equilibria **17**, 2 (1996).

[160] M.P. Kulakov *et al.*, *Phase transition in zinc selenide crystals*, Sov. Phys-Solid State **18**, 3 (1976).

[161] I. Kikuma and M. Furukoshi, *Direct observation of the 3C-2H transformation in ZnSe by high-temperature x-ray diffraction*, J. Cryst. Growth **71**, 136-140 (1985).

[162] L. V. Atroshchenko, E. F. Voronkin, S. N. Galkin, A. I. Lalayants, I. A. Rybalka, V. D. Ryzhikov, A. G. Fedorov, *Effect of Tellurium Doping on the Structural Perfection of ZnSe*, Inorganic Materials **40**, 6 (2004).

[163] I. Kikuma, M. Matsuo and T. Komuro, *Growth and Properties of ZnSe Crystals by a Modified Bridgman Method*, Japanese Journal of Applied Physics **30**, 11A (1991).

[164] I. Dohnke, M. Mühlberg and W. Neumann, *Structural Perfection of ZnSe Crystals Grown by Traveling Heater Method*, Crystal Research and Technology **32**, 8 (1997).

[165] M. Laubenstein and G. Heusser, *Cosmogenic radionuclides in metals as indicator for sea level exposure history,* Applied Radiation and Isotopes **67**, 5 (2009).

[166] C. Arnaboldi *et al.*, *Production of high purity TeO_2 single crystals for the study of neutrinoless double beta decay*, J. Cryst. Growth. **312**, 2999-3008 (2010).

[167] S. Nagorny, *High purity zinc for CUPID-0 experiment*, Article in progress.

[168] P. Benetti *et al.*, *Synthesis of ^{82}Se enriched ZnSe for double beta decay experiments*, Procs. SPLG **2012**, 38-43 (2012).

[169] P. Benetti *et al.*, *Enriched isotopes for double beta decays experiments: ^{82}Se and LUCIFER*, Procs. SPLG **2012**, 34-37 (2012).

[170] M. Berglund and M. E. Wieser, *Isotopic compositions of the elements 2009 (IUPAC Technical Report)*, Pure Appl. Chem. **83**, 397-410 (2011).

[171] J.W. Beeman *et al.*, *Double-beta decay investigation with highly pure enriched ^{82}Se for the LUCIFER experiment*, Eur. Phys. J. C **75**, 591 (2015).

[172] V. Ryzhikov *et al.*, *Growing technology and luminescent characteristics of ZnSe doped crystals*, J. Cryst. Growth **364**, 111-117 (2013).

[173] B. Grynyov *et al.*, *Scintillator crystals, Radiation detectors and instruments on their base*, Ukraine, Kharkov: Institute for Single Crystals ISBN 966-02-3314-0 (2004).

[174] J. W. Beeman *et al.*, *Effect of SiO_2 coating in bolometric Ge light detectors for rare event searches*, Nucl. Instr. and Meth. A **22**, 709 (2013).

[175] M. Mancuso *et al.*, *An experimental study of antireflective coatings in Ge light detectors for scintillating bolometers*, Eur. Phys. J Web of Conf. **65**, 04003 (2013).

[176] A. Langenkämper *et al.*, *Low-Temperature Relative Reflectivity Measurements of Reflective and Scintillating Foils used in Rare Event Searches* arXiv:1703.07152 (2017).

[177] I. Dafinei *et al.*, *Low Temperature Scintillation in ZnSe Crystals Transactions*, IEEE Trans. Nucl. Science **57**, 1470-1474 (2010).

[178] S. Nisi *et al.*, *ICP-MS measurement of natural radioactivity at LNGS* Int. J. Mod. Phys. A **32**, 1743003 (2017).

[179] J.W. Beeman *et al.*, *Current Status and Future Perspectives of the LUCIFER Experiment*, Adv. High Energy Phys. **2013**, 237973 (2013).

[180] A. Borio di Tigliole *et al.*, *Benchmark Evaluation of Reactor Critical Parameters and Neutron Fluxes Distributions at zero power for the TRIGA MARK II reactor of the University of Pavia using the Monte Carlo code MCNP*, Progr. Nucl. Energy **52**, 494-502 (2010).

[181] A. Borio di Tigliole *et al.*, *TRIGA reactor absolute neutron flux measurement using activated isotopes*, Progr. Nucl. Energy **70**, 249-255 (2014).

[182] `http://www.huntsman.com/advanced_materials/a/Home`

[183] C. Rusconi, *Optimization of the bolometric performances of the CUORE-0/CUORE and LUCIFER detectors for the neutrinoless double beta decay search*, Ph.D. Thesis, Insubria University, Italy (2011).

[184] F. Alessandria *et al.*, *Validation of techniques to mitigate copper surface contamination in CUORE*, Astropart. Phys. **45**, 13-22 (2013).

[185] M. Clemenza *et al.*, *Radon-induced surface contaminations in low background experiments*, Eur. Phys. J. C **71**, 1805 (2011).

[186] E. Andreotti *et al.*, *The low radioactivity link of the CUORE experiment*, J. of Instrum. **4**, P09003 (2009).

[187] S. Pirro, *Further developments in mechanical decoupling of large thermal detectors*, Nucl. Instrum. Meth. A5 **59**, 672-674 (2006).

[188] C. Arnaboldi et al., *Front-end electronic systems for large arrays of bolometric experiments*, arXiv:1710.06365 (2017) , submitted to JINST (to be updated).

[189] S. Pirro, *Study of a large mass detector to search for double beta decay and rare events*, Ph.D. Thesis, University of Milano (2000).

[190] C. Arnaboldi at al.,*A programmable multichannel antialiasing filter for the CUORE experiment* , Nucl. Instr. Meth. Phys. Res. A **617**, (2010) 327.

[191] P. Carniti et al., *A High Precision Pulse Generation and Stabilization System for Bolometric Experiments*, arXiv:1710.05565 (2017), submitted to JINST (to be updated).

[192] C. Arnaboldi et al., *Very low noise AC/DC power supply systems for large detector arrays.*, Rev. Sci. Instrum. **86**, (2015) 124703.

[193] P. Carniti et al., *A low noise and high precision linear power supply with thermal foldback protection*, Rev. Sci. Instrum. **87**, (2016) 054706.

[194] C. Alduino *et al.*, *Low energy analysis techniques for CUORE*, Eur. Phys. J. C **77**, 857 (2017).

[195] E. Gatti and P. Manfredi, *Processing the signals from solid-state detectors in elementary-particle physics*, La Rivista del Nuovo Cimento **9**, 1 (1986).

[196] A. Alessandrello *et al.*, *Methods for response stabilization in bolometers for rare decays*, Nucl. Instrum. Meth. A **412**, 454-464 (1998) .

[197] G. Piperno, S. Pirro and M. Vignati, *Optimizing the energy threshold of light detectors coupled to luminescent bolometers* , J. of Instrum. **6** P10005 (2011).

[198] W. Verkerke and D. Kirkby, arXiv:physics/0306116 [physics.data-an] (2003).

[199] D. L. Lincoln *et al.*, *First Direct Double-Beta Decay Q-value Measurement of* ^{82}*Se in Support of Understanding the Nature of the Neutrino*, Phys. Rev. Lett. **110**, 012501 (2013).

[200] J. Kotila and F. Iachello, *Phase space factors for double-β decay*, Phys. Rev. C**85**, 034316 (2012).

[201] S. Stoica and M. Mirea, *New Calculations for Phase Space Factors Involved in Double Beta Decay*, Phys. Rev. C **88**, 037303 (2013).

[202] J. Engel and J. Menendez, *Status and Future of Nuclear Matrix Elements for Neutrinoless Double-Beta Decay: A Review*, Rept. Prog. Phys. **80**, 046301 (2017).

[203] J. M. Yao, L. S. Song, K. Hagino, P. Ring, and J. Meng, *Systematic study of nuclear matrix elements in neutrinoless double-beta decay with a beyond mean-field covariant density functional theory*, Phys. Rev. C **91**, 024316 (2015).

[204] J. Menendez, A. Poves, E. Caurier, and F. Nowacki, *Disassembling the Nuclear Matrix Elements of the Neutrinoless double beta Decay*, Nucl. Phys. A **818**, 139 (2009).